Determination of the quark coupling strength $|V_{ub}|$ using baryonic decays

William Sutcliffe

High Energy Physics
Blackett Laboratory
Imperial College London

A dissertation submitted to Imperial College London
for the degree of Doctor of Philosophy

Abstract

This thesis presents the first determination of $|V_{ub}|$ at a hadron collider and in a baryonic decay. The determination is made by measuring the ratio of branching fractions of the baryonic decays $\Lambda_b^0 \to p\mu^-\overline{\nu}_\mu$ and $\Lambda_b^0 \to \Lambda_c^+\mu^-\overline{\nu}_\mu$ at large momentum transfer squared. The experimental measurement was made using a $2\,\text{fb}^{-1}$ dataset of pp collision events produced at $\sqrt{s} = 8\,\text{TeV}$ by the Large Hadron Collider and collected by the LHCb experiment in 2012. This is the first observation of the decay $\Lambda_b^0 \to p\mu^-\overline{\nu}_\mu$ for which the branching fraction is measured to be $\mathcal{B}_{\Lambda_b^0 \to p\mu^-\overline{\nu}_\mu} = (4.1 \pm 1.0) \times 10^{-4}$. Combining the measured experimental ratio with the latest Lattice QCD predictions for the form factors of $\Lambda_b^0 \to p\mu^-\overline{\nu}_\mu$ and $\Lambda_b^0 \to \Lambda_c^+\mu^-\overline{\nu}_\mu$ decays results in a determination of the ratio of CKM elements, $|V_{ub}|/|V_{cb}| = 0.083 \pm 0.004 \pm 0.004$, where the first uncertainty is experimental and the second uncertainty is theoretical. This precision determination of $|V_{ub}|/|V_{cb}|$ provides an important constraint for global fits of the CKM sector of the Standard Model. Finally, combining the ratio CKM elements, $|V_{ub}|/|V_{cb}|$, with the world average of $|V_{cb}|$ from exclusive measurements allows for a determination of the CKM matrix element $|V_{ub}| = (3.27 \pm 0.15 \pm 0.16 \pm 0.06) \times 10^{-3}$. Here the first uncertainty is experimental, the second uncertainty is theoretical and the final uncertainty is from $|V_{cb}|$. While the measurement agrees well with measurements of $|V_{ub}|$ made using $\overline{B}^0 \to \pi^+ l^- \bar{\nu}_l$ decays the measurement is 3.5σ below the world average of $|V_{ub}|$ from inclusive $B \to X_u l^- \bar{\nu}_l$ decays. This reinforces the long-standing tension between inclusive and exclusive measurements of $|V_{ub}|$.

Declaration

The experimental analysis of $\Lambda_b^0 \to p\mu^-\overline{\nu}_\mu$ and $\Lambda_b^0 \to \Lambda_c^+\mu^-\overline{\nu}_\mu$ decays performed within this thesis was performed by myself, Patrick Owen and Ulrik Egede as collaborators of the LHCb experiment. All of the associated analysis work presented in the thesis are my own contributions apart from that of the normalisation fit and relative efficiency calculation in sections 7.1 and 7.4 of chapter 7, respectively. The work in this thesis was presented publically for the first time at Moriond Electroweak 2015 and is published in [1].

William Sutcliffe, 2015

Acknowledgements

First and foremost, I would like to thank my supervisor, Ulrik Egede, for all his suggestions and guidance throughout my PhD and of course for having the brilliant idea of measuring $|V_{ub}|$ with $\Lambda_b^0 \to p\mu^-\overline{\nu}_\mu$ decays at the LHC, although, seemingly impossible when I first started the PhD. Secondly, I would like to thank Patrick Owen who I worked closely with on the measurement of $|V_{ub}|$ from $\Lambda_b^0 \to p\mu^-\overline{\nu}_\mu$ decays and the measurement would not be possible without. I learnt a huge amount working with Patrick and it was a highly enjoyable experience.

When I started my PhD there were no competitive theoretical predictions for the $\Lambda_b^0 \to p\mu^-\overline{\nu}_\mu$ form factors. Luckily, Stefan Meinel took the massive undertaking upon himself to pioneer a precision determination of the $\Lambda_b^0 \to p\mu^-\overline{\nu}_\mu$ and $\Lambda_b^0 \to \Lambda_c^+\mu^-\overline{\nu}_\mu$ form factors. In addition, Stefan was extremely helpful in written communication when it came to implementing his form factor predictions. Additional thanks go to Winston Roberts for helpful discussions regarding the $\Lambda_b^0 \to N^{*+}\mu^-\overline{\nu}_\mu$ form factors.

A special thanks must also go to the reviewers of the analysis Till Moritz Karbach and Marcello Rotondo. Moritz Karbach, who sadly has passed away, played a key role together with Florian Bernlochner in determining the implication of the $|V_{ub}|$ measurement from $\Lambda_b^0 \to p\mu^-\overline{\nu}_\mu$ decays on a right-handed coupling.

My time at CERN would not have been there same were it not for fellow PhD students Nik Berry, Eluned Smith, Daniel Souza and Jackson Smith, who made it an unforgetable experience. Finally, I thank my friends, family and girlfriend for all their support throughout my PhD and writing this thesis.

Contents

Chapter 1.

Introduction

In the Standard Model of particle physics, quarks and leptons come in three generations each containing a pair of up and down-type quarks or a charged lepton and a neutrino. The properties of quark and lepton pairs in each generation are identical except for their masses. The masses of the quarks and charged leptons are generated from their couplings to the Higgs field. These couplings lead to a puzzling hierarchy between the masses of quarks and charged leptons across generations. Furthermore, the reason for exactly three generations remains a mystery of nature.

The charged weak interactions are the only interactions which allow a change of flavour between quarks and leptons. This was first observed with the discovery of radioactive β^- emissions by Henri Becquerel in 1896 which was later realised to be described by the weak $d \to u$ transition

$$n \to p e^- \bar{\nu}_e \ , \tag{1.1}$$

where a neutron, with quark content udd, decays to a proton (uud) and in the process a electron and its anti-neutrino are emitted. While the weak force only couples leptons to neutrinos within generations, for quarks cross-generational couplings are possible. In addition, while the weak coupling for leptons to neutrinos is universal across the generations, for quarks the couplings are proportional to the elements of the Cabibbo-Kobayashi-Maskawa (CKM) matrix [2, 3]

$$V^{CKM} = \begin{pmatrix} V_{ud} & V_{us} & V_{ub} \\ V_{cd} & V_{cs} & V_{cb} \\ V_{td} & V_{ts} & V_{tb} \end{pmatrix} . \tag{1.2}$$

This structure arises from the cross-generational couplings of quarks to the Higgs boson which leads to a misalignment between the weak and mass eigenstates for quarks. The CKM matrix has an almost diagonal structure as illustrated in Fig 1.1. The smallest and least known element is $|V_{ub}|$ (see Fig 1.1) with $|V_{tb}| : |V_{cb}| : |V_{ub}| \approx \mathcal{O}(1) : \mathcal{O}(0.01) : \mathcal{O}(0.001)$. The hierarchy between the cross-generational couplings again presents another puzzling feature of the Standard Model. An important characteristic of the CKM matrix is that it is unitary. This provides for an essential test of the Standard Model.

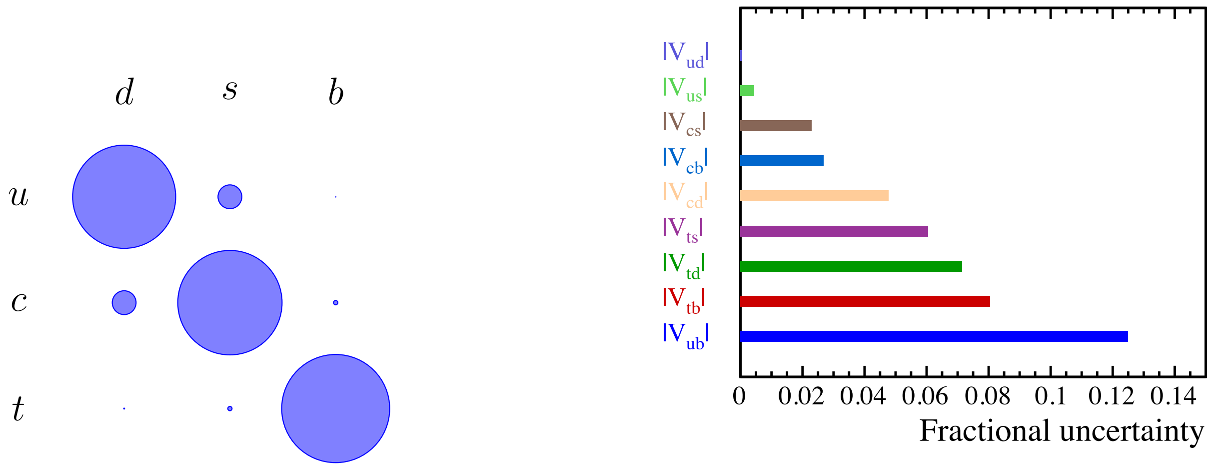

Figure 1.1: Illustration of the magnitudes of the CKM matrix elements, which displays an almost diagonal structure (left). The matrix element $|V_{ub}|$ is the smallest of the CKM matrix elements and it has the largest fractional uncertainty as shown on the right.

The CKM matrix may be parametrised by three real mixing angles and one complex phase. The complex phase leads to CP violation, where C refers to a charge conjugation transformation, $Ce^- \to e^+$, and P is a parity transformation, $Px_i \to -x_i$. A violation of CP in the laws of nature is required to explain the matter anti-matter asymmetry observed in the universe today [4]. Three generations of quarks and leptons is the minimum number of generations for there to be CP violation in the quark sector, which provides a potential explanation for the three generations of nature. However, the CP violation observed in the quark sector is around nine orders of magnitude too small to account for the observed matter-antimatter assymetry in the universe.

To test the unitarity of the CKM matrix and precisely determine the amount of CP violation in the quark sector it is necessary to constrain the parameters of the CKM sector using measurements of a number of observables including the magnitudes of the CKM matrix elements. The large uncertainty on $|V_{ub}|$ is one of the limiting factors in global fits for the four parameters of the CKM sector.

The best existing measurements of $|V_{ub}|$ have been made by the e^+e^- collider beauty factory experiments BaBar [5–7] and Belle [8–10] using semileptonic exclusive $\overline{B}^0 \to \pi^+ l^- \bar{\nu}_l$ and inclusive $B \to X_u l^- \bar{\nu}_l$ decays. The world averages for these approaches are $|V_{ub}| = (3.28 \pm 0.29) \times 10^{-3}$ (exclusive) and $|V_{ub}| = (4.41 \pm 0.15^{+0.15}_{-0.17}) \times 10^{-3}$ (inclusive) [11]. In the exclusive scenario, the dominant uncertainty arises in predicting the influence of QCD on the decay. The nature of these interactions can be encompassed within a form factor which is computed using non-perturbative techniques such as lattice QCD (LQCD) [12] or QCD sum rules [13]. In the inclusive case the differential rate for all possible B meson decays containing a $b \to u l^- \bar{\nu}$ quark level transition is measured. The differential rate is measured in a specific regions of phase space where the background from $b \to c l^- \bar{\nu}$ decays is small. Theoretical predictions for the differential rate in these regions of phase space allow for $|V_{ub}|$ to be determined. The theoretical predictions require a modelling of the probability density distribution for the momentum of the b quark, known as the shape function. The choice of model for the shape function and the limited precision on the mass of b quark result in the dominant uncertainties. The discrepancy between inclusive and exclusive measurements is approximately three standard deviations and has been a long-standing puzzle in flavour physics.

At the Large Hadron Collider, the large production of Λ_b^0 baryons opens up the possibility of a novel exclusive measurement of $|V_{ub}|$ from $\Lambda_b^0 \to p \mu^- \overline{\nu}_\mu$ decays. This thesis presents this measurement, with the aim of providing further insight on the $|V_{ub}|$ puzzle. This is the first determination of $|V_{ub}|$ at a hadron collider and in a baryonic decay. The measurement is made by measuring the ratio of branching fractions of $\Lambda_b^0 \to p \mu^- \overline{\nu}_\mu$ and $\Lambda_b^0 \to \Lambda_c^+ \mu^- \overline{\nu}_\mu$ decays using pp collision events produced by Large Hadron Collider and collected by the LHCb experiment in 2012. The measured ratio, when combined with theoretical input, allows for a precision determination of ratio of CKM elements $|V_{ub}|/|V_{cb}|$. This provides an important constraint for global fits testing the unitarity of the CKM matrix. From the ratio of CKM elements, $|V_{ub}|$ is determined by using the world average of $|V_{cb}|$ from exclusive measurements. In addition, a measurement of the branching fraction of $\Lambda_b^0 \to p\mu^-\overline{\nu}_\mu$ decays, which are observed for the first time, is provided.

This thesis is structured as follows. Chapter 2 provides the reader with an overview of the relevant theoretical framework for the measurement, which includes introductions to the Standard Model, the CKM sector, the matrix elements of semileptonic b-hadron decays and Lattice QCD. Chapter 3 gives a description of the data-taking conditions and the experimental setup. Chapter 4 briefly outlines the strategy for the measurement of $|V_{ub}|$ at the Large Hadron Collider, which includes the justification for a measurement made using $\Lambda_b^0 \to p\mu^-\overline{\nu}_\mu$ decays. Folllowing on from this the main analysis work is split between chapters 5 , 6 and 7. Chapter 5 discusses the implementation of form factors required to model signal, normalisation and background decays in the analysis. After introducing the backgrounds considered, Chapter 6 describes the simulation samples produced for the analysis and the selections made for $\Lambda_b^0 \to p\mu^-\overline{\nu}_\mu$ and $\Lambda_b^0 \to \Lambda_c^+\mu^-\overline{\nu}_\mu$ candidates. Leading on from this, chapter 7 presents the main analysis work performed on the simulated samples and the candidates selected in data. Chapter 7 concludes by presenting the measurements of $|V_{ub}|$, $|V_{ub}|/|V_{cb}|$ and $\mathcal{B}_{\Lambda_b^0 \to p\mu^-\overline{\nu}_\mu}$. Finally, the implications of the measurements are discussed in chapter 8 which leads on to the conclusions of the thesis in chapter 9.

Chapter 2.

The Standard Model

2.1. The Standard Model

2.1.1. The Standard Model Lagrangian and local gauge invariance

The Standard Model (SM) is an $SU(3) \times SU(2) \times U(1)$ gauge theory describing the interactions of leptons and quark with the strong, weak and electromagnetic forces [14–20].

Particle chirality, which is defined by whether a particle transforms in a left-handed or right-handed representation of the Poincare group, has an important role in the Standard Model. Left-handed up and down-type quark pairs, Q_{Lm}, and charged and neutral lepton pairs, L_{Lm}, are doublet representations of $SU(2)$, as defined in table 2.1. Meanwhile, right-handed up and down-type quarks, u_{Rm} and d_{Rm}, and right-handed charged leptons, l_{Rm}, are singlets of $SU(2)$. In addition, quarks come in three colours which transform as a triplet representation of SU(3); this leads to the quark-gluon interactions of QCD described in more detail in section 2.4.1. The neutrinos, which only interact via the weak force, are assumed to be massless in the Standard Model, therefore no right-handed neutrino singlets are included in the theory.

Under a local $SU(3) \times SU(2) \times U(1)$ group transformation, quark and lepton fields transform as the representations defined in table 2.1. For instance, the quark doublet Q_{Lm} which carries the

$SU(3) \times SU(2) \times U(1)$ representation, $(\underline{3}, \underline{2}, \frac{1}{6})$, transforms as

$$\begin{aligned} Q_{Lm} \to Q'_{Lm} &= \exp\left(\frac{i}{2}\theta(x)\cdot\lambda + \frac{i}{2}\varepsilon(x)\cdot\sigma + iY\rho(x)\right) Q_{Lm} \\ &= \exp\left(\frac{i}{2}\theta(x)\cdot\lambda + \frac{i}{2}\varepsilon(x)\cdot\sigma + \frac{i}{6}\rho(x)\right) Q_{Lm} \ , \end{aligned} \tag{2.1}$$

where $\theta = \{\theta_1, \theta_2, \cdots, \theta_8\}$, $\varepsilon = \{\varepsilon_1, \varepsilon_2, \varepsilon_3\}$ and ρ parametrise the transformation and $\lambda/2 = \{\lambda_1/2, \lambda_2/2, \cdots, \lambda_8/2\}$, $\sigma/2 = \{\sigma_1/2, \sigma_2/2, \sigma_3/2\}$[1] and Y are the generators of the group transformations for the groups $SU(3)$, $SU(2)$ and $U_Y(1)$, respectively. While the Dirac kinetic terms for spinor fields, $i\overline{Q}_{Lm}\gamma_\mu\partial_\mu Q_{Lm}$, are not locally invariant under such transformations, this can be resolved by including couplings to gauge fields, $G_\mu^{i=1,\cdots,8}$, $W_\mu^{i=1,2,3}$ and B_μ such that

$$i\overline{Q}_{Lm}\gamma^\mu D_\mu Q_{Lm} = i\overline{Q}_{Lm}\gamma^\mu(\partial_\mu - \frac{i}{2}g_3 G_\mu\cdot\lambda - \frac{i}{2}g_2 W_\mu\cdot\sigma - \frac{i}{6}g_1 B_\mu)Q_{Lm} \ . \tag{2.2}$$

where g_1, g_2, and g_3 are the associated coupling strengths. Under the local $SU(3) \times SU(2) \times U_Y(1)$ group transformation, the gauge fields undergo a coordinated gauge transformation such that

$$\overline{Q}_{Lm}\gamma^\mu D_\mu Q_{Lm} \to \overline{Q}'_{Lm}\gamma^\mu D'_\mu Q'_{Lm} = \overline{Q}_{Lm}\gamma^\mu D_\mu Q_{Lm} \ . \tag{2.3}$$

The Lagrangian of the Standard Model,

$$\mathcal{L}_{SM} = \mathcal{L}_{\text{kinetic\&gauge}} + \mathcal{L}_{\text{Higgs}} + \mathcal{L}_{\text{Yukawa}} \ , \tag{2.4}$$

is formulated by constructing the most general renormalisable $SU(3) \times SU(2) \times U(1)$ gauge theory describing the particle and group properties displayed in table 2.1

The kinetic and gauge term in the SM Lagrangian is given by

$$\begin{aligned} \mathcal{L}_{\text{kinetic\&gauge}} =& -\frac{1}{4}G_{\mu\nu}\cdot G^{\mu\nu} - \frac{1}{4}W_{\mu\nu}\cdot W^{\mu\nu} - \frac{1}{4}B_{\mu\nu}B^{\mu\nu} - \frac{i}{2}\bar{L}_{Lm}\gamma^\mu D_\mu L_{Lm} \\ & - i\bar{l}_{Rm}\gamma^\mu D_\mu l_{Rm} - i\overline{Q}_{Lm}\gamma^\mu D_\mu Q_{Lm} - i\bar{u}_{Rm}\gamma^\mu D_\mu u_{Rm} - i\bar{d}_{Rm}\gamma^\mu D_\mu d_{Rm} \ , \end{aligned} \tag{2.5}$$

where repeated quark and lepton generation indices m are summed over. The kinetic terms for gauge fields take the form $-\frac{1}{4}G_{\mu\nu}\cdot G^{\mu\nu}$ where $G^i_{\mu\nu}$, $W^i_{\mu\nu}$ and $B_{\mu\nu}$ are the associated field strength tensors.

[1]Here λ_i and σ_i are respectively the Gell-Maan and Pauli matrices.

Lepton fields	$SU(3)$	$SU(2)$	$U_Y(1)$
$L_{Lm=e,\mu,\tau} = \left\{ \begin{pmatrix} \nu_e \\ e_L \end{pmatrix}, \begin{pmatrix} \nu_\mu \\ \mu_L \end{pmatrix}, \begin{pmatrix} \nu_\tau \\ \tau_L \end{pmatrix} \right\}$	$\underline{1}$	$\underline{2}$	$-\frac{1}{2}$
$l_{Rm=e,\mu,\tau} = \{e_R, \mu_R, \tau_R\}$	$\underline{1}$	$\underline{1}$	-1
Quark fields			
$Q_{Lm} = \left\{ \begin{pmatrix} u_L \\ d_L \end{pmatrix}, \begin{pmatrix} c_L \\ s_L \end{pmatrix}, \begin{pmatrix} t_L \\ b_L \end{pmatrix} \right\}$	$\underline{3}$	$\underline{2}$	$\frac{1}{6}$
$u_{Rm=u,c,t} = \{u_R, c_R, t_R\}$	$\underline{3}$	$\underline{1}$	$+\frac{2}{3}$
$d_{Rm=d,s,b} = \{d_R, s_R, b_R\}$	$\underline{3}$	$\underline{1}$	$-\frac{2}{3}$
Gauge fields			
$G_\mu^{i=1,\cdots,8}$	$\underline{8}$	$\underline{1}$	0
$W_\mu^{i=1,2,3}$	$\underline{1}$	$\underline{3}$	0
B_μ	$\underline{1}$	$\underline{1}$	0
Higgs doublet			
$\phi = \begin{pmatrix} \phi^+ \\ \phi^0 \end{pmatrix}$	$\underline{1}$	$\underline{2}$	$-\frac{1}{2}$

Table 2.1: Particle and group properties of the Standard Model. Quarks and leptons are described as spinor fields. Left-handed up and down-type quark pairs, Q_{Lm}, and charged and neutral lepton pairs, L_{Rm}, carry doublet representations of SU(2). Meanwhile, right-handed quarks (u_{Rm} and d_{Rm}) and charged leptons (l_{Rm}) carry singlet representations of SU(2). Quarks also carry a triplet representation of SU(3) which results in quark colour.

2.1.2. Electroweak symmetry breaking

The inclusion of a Higgs doublet, ϕ, given by

$$\phi = \begin{pmatrix} \phi^+ \\ \phi^0 \end{pmatrix} \tag{2.6}$$

is the minimal mechanism required to make the weak and electromagnetic forces manifest themselves. In addition, the Yukawa couplings between the Higgs and fermions provide a mechanism for generating the masses of the fermions and the observed flavour structure seen in the CKM sector of the Standard Model.

The Higgs Lagrangian [17–20] is given by

$$\mathcal{L} = -\left(D_\mu \phi\right)^\dagger (D_\mu \phi) - V\left(\phi^+ \phi\right) \ , \tag{2.7}$$

where

$$D_\mu \phi = \left(\partial_\mu - \frac{i}{2} g_2 W_\mu \cdot \sigma - \frac{i}{2} g_1 B_\mu \right) \phi \ . \tag{2.8}$$

Meanwhile, the Higgs potential, $V(\phi^+\phi)$, is given by

$$\begin{aligned} V(\phi^+\phi) &= \lambda(\phi^\dagger\phi)^2 - \mu^2 \phi^\dagger \phi \\ &= \lambda \left(\phi^+\phi - \frac{\mu^2}{2\lambda}\right)^2 - \frac{\mu^4}{4\lambda} \ , \end{aligned} \tag{2.9}$$

where λ is the Higgs self-coupling strength.

The minimum of the potential satisfies

$$\frac{\partial V}{\partial \phi} = 0 \implies \phi^+\phi = \frac{\mu^2}{\lambda} = v \ . \tag{2.10}$$

While this condition is invariant under a $SU(2) \times U(1)$ group transformation the choice of the vacuum expectation of the field ϕ will spontaneously break a number of the symmetries. The vacuum expectation value for the scalar doublet field may be taken without loss of generality as

$$\langle \phi \rangle = \begin{pmatrix} 0 \\ \frac{v}{\sqrt{2}} \end{pmatrix} \ , \tag{2.11}$$

where v is the vacuum expectation value of the Higgs field. The value of v is ~ 246 GeV, which sets the scale of electroweak symmetry breaking. Performing an infinitesimal $SU(2) \times U(1)$ group transformation on the vacuum expectation, $\langle\phi\rangle$, reveals an unbroken symmetry

$$\langle \phi \rangle \to \langle \phi' \rangle = \langle \phi \rangle + \frac{i}{2}(\eta \cdot \sigma + \rho) \langle \phi \rangle = \langle \phi \rangle + \frac{i}{2} \begin{pmatrix} \eta_3 + \rho & \eta_1 - i\eta_2 \\ \eta_1 + i\eta_2 & -\eta_3 + \rho \end{pmatrix} \begin{pmatrix} 0 \\ \frac{v}{\sqrt{2}} \end{pmatrix} \tag{2.12}$$

$$= \langle \phi \rangle \ \text{ if } \eta_1 = \eta_2 = 0 \text{ and } \eta_3 = \rho \ . \tag{2.13}$$

The vacuum expectation is invariant under a, $U(1)$, transformation generated by $\sigma_3/2+Y$. This is the $U(1)$ symmetry governing electromagnetism.

Expanding ϕ about its vacuum expectation, $\langle\phi\rangle$, gives

$$\phi = \exp\left(\frac{i}{\sqrt{2}}\zeta\cdot k\right)\begin{pmatrix} 0 \\ \frac{1}{\sqrt{2}}(v+H(x)) \end{pmatrix} \tag{2.14}$$

where H is the Higgs field, $\zeta = \{\zeta_1(x),\zeta_2(x),\zeta_3(x)\}$ are known as Goldstone fields and $k = \{\sigma_1/2,\sigma_2/2,\sigma_3/2-Y\}$ are the generators of the broken symmetries. Under a suitable gauge transformation ϕ becomes

$$\phi\to\phi' = \exp(-\frac{i}{\sqrt{2}}\zeta\cdot k)\phi = \begin{pmatrix} 0 \\ \frac{1}{\sqrt{2}}(v+H(x)) \end{pmatrix}\ . \tag{2.15}$$

This is known as the unitary gauge. Substituting this expression into the kinetic and gauge term for ϕ and expanding one finds

$$\begin{aligned} -(D_\mu\phi)^\dagger D_\mu\phi = &-\frac{1}{2}\partial_\mu H\partial^\mu H - \frac{1}{8}(v+H)^2 g_2^2(W_\mu^1 - iW_\mu^2)(W^{1\mu}+iW^{2\mu}) \\ &-\frac{1}{8}(v+H)^2(g_2W_\mu^3 - g_1B_\mu)(g_2W^{3\mu}-g_1B^\mu)\ . \end{aligned} \tag{2.16}$$

In this expression one finds two mass terms

$$-\frac{g_2^2v^2}{4}\frac{(W_\mu^1 - iW_\mu^2)}{\sqrt{2}}\frac{(W^{1\mu}+iW^{2\mu})}{\sqrt{2}} = -\frac{g_2^2v^2}{4}W_\mu^+W^{-\mu}\ , \tag{2.17}$$

and

$$-\frac{1}{8}v^2(g_1^2+g_2^2)\frac{(g_2W_\mu^3-g_1B_\mu)}{\sqrt{g_1^2+g_2^2}}\frac{(g_2W^{3\mu}-g_1B^\mu)}{\sqrt{g_1^2+g_2^2}} = -\frac{1}{8}v^2(g_1^2+g_2^2)Z_\mu Z^\mu\ , \tag{2.18}$$

for the normalised combinations of gauge fields $W_\mu^\pm = (W_\mu^1 \mp iW_\mu^2)/\sqrt{2}$ and $(g_2W_\mu^3 - g_1B_\mu)/\sqrt{g_1^2+g_2^2}$, which, respectively, define the $W_\mu^\pm$ and Z_μ electroweak bosons with masses given by, $M_W = g_2v/2$, and, $M_Z = v\sqrt{g_1^2+g_2^2}/2$. Meanwhile, the orthogonal combination of gauge fields to the Z_μ, $(g_1W_\mu^3+g_2B_\mu)/\sqrt{g_1^2+g_2^2}$, remains massless. This combination of gauge fields is the photon, A_μ, of electromagnetism, which corresponds to the unbroken gauge symmetry, $U_{\mathrm{EM}}(1) = \sigma_3/2+Y$.

Under the same substitution the Higgs potential becomes

$$V(\phi\phi^\dagger) = -\lambda v^2 H^2 - \lambda v H^3 - \frac{\lambda}{4}H^4 - \frac{\mu^4}{4\lambda} \ , \tag{2.19}$$

in which the mass term for the Higgs field is $-\lambda v^2 H^2$, which implies that mass of the Higgs boson is $M_H = \sqrt{2\lambda}v$. The masses of the Higgs boson and the electroweak bosons is set by the scale v.

Returning to the gauge couplings of left-handed quark and lepton doublets, Q_{Lm} and L_{Lm}, to W^1_μ and W^2_μ, it is possible to derive the Lagrangian describing charge current interactions mediated by the massive $W^\pm_\mu$ vector bosons

$$\begin{aligned} \mathcal{L}_{CC} &= \frac{i^2}{2}\bar{Q}_{Lm}\gamma^\mu g_2(W^1_\mu\sigma_1 + W^2_\mu\sigma_2)Q_{Lm} + \frac{i^2}{2}\bar{L}_{Lm}\gamma^\mu(W^1_\mu\sigma_1 + W^2_\mu\sigma_2)L_{Lm} \\ &= -\frac{g_2}{\sqrt{2}}\left[(\bar{u}_{Lm}\gamma^\mu d_{Lm} + \bar{\nu}_m\gamma^\mu l_{Lm})W^+_\mu + (\bar{d}_{Lm}\gamma^\mu u_{Lm} + \bar{l}_{Lm}\gamma^\mu \nu_m)W^-_\mu\right] \ . \end{aligned} \tag{2.20}$$

It is important to note that in this form there is no violation of quark and lepton flavour in these interactions and the coupling of $g_2/\sqrt{2}$ is universal for the three generations. In a similar way neutral currents mediated by the photon, A_μ, or the Z_μ boson can be derived. As expected from charge conservation, these currents only connect quarks of up(down)-type quarks to up(down)-type and charged (neutral) leptons to neutral (charged) leptons. The charged weak current only involves left-handed fermions and right-handed anti-fermions. This leads to a violation of parity in the weak interactions.

Somewhat remarkably the electroweak sector is only described by four parameters, g_1, g_2, λ and v. Thirteen of the remaining fourteen parameters of the Standard Model are required to generate masses for the fermions via the Yukawa couplings. The last parameter is the coupling strength g_3 which governs QCD.

2.1.3. The Yukawa couplings

The Yukawa interactions are given by

$$\mathcal{L} = -i(f_{mn}\bar{L}_{Lm}\phi l_{Rn} + h_{mn}\bar{Q}_{Lm}\phi d_{Rn} + k_{mn}\bar{Q}_{Lm}\tilde{\phi}u_{Rn}) + h.c. \ , \tag{2.21}$$

where h.c. denotes Hermitian conjugate and f_{mn}, h_{mn} and k_{mn} are the Yukawa couplings with generation indices m and n. Meanwhile, $\tilde{\phi}$ is defined as

$$\tilde{\phi} = \begin{pmatrix} \phi^{0*} \\ \phi^{+*} \end{pmatrix} . \tag{2.22}$$

Inserting the expansion of ϕ about its vacuum expectation value, in unitary gauge, results in mass terms

$$-\frac{i}{\sqrt{2}} v(f_{mn}\bar{l}_{Lm}l_{Rn} + h_{mn}\bar{d}_{Lm}d_{Rn} + k_{mn}\bar{u}_{Lm}u_{Rn}) + h.c. \, . \tag{2.23}$$

However, given the cross-generational structure of the Yukawa couplings the SU(2) singlet and doublet quark and lepton fields are not mass eigenstates. The mass eigenstates can be obtained by carrying out independent unitary transformations which diagonalise the couplings:

$$\begin{aligned} l_{Lm} &\to U^{l_L}_{mj} l_{Lj}, \qquad & d_{Lm} &\to U^{d_L}_{mj} d_{Lj}, \qquad & u_{Lm} &\to U^{u_L}_{mj} u_{Lj} \\ l_{Rn} &\to U^{l_R}_{nk} l_{Rk}, \qquad & d_{Rn} &\to U^{d_R}_{nk} d_{Rk}, \qquad & u_{Rn} &\to U^{u_R}_{nk} u_{Rk} \, . \end{aligned} \tag{2.24}$$

Under these transformations the mass terms become

$$-\frac{i}{\sqrt{2}} v(U^{l_L\dagger}_{jm} f_{mn} U^{l_R}_{nk} \bar{l}_{Lj} l_{Rk} + U^{d_L\dagger}_{jm} h_{mn} U^{d_R}_{nk} \bar{d}_{Lj} d_{Rk} + U^{u_L\dagger}_{jm} k_{mn} U^{u_R}_{nk} \bar{u}_{Lj} u_{Rk}) + h.c. \, , \tag{2.25}$$

where

$$\begin{aligned} &\frac{v}{\sqrt{2}} U^{l_L\dagger}_{jm} f_{mn} U^{l_R}_{nk} = \begin{pmatrix} m_e & 0 & 0 \\ 0 & m_\mu & 0 \\ 0 & 0 & m_\tau \end{pmatrix}, \; \frac{v}{\sqrt{2}} U^{d_L\dagger}_{jm} h_{mn} U^{d_R}_{nk} = \begin{pmatrix} m_d & 0 & 0 \\ 0 & m_s & 0 \\ 0 & 0 & m_b \end{pmatrix} \text{ and,} \\ &\frac{v}{\sqrt{2}} U^{u_L\dagger}_{jm} k_{mn} U^{u_R}_{nk} = \begin{pmatrix} m_u & 0 & 0 \\ 0 & m_c & 0 \\ 0 & 0 & m_t \end{pmatrix} , \end{aligned} \tag{2.26}$$

are the diagonalised mass matrices for fermions. After this change of basis the charged current interaction shown in equation 2.27 becomes

$$
\begin{aligned}
\mathcal{L}_{CC} =& \frac{ig_2}{\sqrt{2}} \Big[(U^{u_L\dagger}_{jm} U^{d_L}_{mk} \bar{u}_{Lj} \gamma^\mu d_{Lk} + U^{l_L\dagger}_{jm} U^{l_L}_{mk} \bar{\nu}_j \gamma^\mu l_{Lk}) W^+_\mu \\
&+ (U^{d_L\dagger}_{jm} U^{u_L}_{mk} \bar{d}_{Lj} \gamma^\mu u_{Lk} + U^{l_L\dagger}_{jm} U^{l_L}_{mk} \bar{l}_{Lj} \gamma^\mu \nu_k) W^-_\mu \Big] \\
=& \frac{ig_2}{\sqrt{2}} \Big[(V_{jk} \bar{u}_{Lj} \gamma^\mu d_{Lk} + \bar{\nu}_m \gamma^\mu l_{Lm}) W^+_\mu + (V^\dagger_{kj} \bar{d}_{Lj} \gamma^\mu u_{Lk} + \bar{l}_{Lm} \gamma^\mu \nu_m) W^-_\mu \Big] \ ,
\end{aligned} \tag{2.27}
$$

where here the additional freedom to make a unitary transformation of the left-handed neutrino, $\nu_{Lm} \to U^{l_L}_{mj} \nu_{Lj}$, is taken. As a result of this for leptons there are no cross-generational charged weak currents for leptons and the weak coupling strength, $g_2/\sqrt{2}$, is universal across the generations. On the other hand, for quarks, given that independent unitary transformations must be made for up-type and down-type quarks the charged current weak interaction is modified by the CKM matrix,

$$
V^{\mathrm{CKM}}_{jk} = U^{u_L\dagger}_{jm} U^{d_L}_{mk} \ , \tag{2.28}
$$

which allow for cross-generational transitions, $d_k \to u_j$, with couplings $\propto V_{jk}$.

Although it is not explicitly shown here under the same unitary transformations the electromagnetic and weak neutral currents remain unchanged. Therefore at tree-level there are no flavour-changing neutral currents.

2.2. The CKM sector

2.2.1. The CKM matrix

The CKM matrix, is 3×3 unitary matrix which can be parametrised by 4 parameters as

$$
\begin{aligned}
V_{jk}^{CKM} = \begin{pmatrix} V_{ud} & V_{us} & V_{ub} \\ V_{cd} & V_{cs} & V_{cb} \\ V_{td} & V_{ts} & V_{tb} \end{pmatrix} &= \begin{pmatrix} c_{12}c_{13} & s_{12}c_{13} & s_{13}e^{-\delta} \\ -s_{12}c_{23} - c_{12}s_{23}s_{13}e^{i\delta} & c_{12}c_{23} - s_{12}s_{23}s_{13}e^{i\delta} & s_{23}c_{13} \\ s_{12}s_{23} - c_{12}c_{23}s_{13}e^{i\delta} & -c_{12}s_{23} - s_{12}c_{23}s_{13}e^{i\delta} & c_{23}c_{13} \end{pmatrix} \\
&= \begin{pmatrix} 1-\lambda^2/2 & \lambda & A\lambda^3(\rho - i\eta) \\ -\lambda & 1-\lambda^2/2 & A\lambda^2 \\ A\lambda^3(1-\rho-i\eta) & -A\lambda^2 & 1 \end{pmatrix} + \mathcal{O}(\lambda^4)
\end{aligned} \tag{2.29}
$$

where $s_{ij} = \sin\theta_{\mathrm{ij}}$ and $\mathrm{c_{ij}} = \cos\theta_{\mathrm{ij}}$.

In the first line the standard parametrisation [21] is shown with three mixing angles ($\theta_{13} = \sin^{-1}|\mathrm{V_{ub}}|$, θ_{23} and θ_{12}) and a phase $\delta = \arg(\mathrm{V_{ub}})$; this phase is responsible for all CP-violation in the quark sector. Here it can be seen that the magnitude and phase of the matrix element V_{ub} are directly related to fundamental parameters. Alternatively, the CKM matrix may be parametrised in the Wolfenstein parametrisation [22] with parameters λ, A, ρ and η as shown in the second line of equation 2.29. The two parametrisations are related by

$$
\begin{aligned}
s_{12} = \lambda = \frac{|V_{us}|}{\sqrt{|V_{ud}|^2 + |V_{us}|^2}},\ s_{23} = A\lambda^2 = \lambda \left| \frac{V_{cb}}{V_{us}} \right|, \\
s_{13}e^{i\delta} = V_{ub}^* = A\lambda^3(\rho + i\eta) = \frac{A\lambda^3(\bar{\rho} + i\bar{\eta})\sqrt{1 - A^2\lambda^4}}{\sqrt{1-\lambda^2}\left[1 - A^2\lambda^4(\bar{\rho} + i\bar{\eta})\right]} \ .
\end{aligned} \tag{2.30}
$$

which ensures that

$$
\bar{\rho} + i\bar{\eta} = -\frac{V_{ud}V_{ub}^*}{V_{cd}V_{cb}^*} \ . \tag{2.31}
$$

The unitarity of the CKM matrix,

$$
V_{ij}V_{jk}^* = \delta_{jk} \ , \tag{2.32}
$$

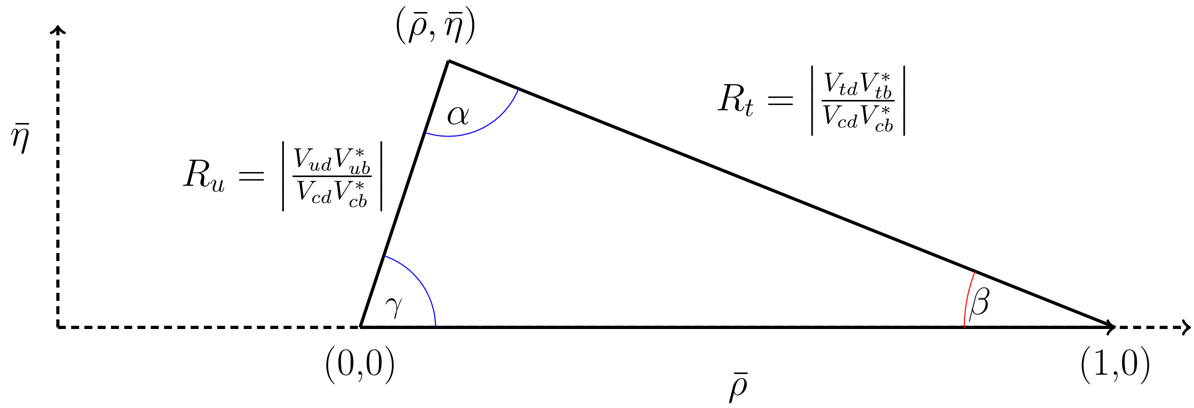

Figure 2.1: Illustration of the unitarity triangle described by equation 2.34 in the is defined as complex plane $(\bar\rho, \bar\eta)$.

provides an essential test of the Standard Model. The six vanishing unitarity relations expressed by equation 2.32 are of particular interest as geometrically they represent triangles in the complex plane. The triangle most commonly used for testing the unitarity of the CKM matrix is given by

$$V_{ud}V_{ub}^* + V_{cd}V_{cb}^* + V_{td}V_{tb}^* = 0 \ , \tag{2.33}$$

which when normalised becomes

$$\frac{V_{ud}V_{ub}^*}{V_{cd}V_{cb}^*} + 1 + \frac{V_{td}V_{tb}^*}{V_{cd}V_{cb}^*} = 0 \ . \tag{2.34}$$

Fig 2.1 shows the geometrical interpretation of equation 2.34 as a triangle in the complex plane defined by $\bar\rho + i\bar\eta = -V_{ud}V_{ub}^*/V_{cd}V_{cb}^*$. The six unitarity triangles have the same area, $J/2$, where the Jarlskog invariant [23], J, is a phase-convention independent measure of CP violation defined by

$$\mathrm{Im}\left[V_{ij}V_{kl}V_{il}^*V_{kj}^*\right] = J\sum_{mn}\epsilon_{ikm}\epsilon_{jln} \ . \tag{2.35}$$

2.2.2. Constraining the CKM sector

The four parameters of the CKM sector can be overconstrained by making measurements of a number of observables which are sensitive to the magnitudes and phases of various combinations of the CKM elements. Measurements of the magnitudes of the CKM elements are traditionally made using semileptonic and leptonic decays. This reveals an almost diagonal hierarchical structure to the CKM matrix (values from [11]),

$$\begin{pmatrix} |V_{ud}| & |V_{us}| & |V_{ub}| \\ |V_{cd}| & |V_{cs}| & |V_{cb}| \\ |V_{td}| & |V_{ts}| & |V_{tb}| \end{pmatrix} \approx \begin{pmatrix} 0.973 & 0.225 & 0.004 \\ 0.225 & 0.986 & 0.041 \\ 0.008 & 0.040 & 1.021 \end{pmatrix} , \tag{2.36}$$

this is further illustrated in Fig 1.1. The smallest and least known element is $|V_{ub}|$. The uncertainty on $|V_{ub}|$ dominates the uncertainty on the length of the unitarity triangle's side, R_u, opposite the angle β. After $|V_{ub}|$ the next least known elements are $|V_{tb}|$ and $|V_{td}|$ which enter into the length of the unitary triangle opposite the angle γ: $R_t = V_{td}V_{tb}^*/V_{cd}V_{cb}^*$. However, the combination of $|V_{td}V_{tb}^*|$ can be more precisely determined by measuring the mass difference of the B^0 meson mass eigenstates, $\Delta m_d \propto |V_{td}V_{tb}^*|^2$, which drives B^0-$\overline{B}^0$ oscillations. The ratio of B^0 and B_s^0 mass difference $\Delta m_d/\Delta m_s \propto |V_{td}V_{tb}^*|^2/|V_{ts}V_{tb}^*|^2$ is often used as a constraint given the significantly reduced theory uncertainty for the ratio. The uncertainty on determinations of the magnitude of CKM elements and their combinations is in general dominated by the theory uncertainty on form factors which encompass the nature of QCD; this topic will be addressed in more detail later in sections 2.3 and 2.4.

The measurement of a number of CP-violating observables can be used to extract the phases of CKM elements. Of particular importance are measurements which give direct information on the angles of the unitarity triangle. The angle β can be determined by considering decays of B^0 and $\overline{B}^0$ mesons to the same final state, f. A $B^0/\overline{B}^0$ meson produced at time zero may at some time t later decay as $B^0/\overline{B}^0 \to f$. Alternatively at time t it may decay as $\overline{B}^0/B^0 \to f$ due to B^0-$\overline{B}^0$ oscillations. Given that the two paths have a phase difference, interference occurs resulting in a time-dependent asymmetry, $\mathcal{A_{CP}} \propto \sin(2\beta) \cdot \sin(\Delta m_d t)$. Measurements of $\sin(2\beta)$ have been made using $b \to c\bar{c}s$, $b \to c\bar{c}d$ and $b \to c\bar{u}d$ transitions, which involve CP eigenstates to the same final state such as $B^0 \to J/\psi\, K^0_{S/L}$ [24–26] and $B^0 \to J/\psi\, \pi^0$ [27]. The angle $\alpha = arg(V_{tb}^* V_{td}/V_{ub}^* V_{ud})$ is also measured using time-dependant CP asymmetries, however, only $b \to u\bar{u}d$ transitions give access to the required relative phase. While the angles β and α depend on $V_{tb}^* V_{td}$, the angle $\gamma = arg(-V_{ud}V_{ub}^*/V_{cd}V_{cb}^*)$ contains no elements involving the top quark. This important distinction means that γ can be measured using only tree-level processes. For instance γ may be determined by measuring the interference between $B^- \to D^0 K^-(b \to c\bar{u}s)$ and $B^- \to \overline{D}^0 K^-(b \to u\bar{c}s)$ decays when the D^0 and $\overline{D}^0$ mesons decay to the same final state [28]. Additional constraints on the CKM sector come from the measurement of CP-violation in K^0-$\overline{K}^0$ mixing and the CP violating phase $\beta_s = arg(-V_{ts}^* V_{tb}/V_{cs}^* V_{cb})$ measured using $B_s^0 \to J/\psi\, \phi$ decays [29].

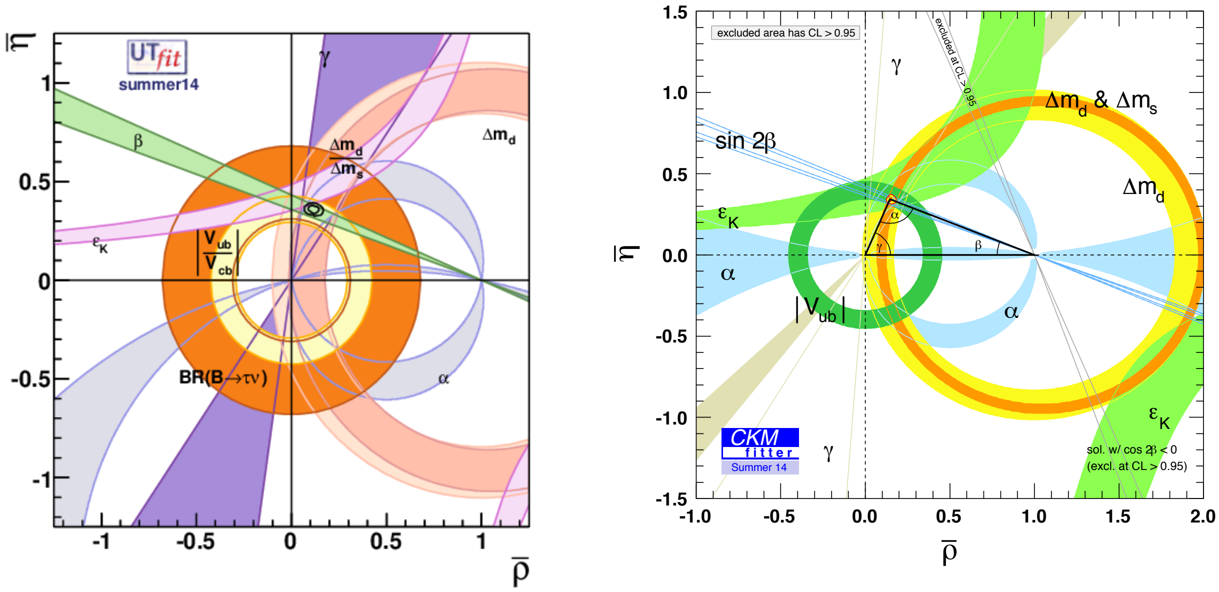

$\bar{\rho} = 0.132 \pm 0.023 \quad \bar{\eta} = 0.352 \pm 0.014$

$A = 0.821 \pm 0.012 \quad \lambda = 0.22534 \pm 0.00065$

$|V_{ub}| = 0.00363 \pm 0.00012$

$\bar{\rho} = 0.145^{+0.013}_{-0.007} \quad \bar{\eta} = 0.343^{+0.011}_{-0.012}$

$A = 0.810^{+0.018}_{-0.024} \quad \lambda = 0.2255^{+0.0007}_{-0.0003}$

$|V_{ub}| = 0.00355^{+0.00017}_{-0.00015}$

Figure 2.2: Global fits for the CKM parameters $\bar{\rho}$, $\bar{\eta}$, A and λ made by the UTfit (left) and CKMfitter (right) collaborations as of Summer 2014. Figures taken from [30] and [31].

The parameters of the CKM sector $\bar{\rho}$, $\bar{\eta}$, A and λ may be determined through a global fit with a number of measurements as constraints. Fig 2.2 shows the apex of the unitarity triangle determined from global fits by the CKMfitter [29] and UTfit collaborations [30], which use frequentist and Bayesian approaches, respectively. The strongest constraints on the apex of the uniarity triangle come from the combinations of the parameters (γ, R_u), (β, R_t), (R_u, R_t) and (β, γ).

2.2.3. Probing new physics in the CKM sector

A lack of consistency between contraints on the apex of the unitarity triangle from different measurements could indicate new physics influencing these measurements. An example of this, is the potential contribution from heavy new particles in loop-level processes such as those which govern $B^0_{d/s}$-$\overline{B}^0_{d/s}$ mixing. Given that flavour changing neutral decays, $\Delta F = 2$, are forbidden in the Standard Model at tree-level, these loop-level decays are particularly sensitive to new physics.

Although new physics may influence many measurements of CKM observables, including those made with tree-level processes, here for simplicity new physics is assumed to only have a significant impact $B^0_{d/s}$-$\overline{B}^0_{d/s}$ mixing.

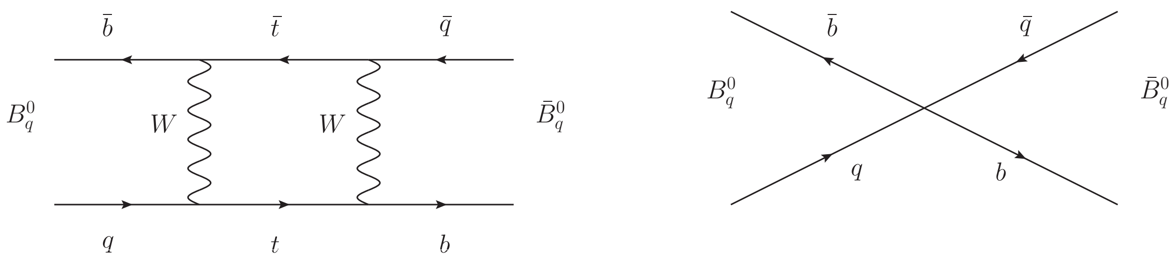

Figure 2.3: Loop-level diagram contributing to B^0_q-$\overline{B}^0_q$ mixing in the Standard Model (left). In effective field theory heavy degrees of freedom contributing in loops are integrated out leaving an effective 4-point fermion interaction (right).

An important approach to handling possible new physics contributions in loops is effective field theory, where heavy degrees of freedom above a particular cutoff energy scale, Λ, are integrated out. In practice matrix elements between initial, i and final f states may be written using an effective Hamiltonian as

$$\langle f \left| \mathcal{H}_{\text{eff}} \right| i \rangle = \sum_k \frac{1}{\Lambda^k} \sum_i \mathcal{C}_{k,i} \left. \langle f \left| \mathcal{O}_{k,i} \right| i \rangle \right|_{\Lambda} . \tag{2.37}$$

where the effective Hamiltonian, $\mathcal{H}_{\text{eff}}$, is an expansion of all possible operators contributing to the process at energies below the cutoff scale, Λ [32]. Meanwhile, the coefficients of these operators, $\mathcal{C}_{k,i}$, which are known as Wilson coefficients, encode the high energy physics above the cutoff scale, Λ, which has been integrated out. A classic example of an effective theory is Fermi theory in which the heavy W has been integrated out to leave a 4-point fermion interaction.

The impact of new physics on B_q-$\overline{B}^0_q$ mixing can be described model-independently [33, 34] by introducing an amplitude, $|\Delta_q|$, and a complex phase ϕ^{Δ}_q defined by

$$|\Delta_q| e^{i\phi^{\Delta}_q} = \frac{\left\langle \overline{B}^0_q \left| \mathcal{H}^{NP}_{eff} \right| \bar{B}^0_q \right\rangle}{\left\langle B^0_q \left| \mathcal{H}^{SM}_{eff} \right| \overline{B}^0_q \right\rangle} \tag{2.38}$$

where

$$\mathcal{H}_{\text{eff}}^{\text{NP/SM}} = (V^*_{tq} V_{tb})^2 C^{\text{NP/SM}} \bar{b}_L \gamma_\mu q_L \bar{q}_L \gamma^\mu b_L + \text{h.c.} \, . \tag{2.39}$$

New physics will alter the Wilson coefficient, C, from its determination assuming the Standard Model which is given by

$$C^{\rm SM} = \frac{G^2}{4\pi^2} M_W^2 \hat{\eta}_B S\left(\frac{\overline{m}_t^2}{M_W^2}\right) \ , \tag{2.40}$$

where $\overline{m}_t$ is the top mass in the $\overline{\rm MS}$ scheme, $\hat{\eta} = 0.8393 \pm 0.0034$ encompasses QCD corrections and the Inami-Lim function, S, evaluates to $S(\bar{m}_t^2/M_W^2) = 2.35$.

Given equation 2.38 and that

$$\Delta m_q^{\rm NP/SM} = \left|\left\langle B_q^0 \left| \mathcal{H}_{eff}^{\rm NP/SM} \right| \overline{B}_q^0 \right\rangle\right| / M_{B_q} \ , \tag{2.41}$$

it is possible to show that

$$\Delta m_q^{\rm NP} = \left|\Delta_q\right| \Delta m_q^{\rm SM} \ . \tag{2.42}$$

In addition, a number CP asymmetries measured using B^0 and B_s^0 meson decays will be modified by the additional phase parameters, ϕ_d^Δ and ϕ_s^Δ. For instance, the B^0-$\overline{B}^0$ mixing induced CP-asymmetry in $b \to c\bar{c}s$ transitions will give $\sin(2\beta + \phi_{\rm d}^\Delta)$ rather than $\sin(2\beta)$.

In order to demonstrate the power of probing new physics through the comparison of constraints on the CKM sector from a variety of measurements, a simple fit is considered for the apex $(\bar{\rho}, \bar{\eta})$ and new physics parameters, $|\Delta_q|$ and ϕ_q^Δ. A Gaussian likelihood is constructed, which is given by

$$\mathcal{L}\left(\vec{x} \left| \bar{\rho}, \bar{\eta}, \left|\Delta_q\right|, \phi_q^\Delta \right.\right) = \prod_i \frac{1}{\sqrt{2\pi\sigma_i}} \exp\left(-\frac{\left(x_i - x_i^{\rm model}(\bar{\rho}, \bar{\eta}, \left|\Delta_q\right|, \phi_q^\Delta)\right)^2}{2\sigma_i^2}\right) \ , \tag{2.43}$$

where the fit inputs are experimental measurements, $\vec{x} = \{R_u, R_t, \sin 2\beta, \gamma\}$, and their corresponding uncertainties, $\vec{\sigma}$. In the Standard Model

$$\vec{x}^{\rm SM}(\bar{\rho}, \bar{\eta}) = \left\{\sqrt{\bar{\rho}^2 + \bar{\eta}^2}, \sqrt{(1-\bar{\rho})^2 + \bar{\eta}^2}, \sin\left(2\tan^{-1}\left(\frac{\bar{\eta}}{1-\bar{\rho}}\right)\right), \tan^{-1}\left(\frac{\bar{\eta}}{\bar{\rho}}\right)\right\} \ , \tag{2.44}$$

meanwhile, for the case of new physics parametrised by equation 2.38

$$\vec{x}^{\mathrm{SM+NP}}(\bar{\rho},\bar{\eta},|\Delta_q|,\phi_q^{\Delta}) = \Big\{\sqrt{\bar{\rho}^2+\bar{\eta}^2}, \sqrt{|\Delta_d|(1-\bar{\rho})^2+|\Delta_d|\,\bar{\eta}^2}, \\ \sin\left(2\tan^{-1}\left(\frac{\bar{\eta}}{1-\bar{\rho}}\right)+\phi_{\mathrm{d}}^{\Delta}\right), \tan^{-1}\left(\frac{\bar{\eta}}{\bar{\rho}}\right)\Big\} \;. \tag{2.45}$$

This treatment, for simplicity, assumes that $|V_{td}V_{tb}^*|$ is calculated from Δm_d and all other required CKM elements are determined from tree-level decays. Potential correlations between form factor uncertainties entering into the determination of the CKM parameters are ignored. In addition, any correlations between experimental measurements, which should be negligible, are ignored. A simple toy maximum likelihood fit is constructed in which the experimental inputs are first computed using the model $\vec{x}^{\mathrm{exp}} = \vec{x}^{\mathrm{SM+NP}}(0.145, 0.343, 0.9, 5.73^o)$. Fig 2.4 compares fits, assuming the SM only, to fits with new physics parameters, $|\Delta_q|$ and ϕ_q^{Δ}, included. In Fig 2.4(a) and (b) the uncertainties on γ and R_u are 10% while the uncertainties on sin2β and R_t are 2%. Given the large uncertainty on γ and R_u it is not possible to resolve the new physics phase and amplitude. On the other hand, in Fig 2.4(c) and (d) the uncertainties on γ and R_u are artificially reduced to 1% and 3% while the central values are kept the same; this reflects the expected uncertainties from Belle 2 and LHCb on $|V_{ub}|$, $|V_{cb}|$ and γ measurements in the next ten years [35]. The reduction in the uncertainties on γ and R_u makes the tension between loop-level and tree-level observables become apparent. The sensitivity to the New Physics phase and amplitude will depend on the uncertainty of the pairs of adjacent parameters, (R_u, β), and (R_t, γ), respectively.

Fig 2.5 shows a global fit for the real and imaginary parts of Δ_d by the CKMfitter group. As discussed above the observables Δm_d and $\sin(2\beta + \phi_{\mathrm{d}}^{\Delta})$ directly constrain the new physics amplitude and phase under the assumption that new physics only shows up in the B_q^0-$\overline{B}_q^0$ mixing.

2.3. Semileptonic *b*-hadron decays

In order to measure $|V_{ub}|$ via an exclusive decay mode, theory predictions for the hadronic form factors are required. This section presents an overview of the relevant form factors for $\Lambda_b^0 \to p l^- \bar{\nu}_l$, $\overline{B}_s^0 \to K^+ l^- \bar{\nu}_l$ and $\overline{B}^0 \to \pi^+ l^- \bar{\nu}_l$ decays. To stay general, the effect of a potential right-handed current in the $b \to u$ transition arising from new physics beyond the SM is considered.

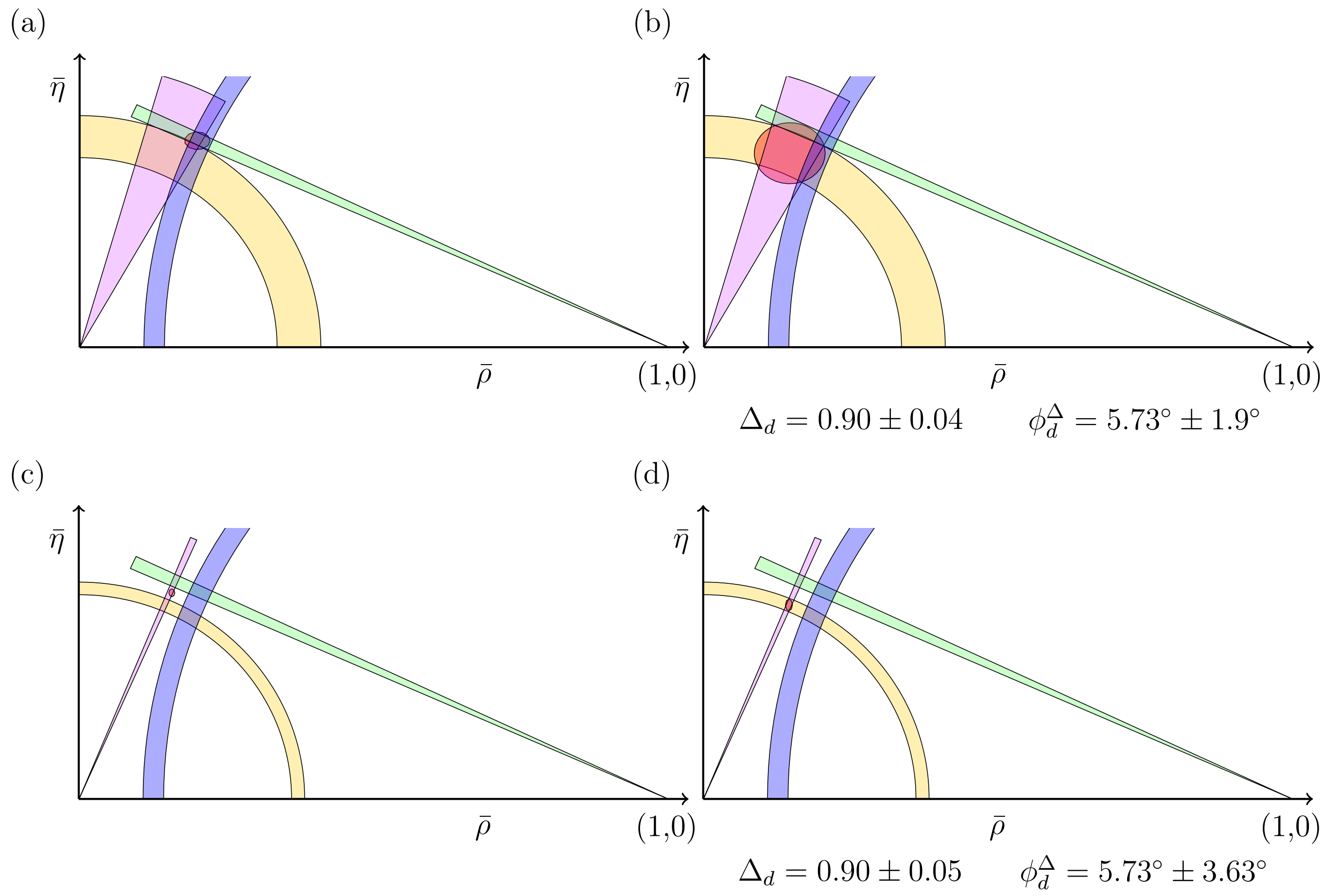

Figure 2.4: A comparison of toy fits for the apex, $\bar{\rho}, \bar{\eta}$, of the unitary triangle assuming the SM only (a) and (c) to those including new physics contributions to B-mixing (b) and (d). For fits (a) and (b) the uncertainties on γ and R_u are 10%, meanwhile, for fits (c) and (d) the corresponding uncertainties are 3%.

The effective weak Hamiltonian for $b \to q l^- \nu_l$ transitions, with the inclusion of a right-handed current, is given by

$$\mathcal{H}_{\text{eff}} = \frac{G_{\text{F}}}{\sqrt{2}} V_{qb}^{L} \left[(1+\epsilon_q^{\text{R}})\bar{q}\gamma^{\mu} b - (1-\epsilon_q^{\text{R}})\bar{q}\gamma^{\mu}\gamma_5 b \right] \bar{l}\gamma_{\mu}(1-\gamma_5)\nu \ , \tag{2.46}$$

where $\gamma_5 = i\gamma_0\gamma_1\gamma_2\gamma_3$ such that $\frac{(1-\gamma_5)}{2}\psi = \psi_L$ and $\frac{(1+\gamma_5)}{2}\psi = \psi_R$. In the Standard Model $\epsilon_q^{\text{R}} = 0$.

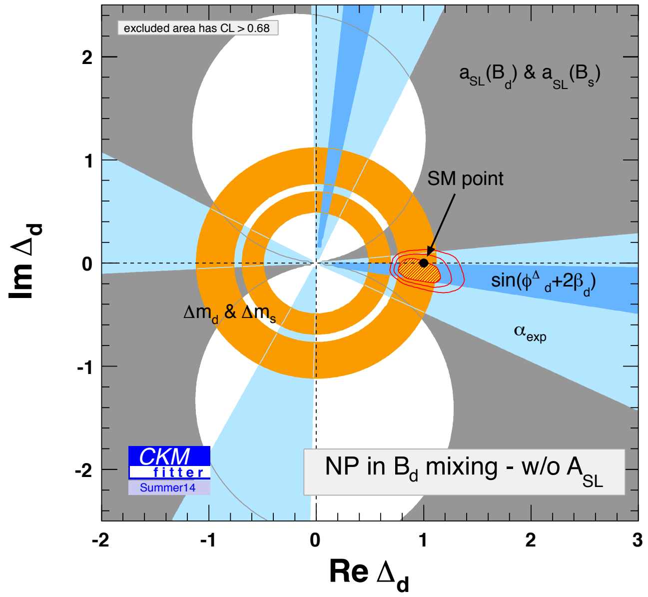

Figure 2.5: Global fit by the CKMfitter group for new physics in B^0_d-$\overline{B}^0_d$ mixing parameterised by a complex parameter, Δ_d. Taken from Reference [29].

The matrix element for a semileptonic decay of a b-hadron to an exclusive final state $X_q l \bar{\nu}$ can be computed according to

$$\begin{aligned}\mathcal{M} &= -i \left\langle X_q(p', s') l^-(k', r') \bar{\nu}_l(k, r) \left| \mathcal{H}_{\text{eff}} \right| B(p, s) \right\rangle \\ &= -i \frac{G_{\text{F}}}{\sqrt{2}} V_{qb} H^{\mu} \bar{u}_l(k', r') \gamma_{\mu} (1 - \gamma_5) v_{\bar{\nu}_l}(k, r) \ ,\end{aligned} \tag{2.47}$$

where p and k denote 4-momentums, s and r denote spin, u and v are dirac spinors and

$$H^{\mu} = (1 + \epsilon^{\text{R}}_q) \left\langle X_q(p', s') \left| \bar{q} \gamma^{\mu} b \right| B(p, s) \right\rangle - (1 - \epsilon^{\text{R}}_q) \left\langle X_q(p', s') \left| \bar{q} \gamma^{\mu} \gamma_5 b \right| B(p, s) \right\rangle \ , \tag{2.48}$$

is the hadronic matrix element. It is non-trivial to calculate H^{μ} given the potential contributions from QCD as shown in Fig 2.6. However, in general Lorentz and discrete symmetries mean that the vector, $\langle X_q \left| \bar{q} \gamma^{\mu} b \right| B \rangle$, and axial vector, $\langle X_q \left| \bar{q} \gamma^{\mu} \gamma_5 b \right| B \rangle$, hadronic matrix elements may be decomposed in terms of form factors, which encompass the QCD effects. Given the nature of QCD the form factors must be computed non-perturbatively using techniques such as Light Cone Sum Rules (LCSR) [13] or Lattice QCD (LQCD) [12]; the latter approach will be discussed in more detail in section 2.4.

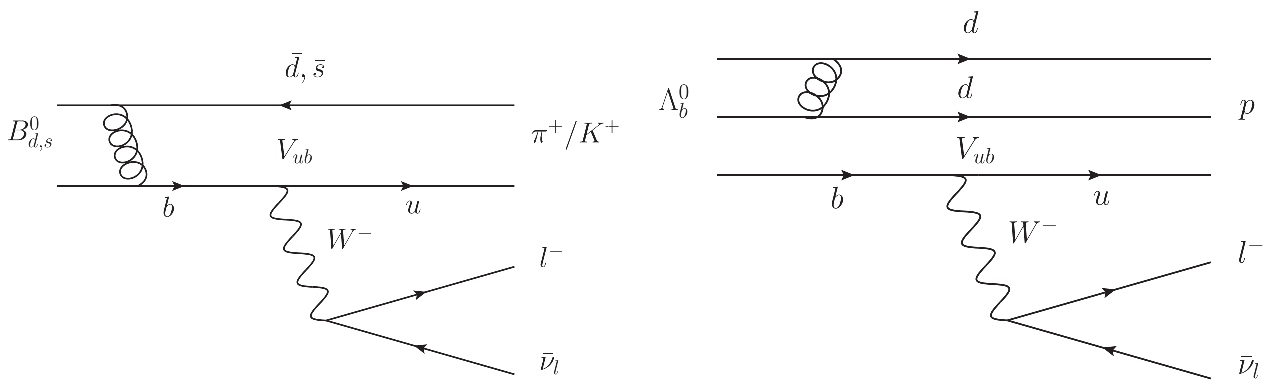

Figure 2.6: Higher order Feynman diagrams for the semileptonic decays $\overline{B}^0 \to \pi^+ l^- \bar{\nu}_l$, $\overline{B}^0_s \to K^+ l^- \bar{\nu}_l$ and $\Lambda^0_b \to p l^- \bar{\nu}_l$ which include a potential contribution to the interaction from QCD.

For the case of pseudoscalar meson transitions, $B^0_{d/s}(J^P = 0^-) \to X = \pi^+/K^+(J^P = 0^-)$, the vector part of H^μ is given by

$$\left\langle X(p', s')\left|\bar{u}\gamma^\mu b\right| B^0_q(p, s)\right\rangle = f_+(q^2)\left(p^\mu + p'^\mu - \frac{M^2_{B_q} - M^2_X}{q^2} q^\mu\right) + f_0(q^2)\frac{M^2_{B_q} - M^2_X}{q^2} q^\mu \ , \quad (2.49)$$

where $q^\mu = p^\mu_B - p^\mu_X$ is the momentum transfer. The axial-vector part of H^μ is zero because of the constraint on the spin of the outgoing u quark. In references, [36] and [37], the latest LQCD predictions for the scalar and vector form factors, f_0 and f_+, of $\overline{B}^0 \to \pi^+ l^- \bar{\nu}_l$ and $\overline{B}^0_s \to K^+ l^- \bar{\nu}_l$ decays are presented.

From the matrix element in equation 2.47 the differential decay rate for $B^0_q \to X l^- \bar{\nu}_l$ decays, where X is a pseudoscalar meson, can be computed as

$$\begin{aligned} \frac{d\Gamma_{B^0_q \to X l^- \bar{\nu}_l}}{dq^2} = \frac{G^2_{\rm F}|V_{ub}|^2(1+\epsilon^{\rm R}_u)^2}{24\pi^3} \frac{(q^2 - m^2_l)^2\sqrt{E^2_X - M^2_X}}{q^4 M^2_{B^0_q}} &\Bigg[(1 + \frac{m^2_l}{2q^2}) M^2_{B^0_q}(E^2_X - M^2_X)|f_+(q^2)|^2 \\ &+ \frac{3m^2_l}{8q^2}(M^2_{B^0_q} - M^2_X)|f_0(q^2)|^2\Bigg] \ , \end{aligned} \quad (2.50)$$

where

$$E_X = \frac{M^2_{B^0_q} + M^2_X - q^2}{2M_{B^0_q}} \ . \quad (2.51)$$

Given that the hadronic matrix element is purely vector, the effect of an additional right-handed current is to modify the coupling strength, $V_{ub}^L \to (1+\epsilon_R)V_{ub}^L$. On the other hand, for leptonic $b\bar{u}$ annihilation decays such as $B^- \to l^-\bar{\nu}_l$ only an axial vector contribution is possible. As a result of this, the presence of a right-handed $b \to u$ current will modify the amplitude for these decays according to $V_{ub}^L \to (1-\epsilon_R)V_{ub}^L$. For inclusive $B \to X_u l^- \bar{\nu}_l$ decays the coupling strength will a have weaker dependence on ϵ_R, which is given by $V_{ub}^L \to \sqrt{1+\epsilon_R^2}V_{ub}^L$ [38]. In light of this a right-handed $b \to u$ current has been suggested as a potential explanation for the $|V_{ub}|$ puzzle [38–40]. Fig 2.7 shows results from a simple χ^2 fit for the parameters $|V_{ub}^L|$ and ϵ_R, which uses measurements of $|V_{ub}|$ from $\overline{B}^0 \to \pi^+ l^- \bar{\nu}_l$, $B^- \to \tau^- \bar{\nu}_\tau$ and inclusive $B \to X_u l^- \bar{\nu}_l$ decays as constraints. This shows that the observed discrepancies in $|V_{ub}|$ measurements could be resolved by the inclusion of a right-handed coupling with $\epsilon_R = -0.17 \pm 0.06$. However, Crivellin et al. showed in Reference [41] that the right-handed coupling required to resolve the $|V_{ub}|$ puzzle is excluded by measurements of the branching fraction of $Z \to b\bar{b}$ decays.

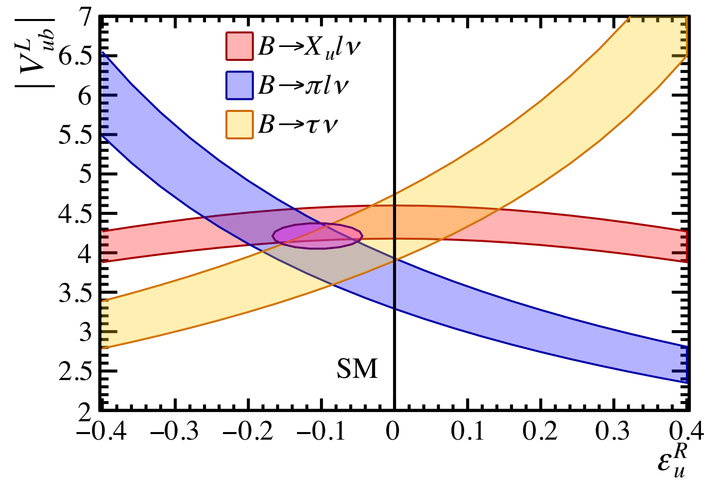

Figure 2.7: A χ^2 fit for the parameters V_{ub}^L and ϵ_u^R as defined in equation 2.46 using constraints from measurements of $|V_{ub}|$ made using $\overline{B}^0 \to \pi^+ l^- \bar{\nu}_l$, $B^- \to \tau^- \bar{\nu}_\tau$ and inclusive B decays.

For the case of a baryonic transition, $\Lambda_b^0(J^P = \frac{1}{2}^+) \to p(J^P = \frac{1}{2}^+)$, the vector and axial-vector parts of H^μ can each be expressed in terms of three form factors. In the helicity basis, the vector form factors, f_0, f_+, $f_\perp$, and axial vector form factors, g_0, g_+, $g_\perp$, are defined by

$$\begin{aligned}
\langle p(p',s')|\overline{q}\,\gamma^\mu\,b|\Lambda_b(p,s)\rangle &= \overline{u}_p(p',s')\bigg[f_0(q^2)\,(m_{\Lambda_b}-m_p)\frac{q^\mu}{q^2} \\
&\quad + f_+(q^2)\frac{m_{\Lambda_b}+m_p}{s_+}\left(p^\mu+p'^\mu-(m_{\Lambda_b}^2-m_p^2)\frac{q^\mu}{q^2}\right) \\
&\quad + f_\perp(q^2)\left(\gamma^\mu-\frac{2m_p}{s_+}p^\mu-\frac{2m_{\Lambda_b}}{s_+}p'^\mu\right)\bigg]u_{\Lambda_b}(p,s), \qquad (2.52) \\
\langle p(p',s')|\overline{q}\,\gamma^\mu\gamma_5\,b|\Lambda_b(p,s)\rangle &= -\overline{u}_p(p',s')\,\gamma_5\bigg[g_0(q^2)\,(m_{\Lambda_b}+m_p)\frac{q^\mu}{q^2} \\
&\quad + g_+(q^2)\frac{m_{\Lambda_b}-m_p}{s_-}\left(p^\mu+p'^\mu-(m_{\Lambda_b}^2-m_p^2)\frac{q^\mu}{q^2}\right) \\
&\quad + g_\perp(q^2)\left(\gamma^\mu+\frac{2m_p}{s_-}p^\mu-\frac{2m_{\Lambda_b}}{s_-}p'^\mu\right)\bigg]u_{\Lambda_b}(p,s)\;, \qquad (2.53)
\end{aligned}$$

where $q^\mu = p^\mu - p'^\mu$ and

$$s_\pm = (m_{\Lambda_b^0} \pm m_p)^2 - q^2 \quad . \tag{2.54}$$

The expression above also applies for the form factors of the corresponding $b \to c$ transition, $\Lambda_b^0 \to \Lambda_c^+\mu^-\overline{\nu}_\mu$, but with the proton replaced with the Λ_c^+ baryon. Reference [42] presents the latest LQCD predictions for the $\Lambda_b^0 \to p\mu^-\overline{\nu}_\mu$ and $\Lambda_b^0 \to \Lambda_c^+\mu^-\overline{\nu}_\mu$ decays. Sections 2.4.6 and 5.2.3 provide a more detailed discussion of the LQCD calculation.

The differential rate for $\Lambda_b^0 \to p\mu^-\overline{\nu}_\mu$ decays can be computed in terms of the form factors as

$$\begin{aligned}
\frac{\mathrm{d}\Gamma}{\mathrm{d}q^2} &= \frac{G_F^2|V_{qb}^L|^2\sqrt{s_+s_-}}{768\pi^3 m_{\Lambda_b}^3}\left(1-\frac{m_\ell^2}{q^2}\right)^2 \\
&\quad \times\bigg\{4\left(m_\ell^2+2q^2\right)\left(s_+\left[(1-\epsilon_u^R)g_\perp\right]^2+s_-\left[(1+\epsilon_u^R)f_\perp\right]^2\right) \\
&\quad +2\frac{m_\ell^2+2q^2}{q^2}\left(s_+\left[(m_{\Lambda_b}-m_p)\,(1-\epsilon_u^R)g_+\right]^2+s_-\left[(m_{\Lambda_b}+m_p)\,(1+\epsilon_u^R)f_+\right]^2\right) \\
&\quad +\frac{6m_\ell^2}{q^2}\left(s_+\left[(m_{\Lambda_b}-m_p)\,(1+\epsilon_u^R)f_0\right]^2+s_-\left[(m_{\Lambda_b}+m_p)\,(1-\epsilon_u^R)g_0\right]^2\right)\bigg\}\,. \qquad (2.55)
\end{aligned}$$

Fig 2.8 shows a comparison of the differential rates of $\Lambda_b^0 \to p\mu^-\overline{\nu}_\mu$, $\overline{B}{}_s^0 \to K^+\mu^-\overline{\nu}_\mu$ and $\overline{B}{}^0 \to \pi^+\mu^-\overline{\nu}_\mu$ decays using form factors taken from [36, 37, 42]. The predicted branching fraction for

$\Lambda_b^0 \to p\mu^-\overline{\nu}_\mu$ decays is substantially larger than that of $\overline{B}{}_s^0 \to K^+\mu^-\overline{\nu}_\mu$ or $\overline{B}{}^0 \to \pi^+\mu^-\overline{\nu}_\mu$ decays as shown in Table 2.2.

Decay	B lifetime / ps	$\mathcal{B}_{\text{theory}}$	$\mathcal{B}_{\text{exp}}$
$\Lambda_b^0 \to p\mu^-\overline{\nu}_\mu$	1.466	4.7×10^{-4}	-
$\overline{B}{}^0 \to \pi^+\mu^-\overline{\nu}_\mu$	1.519	1.3×10^{-4}	1.45×10^{-4}
$\overline{B}{}_s^0 \to K^+\mu^-\overline{\nu}_\mu$	1.511	0.9×10^{-4}	-

Table 2.2: Summary of the branching fraction predictions for $\Lambda_b^0 \to p\mu^-\overline{\nu}_\mu$, $\overline{B}{}_s^0 \to K^+\mu^-\overline{\nu}_\mu$ and $\overline{B}{}^0 \to \pi^+\mu^-\overline{\nu}_\mu$ decays made using form factor predictions from [36, 37, 42] and taking $|V_{ub}| = 3.5 \times 10^{-3}$. The experimental lifetimes and branching fractions presented in the table are taken from [11].

The contribution of both vector and axial vector parts of H^μ for $\Lambda_b^0 \to p\mu^-\overline{\nu}_\mu$ decays means that the shape of the differential rate in q^2 is dependent on ϵ_u^R. Fig 2.8 shows the differential rate for $\Lambda_b^0 \to p\mu^-\overline{\nu}_\mu$ decays for different values of ϵ_u^R. As a result of this, a measurement of $|V_{ub}|$ from $\Lambda_b^0 \to p\mu^-\overline{\nu}_\mu$ decays gives yet another constraint on the plane of ϵ_u^R-V_{ub}^L.

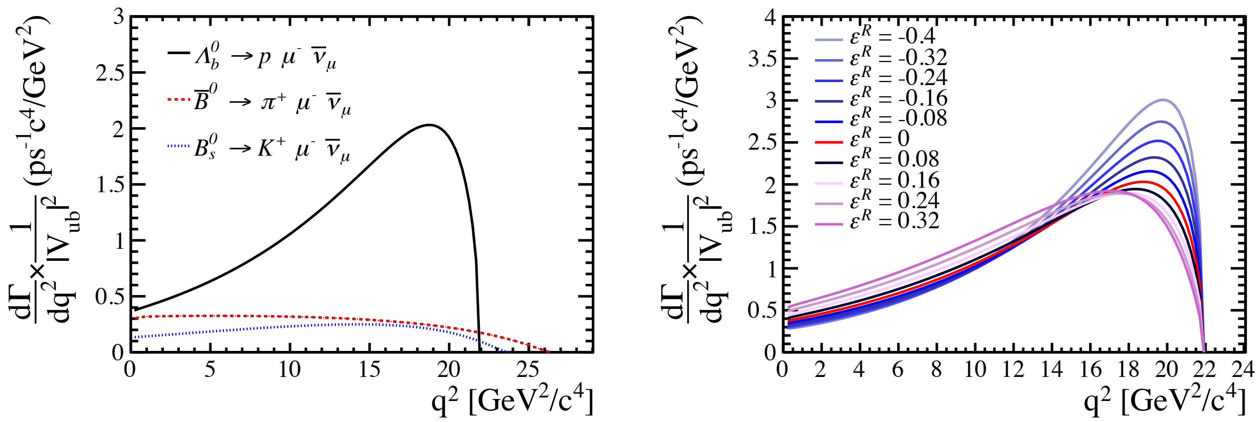

Figure 2.8: Comparison of the differential rates of $\Lambda_b^0 \to p\mu^-\overline{\nu}_\mu$, $\overline{B}{}_s^0 \to K^+\mu^-\overline{\nu}_\mu$ and $\overline{B}{}^0 \to \pi^+\mu^-\overline{\nu}_\mu$ decays (left). Differential rate of $\Lambda_b^0 \to p\mu^-\overline{\nu}_\mu$ decays for different values of ϵ_u^R (right).

2.4. Lattice QCD

The determination of $|V_{ub}|$ presented within this thesis requires theoretical input from a pioneering calculation of the $\Lambda_b^0 \to p\mu^-\overline{\nu}_\mu$ and $\Lambda_b^0 \to \Lambda_c^+\mu^-\overline{\nu}_\mu$ form factors made using Lattice QCD (LQCD).

This section provides the reader with an introduction to the topic of LQCD and then summarises the features of the calculation.

2.4.1. QCD

The QCD interaction Lagrangian for quarks and gluons is given by

$$\mathcal{L}_{\text{QCD}} = -\frac{1}{4}G_{\mu\nu}\cdot G^{\mu\nu} + \bar{q}_f^i\left(\delta_{ij}\gamma_\mu\partial_\mu - \frac{ig_3}{2}\gamma^\mu G_\mu\cdot\lambda_{ij} - m_f\delta_{ij}\right)\bar{q}_f^j \tag{2.56}$$

where in this notation $f = u, c, t, d, s, b$ refers to the quark flavours, m_f are the quark masses arising from the Yukawa interactions, i and j denote colour indices. An important feature of QCD is the behaviour of the coupling constant, $\alpha_s = g_s^2/4\pi$, under renormalisation,

$$\alpha_s(\mu_R^2) = \frac{12\pi}{(11n - 2f)\cdot\ln\left(\frac{\mu_R^2}{\Lambda_{\text{QCD}}^2}\right)}\ , \tag{2.57}$$

where $n = 3$ is the number of colors, $f = 6$ is the number of quark flavours, and μ_R is the energy scale. Meanwhile, $\Lambda_{\text{QCD}} \approx 200\,\text{MeV}$ is a constant of the theory, which sets the energy scale at which the coupling constant diverges. For energies close to or below Λ_{QCD}, QCD can not be solved perturbatively. The divergent nature of the strong coupling constant leads to quarks only ever being observed in bound states, a phenomenon known as confinement. When $\mu_R \gg \Lambda_{\text{QCD}}$ the strong coupling constant becomes small enough for perturbation theory to applied to QCD. For QCD interactions within b-hadron the energy scale, μ_R, is given by the mass of the hadron, m_B. This energy scale is still in the regime where QCD must be handled non-perturbatively.

2.4.2. The concept of the lattice

Lattice QCD is a non-perturbative technique in which the QCD action,

$$S_{\text{QCD}} = \int d^4x\mathcal{L}_{\text{QCD}}\ , \tag{2.58}$$

is numerically computed by discretising space-time on a lattice [12, 43]. A more intuitive example of this technique is to consider the quantum mechanical path, $x(t)$, of a particle in time, t, between boundary positions, $x(0)$ and $x(t_f)$. In the path integral formalism of quantum mechanics, the

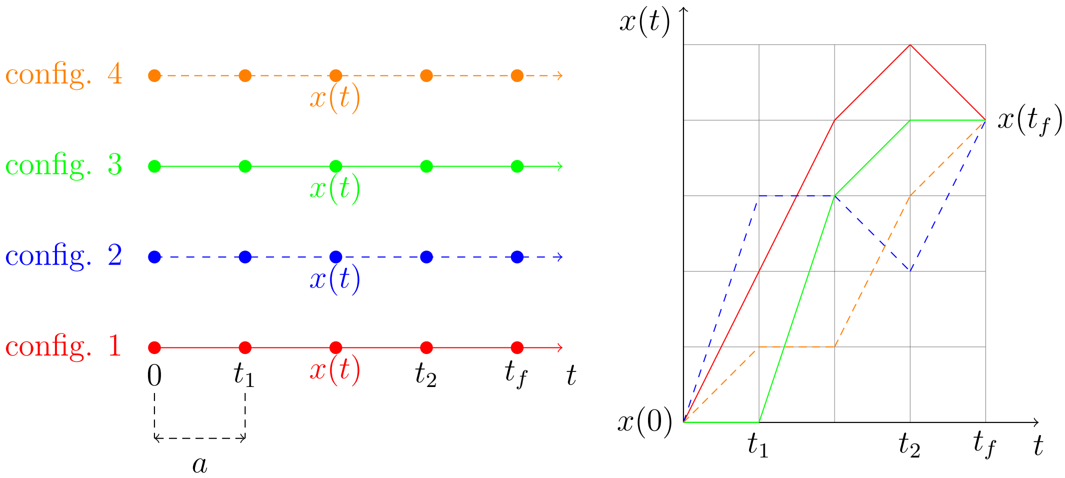

Figure 2.9: Illustration of a one-dimensional lattice representing a particle's position, $x(t)$, at lattice points, $t = 0, 1, 2, 3, 4$. Four different lattice configurations are shown which correspond to different possible paths the particle could take. In practice an ensemble of configurations/paths is generated where the probability of given configuration is $\propto \exp(-\int dt\mathcal{L})$. This allows the numerical evaluation of correlation functions such as $\langle x(t_1)x(t_2)\rangle$

particle can be seen as traversing all possible paths but with the probability of any given path being proportional to $\exp(-\int dt\mathcal{L})$. Expectations of operator combinations known as correlation functions may be computed according to

$$\langle \mathcal{O}(x(t_1)x(t_2))\rangle = \frac{\int \mathcal{D}x(t)\mathcal{O}(x(t_1)x(t_2))e^{-\int dt\mathcal{L}}}{\int \mathcal{D}x(t)e^{-\int dt\mathcal{L}}} , \tag{2.59}$$

where $\int \mathcal{D}x(t)$ denotes an integral over all configurations of $x(t)$ (paths).

This expectation may be solved numerically using a simple one-dimensional lattice in time with temporal spacing a. In practice this involves using Hybrid Monte Carlo methods [44] to generate a large ensemble of N_{conf} lattice configurations such that the probability to find a given configuration within the ensemble is proportional to $\exp(-\int dt\mathcal{L})$. Each lattice configuration directly corresponds to a different path traversed by the particles as illustrated in Fig 2.9.

The computation of the correlation function in equation 2.59 now reduces to simply averaging the correlation functions computed for each of the configurations,

$$\langle \mathcal{O}(x(t_1)x(t_2))\rangle = \frac{1}{N_{\text{conf}}}\sum_{n=1}^{N_{\text{conf}}} \mathcal{O}(x(t_1), x(t_2)) . \tag{2.60}$$

The corresponding statistical uncertainty can be calculated using the sample standard deviation and is proportional to $1/\sqrt{N_{conf}}$. In practice a computation of the action, $\int dt\mathcal{L}$, on the lattice is only exact in the limit of $a \to 0$ known as the continuum limit. While this is not possible computationally, lattice results computed using a range of lattice spacings may be extrapolated to the continuum limit.

2.4.3. Discretising QCD

This concept of using a lattice to numerically calculate correlation functions using the path integral formalism extends naturally to QCD. The analogue of the position, $x(t)$, is the quark field, $q(t,x,y,z)$, which is represented at points in a 4-dimensional lattice such that any given point in space-time is given by $(t,x,y,z) = a(n_1,n_2,n_3,n_4)$, where $n_{i=1\cdots4}$ are integers with ranges, $0 \leq n_0 \leq N_t$ and $0 \leq n_{i=1,2,3} \leq N_s$. The energy scale, μ_R, on the lattice is set by the lattice spacing, a, as $\mu_R = 1/a$. Typically in LQCD simulations light quark masses, $m_{q=u,d,s} < 1/a$, are taken as being equal and such simulations are known as $N_f = 2+1$ simulations. The masses of the light quarks can be tuned to their physical values by computing the mass of the pion on the lattice.

In analogue of equation 2.59 correlation functions of operator combinations may be expressed as

$$\langle \mathcal{O}(G_\mu, q_f, \bar{q}_f) \rangle = \frac{\int \mathcal{D}q\mathcal{D}\bar{q}\mathcal{D}G_\mu \prod_f \mathcal{O}(q_f,\bar{q}_f,G_\mu) e^{-\int d^4x \mathcal{L}_{\mathrm{QCD}}}}{\int \mathcal{D}q_f\mathcal{D}\bar{q}_f\mathcal{D}G_\mu e^{-\int dx^4 \mathcal{L}_{\mathrm{QCD}}}} , \tag{2.61}$$

where $\mathcal{D}q_f$, $\mathcal{D}\bar{q}_f$ and $\mathcal{D}G_\mu$ denote integrals over all possible quark and gluon field configurations.

To better understand how the gluon field may be represented on the lattice it is helpful to first consider the discretisation of the quark kinetic terms on the lattice. This is achieved by using a simple finite difference of quark fields between neighbouring points

$$\bar{q}(x)\gamma^\mu\partial_\mu q(x) = \bar{q}(x)\gamma^\mu \frac{q(x+a\hat{x}_\mu) - q(x-a\hat{x}_\mu)}{2a} + \mathcal{O}(a^2) , \tag{2.62}$$

where $\hat{x}_\mu$ denotes a normalised direction to an adacent lattice position in the μ^{th} direction, e.g $\hat{x}_1 = (0,1,0,0)$. This leads to quark bilinears between adjacent points, $q(x)\gamma^\mu q(x+a\hat{x}_\mu)$, which under a local SU(3) transformation, $q(x) \to V(x)q(x)$, transform as

$$q(x)\gamma^\mu q(x+a\hat{x}_\mu) \to \bar{q}(x)V^\dagger(x)\gamma^\mu V(x+a\hat{x}_\mu)q(x+a\hat{x}_\mu) . \tag{2.63}$$

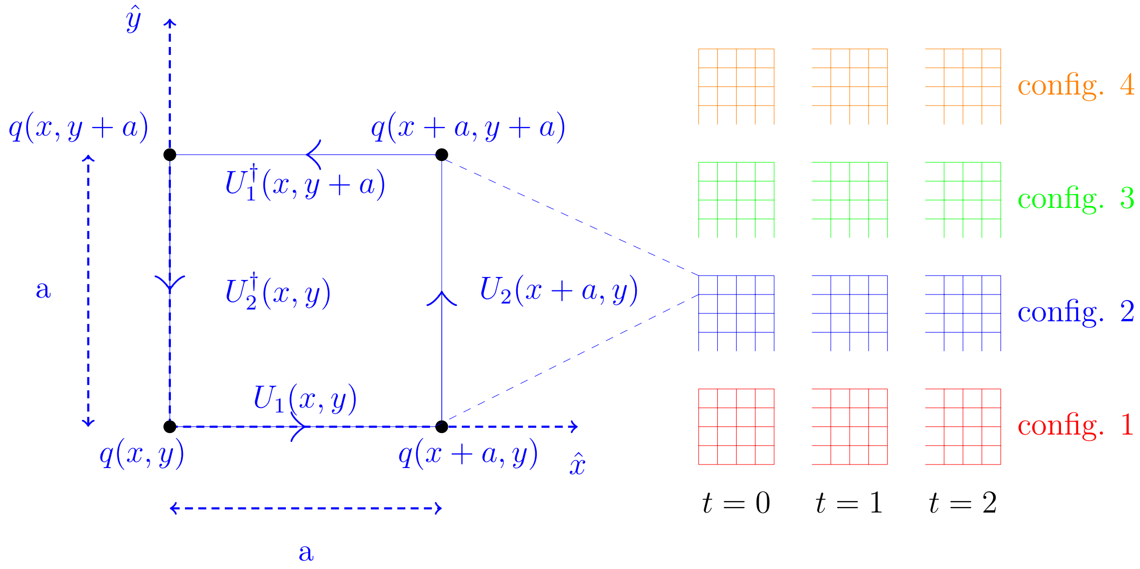

Figure 2.10: Illustration of the lattice approach to QCD in two spatial dimensions, x and y, and one temporal dimension, t. Quark fields $q(t, x, y)$ are represented as sites on the lattice, meanwhile, gluon fields, $U_\mu(t, x, y)$ ($\mu = \{0, 1, 2\}$), are represented by links between adjacent points. In this convention $U_1(t, x, y)$ represents the link from lattice point, (t, x, y), to the adjacent point, $(t, x+a, y)$. Lattice QCD calculations rely on computing correlation functions using an ensemble of configurations of the quark and gluon fields on the lattice.

The formulation of a gauge covariant derivative requires the introduction of a lattice gluon, $U_\mu(x) \in SU(3)$, which transforms as $U_\mu(x) \to V(x)U_\mu(x)V^\dagger(a + a\hat{x}_\mu)$. The lattice gluon naturally defines the link from the lattice point, x, to an adjacent lattice point in the $\hat{x}_\mu$ direction. A lattice covariant derivative can now be written as

$$\bar{q}(x)\gamma^\mu D_\mu[U]q(x) = \bar{q}(x)\gamma^\mu \frac{U_\mu(x)q(x+a\hat{x}_\mu) - U_\mu^\dagger(x-a\hat{x}_\mu)q(x-a\hat{x}_\mu)}{2a} + \mathcal{O}(a^2)\,. \tag{2.64}$$

This naive discretisation suffers from a problem known as fermion doubling describing 2^d fermions in the continuum limit. This can be solved by introducing a Wilson term [43] to the action, however, this leads to $\mathcal{O}(a)$ discretisation errors. A commonly used variant is the Clover action [45] which reduces the discretisation error to $\mathcal{O}(a^2)$. Until recently, these lattice action formalisms were not possible for heavy, b and c quarks as their masses are larger than the lattice cutoff, $m_q > 1/a$ where $1/a$ = 2-4 GeV assuming a lattice spacing of $a \approx$ 0.1-0.05fm. This is a result of $\mathcal{O}(am_q)$ discretisation errors which grow uncontrollably. A solution of this was to use the Eichten-Hill action [46] which relies on heavy quark effective theory in which the mass of the heavy quark is assumed to be infinity.

The field strength action is represented on the lattice as a trace of lattice gluon fields around a closed loop [43] as

$$S_g = \sum_{x,\mu,\nu} \beta \left[1 - \frac{1}{3} \mathrm{ReTr} \left[\mathrm{U}_\mu(\mathrm{x}) \mathrm{U}_\nu(\mathrm{x} + \mathrm{a}\hat{\mathrm{x}}_\mu) \mathrm{U}^\dagger_\mu(\mathrm{x} + \mathrm{a}\hat{\mathrm{x}}_\nu) \mathrm{U}^\dagger_\nu(\mathrm{x}) \right] \right] \to \beta \mathrm{Tr} \left[\mathrm{G}^{\mu\nu} \mathrm{G}_{\mu\nu} \right] \ . \tag{2.65}$$

In the continuum limit of $a \to 0$ this gives the kinetic term for the Gluon fields.

For lattice QCD calculations large numbers of configurations of the gauge fields, $U(x)$, on all links are generated by a number of different collaborations including the RBC, MILC and UKQCD collaborations. These configurations are generated according to the probablity measure

$$\mathcal{D}U e^{-S_g} \int \prod_f \mathcal{D}q_f \mathcal{D}\bar{q}_f e^{-S_Q} \ , \tag{2.66}$$

where S_Q is the action associated with the quark fields and their interactions with gluons. This allows for correlation functions $\langle \mathcal{O}(U, q, \bar{q}) \rangle$ to be computed by averaging over the configurations. Gauge configurations are available for a number of different parameters including N_s, N_t, a, the valence and sea quark masses and the resulting pion mass.

2.4.4. Relating correlation functions to hadronic matrix elements

The required hadronic matrix elements, $\langle X(k)| J^{\mathrm{V/AV}}_\mu |\Lambda_b(p)\rangle$, of vector and axial vector currents ($J^{\mathrm{V/AV}}_\mu$) may be determined from the three-point correlation function

$$C_{X J_\mu \Lambda^0_b}(t_x, t_y; \vec{k}, \vec{p}) = \iint \left\langle X(t_x, \vec{x}) J^{\mathrm{V/AV}}_\mu(0) \Lambda^0_b(t_y, \vec{y}) \right\rangle e^{-i\vec{k}\cdot\vec{x}} e^{-i\vec{p}\cdot\vec{y}} dx^3 dy^3 \ , \tag{2.67}$$

where the momentum of the Λ^0_b baryon and the final state particle, X, are given by $\vec{p}$ and $\vec{k}$, respectively. Inserting complete sets of particle states,

$$\sum_i \int \frac{d^3k}{2E_{X_i}} |X_i(\vec{k})\rangle\langle X_i(\vec{k})| = 1 \tag{2.68}$$

and

$$\sum_j \int \frac{d^3p}{2E_{\Lambda_{bj}}} |\Lambda_{bj}(\vec{p})\rangle\langle \Lambda_{bj}(\vec{p})| = 1 \ , \tag{2.69}$$

it is possible rewrite the correlation function as

$$\begin{aligned}
C_{XJ_\mu\Lambda_b^0}(t_x, t_y; \vec{k}, \vec{p}) &= \sum_{i,j} \frac{e^{-E_{X_i}t_x + E_{\Lambda_{bj}}t_y}}{2E_{\Lambda_{bj}}2E_{X_i}} \langle 0|X(0)|X_i(\vec{k})\rangle\langle X_i(\vec{k})|J_\mu^{\mathrm{V/AV}}|\Lambda_{bj}(\vec{p})\rangle\langle\Lambda_{bj}(\vec{p})|\Lambda_b(0)|0\rangle \\
&= \frac{e^{-E_X t_x + E_{\Lambda_b}t_y}}{2E_{\Lambda_b}2E_X} \langle 0|X(0)|X(\vec{k})\rangle\langle X(\vec{k})|J_\mu^{\mathrm{V/AV}}|\Lambda_b(\vec{p})\rangle\langle\Lambda_b(\vec{p})|\Lambda_b(0)|0\rangle \\
&+ \text{ excited contributions },
\end{aligned} \tag{2.70}$$

as shown in the LQCD review by the Particle Data Group [11]. The ground state contribution can be obtained by a spectral decomposition. Meanwhile, the matrix elements $\langle 0|X(0)|X(\vec{k})\rangle$ and $\langle\Lambda_b(\vec{p})|\Lambda_b(0)|0\rangle$ are determined by computing 2-point correlation functions. This allows for the required hadronic matrix element, $\langle X(k)|J_\mu^{\mathrm{V/AV}}|\Lambda_b(p)\rangle$, to be evaluated by computing a combination of 3-point and 2-point correlation functions on the lattice.

2.4.5. Lattice systematic uncertainties

In general for a lattice calculation the following systematic sources of uncertainty must be quantified:

- Continuum limit uncertainties: The results of lattice calculations must be extrapolated to the continuum limit, $a \to 0$ which in general requires an understanding of the functional form of the leading discretisation errors.
- Finite volume effects: The computation of actions involves an integral over all space and time, however, in practice the lattice has a finite volume leading to shifts in physical quantities estimated on the lattice.
- Chiral extrapolation: The predicted mass of the pion will vary between different lattice configurations. In practice an extrapolation of results to the physical mass of the pion is required.
- Operator matching: Operators defined in terms of the lattice scheme must be matched to their continuum versions under the appropiate renomalisations. This often requires non-perturbative techniques each with their own systematic uncertainties.

2.4.6. Lattice caculation for the $\Lambda_b^0 \to p\mu^-\overline{\nu}_\mu$ and $\Lambda_b^0 \to \Lambda_c^+\mu^-\overline{\nu}_\mu$ form factors

Determinations of the $\Lambda_b^0 \to p\mu^-\overline{\nu}_\mu$ and $\Lambda_b^0 \to \Lambda_c^+\mu^-\overline{\nu}_\mu$ form factors were made using three ensembles of gauge field configurations generated by the RBC and UKQCD collaborations [47]. The first was generated at a coarse lattice spacing $a = 0.11$fm with volume $N_s^3 \times N_t = 24^3 \times 64$ and gauge coupling $\beta = 2.13$. The other two ensembles were generated with a finer lattice spacing, $a = 0.085$fm, with volume $N_s^3 \times N_t = 32^3 \times 64$ and gauge coupling $\beta = 2.35$. Ensembles were further divided into datasets differing by the masses of up and down valence quarks.

The first lattice calculation of the $\Lambda_b^0 \to p\mu^-\overline{\nu}_\mu$ form factors was made using the static quark approximation of $m_b \to \infty$ where leading order Heavy Quark Effective Theory (HQET)[2] becomes exact. This allows the Eichten-Hill action to be applied for the heavy b quark while u, d and s quarks are represented by the heavy-domain wall actions and gluons by the Iwasaki action [48] as were used for generating the configurations. By computing various ratios of forward and backward 3-point correlation functions to 2-point correlation functions the two $\Lambda_b^0 \to p\mu^-\overline{\nu}_\mu$ HQET form factors are determined. Lattice data is only available at high q^2 as the momentum of the proton is restricted by the lattice cutoff, $\mathcal{O}(1/a)$. The theoretical prediction for the width of the decay for $q^2 > 14\,\mathrm{GeV}^2/c^4$ determined using the HQET form factors is

$$\frac{1}{|V_{ub}|^2}\int_{14\,\mathrm{GeV}^2/c^4}^{q^2_{max}} \frac{d\Gamma}{dq^2} = 15.3 \pm 2.4 \pm 3.4\mathrm{ps}^{-1} \tag{2.71}$$

where the first uncertainty is on the form factors (15.7%) and the second uncertainty is associated with the use of the static quark approximation, (22.2%).

In order to provide a competitive measurement of the $|V_{ub}|$ from $\Lambda_b^0 \to p\mu^-\overline{\nu}_\mu$ decays Stefan Meinel et al. [42] computed the form factors of $\Lambda_b^0 \to p\mu^-\overline{\nu}_\mu$ and $\Lambda_b^0 \to \Lambda_c^+\mu^-\overline{\nu}_\mu$ decays with a fully relativistic treatment of the b quark. While the same actions were used to describe gluons, up, down and strange quarks, a new anisotropic heavy clover action was used to describe the heavy bottom or charm quark. By tuning the parameters of the clover actions describing heavy bottom and charm quarks $\mathcal{O}(m_b a)$, discretisation errors were removed leaving $\mathcal{O}a^2|\vec{p}|^2$ errors. The fully relativistic LQCD predictions for the $\Lambda_b^0 \to p\mu^-\overline{\nu}_\mu$ and $\Lambda_b^0 \to \Lambda_c^+\mu^-\overline{\nu}_\mu$ form factors lead to the

[2] An effective field theory involving an expansion of the Langrangian describing weak decays of a heavy quark in inverse powers of the heavy quark's mass.

following theoretical predictions:

$$\frac{1}{|V_{ub}|^2}\int_{15\,\mathrm{GeV}^2/c^4}^{q^2_{max}} \frac{d\Gamma_{\Lambda_b^0\to p\mu^-\overline{\nu}_\mu}}{dq^2} = 12.31 \pm 0.76 \pm 0.77\mathrm{ps}^{-1} \tag{2.72}$$

and

$$\frac{1}{|V_{cb}|^2}\int_{7\,\mathrm{GeV}^2/c^4}^{q'^2_{max}} \frac{d\Gamma_{\Lambda_b^0\to \Lambda_c^+\mu^-\overline{\nu}_\mu}}{dq^2} = 8.37 \pm 0.16 \pm 0.34\mathrm{ps}^{-1}\ , \tag{2.73}$$

for which the ratio is

$$R_{\mathrm{FF}} = \frac{\int_{15\,\mathrm{GeV}^2/c^4}^{q^2_{max}} \frac{1}{|V_{ub}|^2}\frac{d\Gamma}{dq^2}_{\Lambda_b^0\to p\mu^-\overline{\nu}_\mu} dq^2}{\int_{7\,\mathrm{GeV}^2/c^4}^{q'^2_{max}} \frac{1}{|V_{cb}|^2}\frac{d\Gamma}{dq^2}_{\Lambda_b^0\to \Lambda_c^+\mu^-\overline{\nu}_\mu} dq^2} = 1.471 \pm 0.0095 \pm 0.1409\ . \tag{2.74}$$

In all cases the first uncertainty is statistical and the second uncertainty is systematic. The dominant systematic uncertainties are those associated with the required chiral extrapolation and the finite volume of the lattices.

A more detailed description of the form factor parametrisations in q^2, form factor uncertainties and modelling of the form factors for the experimental analysis are presented in chapter 5.

Chapter 3.

Experimental setup

The $|V_{ub}|$ measurement presented in this thesis was performed with data collected in 2012 by the LHCb experiment using proton-proton collisions produced by the Large Hadron Collider. This section gives an overview of the aspects of the collider and experiment which are relevant for the measurement.

3.1. The Large Hadron Collider

The Large Hadron Collider (LHC) is a proton-proton collider, 27 km in circumference, located near Geneva, Switzerland, at the research facility, CERN. The LHC is currently the highest energy particle collider in the world having run at centre of mass energies $\sqrt{s} = 7\,\mathrm{TeV}$, $\sqrt{s} = 8\,\mathrm{TeV}$ and $\sqrt{s} = 13\,\mathrm{TeV}$ in 2011, 2012 and 2015, respectively.

Before entering the LHC, protons obtained from ionising hydrogen are accelerated through a series of accelerators up to an initial injection energy of $450\,\mathrm{GeV}$. Bunches of protons are subsequently injected into the LHC which accelerates the protons to the required collision energies. The proton beams are brought to collide in four different experiments around the LHC ring every $25/50$ ns.

3.2. The LHCb experiment

The LHCb experiment is designed to carry out a wide range of heavy flavour physics measurements by exploiting the large production cross-sections for beauty and charm quarks through $pp \to b\bar{b}X$

and $pp \to c\bar{c}X$ interactions. In particular, the production cross-section, $\sigma(pp \to b\bar{b}X)$, for $\sqrt{s} = 7\,\text{TeV}$ pp collisions has been measured to be $(284 \pm 29 \pm 40)\mu\text{b}$ [49]. This cross-section is five orders of magnitude larger than the corresponding production cross-section for $ee^+ \to \Upsilon(4s) \to B\overline{B}$ at the B-factories BaBar [50] and Belle [51].

Beauty or charm hadrons are produced from the hadronisation of any beauty or charm quarks produced in the proton-proton collisions. This gives LHCb the opportunity to study a range of beauty hadrons including Λ_b^0 baryons, which were not produced at the B factories.

In order to provide a clean environment for flavour physics measurements the LHCb detector is designed for a luminosity of around 3×10^{32} cm^{2}s^{-1} corresponding to an average of less than two pp interactions per bunch crossing. Beam optics are used to the reduce the LHC's nominal luminosity ($\sim 7 \times 10^{33}$ cm^{2}s^{-1} in 2012) to the required level.

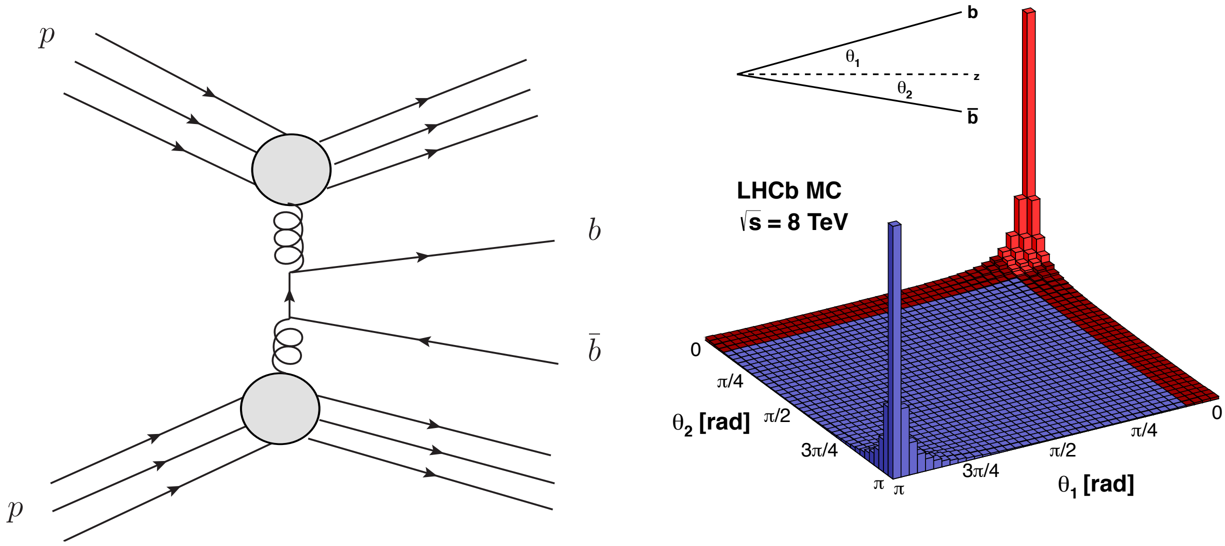

Figure 3.1: Diagram depicting $pp \to b\bar{b}X$ via gluon-gluon fusion, the dominant production mechanism (left). Angular distribution for $pp \to b\bar{b}X$ production using Pythia at $\sqrt{s} = 8\,\text{TeV}$ (right) taken from [52]. The red region corresponds to the angular acceptance of the LHCb detector.

The production mechanism for $b\bar{b}$ and $c\bar{c}$ pairs from pp interactions is predominantly gluon-gluon fusion as shown in Fig 3.1. Interacting gluons will each have a fraction of the proton's momentum as determined by the proton's structure functions. Any misbalance between the fractions carried by the gluons results in their interaction being boosted with respect to the proton-proton centre of mass frame. As a result of this, $b\bar{b}$ and $c\bar{c}$ pairs are produced predominantly in the forward and backward regions of the LHC beam line (see Fig 3.1).

The LHCb detector [53] is a single-arm spectrometer with a forward angular acceptance of 300 mrad exploiting the forward production of $b\bar{b}$ and $c\bar{c}$ pairs. This corresponds to a pseudorapidity, η, coverage of $2 < \eta < 5$, where

$$\eta = -\ln\left|\tan\frac{\theta}{2}\right| , \tag{3.1}$$

in which θ is the angle between a particle's momentum and the beam axis. This coverage accepts 25% of all $b\bar{b}$ pairs.

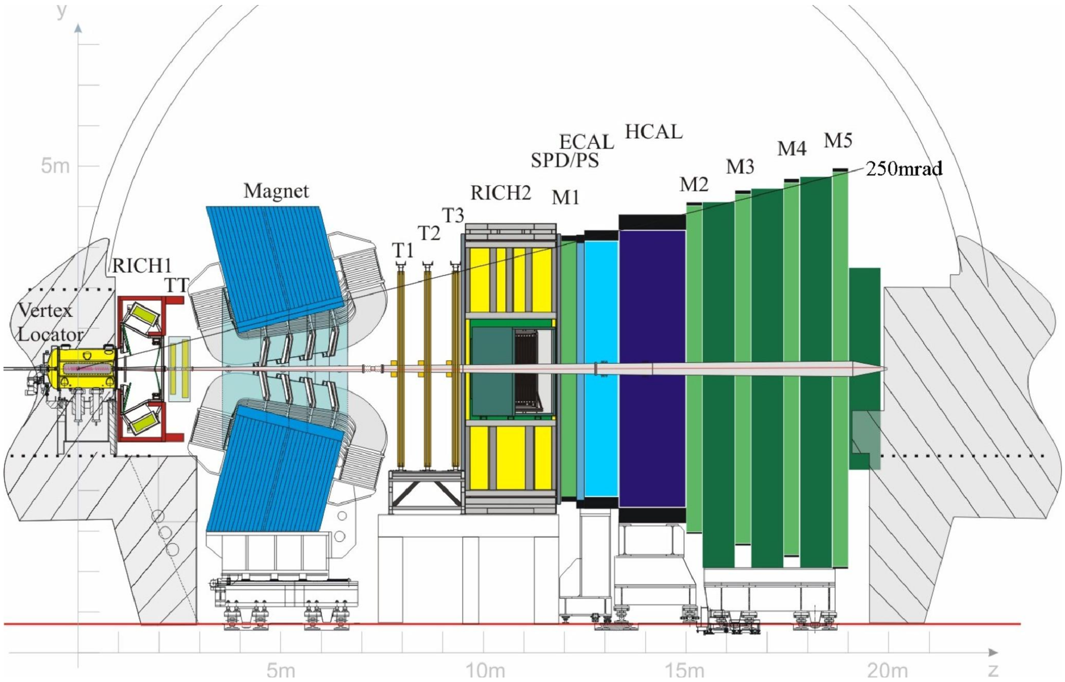

Figure 3.2: Schematic of the LHCb detector.

Fig 3.2 shows the layout of the LHCb detector. The detector lies along the direction, z, which is defined by the centre axis of the LHC beams. Meanwhile, the x-y plane is defined as the plane transverse to z. The position at which the beams collide ($z = 0$) is surrounded by a Vertex Locator (VELO). Further downstream ($z > 0$) of the VELO is the detector's magnet which provides an integrated field of 4 Tm in the x-y plane. Tracking detectors which are located before (TT) and after the magnetic field (T1, T2 and T3), provide forward tracking. The detector has two Ring Imaging Cherenkov (RICH) detectors which provide particle identification for charged hadrons.

After the RICH2 detector, additional particle identification is provided by Electromagnetic and hadronic calorimeters (ECAL & HCAL), a scintillator pad detector and preshower (SPD/PS) and five muon detectors (M1–5).

In 2012 alone, over 10^{12} $b\bar{b}$ pairs were produced within the LHCb detector's acceptance corresponding to an integrated luminosity of approximately 2fb^{-1}. This can be compared with the Belle and BaBar datasets which correspond to 8×10^9 [9] and 5×10^9 $B\bar{B}$ pairs [6], respectively. While LHCb has the virtue of statistics, the hadronic environment makes measurements involving neutrinos or neutrals difficult. This is because, unlike the case at the B factories (see Fig 3.3), no initial energy and momentum constraints are available since the interacting energies and momenta of quarks and gluons within the proton are not known. For this reason, while the LHCb experiment was expected to perform searches for rare B decays and precision measurements of CP-violation and CKM-observables such as the angles β and γ, a measurement of $|V_{ub}|$ was not anticipated [54].

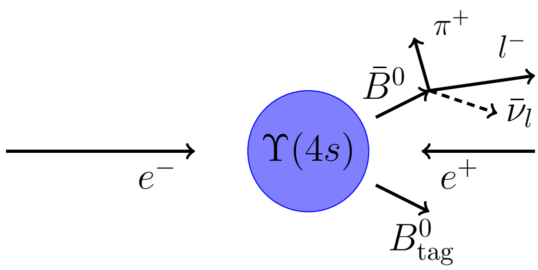

Figure 3.3: Topology for an $e^-e^+ \to \Upsilon(4s) \to B^0(\overline{B}^0 \to \pi^+ l^- \bar{\nu}_l)$ event at the B-factories Belle and BaBar. Knowledge of the energies and momenta of the colliding e^+ and e^- beams together with the possibility of fully reconstructing the non-signal B^0 (tagging), the signal pion and the signal lepton allows for the 4-momentum of the neutrino to be determined. The possibility of reconstructing the non-signal B^0 with a reasonable efficiency relies on the hermetic nature of the Belle and BaBar detectors.

3.2.1. Reconstructing semileptonic decays with LHCb

A Λ_b^0 baryon with momentum $50\,\mathrm{GeV}/c$ will travel roughly 4 mm before decaying. The direction of the Λ_b^0 baryon can be obtained by reconstructing the production and decay vertices. This direction provides a crucial constraint for reconstructing semileptonic decays of b-hadrons within a hadronic environment. Knowledge of the primary and secondary vertex positions allows a number of variables to be determined which are critical for distinguishing between particles produced at the displaced vertex of a b-hadron to particles originating from or close to the primary vertex. This includes the distance between the primary and secondary vertices, known as the flight distance, and the shortest distance between the direction of a particle to the primary vertex, known as the impact parameter (IP) (see Fig 3.4). Often it is useful to test the hypothesis that the flight distance or impact parameter are non-zero against the hypothesis that they are zero. The compatibility of the impact parameter of a track or a combination of tracks with being zero with respect to a vertex can be tested using the difference in χ^2 from fits for the vertex with and without the track or tracks included; this is known as the impact parameter χ^2. In a similar way, the difference in χ^2 when two vertices are combined in to a single vertex is known as the flight distance χ^2, which is used to test the compatibility of the flight distance with zero.

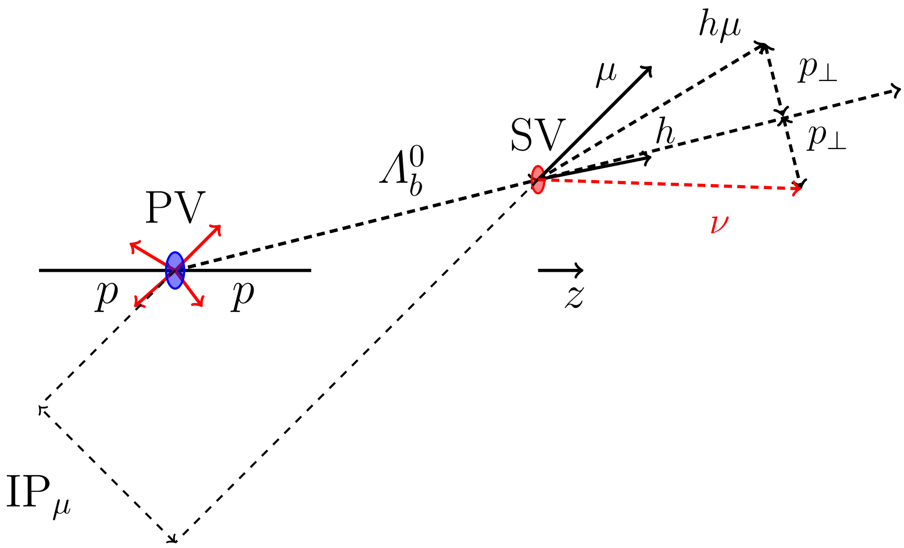

Figure 3.4: Illustration of a $\Lambda_b^0 \to h\mu^-\overline{\nu}_\mu$ decay produced from a pp collision. The impact parameter (IP) of the displaced proton and muon tracks with respect to the primary vertex help to discriminate these particles from any prompt tracks as shown in red. Conservation of momentum with respect to the flight direction of the Λ_b^0 baryon allows for the component of momentum of the neutrino perpendicular to the flight direction to be determined.

For a semileptonic decay $\Lambda_b^0 \to h\mu^-\overline{\nu}_\mu$, momentum conservation with respect to the flight direction of the Λ_b^0 baryon allows for the component of the neutrino momentum perpendicular to the flight direction to be determined, $p_\perp$ (see Fig 3.4). This makes it possible to reconstruct a corrected mass,

$$m_{\text{corr}} = \sqrt{p_\perp^2 + m_{h\mu}^2} + p_\perp \,, \tag{3.2}$$

which peaks at the mass of the Λ_b^0 baryon. The corrected mass is discussed in greater detail later in section 6.3.5.

3.2.2. The tracking and vertex locator

The reconstruction of primary and secondary vertices is made possible by LHCb detector's vertex locator, the VELO, which consists of a series of silicon modules placed around the pp interaction point along the beam direction. The VELO determines the position of vertices in cylindrical polar coordinates, (R, Φ, z). Modules placed on either side of the beam consist each of two semi-circular discs, one containing R sensors and the other Φ sensors as shown in Fig 3.5. The modules are retractable allowing the VELO to close in on the interaction region at the beginning of each fill such that the sensors are only 7mm from the interacting beams.

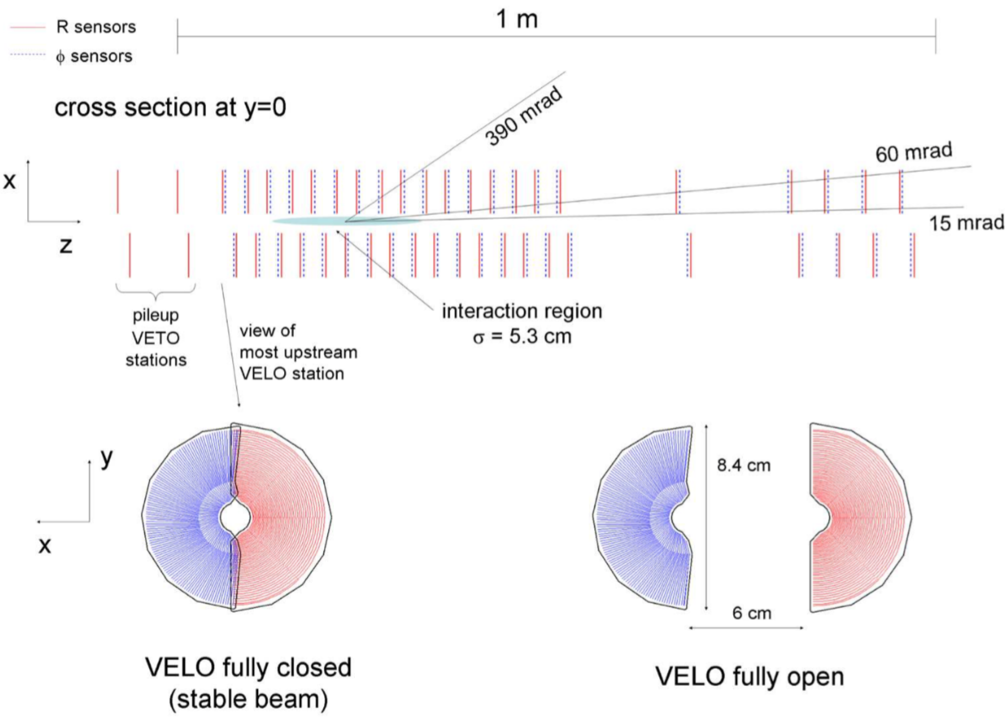

Figure 3.5: Schematic of the LHCb's vertex locator (the VELO). Semi-circular silicon modules consisting of R and Φ sensors are placed along the beam (z) direction in the x-y plane (top). The VELO is retractable as illustrated (bottom). Figure taken from [53].

The reconstruction of the primary vetex positions begins by finding potential positions (seed positions) for candidate primary vertices. These are points where at least four tracks pass close enough together. Tracks are considered as close if their distance of closest approach (DOCA) is less than 1 mm. A full description of the seeding algorithms and primary vertex reconstruction is given in Reference [55]. Starting from the seed positions the primary vertex is determined by minimising the primary vertex χ^2_{PV} defined by

$$\chi^2_{\mathrm{PV}} = \sum_{i=1}^{n_{\mathrm{tracks}}} \chi^2_{\mathrm{IP,i}} \cdot w_i \ , \tag{3.3}$$

where for the i$^{\mathrm{th}}$ track $\chi^2_{\mathrm{IP,i}} = \mathrm{IP}^2_{\mathrm{i}}/\sigma^2_{\mathrm{IP,i}}$. In this expression $\sigma_{\mathrm{IP,i}}$ is the uncertainty on the impact parameter as propagated from the uncertainties on the track's momentum components. Finally, w_i is a weight defined by

$$\begin{cases} w_i = (1 - \frac{\chi^2_{\mathrm{IP,i}}}{C^2_{\mathrm{T}}})^2, & \text{if } \chi^2_{\mathrm{IP}} < C^2_T \\ 0, & \text{otherwise} \ . \end{cases} \tag{3.4}$$

The parameter C_{T} is reduced throughout the iterative minimisation until $C_{\mathrm{T}} = 3$. This means that only tracks with $\chi^2_{\mathrm{IP,i}} < 9$ contribute to the vertex χ^2 and hence belong to the vertex. Primary vertices are only accepted if they have a minimum of 5 tracks.

Downstream of the VELO, LHCb has four tracking stations: the Tracker Turecensis (TT) before the magnet and the outer tracking stations T1, T2 and T3 after the magnet as shown in Fig 3.6. The TT is a four-layered silicon strip tracker, meanwhile, the outer tracking stations T1, T2 and T3 consist of silicon strip detectors close to the beam pipe and straw drift tubes further out. The trajectories of charged particles traversing through the tracking system are reconstructed by performing track fits to hits in the VELO, TT and the tracking stations T1, T2 and T3. Tracks are classified as VELO, upstream, long and downstream tracks depending on which tracking systems they have hits in as illustrated in Fig 3.6. The bending of charged particles in the magnetic field allows for their momentum to be measured with a precision of $\delta p/p \approx 0.4$–0.6. The decay vertex of the b-hadron may be determined by carrying out a vertex fit to the tracks associated with any charged particles it decays into.

Tracks which do not correspond to the trajectory of a charged particle are known as fakes or ghosts. A number of variables associated with the tracks including the χ^2 of the track fit are used within a neural network to discriminate fake tracks from the tracks of real particles. The output of the neural network is known as the ghost probability.

The resolution on the reconstructed primary and secondary vertex positions will dominate the resolution on physical quantities reconstructed using the Λ^0_b flight direction. A critical part of the selection of $\Lambda^0_b \to p\mu^-\overline{\nu}_\mu$ candidates for the $|V_{ub}|$ analysis involves the propagation of the

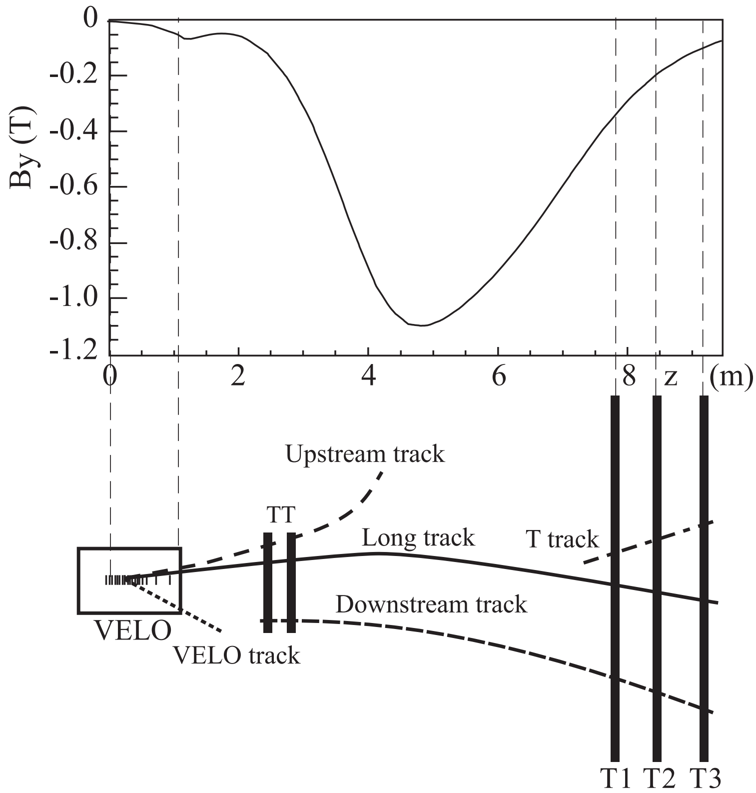

Figure 3.6: Diagram showing the tracking systems, magnetic field profile and the characterisation of tracks based on which tracking systems hits are found in. Taken from [56].

uncertainties on the primary and secondary vertex position on to the final reconstructed mass fit variable. Fig 3.7 shows the primary vertex resolution in x and y as a function of track multiplicity.

3.2.3. Particle identification

Particle Identification (PID) for charged particles is provided by two Ring Imaging Cherenkov detectors, RICH1 and RICH2. These measure the angle of emittance of Cherenkov radiation, θ_c, from a charged particle which is related to the particle's momentum, p, mass, m, and the refractive index, n, of the medium that the particle traverses by

$$\cos\theta_c = \frac{\sqrt{m^2 + p^2}}{np} \; . \tag{3.5}$$

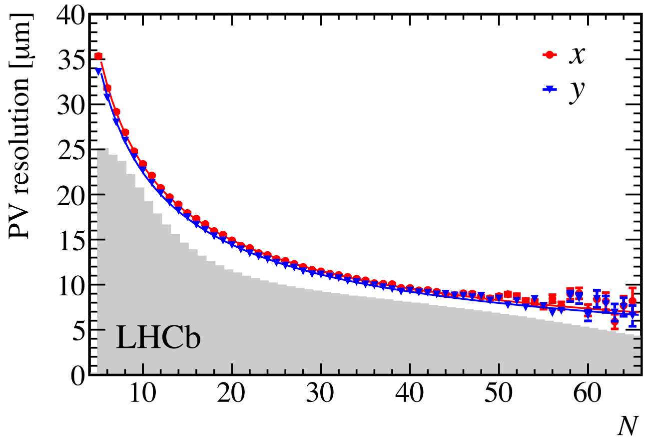

Figure 3.7: Resolution on the x and y positions of primary vertices as a function of the number of tracks. Taken from [56]. The superimposed histogram in grey shows the distribution of the number of tracks per event.

Fig 3.8 shows the Cherenkov angle against particle momentum for isolated rings produced by particles traversing in the C_4F_{10} radiator ($n = 1.0014$) of the RICH1 detector. Clear bands are observed corresponding to protons, kaons, pions and muons as a result of their differing masses. The starting positions of the bands reflect the momentum thresholds at which the different particle species begin to produce Cherenkov radiation. In order to maintain particle identification below these thresholds a second radiator, silica aerogel ($n = 1.03$), is included in a 50 mm thick wall, at the entrance of RICH1[1]. At higher momentums above 40 GeV/c, it is difficult to distinguish charged hadrons with the RICH1 as $\theta_c \to \cos^{-1}(1/n)$ for all particle species. The RICH2 detector provides particle identification in the momentum range, 15–100 GeV/c^2, by using a lower refractive index medium, CF_4, with $n = 1.0005$

In practice there are a number of overlapping rings in the RICH detectors associated with multiple tracks in the same event. In order to correctly identify the particle-type of the tracks an overall log-likelihood for the measured rings is constructed assuming particles are of given mass hypothesises. Starting from the assumption that all particles are pions the log-likelihood is minimised by accepting changes of the mass hypothesis of single particles if this reduces the overall log-likelihood. The change in the log-likelihood between two mass hypothesises, X and Y, for a given particle is denoted by, $\Delta\log\mathcal{L}(\mathrm{X}-\mathrm{Y})$. This variable can be used to discriminate between the two particle hypotheses, X and Y. Fig 3.9 shows proton identification and $K/\pi \to p$ mis-identification

[1]The aerogel has now been removed from the LHCb detector due to its poor performance in the 2011 and 2012 data taking periods.

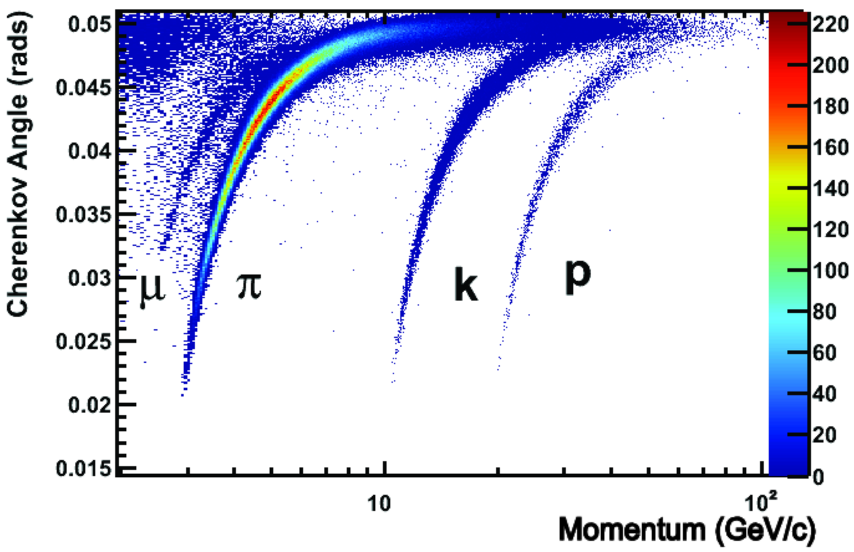

Figure 3.8: Cherenkov angle, θ_c, against momentum for rings associated with isolated tracks in the C_4F_{10} radiator of the RICH2 detector. Taken from [57].

rates using the selection criteria: $\Delta\log\mathcal{L}(\mathrm{p}-\mathrm{K}/\pi) > 5,0$. The efficiencies and misidentification rates for different $\Delta\log\mathcal{L}(\mathrm{X}-\mathrm{Y})$ selections are determined using calibration samples of pions and kaons from $D^{*+} \to \pi^+(D^0 \to K^-\pi^+)$ decays and protons from $\Lambda_b^0 \to (\Lambda_c^+ \to pK^-\pi^+)\mu^-\overline{\nu}_\mu$ decays, where in both cases no particle identification criteria is placed on the hadron of interest.

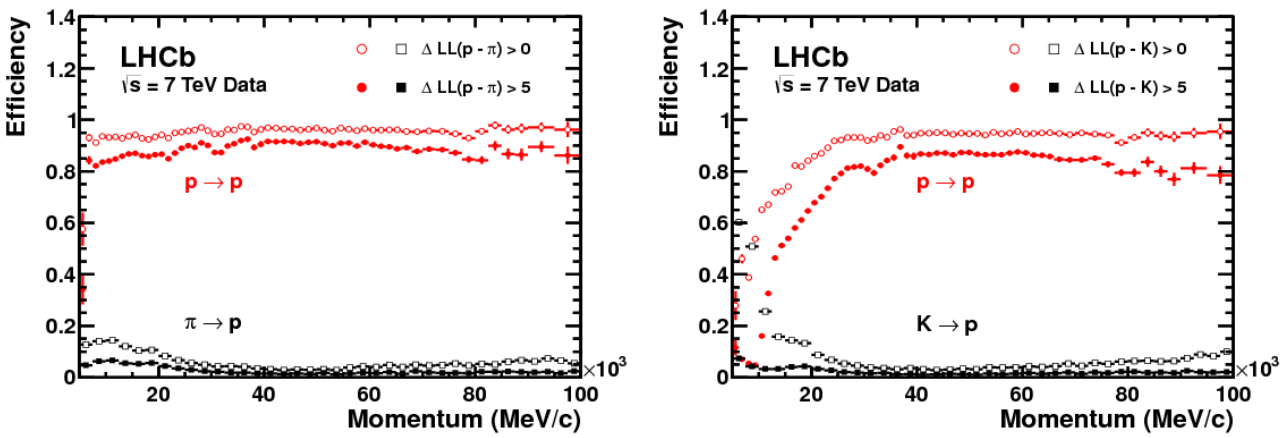

Figure 3.9: Proton identification efficiency and $\pi/K \to p$ misidentification rates for the requirements $\Delta\log\mathcal{L}(\mathrm{p}-\pi) > 0,5$ and $\Delta\log\mathcal{L}(\mathrm{p}-\mathrm{K}) > 0,5$. Taken from [57].

In addition to the particle identification provided by the RICH detectors there are separate detector systems for detecting electrons and muons. Electromagnetic and hadronic calorimeters (ECAL & HCAL) in conjunction with a scintillator pad detector and preshower (SPD/PS) are used to identify electrons and photons via their deposited energy. Meanwhile, there are five stations M1–5 containing Multi-Wire Proportional Chambers (MWPCs) for detecting muons. The Muon stations M2–5, which are located behind the HCAL, are each separated by 80cm thick plates of iron to absorb any remaining hadrons.

Momentum range	Muon stations
$3\,\mathrm{GeV}/c < p < 6\,\mathrm{GeV}/c$	M2 & M3
$6\,\mathrm{GeV}/c < p < 10\,\mathrm{GeV}/c$	M2 & M3 & (M4 | M5)
$p > 10\,\mathrm{GeV}/c$	M2 & M3 & M4 & M5

Table 3.1: Tracks are required to have hits in specific combinations of the muon stations based on their momentum in order to be positively identified as muons according to the binary decision `isMuon=true`. The full requirements, which depend on the momentum of the track, are outlined above.

Muon identification is made by a binary decision, known as `isMuon`, which is based on in which muon stations a track leaves hits and the track momentum (see table 3.1). The muon identification efficiency of this criteria is excellent with on average $98.13 \pm 0.04\%$ of muons being identified correctly as muons and around 1% of charged hadrons being misidentified as muons [58]. Fig 3.10 shows the muon identification efficiency as a function of muon momentum as determined from a $J/\psi \to \mu^+\mu^-$ tag and probe study [59]. In addition, the $\pi \to \mu$ misidentification rate is shown which has been determined from the pion PID calibration samples. For higher transverse momenta, the muon identification efficiency is higher and the rate of misidentification of hadrons as muons is lower.

3.2.4. Trigger

The rate at which a full detector readout for a given pp interaction can be sustained is ~5 kHz. However, at nominal running conditions in 2012 the rate of non-empty bunch-crossings was around 11 MHz [60]. A two-levelled trigger system is used to achieve the required reduction in the event rate, while maintaining a high fraction of events containing beauty and charm hadrons.

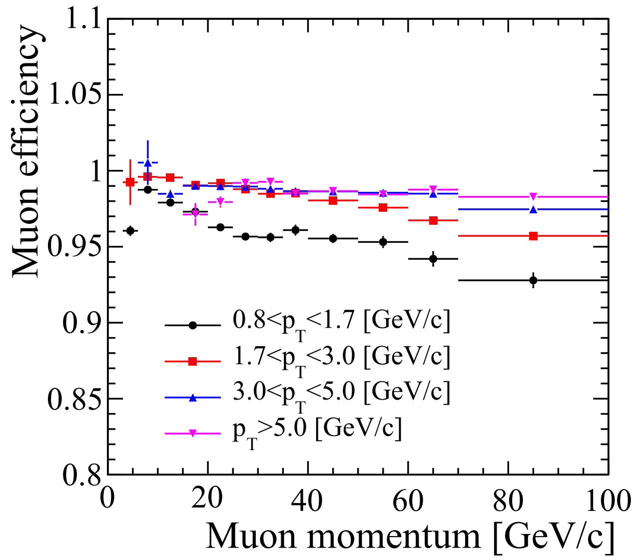

Figure 3.10: Muon identification efficiency (left) and the $\pi \to \mu$ misidentification rate (right) as a function of particle momentum for the `isMuon = true` binary decision. Results are displayed in a number of ranges of transverse muon momentum. Taken from [56].

The first level of this system, the L0 trigger, is hardware-based and reduces the event rate to $\sim$1 MHz. The L0 triggers on high transverse energy hadrons, electrons or photons in the calorimeter system and/or high transverse momentum muon candidates in the muon stations. The analysis work presented in this thesis used candidates triggered at the hardware level by the requirement that the event contained at least one muon with a transverse momentum, p_{T}, greater than $0.5\,\mathrm{GeV}/c$. In addition, the event is only triggered if the SPD hit multiplicity is below 600.

The second level of the trigger involves two software-based triggers, known as the Higher Level Triggers (HLT1 and HLT2). The HLT1 adds information from the tracking and VELO systems allowing for a 1 MHz to 40 kHz reduction in the event rate. Tracks in the VELO are used to reconstruct any vertices with at least five tracks originating from them. These vertices are classified as primary vertices if the vertex is within a radius of 300μm from the mean position of the pp interaction envelope in the transverse plane. A forward reconstruction of VELO tracks using hits in the inner and outer tracking stations is made using a simplified material geometry description. Given time constraints, only tracks in the VELO which are likely to come from b/c-hadron decays are considered. For events with muons, VELO tracks are chosen if they match well with hits found in the muon chambers. In the absence of muons, VELO tracks are selected based on their smallest impact parameter with respect to any of the identified PVs. For the $|V_{ub}|$ analysis, candidates were triggered at HLT1 by the requirement of at least one muon with $p_{\mathrm{T}} > 1\,\mathrm{GeV}/c$.

At the reduced rate of around 40 kHz a full event reconstruction of all VELO tracks is made by HLT2. Several exclusive and inclusive selections [61] are performed by the HLT2. The inclusive trigger lines apply a n-body topological search for b-hadron decays in which only n of the daughter particles are reconstructed. Tracks are combined into two-body objects if their distance of closest approach (DOCA) is less than 0.2 mm. The algorithm continues to form higher n-body objects if the DOCA between an additional track and a $n-1$-body object satisfies, DOCA < 0.2 mm. A multivariate selection is now made combining the discriminating power of the n-body corrected and invariant masses, the IP χ^2 and flight distance χ^2 of the n-body vertex with respect to the primary vertex and finally, the sum track p_{T}s and the minimum track p_{T}. The two-body topological selection including a muon requirement is the ideal trigger for a search for the decay $\Lambda_b^0 \to p\mu^-\overline{\nu}_\mu$. The final readout rate of the HLT2 is around 5kHz and the chosen events are subsequently written to permanent storage.

The total efficiency for selecting an event, ϵ_{tot}, will depend on the trigger efficiency, $\epsilon_{\mathrm{trig|sel}}$, according to

$$\epsilon_{\mathrm{tot}} = \epsilon_{\mathrm{trig|sel}} \cdot \epsilon_{\mathrm{reco\&sel|acc}} \cdot \epsilon_{\mathrm{acc}} \ , \tag{3.6}$$

where the efficiency for candidates to be in the detector acceptance, ϵ_{acc}, and the efficiency for reconstruction and selection, $\epsilon_{\mathrm{reco\&sel|acc}}$, are determined from simulation.

The trigger efficiency can be determined according to

$$\epsilon_{\mathrm{trig|sel}} = \frac{N_{\mathrm{trig|sel}}}{N_{\mathrm{sel}}} \ , \tag{3.7}$$

where $N_{\mathrm{trig|sel}}$ is the number of selected events passing the trigger and N_{sel} is the number of events that would have been selected in the absence of the trigger. However, in data the number of selected events is unknown as all events have been triggered. In order to determine the trigger efficiency from data the TISTOS method is employed [62]. Events may be triggered independent of signal (TIS) or/and triggered on the signal candidate (TOS). The trigger efficiency can be rewritten as

$$\begin{aligned}\epsilon_{\mathrm{trig|sel}} &= \frac{N_{\mathrm{trig|sel}}}{N_{\mathrm{TIS|sel}}} \times \frac{N_{\mathrm{TIS|sel}}}{N_{\mathrm{sel}}} \\ &= \frac{N_{\mathrm{trig|sel}}}{N_{\mathrm{TIS|sel}}} \times \epsilon_{\mathrm{TIS}} \ ,\end{aligned} \tag{3.8}$$

where $N_{\mathrm{TIS|sel}}$ is the number of TIS events after the selection has been applied. While the efficiency ϵ_{TIS} cannot be determined exactly from data it can be approximated as

$$\epsilon_{\mathrm{TIS}} \approx \epsilon_{\mathrm{TISTOS}} \equiv \frac{N_{\mathrm{TIS\&TOS}}}{N_{\mathrm{TOS}}} \ , \tag{3.9}$$

using the number events that are TOS, N_{TOS} and the number of events that are both TOS and TIS, $N_{\mathrm{TIS\&TOS}}$. This approximation assumes that the efficiency, ϵ_{TIS}, is independent of the chosen subsample of data. The validity of this assumption is demonstrated in Reference [62].

3.2.5. Simulation

Simulated events are required to model signal and background decays of b-hadrons. The simulation of b-hadron decays starts with the generation of $pp \to b\bar{b}X$ interactions at the appropriate centre of mass energy using PYTHIA 6.4 [63] or 8.1 [64]. The generated $b\bar{b}$ pair is repeatedly hadronised until a b-hadron of the required type is produced from one of the b quarks. The subsequent decay of the b-hadron is modelled using EVTGEN [65], meanwhile, any potential final state electromagnetic radiation is handled using the PHOTOS package [66]. At this stage requirements may be made on the generated b-hadron and its daughter particles such as detector acceptance requirements. All particles produced by the $pp \to b\bar{b}X$ interactions are passed through a full simulation of the LHCb detector based on theGEANT4 [67] framework. The simulated response of the detector is digitised to emulate the response of the read-out electronics and subsequently passed through the same reconstruction procedures applied to actual data. This includes a full emulation of the trigger response on the simulated events.

Chapter 4.

The strategy for $|V_{ub}|$ at the LHC

This chapter outlines the strategy employed for the measurement of $|V_{ub}|$ at the Large Hadron Collider presented in this thesis. This includes a discussion motivating the choice to measure $|V_{ub}|$ with $\Lambda_b^0 \to p\mu^-\overline{\nu}_\mu$ decays.

In order to measure $|V_{ub}|$ with the LHCb experiment an exclusive approach is employed. The choice of an exclusive measurement as opposed to an inclusive measurement is made as it is very difficult to separate the large $b \to c$ background from the $b \to u$ inclusive signal at LHCb. In particular at the LHC it is not possible to reconstruct the lepton energy with a precision that allows for one to exploit the $b \to u$ kinematic endpoint in the same way as employed by the B factories.

At LHCb the large numbers of $b\bar{b}$ pairs produced, over 600 billion in 2012, coupled with the fraction of $b \to u$ processes ($\sim 10^{-4}$) provides for a high statistics environment to study such transitions. This can be compared to the latest $|V_{ub}|$ determinations from $\overline{B}^0 \to \pi^+ l^- \overline{\nu}_l$ decays by the BaBar and Belle experiments which used data samples containing respectively 462 million [6] and 772 million [9] $B\bar{B}$ pairs collected from e^+e^-collisions at the $\Upsilon(4s)$ resonance. The sizable fragmentation fractions of b quarks to B_s^0 mesons and Λ_b^0 baryons at the LHC allows for the possibility of novel determinations of $|V_{ub}|$ from $\Lambda_b^0 \to p\mu^-\overline{\nu}_\mu$ and $\overline{B}_s^0 \to K^+\mu^-\overline{\nu}_\mu$ decays.

The decays $\overline{B}^0 \to \pi^+\mu^-\overline{\nu}_\mu$, $\overline{B}_s^0 \to K^+\mu^-\overline{\nu}_\mu$ and $\Lambda_b^0 \to p\mu^-\overline{\nu}_\mu$ which have a ground state hadron in the final state are golden modes for the lattice. While the decay $\overline{B}_s^0 \to K^+\mu^-\overline{\nu}_\mu$ allows for a determination of $|V_{ub}|$ with the smallest theoretical uncertainty (see [36]) the proton in the decay $\Lambda_b^0 \to p\mu^-\overline{\nu}_\mu$ makes for a much more distinctive final state at the LHC. This can be seen in Fig. 4.1 which shows the corrected $h\mu$ mass distribution for kaons, pions and protons when applying a loose selection to a simulated sample of 10 million inclusive $b\bar{b}$ events. The selected hadron is found to be a pion or kaon 82% and 15% of the time, respectively. Meanwhile, only 3% of the selected events contain a proton. This demonstrates that an analysis of $\overline{B}^0 \to \pi^+\mu^-\overline{\nu}_\mu$ and $\overline{B}^0_s \to K^+\mu^-\overline{\nu}_\mu$ decays would face larger backgrounds than that for $\Lambda^0_b \to p\mu^-\overline{\nu}_\mu$ decays.

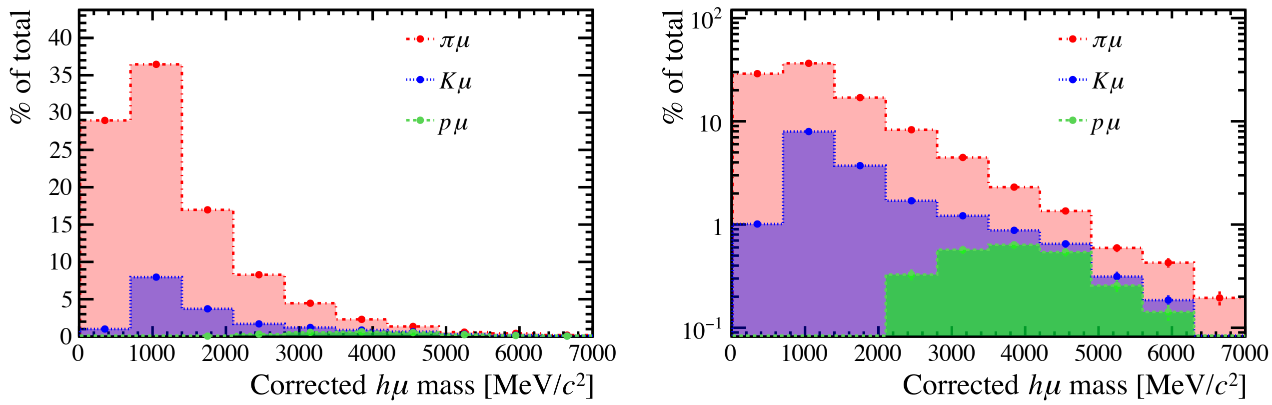

Figure 4.1: Percentage of $h\mu$ candidates that are $p\mu$, $\pi\mu$ or $K\mu$ in a sample of simulated $b\bar{b}$ events in bins of the $h\mu$ corrected mass with a linear scale (left) and a logarithmic scale (right).

While Λ^0_b baryons were not produced at the B factories, around 20% of the B-hadrons produced at the LHC are Λ^0_b baryons. Fig. 4.2 shows the ratio of Λ^0_b production to B^0 production measured as a function of p_{T} for Λ^0_b baryons produced within LHCb [68]. This can be compared with the measured ratio of B^0_s production to B^0 production at LHCb, $f_s/f_d = 0.267^{+0.021}_{-0.020}$ [69]. The large production of $b\bar{b}$ pairs combined with the substantial fragmentation of b quarks to Λ^0_b baryons and the large branching fraction of $\Lambda^0_b \to p\mu^-\overline{\nu}_\mu$ compared to other exclusive $b \to u$ transitions results in a large number of $\Lambda^0_b \to p\mu^-\overline{\nu}_\mu$ candidates. As a result of this, the analysis was designed to minimise potential source of systematic uncertainties by selecting the best $\Lambda^0_b \to p\mu^-\overline{\nu}_\mu$ candidates rather than being optimised based on statistics.

A precision determination of $|V_{ub}|$ from $\Lambda^0_b \to p\mu^-\overline{\nu}_\mu$ decays alone would require precise measurements of the $b\bar{b}$ cross-section and the Λ^0_b production fraction. Given the limited precision on these measurements, a normalisation is made to $\Lambda^0_b \to \Lambda^+_c\mu^-\overline{\nu}_\mu$ decays. A measurement of the ratio of the branching fractions of $\Lambda^0_b \to p\mu^-\overline{\nu}_\mu$ and $\Lambda^0_b \to \Lambda^+_c\mu^-\overline{\nu}_\mu$ decays for $q^2 > 15\ \mathrm{GeV}^2/c^4$ and $q^2 > 7\ \mathrm{GeV}^2/c^4$ is made. This measurement, when combined with the recent LQCD calculation for the form factors of the decays, allows for a determination of $|V_{ub}|^2/|V_{cb}|^2$ according to

$$\frac{|V_{ub}|^2}{|V_{cb}|^2} = \frac{\mathcal{B}_{\Lambda^0_b \to p\mu^-\overline{\nu}_\mu | q^2 > 15\,\mathrm{GeV}^2/c^4}}{\mathcal{B}_{\Lambda^0_b \to \Lambda^+_c\mu^-\overline{\nu}_\mu | q^2 > 7\,\mathrm{GeV}^2/c^4}} R_{\mathrm{FF}}\ , \tag{4.1}$$

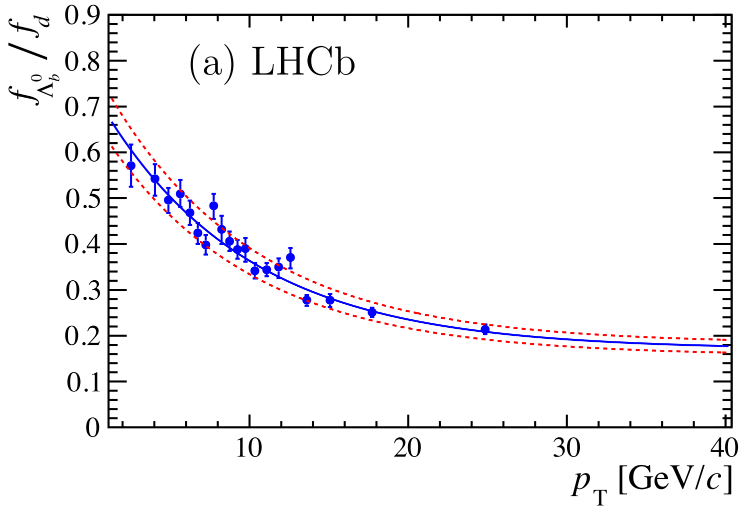

Figure 4.2: Ratio of the production of Λ_b^0 baryons to B^0 mesons measured at LHCb as a function of the p_{T} of the Λ_b^0 baryon. From [68].

where here $\mathcal{B}$ denotes the relevant branching fractions and R_{FF} is

$$R_{\mathrm{FF}} = \frac{\int_{15\,\mathrm{GeV}^2/c^4}^{q^2_{max}} \frac{1}{|V_{ub}|^2} \frac{d\Gamma}{dq^2}_{\Lambda_b^0 \to p\mu^-\overline{\nu}_\mu} dq^2}{\int_{7\,\mathrm{GeV}^2/c^4}^{q'^2_{max}} \frac{1}{|V_{cb}|^2} \frac{d\Gamma}{dq^2}_{\Lambda_b^0 \to \Lambda_c^+\mu^-\overline{\nu}_\mu} dq^2} = 1.471 \pm 0.0095 \pm 0.1409\,,$$

as was first defined in equation 2.74 of section 2.4.6. The choice to measure these decays at high q^2 reflects the fact that LQCD calculations have least uncertainty towards the kinematic endpoint in q^2. The specific ranges were chosen based on the availability of lattice predictions for the form factors in these regions.

The required ratio of branching fractions can be determined experimentally according to the expression,

$$\frac{\mathcal{B}_{\Lambda_b^0 \to p\mu^-\overline{\nu}_\mu | q^2 > 15\,\mathrm{GeV}^2/c^4}}{\mathcal{B}_{\Lambda_b^0 \to \Lambda_c^+\mu^-\overline{\nu}_\mu | q^2 > 7\,\mathrm{GeV}^2/c^4}} = \frac{N_{\Lambda_b^0 \to p\mu^-\overline{\nu}_\mu | q^2 > 15\,\mathrm{GeV}^2/c^4}}{N_{\Lambda_b^0 \to (\Lambda_c^+ \to pK^-\pi^+)\mu^-\overline{\nu}_\mu | q^2 > 7\,\mathrm{GeV}^2/c^4}} \cdot \frac{\mathcal{B}(\Lambda_c^+ \to pK^-\pi^+)}{\epsilon_{rel}}\,, \tag{4.2}$$

where $N_{\Lambda_b^0 \to p\mu^-\overline{\nu}_\mu | q^2 > 7\,\mathrm{GeV}^2/c^4}$ and $N_{\Lambda_b^0 \to (\Lambda_c^+ \to pK^-\pi^+)\mu^-\overline{\nu}_\mu | q^2 > 15\,\mathrm{GeV}^2/c^4}$ are the yields for the decays $\Lambda_b^0 \to p\mu^-\overline{\nu}_\mu$ and $\Lambda_b^0 \to (\Lambda_c^+ \to pK^-\pi^+)\mu^-\overline{\nu}_\mu$, respectively. These yields are determined by fitting corrected mass distributions for the selected $p\mu$ and $\Lambda_c^+\mu$ candidates. Meanwhile, the relative efficiency for selecting the two modes, $\epsilon_{\rm rel}$, is defined as

$$\epsilon_{\rm rel} = \frac{\epsilon_{\Lambda_b^0 \to p\mu^-\overline{\nu}_\mu | q^2 > 15\,{\rm GeV}^2/c^4}}{\epsilon_{\Lambda_b^0 \to (\Lambda_c^+ \to pK^-\pi^+)\mu^-\overline{\nu}_\mu | q^2 > 7\,{\rm GeV}^2/c^4}} \,. \tag{4.3}$$

This efficiency is determined from simulation after a number of data driven corrections have been applied. Finally, $B_{\Lambda_c^+ \to pK^-\pi^+}$ is the branching fraction of $\Lambda_c^+ \to pK^-\pi^+$ for which the Belle measurement of $\mathcal{B}_{\Lambda_c^+ \to pK^-\pi^+} = (6.84 \pm 0.24^{+0.21}_{-0.27})\%$ [70] is used. At the time at which the analysis was performed, this was the only available determination of $\mathcal{B}_{\Lambda_c^+ \to pK^-\pi^+}$ with a competitive uncertainty. More recently, BESIII has measured a substantially lower value of $\mathcal{B}_{\Lambda_c^+ \to pK^-\pi^+} = (5.84 \pm 0.27 \pm 0.23)\%$ [71]. The latest HFAG average combining the Belle and BESIII measurements is $\mathcal{B}_{\Lambda_c^+ \to pK^-\pi^+} = (6.46 \pm 0.24)\%$. In section 7.5.2 determinations of $|V_{ub}|$ using the Belle, BESIII and HFAG values for $\mathcal{B}_{\Lambda_c^+ \to pK^-\pi^+}$.

The branching fraction of $\Lambda_b^0 \to p\mu^-\overline{\nu}_\mu$ decays, $\mathcal{B}_{\Lambda_b^0 \to p\mu^-\overline{\nu}_\mu}$, can also be measured by extrapolating the measured branching fraction to the full q^2 regions acccording to

$$\mathcal{B}_{\Lambda_b^0 \to p\mu^-\overline{\nu}_\mu} = \frac{\mathcal{B}_{\Lambda_b^0 \to p\mu^-\overline{\nu}_\mu | q^2 > 15\,{\rm GeV}^2/c^4}}{\mathcal{B}_{\Lambda_b^0 \to \Lambda_c^+ \mu^-\overline{\nu}_\mu | q^2 > 7\,{\rm GeV}^2/c^4}} \cdot B_{ext.} \,, \tag{4.4}$$

where here the extropolation factor is defined as

$$\begin{aligned} B_{ext.} &= \tau_{\Lambda_b^0} \cdot |V_{cb}|^2 \cdot \int_{7\,{\rm GeV}^2/c^4}^{q^{2\prime}_{max}} \frac{d\Gamma}{dq^2}_{\Lambda_b^0 \to \Lambda_c^+ \mu^-\overline{\nu}_\mu} dq^2 \cdot \frac{\int_{0\,{\rm GeV}^2/c^4}^{q^2_{max}} \frac{d\Gamma}{dq^2}_{\Lambda_b^0 \to p\mu^-\overline{\nu}_\mu} dq^2}{\int_{15\,{\rm GeV}^2/c^4}^{q^2_{max}} \frac{d\Gamma}{dq^2}_{\Lambda_b^0 \to p\mu^-\overline{\nu}_\mu} dq^2} \\ &= \tau_{\Lambda_b^0} \cdot |V_{cb}|^2 \cdot B_{\rm FF} \,, \end{aligned} \tag{4.5}$$

where $B_{\rm FF} = 17.45 \pm 1.60 \pm 3.78$.

Chapter 5.

Form factor modelling

An accurate simulation of signal, normalisation and background decays is essential for determining the signal and normalisation efficiencies and obtaining the various mass shapes used in the signal and normalisation fits. An integral part of simulating these decays is modelling their form factors and the associated uncertainties. This chapter describes the form factor predictions and their implementation for the $|V_{ub}|$ analysis.

5.1. EvtGen

As described in section 3.2.5 the modelling of b-hadron decays in the LHCb simulation framework is handled by the B-physics Monte Carlo generator, EvtGen [65]. New decay models were created in EvtGen implementing the form factor predictions for $\Lambda_b^0 \to p\mu^-\overline{\nu}_\mu$, $\Lambda_b^0 \to N^{*+}\mu^-\overline{\nu}_\mu$, $\Lambda_b^0 \to \Lambda_c^+\mu^-\overline{\nu}_\mu$ and $\Lambda_b^0 \to \Lambda_c^{*+}\mu^-\overline{\nu}_\mu$ decays.

5.1.1. EvtGen B decay algorithm

EvtGen employs an accept-reject method to generate $\Lambda_b^0 \to X\mu^-\overline{\nu}_\mu$ decays according to a particular model. Kinematics for the $\Lambda_b^0 \to X\mu^-\overline{\nu}_\mu$ decay are first generated according to phase-space. This allows the amplitude, $\mathcal{A}$, for the decay under a given model to be computed. Decays may be generated according to a given model by accepting generated decays with the probability,

$$p^{\Lambda_b^0 \to X\mu^-\overline{\nu}_\mu} = \sum_{s_X, s_\mu} \left| \mathcal{A}_{s_X, s_\mu}^{\Lambda_b^0 \to X\mu^-\overline{\nu}_\mu} \right|^2 , \tag{5.1}$$

where s_X and s_μ are spin indices.

In the case of a decay, $\Lambda_b^0 \to (X \to f)\mu^-\overline{\nu}_\mu$, the full decay is again generated according to phase-space until a decay is accepted based on the probability $p_{\Lambda_b^0 \to X\mu^-\overline{\nu}_\mu}$. Subsequently, an additional acceptance requirement is made based on the probability,

$$p^{X\to f} = \frac{1}{\mathrm{Tr}\rho^{\mathrm{X}}} \sum_{s_X, s'_X} \rho^X_{s_X, s'_X} \mathcal{A}^{X\to f}_{s_X} \mathcal{A}^{*X\to f}_{s'_X} \ , \tag{5.2}$$

where, $\rho^X_{s_X, s'_X}$, refers to a spin density matrix given by

$$\rho^X_{s_X, s'_X} = \sum_{s_\mu} \mathcal{A}^{\Lambda_b^0 \to X\mu^-\overline{\nu}_\mu}_{s_X, s_\mu} \mathcal{A}^{*\Lambda_b^0 \to X\mu^-\overline{\nu}_\mu}_{s'_X, s_\mu} \ . \tag{5.3}$$

5.1.2. Baryonic form factors within EvtGen

Within EvtGen, baryonic vector and axial vector form factors for $\Lambda_b^0 \to p\mu^-\overline{\nu}_\mu$ and $\Lambda_b^0 \to \Lambda_c^+\mu^-\overline{\nu}_\mu$ decays are implemented according to the convention

$$\left\langle X(p', s') \left| \bar{q}\gamma^\mu u \right| \Lambda_b^0(p, s) \right\rangle = \bar{u}_X(p', s') \left(F_1(q^2)\gamma^\mu + F_2(q^2)\frac{p^\mu}{m_{\Lambda_b}} + F_3(q^2)\frac{p'^\mu}{m_X} \right) u_{\Lambda_b}(p, s) \ . \tag{5.4}$$

and

$$\left\langle X(p', s') \left| \bar{q}\gamma^\mu \gamma_5 u \right| \Lambda_b^0(p, s) \right\rangle = -\bar{u}_X(p', s') \left(G_1(q^2)\gamma^\mu + G_2(q^2)\frac{p^\mu}{m_{\Lambda_b}} + G_3(q^2)\frac{p'^\mu}{m_X} \right) \gamma_5 u_{\Lambda_b}(p, s) \ . \tag{5.5}$$

5.2. Form factor models

5.2.1. Static quark form factors

Given the time frame of the analysis work, $\Lambda_b^0 \to p\mu^-\overline{\nu}_\mu$ decays were simulated[1] using the static-b quark LQCD predictions [72].

[1]Simulated $\Lambda_b^0 \to p\mu^-\overline{\nu}_\mu$ decays were later re-weighted to form factor predictions presented in section 5.2.3.

In leading order HQET the hadronic matrix element may be expressed in terms of two form factors,

$$\begin{aligned}\left\langle X(p',s')\left|\bar{q}\gamma^{\mu}(1-\gamma_5)u\right|\Lambda_b^0(p,s)\right\rangle =&\bar{u}_X(p',s')\left(F_1^{\mathrm{HQET}}+\gamma^{\rho}\frac{p_{\rho}}{m_X}F_2^{\mathrm{HQET}}\right)\\ &\times\left(c_{\gamma}\gamma^{\mu}+c_p\frac{p^{\mu}}{m_{\Lambda_b}}-c_{\gamma}\gamma^{\mu}\gamma_5+c_p\frac{p^{\mu}}{m_{\Lambda_b}}\gamma_5\right)u_{\Lambda_b}(p,s)\ ,\end{aligned} \tag{5.6}$$

where c_γ and c_p are one-loop matching coefficients. Parametrisations of the HQET form factors and their conversions to the EvtGen convention (see equations 5.4 and 5.5) are shown in appendix A.1 together with the definitions of c_γ and c_p.

5.2.2. Quark model

In Reference [73] Pervin et al. calculate the form factors for $\Lambda_b^0 \to p\mu^-\overline{\nu}_\mu$, $\Lambda_b^0 \to N^{*+}\mu^-\overline{\nu}_\mu$, $\Lambda_b^0 \to \Lambda_c^+\mu^-\overline{\nu}_\mu$ and $\Lambda_b^0 \to \Lambda_c^{*+}\mu^-\overline{\nu}_\mu$ decays using the non-relativistic quark model developed by Isgur et al. [74–76]. Wavefunctions are formulated for initial and final state baryons which include colour, spin, momentum and flavour parts. Quark interactions within the baryons are described by a phenomenological Hamiltonian with separate potentials encompassing quark confinement and hyperfine interactions. The free parameters of the Hamiltonian and the baryonic wavefunctions are tuned in order to reproduce the observed spectrum of ground and excited state baryon masses. The form factors can finally be determined by calculating the required hadronic matrix elements using the baryonic wavefunctions.

The key parameters governing the form factors of a given transition are the spatial wave function size parameters for initial and final states, λ and λ', and the heavy and light quark masses. Form factors were computed under two choices of the expansion bases for wavefunctions: the harmonic oscillator basis and the Sturmian basis [77]. For the $|V_{ub}|$ analysis, $\Lambda_b^0 \to \Lambda_c^+\mu^-\overline{\nu}_\mu$, $\Lambda_b^0 \to \Lambda_c^{*+}\mu^-\overline{\nu}_\mu$ and $\Lambda_b^0 \to N^{*+}\mu^-\overline{\nu}_\mu$ decays were simulated using the form factors determined using the harmonic oscillator basis. Table 5.1 shows the states simulated and the corresponding values of the form factor parameters (see [73] for definitions of the form factors and their parametrisations). Meanwhile, Fig 5.1 shows the simulated q^2 distribution for a range of $\Lambda_b^0 \to \Lambda_c^{*+}\mu^-\overline{\nu}_\mu$ and $\Lambda_b^0 \to N^{*+}\mu^-\overline{\nu}_\mu$ transitions.

Given that no theory uncertainty was available for the quark model predictions, Gaussian variations are made on the baryonic wavefunction parameters λ and λ'. The standard deviations

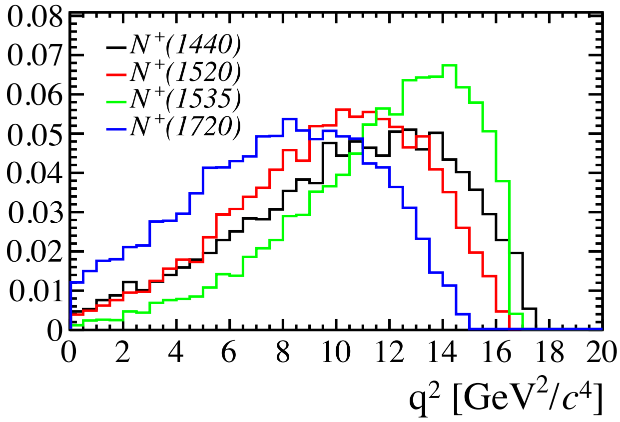

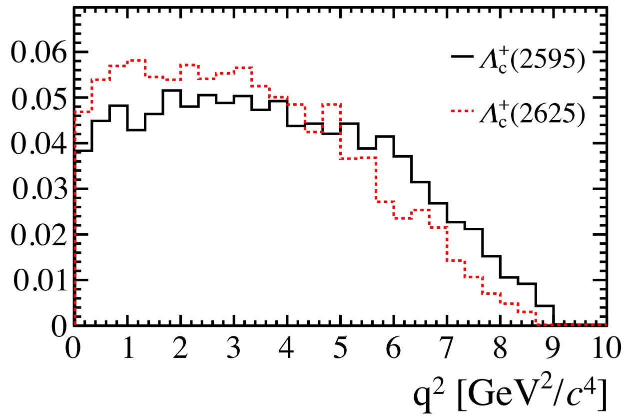

Figure 5.1: Simulated q^2 distributions for a number of different $\Lambda_b^0 \to N^{*+}\mu^-\overline{\nu}_\mu$ decays and $\Lambda_b^0 \to \Lambda_c^{*+}\mu^-\overline{\nu}_\mu$ decays. The form factors of these decays are modelled using the quark model predictions of Pervin et al. [73].

$\Lambda_b^0 \to X$	J^P	m_q	m_Q	λ	λ'
$\Lambda_b^0 \to p$	$\frac{1}{2}^+$	$0.4\,\mathrm{GeV}/c^2$	$5.28\,\mathrm{GeV}/c^2$	0.59	0.48
$\Lambda_b^0 \to N^+(1440)$	$\frac{1}{2}^+$	$0.4\,\mathrm{GeV}/c^2$	$5.28\,\mathrm{GeV}/c^2$	0.59	0.48
$\Lambda_b^0 \to N^+(1535)$	$\frac{1}{2}^-$	$0.4\,\mathrm{GeV}/c^2$	$5.28\,\mathrm{GeV}/c^2$	0.59	0.37
$\Lambda_b^0 \to N^+(1520)$	$\frac{3}{2}^-$	$0.4\,\mathrm{GeV}/c^2$	$5.28\,\mathrm{GeV}/c^2$	0.59	0.37
$\Lambda_b^0 \to N^+(1720)$	$\frac{1}{2}^+$	$0.4\,\mathrm{GeV}/c^2$	$5.28\,\mathrm{GeV}/c^2$	0.59	0.35
$\Lambda_b^0 \to \Lambda_c^+$	$\frac{1}{2}^+$	$1.89\,\mathrm{GeV}/c^2$	$5.28\,\mathrm{GeV}/c^2$	0.59	0.55
$\Lambda_b^0 \to \Lambda_c^+(2595)$	$\frac{1}{2}^-$	$1.89\,\mathrm{GeV}/c^2$	$5.28\,\mathrm{GeV}/c^2$	0.59	0.47
$\Lambda_b^0 \to \Lambda_c^+$	$\frac{3}{2}^-$	$1.89\,\mathrm{GeV}/c^2$	$5.28\,\mathrm{GeV}/c^2$	0.59	0.47

Table 5.1: Values of the initial and final state baryonic wavefunction parameters, λ and λ', and quark mass parameters which were used to simulated the the decays $\Lambda_b^0 \to X\mu^-\overline{\nu}_\mu$ according to the quark model form factor predictions. The values are taken from [73].

for the Gaussian variations are taken to be 50% of the nominal parameter values. Fig 5.2 shows the differential rate for $\Lambda_b^0 \to N^+(1440)\mu^-\overline{\nu}_\mu$ decays and the uncertainty band associated with the form factor variations.

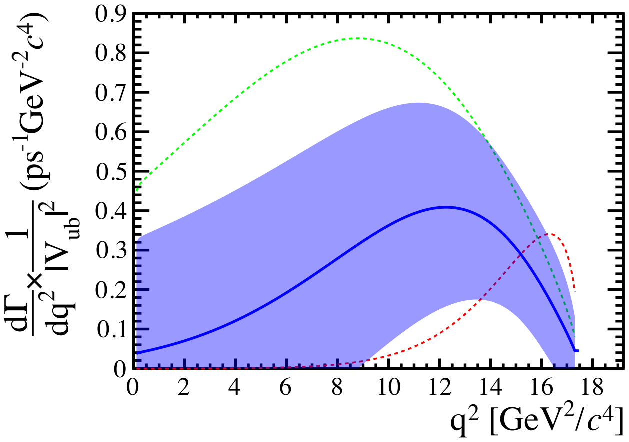

Figure 5.2: Differential rate for $\Lambda_b^0 \to N^+(1440)\mu^-\overline{\nu}_\mu$ decays as predicted by the quark model of Pervin et al [73]. The uncertainty band are formed by making Gaussian variations in the baryonic wavefunction parameters with a standard deviation which is 50% of the nominal parameter values. The dashed lines show two random variations of the differential rate obtained according to Gaussian variations in the form factor parameters.

5.2.3. Relativistic LQCD form factors and their uncertainties

Simulated $\Lambda_b^0 \to p\mu^-\overline{\nu}_\mu$ and $\Lambda_b^0 \to \Lambda_c^+\mu^-\overline{\nu}_\mu$ decays were re-weighted to the relativistic b-quark LQCD form factor predictions of Meinel et al. [42]. The form factor predictions were expressed in the helicity definition of the form factors (see equation 2.53). A conversion between the helicity and EvtGen definitions of the form factors is found in appendix A.2.

The parametrisation of a given helicity form factor, $f(q^2)$, in q^2 is handled using a simplified first order z-expansion[2]:

$$f(q^2) = \frac{1}{1 - \frac{q^2}{(m^f_{\rm pole})^2}} \left[a_0^f + a_1^f z^f(q^2)\right] \ . \tag{5.7}$$

where a_0^f and a_1^f are the z-expansion coefficients and $m^f_{\rm pole}$ is the mass of the leading pole which has been factorised out. The form factors have singularities at the poles, which physically correspond to the masses of excited B^* states which can decay as $B^* \to B\pi$. The expansion parameter, $z^f(q^2)$,

[2] This is a simplified version of the BCL z-expansion presented in [78].

is given by

$$z^f(q^2) = \frac{\sqrt{t_+^f - q^2} - \sqrt{t_+^f - t_0}}{\sqrt{t_+^f - q^2} + \sqrt{t_+^f - t_0}}\,, \tag{5.8}$$

where the constant t_0 is set to the kinematic endpoint in q^2 ($t_0 = (m_{\Lambda_b} - m_X)^2$) such that $z = 0$ corresponds to the kinematic endpoint. Meanwhile, the constant t_f sets the point where the $z^f(q^2)$ becomes complex. The kinematically allowed region $0 < q^2 < t_0$ maps onto

$$0 < z < \frac{\sqrt{t_+^f} - \sqrt{t_+^f - t_0}}{\sqrt{t_+^f} + \sqrt{t_+^f - t_0}}\,, \tag{5.9}$$

where z is real and positive. In the region, $t_0 < q^2 \leq t_+$, the expansion parameter remains real but becomes negative mapping on to $-1 \leq z < 0$. Finally, $q^2 > t_f$, maps onto a circle in the complex plane. The conformal mapping of $q^2 \to z(q^2)$ is illustrated in Fig 5.3. Physically, t_+^f is set at the lowest point in q^2 where branch cuts or remaining poles in the form factors are located. Tables 5.2 and 5.3 summarise the values of t_+^f and m_{pole}^f used for each of the helicity form factors of $\Lambda_b^0 \to p\mu^-\overline{\nu}_\mu$ and $\Lambda_b^0 \to \Lambda_c^+\mu^-\overline{\nu}_\mu$ decays, respectively.

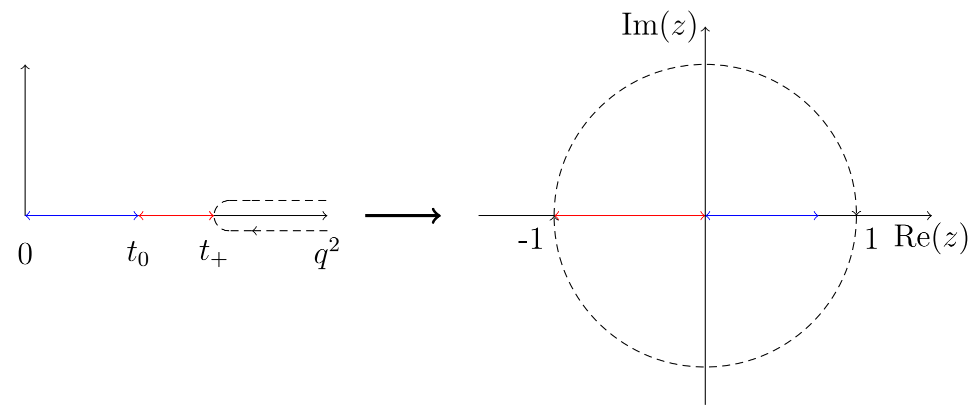

Figure 5.3: Conformal mapping of $q^2 \to z(q^2)$. The kinematically allowed region is $0 < q^2 < t_0$ is shown in blue.

f	J^P	$t_+^f(\Lambda_b \to p)$	$m_{\text{pole}}^f(\Lambda_b \to p)$	$\Delta^f(\Lambda_b \to p)$
f_+, $f_\perp$	1^-	$(m_B + m_\pi)^2$	$m_B + \Delta^f$	46 MeV/c^2
f_0	0^+	$(m_B + m_\pi)^2$	$m_B + \Delta^f$	377 MeV/c^2
g_+, $g_\perp$	1^+	$(m_B + m_\pi)^2$	$m_B + \Delta^f$	427 MeV/c^2
g_0	0^-	$(m_B + m_\pi)^2$	$m_B + \Delta^f$	0

Table 5.2: Summary of values of t_+^f and m_{pole}^f for $\Lambda_b \to p$ transitions taken from [42], where $m_B = 5.279\,\text{GeV}/c^2$ and $m_\pi = 134.8\,\text{MeV}/c^2$.

In order to determine the z-expansion parameters from a fit to lattice data the z-expansion is modified to account for the lattice spacing and pion mass as

$$f(q^2) = \frac{1}{1 - \frac{q^2}{(m_{\text{pole}}^f)^2}} \left[a_0^f (1 + c_0^f \frac{m_\pi^2 - m_{\pi,\text{phy}}^2}{\Lambda_\chi^2} + a_1^f z^f(q^2) \right] \times \left[1 + b^f \frac{|\vec{p}'|^2 a^2}{\pi^2} + d^f \frac{\Lambda_{\text{QCD}}^2 a^2}{\pi^2} \right] \;, \quad (5.10)$$

where c_0^f allows a dependence on the lattice pion mass m_π and b^f and d_f allow for proton momentum, $\vec{p}'$, dependent and independent discretisation errors which are proportional to a^2. In the continuum limit ($a \to 0$) and chiral limits ($m_\pi \to m_{\pi,\text{phys}}$) the lattice z-expansion simplifies to the expression in equation 5.7

A second order z-expansion with higher order dependences in lattice spacing, proton momentum and $m_\pi - m_{\pi,\text{phys}}$ is used to assess the systematic uncertainties associated with continuum, chiral and z-expansion extrapolations.

The higher order z-expansion simplifies in the continuum and chiral limits to

$$f_{\text{HO}}(q^2) = \frac{1}{1 - \frac{q^2}{(m_{pole}^f)^2}} \left[a_{0\text{HO}}^f + a_{1\text{HO}}^f z^f(q^2) + a_{2\text{HO}}^f z^{2f}(q^2) \right] \;. \quad (5.11)$$

The covariance information for the form factor parameters also accounts for systematic uncertainties associated with finite volume effects, the matching of lattice and continuum currents, scale setting, b-quark parameter tuning and missing isospin symmetry breaking.

Given that there are six form factors, there are 12 and 18 expansion coefficients for the nominal and higher order parametrisations, respectively. This reduces to 11 and 17 free parameters given a constraint that at the kinematic endpoint, $g_\perp|_{z=0} = g_+|_{z=0} \implies a_0^{g_\perp} = a_0^{g_+}$. All the information

f	J^P	$t_+^f(\Lambda_b \to \Lambda_c)$	$m_{\text{pole}}^f(\Lambda_b \to \Lambda_c)$	$\Delta^f(\Lambda_b \to \Lambda_c)$
f_+, $f_\perp$	1^-	$(m_{\text{pole}}^f)^2$	$m_{B_c} + \Delta^f$	56 MeV/c^2
f_0	0^+	$(m_{\text{pole}}^f)^2$	$m_{B_c} + \Delta^f$	449 MeV/c^2
g_+, $g_\perp$	1^+	$(m_{\text{pole}}^f)^2$	$m_{B_c} + \Delta^f$	492 MeV/c^2
g_0	0^-	$(m_{\text{pole}}^f)^2$	$m_{B_c} + \Delta^f$	0

Table 5.3: Summary of values of t_+^f and m_{pole}^f for $\Lambda_b \to \Lambda_c^+$ transitions taken from [42], where $m_{B_c} = 6.276\,\text{GeV}/c^2$.

required to model the $\Lambda_b^0 \to p\mu^-\overline{\nu}_\mu$ and $\Lambda_b^0 \to \Lambda_c^+\mu^-\overline{\nu}_\mu$ form factors and their uncertainties are encoded in the nominal and higher order (HO) z-expansion coefficients, $\vec{a}_{\text{nom/HO}}$, and their associated covariance matrices.

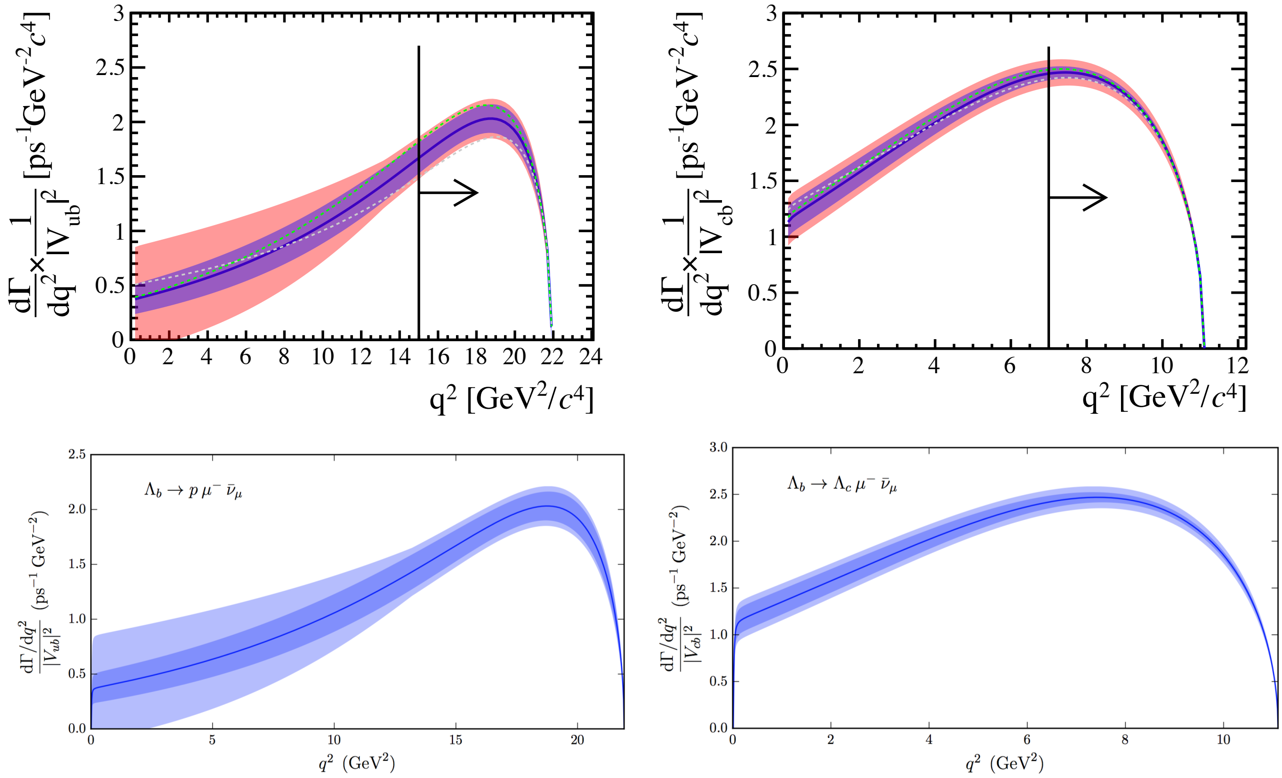

Figure 5.4: Uncertainty bands on the differential rates of $\Lambda_b^0 \to p\mu^-\overline{\nu}_\mu$ (left) and $\Lambda_b^0 \to \Lambda_c^+\mu^-\overline{\nu}_\mu$ (right) decays as determined using a Monte Carlo approach. The blue shaded band includes only the statistical error while the red band includes systematic effects. The dashed lines show the differential rate for two random variations of the form factor parameters generated according to equation 5.12. The corresponding plots from [42] are shown below.

A Monte Carlo approach is taken to model the theoretical uncertainty on the $\Lambda_b^0 \to \Lambda_c^+ \mu^- \overline{\nu}_\mu$ and $\Lambda_b^0 \to p\mu^- \overline{\nu}_\mu$ form factors and to subsequently understand how this could potentially impact the signal and normalisation selection efficiencies and mass shapes. Form factor parameters, $\vec{a}$, are generated according to the multivariate Gaussian,

$$G(\vec{a}, \vec{\mu}, V) = \frac{1}{(2\pi)^{\frac{n}{2}} \sqrt{|V|}} e^{-\frac{1}{2}(\vec{a}-\vec{\mu})^T V^{-1} (\vec{a}-\vec{\mu})} , \tag{5.12}$$

where $\vec{\mu}$ are the default values of the form factor parameters, n is the number of parameters and V is the associated covariance matrix as presented in Ref. [42]. Each set of generated form factor parameters represents a potential variation in the form factors.

A physics observable, O, may be computed from the nominal and HO form factor parametrisations according to

$$O = O_{\text{nom}} \pm \sigma_{O,\text{nom}} \pm \max\left(|\mathrm{O}_{\mathrm{HO}} - \mathrm{O}_{\mathrm{nom}}|, \sqrt{\sigma^2_{\mathrm{O,HO}} - \sigma^2_{\mathrm{O,nom}}} \right) , \tag{5.13}$$

where the uncertainty on the observable O computed using the nominal parametrisation, $\sigma_{O,\text{nom}}$, quantifies the statistical uncertainty. Meanwhile, the systematic uncertainty is quantified by the maximum of the absolute difference between values of the observable computed under the higher order (HO) and nominal parametrisations, $|O_{\text{HO}} - O_{\text{nom}}|$, or the difference in quadrature of the corresponding uncertainties, $\sqrt{\sigma^2_{O,\text{HO}} - \sigma^2_{O,\text{nom}}}$. The nominal and HO uncertainties in the observable, O, are determined using

$$\sigma^2_O = \sum_1^{N_{\text{var}}} \frac{(O_i - O_{\text{nom}})}{N_{\text{var}} - 1} , \tag{5.14}$$

where O_i is the observable computed under a generated variation of the form factor parameters and N_{var} is the number of variations.

Fig. 5.4 shows the differential rate for $\Lambda_b^0 \to p\mu^- \overline{\nu}_\mu$ and $\Lambda_b^0 \to \Lambda_c^+ \mu^- \overline{\nu}_\mu$ decays and the associated uncertainty bands formed using 10,0000 variations of the form factor parameters generated according to equation 5.12. The uncertainty bands are determined using equations 5.13 and 5.14. These agree well with the uncertainty bands shown by Meinel et al. in [42], which were determined analytically. The uncertainty on the form factors is lowest towards the kinematic endpoint in q^2. An additional check is made by computing the integrals and ratio defined in equations 2.72, 2.73 and 2.74. Fig 5.5 compares the distributions of the integrated differential rates and the ratio of the two for nominal and higher order parametrisations.

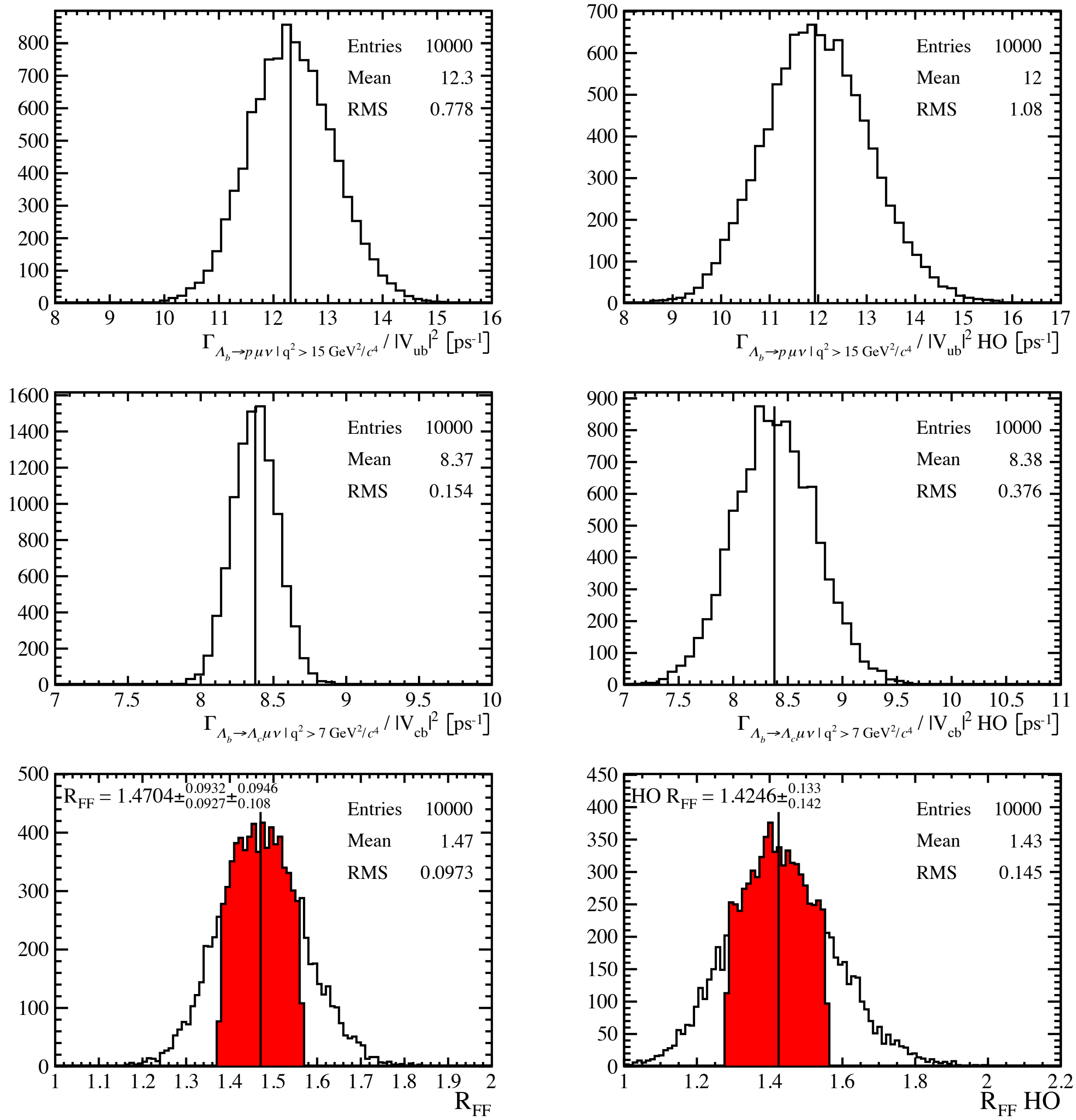

Figure 5.5: Distributions for $\Gamma_{\Lambda_b^0 \to p\mu^-\overline{\nu}_\mu | q^2 > 15\,\mathrm{GeV}^2/c^4}$, $\Gamma_{\Lambda_b^0 \to \Lambda_c^+\mu^-\overline{\nu}_\mu | q^2 > 7\,\mathrm{GeV}^2/c^4}$ and the ratio of the two, R_{FF}, under variations in the $\Lambda_b^0 \to p\mu^-\overline{\nu}_\mu$ and $\Lambda_b^0 \to \Lambda_c^+\mu^-\overline{\nu}_\mu$ form factors made using the nominal and higher order (HO) parametrisations.

5.2.4. LCSR form factors

Light Cone Sum Rules have been used to compute the $\Lambda_b^0 \to p\mu^-\overline{\nu}_\mu$ form factors in Reference [79]. This involves evaluating the vacuum-to-proton correlation function of a time ordered product ($T\{\}$) of heavy baryon and vector/axial vector currents, $\Lambda_b(0)$ and $J^{\mathrm{V/AV}}(x)$, given by

$$C_{\mathrm{V/AV}}(p', q) = i \int d^4x e^{iq\cdot x} \left\langle 0 \left| T\left\{\Lambda_b(0), J^{\mathrm{V/AV}}(x)\right\} \right| X(p') \right\rangle \ , \tag{5.15}$$

where q is the momentum transfer and the proton state, $\mid X(p')\rangle$, has 4-momentum, p'. An expansion of the currents is made about the light-cone ($x^2 = 0$) which corresponds to $q^2 = 0$. For this reason, LCSR predictions are most precise in the low q^2 region close to $q^2 = 0$.

The form factors were expressed in the convention

$$\begin{aligned}\left\langle \Lambda_b^0(p'+q, s) \left|\bar{q}\gamma^\mu u\right| X(p', s') \right\rangle = \bar{u}_{\Lambda_b}(p'+q, s) \Bigg(& f_1(q^2)\gamma^\mu + i\frac{f_2(q^2)}{m_{\Lambda_b}}\sigma^{\mu\nu}q_\nu \\ & + \frac{f_3(q^2)}{m_{\Lambda_b}}q^\mu \Bigg) u_X(p', s') \ ,\end{aligned} \tag{5.16}$$

and

$$\begin{aligned}\left\langle \Lambda_b^0(p'+q, s) \left|\bar{q}\gamma^\mu\gamma_5 u\right| X(p', s') \right\rangle = \bar{u}_{\Lambda_b}(p'+q, s) \Bigg(& g_1(q^2)\gamma^\mu + i\frac{g_2(q^2)}{m_{\Lambda_b}}\sigma^{\mu\nu}q_\nu \\ & + \frac{g_3(q^2)}{m_{\Lambda_b}}q^\mu \Bigg) \gamma_5 u_X(p', s') \ ,\end{aligned} \tag{5.17}$$

which is related to the EvtGen convention in appendix A.3.

Technique	$\mathcal{B}_{\Lambda_b^0 \to p\mu^-\overline{\nu}_\mu}$
LCSR	3.5×10^{-4}
Static LQCD	5.9×10^{-4}
LQCD	4.5×10^{-4}
Quark Model	1.2×10^{-4}

Table 5.4: Summary of branching fraction predictions for the decay $\Lambda_b^0 \to p\mu^-\overline{\nu}_\mu$ (assuming $|V_{ub}| = 3.5 \times 10^{-3}$) using different techniques for calculating the form factors.

5.3. Form factor comparisons

Fig 5.6 compares the differential rate of $\Lambda_b^0 \to p\mu^-\overline{\nu}_\mu$ and $\Lambda_b^0 \to \Lambda_c^+\mu^-\overline{\nu}_\mu$ decays for a number of different form factor predictions. Meanwhile, Table 5.4 summarises the corresponding branching fraction predictions. For $\Lambda_b^0 \to p\mu^-\overline{\nu}_\mu$ decays, while the LCSR, LQCD and static LQCD form factor predictions appear to be consistent, the quark model predicts a radically different q^2 behaviour and branching fraction. For $\Lambda_b^0 \to \Lambda_c^+\mu^-\overline{\nu}_\mu$ decays, the quark model predicts a similar q^2-dependence to that predicted by LQCD. This is because the non-relativistic treatment of the quark model is a better approximation for the heavy-to-heavy $b \to c$ transition than the heavy-to-light $b \to u$ transition.

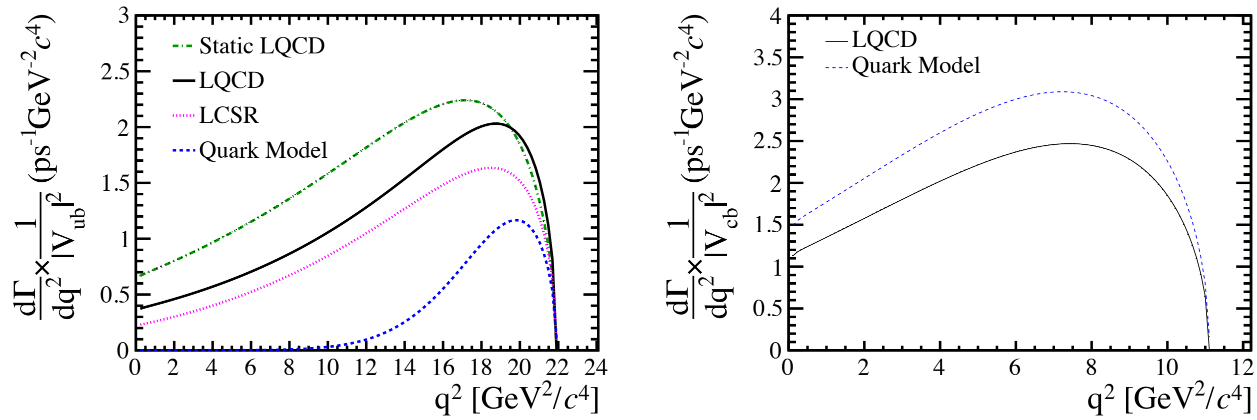

Figure 5.6: Comparison of predicted differential rates of $\Lambda_b^0 \to p\mu^-\overline{\nu}_\mu$ (left) and $\Lambda_b^0 \to \Lambda_c^+\mu^-\overline{\nu}_\mu$ (right) decays for a variety of form factor predictions.

Fig 5.7 and 5.8 compare the q^2 distributions for $\Lambda_b^0 \to p\mu^-\overline{\nu}_\mu$ and $\Lambda_b^0 \to \Lambda_c^+\mu^-\overline{\nu}_\mu$ decays simulated using implementations of the form factors in EvtGen with the simulated phase-space distribution. While the phase-space q^2 distribution falls off in q^2, the rapid predicted growth of the form factors with q^2 results in a radically different behaviour in which the distribution peaks at high q^2. In order to validate the implementation of the form factors within EvtGen, the simulated q^2 distributions are fitted using the analytical expression for the differential rate (see equation 2.55).

Fig 5.9 compares the $M_{p\mu}^2$-q^2 distributions for $\Lambda_b^0 \to p\mu^-\overline{\nu}_\mu$ decays simulated according to the LCSR and LQCD predictions to the phase-space distribution. While the phase-space distribution is uniform in the kinematically allowed region, in reality most $\Lambda_b^0 \to p\mu^-\overline{\nu}_\mu$ decays will occupy a small region of the available phase-space at high q^2 due to the form factors of the decay.

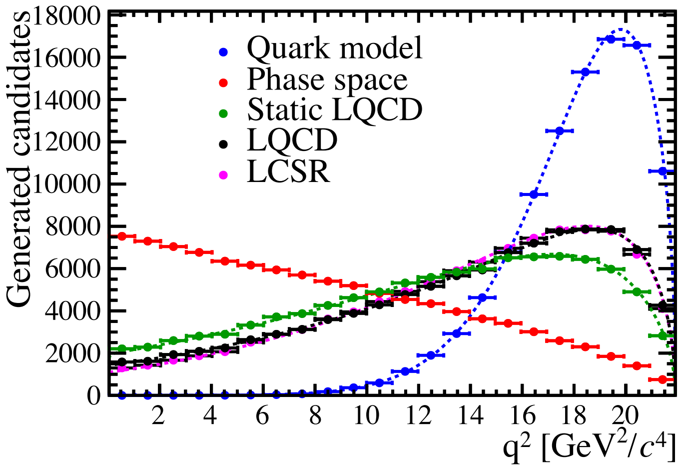

Figure 5.7: Comparison of the q^2 distributions for simulated $\Lambda_b^0 \to p\mu^-\overline{\nu}_\mu$ decays which are generated according to quark model, phase-space, static LQCD and relativistic LOCD predictions. The dashed lines in both cases show fits to the generated Monte Carlo data according to the expression for the differential rate of these decays given in equation 2.55.

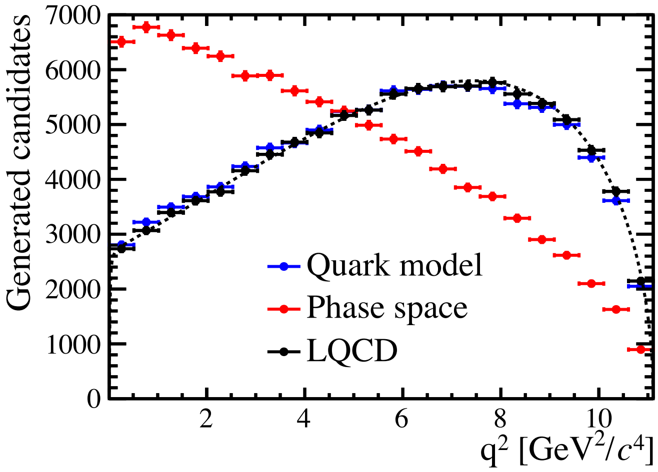

Figure 5.8: Comparison of the q^2 distributions for $\Lambda_b^0 \to \Lambda_c^+\mu^-\overline{\nu}_\mu$ decays which are generated according to phase-space, quark model and relativistic LQCD predictions. The dashed lines in both cases show fits to the generated Monte Carlo data according to the expression for the differential rate of these decays given in equation 2.55.

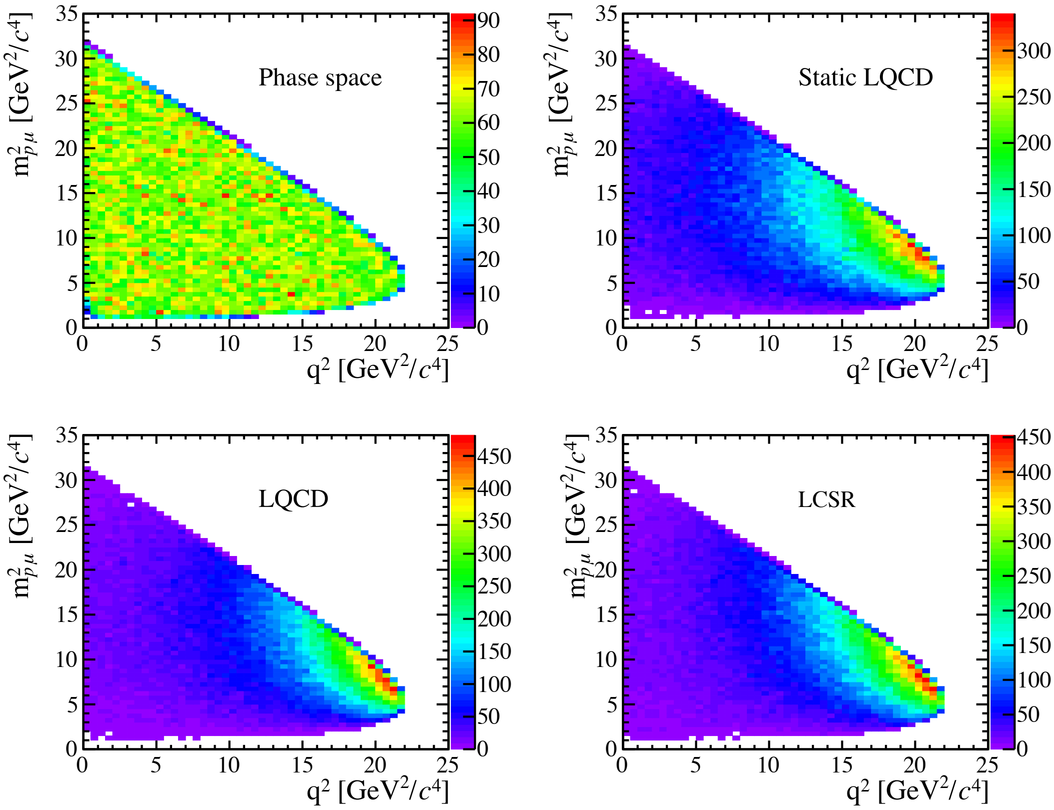

Figure 5.9: Two-dimensional $m^2_{p\mu}$-q^2 distributions for $\Lambda_b^0 \to p\mu^-\overline{\nu}_\mu$ decays generated according to phase-space, LQCD, static LQCD and LCSR predictions.

5.4. EvtGen re-weighting

For the analysis, it is necessary to re-weight simulation samples effectively to the latest LQCD form factor predictions and variations of these within their associated uncertainties. Rather than a naive one-dimensional re-weighting in q^2, or a more complicated n-dimensional re-weighting in n kinematic variables, a re-weighting is made which exploits the accept and reject method employed by EvtGen. Given a sample of $B \to X_u\mu^-\overline{\nu}_\mu$ decays generated with EvtGen decay model A it is possible to re-weight to a second decay model B by applying a weight to the i^{th} event, w^i, given by

$$w^i = \frac{p^i(k^i_X, k^i_\mu, k^i_\nu)_B}{p^i(k^i_X, k^i_\mu, k^i_\nu)_A} \,, \tag{5.18}$$

where $p^i(k^i_X, k^i_\mu, k^i_\nu)_A$ and $p^i(k^i_X, k^i_\mu, k^i_\nu)_B$ are the accept probabilites for models A and B, which are a function of the 4-momentums of the daughter particles, k^i_X, k^i_μ and k^i_ν. Fig 5.10 shows the

q^2 distribution for simulated $\Lambda_b^0 \to p\mu^-\overline{\nu}_\mu$ and $\Lambda_b^0 \to \Lambda_c^+\mu^-\overline{\nu}_\mu$ decays passing the final analysis selection, excluding that on q^2, before and after re-weighting. It can be seen that the re-weighting increases the fraction of simulated $\Lambda_b^0 \to p\mu^-\overline{\nu}_\mu$ decays at high q^2.

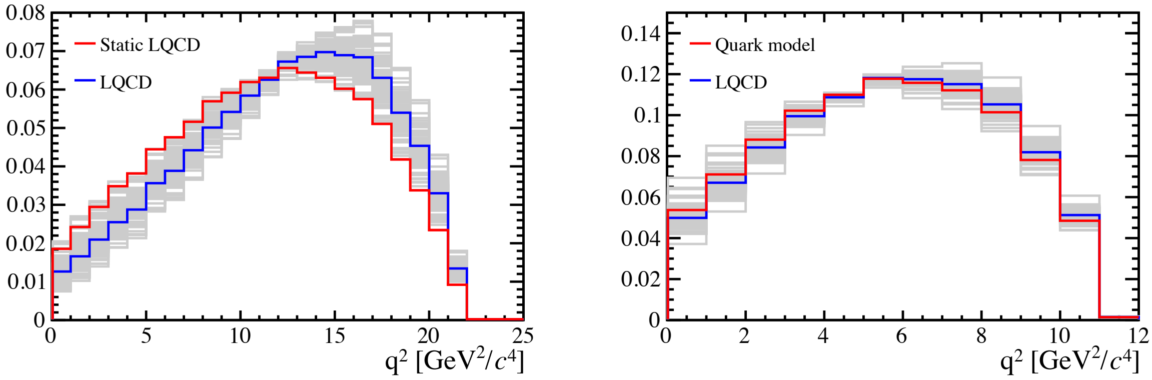

Figure 5.10: The q^2 distributions for simulated $\Lambda_b^0 \to p\mu^-\overline{\nu}_\mu$ (left) and $\Lambda_b^0 \to \Lambda_c^+\mu^-\overline{\nu}_\mu$ (right) decays before and after re-weighting from the static LQCD and quark model form factors to the relativistic LQCD form factors. The grey curves show re-weightings to random variations of the form factors which are used to assess the various experimental systematic uncertainties associated with the theoretical uncertainty on the form factors.

Chapter 6.

Finding $b \to ul\nu_l$ at a hadron collider

It has often been thought that a measurement of $|V_{ub}|$ is impossible to perform within a hadronic environment. This is due to the challenge of isolating the semileptonic $b \to u$ signal from the large amount of background with no knowledge of the energies and momenta of interacting partons. This chapter describes the search strategy for signal $\Lambda_b^0 \to p\mu^-\overline{\nu}_\mu$ decays at the Large Hadron Collider. The chapter includes a description of the backgrounds facing the search, simulation samples produced for modelling signal, normalisation and background decays and the selections made for signal and normalisation $\Lambda_b^0 \to p\mu^-\overline{\nu}_\mu$ and $\Lambda_b^0 \to \Lambda_c^+\mu^-\overline{\nu}_\mu$ decays.

6.1. Backgrounds

Even with the distinctive nature of final state protons, a search for the decay $\Lambda_b^0 \to p\mu^-\overline{\nu}_\mu$ faces large backgrounds at LHCb. Given the missing neutrino a lot of this background is irreducible and must be modelled using simulation and/or estimated using data.

The largest background that a search for $\Lambda_b^0 \to p\mu^-\overline{\nu}_\mu$ decays faces is from the corresponding $b \to c$ transition, $\Lambda_b^0 \to \Lambda_c^+\mu^-\overline{\nu}_\mu$, when the Λ_c^+ decays to a proton and additional particles. This background can be further divided in to two categories in which the additional particles are all purely neutral or there is at least one charged particle among them. It is possible to exploit the tracks associated with additional charged particles to reduce the majority of background of the latter category. The low efficiency for reconstructing neutral particles makes it difficult to effectively reduce background involving additional particles which are purely neutral. Background involving Λ_c^+ baryons may also arise from $\Lambda_b^0 \to \Lambda_c^{*+}\mu^-\overline{\nu}_\mu$ decays in which Λ_c^{*+} represents higher-mass resonances of the Λ_c^+. This is a background to the searches for both signal and normalisation decays. The most prominent resonances that contribute to this background are the $\Lambda_c^+(2595)$ and $\Lambda_c^+(2625)$ resonances. The final $b \to c$ background considered is that arising from $\Lambda_b^0 \to D^0 p \mu^- \overline{\nu}_\mu$ decays.

While the largest component of background is from semileptonic $b \to c$ transitions the least understood background is from the excited $b \to u$ transitions such as $\Lambda_b^0 \to N^{*+} \mu^- \overline{\nu}_\mu$ and $\Lambda_b^0 \to \Delta^+ \mu^- \overline{\nu}_\mu$ decays, where a proton is produced from the cascade of decays from the N^{*+} or Δ^+ baryons. The latter decay, $\Lambda_b^0 \to \Delta^+ \mu^- \overline{\nu}_\mu$, is not considered as a background as this decay is forbidden by isospin conservation[1].

Given the much larger occurrence of pions and kaons from the decays of b-hadrons there is a substantial background in which a pion or kaon is misidentified as a proton. The final background considered is combinatorial background in which the selected proton and muon originate from the decays of different b-hadrons.

Each of these backgrounds will be discussed in more detail in sections 6.2, 7.2 and 7.3.

6.2. Simulated samples

A large number of simulated samples were produced for the analysis in order to model signal, normalisation and background decays. Table 6.1 summarises these samples. Tight cuts on the proton ($p > 14600\,\mathrm{MeV}/c$ and $p_\mathrm{T} > 950\,\mathrm{MeV}/c$), muon ($p > 4900\,\mathrm{MeV}/c$ and $p_\mathrm{T} > 1450\,\mathrm{MeV}/c$) and their vector sum ($p_\mathrm{T} > 1400\,\mathrm{MeV}/c$) were applied on all samples used for determining mass shapes. Furthermore, for these samples, only events which passed the preselection were stored.

The normalisation decay, $\Lambda_b^0 \to (\Lambda_c^+ \to pK^-\pi^+)\mu^- \overline{\nu}_\mu$, is simulated using form factors predicted by the quark model predictions in Ref. [73]. The $\Lambda_c^+ \to pK^-\pi^+$ transition is modelled as consisting of a non-resonant $\Lambda_c^+ \to pK^-\pi^+$ component and components for the resonant modes, $\Lambda_c^+ \to p\overline{K}^{*0}$, $\Lambda_c^+ \to \Delta^{++}K^-$ and $\Lambda_c^+ \to \Lambda(1520)\pi^+$, with the relative fractions between the components set to those quoted by the PDG [11]. Meanwhile, cascade background from $\Lambda_b^0 \to (\Lambda_c^{*+} \to (\Lambda_c^+ \to pK^-\pi^+)\pi\pi)\mu^- \overline{\nu}_\mu$ decays is modelled using two separate samples handling the most prominent $\Lambda_b^0 \to \Lambda_c^{*+} \mu^- \overline{\nu}_\mu$ transitions, $\Lambda_b^0 \to \Lambda_c^+(2625)\mu^- \overline{\nu}_\mu$ and $\Lambda_b^0 \to \Lambda_c^+(2595)\mu^- \overline{\nu}_\mu$. These samples contain

[1]The isospin of the Λ_b^0 baryon ($I = 0$) and the b quark ($I = 0$) constrain the total isospin of the u and d spectator quarks to be $I = 0$. Given that the isospin of the u quark from the $b \to u$ transition is $I = 1/2$ it is not possible to produce a particle with isospin $I = 3/2$ such as the Δ^+.

a cocktail of $\Lambda_c^{*+} \to \Lambda_c^+ \pi\pi$ decay modes for which the relative fractions are determined based on isospin arguments.

Decay	Size	Type	Form factor model
Samples for the signal fit mass shapes			
$\Lambda_b^0 \to p\mu^-\overline{\nu}$	0.6M	Signal	Static LQCD
$\Lambda_b^0 \to \Lambda_c^+\mu^-\overline{\nu}$, $\Lambda_c^+ \to pX$ neutral	3M	Background	Quark model
$\Lambda_b^0 \to \Lambda_c^+\mu^-\overline{\nu}$, $\Lambda_c^+ \to pX$ charged	3M	Background	Quark model
$\Lambda_b^0 \to \Lambda_c(2625)\mu^-\overline{\nu}$, $\Lambda_c^+ \to pX$	0.6M	Background	Quark model
$\Lambda_b^0 \to \Lambda_c(2595)\mu^-\overline{\nu}$, $\Lambda_c^+ \to pX$	0.3M	Background	Quark model
$\Lambda_b^0 \to D^0 p\mu^-\overline{\nu}$	0.6M	Background	Phase Space
$\Lambda_b^0 \to N^{*+}\mu^-\overline{\nu}$, $N^{*+} \to pX$	0.5M	Background	Quark Model
Samples for the normalisation fit mass shapes			
$\Lambda_b^0 \to \Lambda_c^+\mu^-\overline{\nu}$, $\Lambda_c^+ \to pK^-\pi^+$	0.6M	Normalisation	Quark model
$\Lambda_b^0 \to \Lambda_c(2625)\mu^-\overline{\nu}$, $\Lambda_c^+ \to pK^-\pi^+$	0.1M	Background	Quark model
$\Lambda_b^0 \to \Lambda_c(2595)\mu^-\overline{\nu}$, $\Lambda_c^+ \to pK^-\pi^+$	0.1M	Background	Quark model
Samples used for the efficiency determination			
$\Lambda_b^0 \to p\mu^-\overline{\nu}$	1M	Signal	Static Quark
$\Lambda_b^0 \to \Lambda_c^+\mu^-\overline{\nu}$, $\Lambda_c^+ \to pK^-\pi^+$	10M	Normalisation	Quark model

Table 6.1: A summary of simulated samples produced for the analysis.

The signal decay, $\Lambda_b^0 \to p\mu^-\overline{\nu}_\mu$, is simulated with the static LQCD predictions in Ref. [72]. The largest simulation samples are those for $\Lambda_b^0 \to (\Lambda_c^+ \to pX)\mu^-\overline{\nu}_\mu$ decays, which are simulated using two separate samples with one containing $\Lambda_c^+ \to pX$ modes where X is purely neutral and the other containing modes with at least one charged particle in addition to the proton. Cascade background from $\Lambda_b^0 \to (\Lambda_c^{*+} \to (\Lambda_c^+ \to pX)\pi\pi)\mu^-\overline{\nu}_\mu$ decays is simulated in a similar manner to that for $\Lambda_b^0 \to (\Lambda_c^{*+} \to (\Lambda_c^+ \to pK^-\pi^+)\pi\pi)\mu^-\overline{\nu}_\mu$ decays using two separate samples for the $\Lambda_c^+(2625)$ and $\Lambda_c^+(2593)$ states. The background from $\Lambda_b^0 \to N^{*+}\mu^-\overline{\nu}_\mu$ decays is modelled using a cocktail of decays consisting of the four lowest lying N^{*+} states in mass for their J^P values, $N^{*+}(J^P) = \left\{N^+(1440)\left(\frac{1}{2}^+\right), N^+(1520)\left(\frac{3}{2}^-\right), N^+(1535)\left(\frac{1}{2}^-\right), N^+(1720)\left(\frac{3}{2}^+\right)\right\}$. The form factors and relative rates for these modes are simulated according to the quark model predictions. Meanwhile, the branching fractions for these N^{*+} states to decay to the dominant final states $(\Delta \to p\pi)\pi$ and $p\pi$ are determined using isospin arguments on the PDG quoted values for the branching fractions of $N^{*+} \to (\Delta \to N\pi)\pi$ and $N^{*+} \to N\pi$ decays. The details of this calculation is provided in appendix ?? Finally, the decay $\Lambda_b^0 \to D^0 p \mu^- \overline{\nu}_\mu$ is simulated according to phase-space with the D^0 decaying to all possible modes.

6.3. Selection for $\Lambda_b^0 \to p \mu^- \overline{\nu}_\mu$ and $\Lambda_b^0 \to \Lambda_c^+ \mu^- \overline{\nu}_\mu$ decays

6.3.1. Preselection for $\Lambda_b^0 \to p \mu^- \overline{\nu}_\mu$ decays

Prior to the analysis of LHCb data a number of preselections are applied to the data known as stripping selections. A stripping selection was developed specifically for the analysis of $\Lambda_b^0 \to p \mu^- \overline{\nu}_\mu$ decays presented here. The selection criteria for candidate proton and muons and their combination are shown in Table 6.2.

Tracks are identified as muons by whether or not they penetrate through to the muon chambers according to the `isMuon` binary decision described in section 3.2.3. Meanwhile, for the proton tight cuts are made on the PID discriminators $\Delta\log\mathcal{L}(\mathrm{p}-\pi)$ and $\Delta\log\mathcal{L}(\mathrm{p}-\mathrm{K})$ (see section 3.2.3) to respectively discriminate against pions and kaons. Given the poor discrimination between protons and kaons/pions at low momentum (see Fig 3.9), candidate protons are required to have a momentum greater than 15000 MeV/c.

The vertex of the Λ_b^0 baryon is obtained via a vertex fit to the proton and muon tracks. This vertex is required to be displaced from the primary vertex by selecting events with a large flight distance χ^2. This accounts for the significant lifetime of Λ_b^0 baryons which results in a displaced decay vertex. In addition the proton and muon candidates are required to have a significant impact parameter with respect to the primary vertex. This suppresses background from prompt charm production, $pp \to c\bar{c}$, to a negligible level.

Only candidate protons and muons which are compatible with originating from a shared vertex are selected. This is achieved by selecting events in which the χ^2 for the corresponding proton-muon vertex fit is small. This selection reduces background from $B \to (H_c \to hX)\mu^- \overline{\nu}_\mu$ decays, in which h is a proton or a hadron misidentified as a proton. This is due to the considerable lifetime of H_c hadrons which means that the hadron and muon form a poor quality vertex. The lifetime of Λ_c^+ baryons is around a factor of two times smaller than that of D^0 mesons and a factor of five times smaller than that of D^+ mesons. Therefore, while this selection also reduces the efficiency

Candidate	Selection
Proton	$p_{\mathrm{T}} > 1000\,\mathrm{MeV}/c$
Proton	$p > 15000\ \mathrm{MeV}/c$
Proton	IP $\chi^2 > 16$
Proton	track $\chi^2 > 6$
Proton	$\Delta\log\mathcal{L}(\mathrm{p}-\pi) > 10$
Proton	$\Delta\log\mathcal{L}(\mathrm{p}-\mathrm{K}) > 10$
Proton	ghost prob. < 0.35
Muon	$p_{\mathrm{T}} > 1500\,\mathrm{MeV}/c$
Muon	$p > 3000\ \mathrm{MeV}/c$
Muon	IP $\chi^2 > 16$
Muon	track $\chi^2 > 6$
Muon	`isMuon` $=$ true
Muon	ghost prob. < 0.35
Combination	$p_{\mathrm{T}} > 1500\ \mathrm{MeV}/c$
Combination	mass $> 1000\ \mathrm{MeV}/c$
Combination	flight distance $\chi^2 > 150$
Combination	$\cos\theta > 0.9994$
Combination	vertex $\chi^2 < 4$

Table 6.2: Preselection for $\Lambda_b^0 \to p\mu^-\overline{\nu}_\mu$ candidates. The variable $\cos\theta$ is the cosine of the angle between the momentum direction of the combined $p\mu$ pair and the flight direction of the Λ_b^0 baryon. See sections 3.2.1, 3.2.2 and 3.2.3 for the definitions of all other selection variables used.

for selecting the normalisation decay, $\Lambda_b^0 \to (\Lambda_c^+ \to pK^-\pi^+)\mu^-\overline{\nu}_\mu$, the efficiency is still sufficient to select a considerable number of $\Lambda_b^0 \to (\Lambda_c^+ \to pK^-\pi^+)\mu^-\overline{\nu}_\mu$ normalisation candidates.

Events are required to pass the trigger decisions described in sections 3.2.4. It is also required that these triggers were triggered by the candidate protons, muons and their combinations as relevant.

Only 50% of the events in the region below 4000 MeV/c^2 in corrected mass were selected at random on a event by event basis and stored for further analysis. This was due to the large rates of backgrounds and the small fraction of $\Lambda_b^0 \to p\mu^-\overline{\nu}_\mu$ signal expected in this region. Data in the region below 4000 MeV/c^2 in corrected mass is scaled up by factor of two in the final signal fit.

6.3.2. Preselection for $\Lambda_b^0 \to \Lambda_c^+ \mu^- \overline{\nu}_\mu$ decays

Candidates for the normalisation decay, $\Lambda_b^0 \to (\Lambda_c^+ \to pK^-\pi^+)\mu^-\overline{\nu}_\mu$, are built by combining the proton passing the initial selection for $\Lambda_b^0 \to p\mu^-\overline{\nu}_\mu$ decays with pion and kaon candidates to form a Λ_c^+ candidate. The Λ_c^+ candidate is then subsequently combined with the muon from the $\Lambda_b^0 \to p\mu^-\overline{\nu}_\mu$ preselection to form a Λ_b^0 candidate. In a similar manner the background decay, $\Lambda_b^0 \to (\Lambda_c^+ \to pK_\mathrm{S}^0)\mu^-\overline{\nu}_\mu$, is selected by combining the proton and muon candidates with an additional K_S^0 candidate, which is reconstructed using the decay $K_\mathrm{S}^0 \to \pi^+\pi^-$. Table 6.3 shows the selection criteria for pion, kaon, K_S^0, Λ_c^+ and $\Lambda_c^+\mu$ candidates.

Candidate	Selection
Kaon	$p_\mathrm{T} > 300\,\mathrm{MeV}/c$
Kaon	$p > 2000\ \mathrm{MeV}/c$
Kaon	IP $\chi^2 > 9$
Kaon	ghost prob. < 0.35
Kaon	$\Delta\log\mathcal{L}(\mathrm{K}-\pi) > 0$
Pion	$p_\mathrm{T} > 300\,\mathrm{MeV}/c$
Pion	$p > 2000\ \mathrm{MeV}/c$
Pion	IP $\chi^2 > 9$
Pion	$\Delta\log\mathcal{L}(\pi-\mathrm{K}) > 0$
Pion	ghost prob. < 0.35
K_S^0 pions	$p > 2000\ \mathrm{MeV}/c$
K_S^0 pions	IP $\chi^2 > 9$
K_S^0	$462.6 < m_{\pi\pi} < 532.6\ \mathrm{MeV}/c^2$
K_S^0	$\cos\theta_{\Lambda_b^0 K_s^0} > 0.99$
Λ_c^+	vertex $\chi^2 < 6$
Λ_c^+	$\cos\theta_{\Lambda_b^0 \Lambda_c^+} > 0.99$
$\Lambda_c^+\mu$	vertex $\chi^2 < 6$
$\Lambda_c^+\mu$	$\cos\theta_{\Lambda_b^0(\Lambda_c^+\mu)} > 0.99$

Table 6.3: Preselection for $\Lambda_b^0 \to \Lambda_c^+\mu^-\overline{\nu}_\mu$ candidates. The variable $\cos\theta_{\Lambda_b^0 X}$ is the cosine of the angle between the Λ_b^0 flight direction and the direction of the reconstructed momentum for X. See sections 3.2.1, 3.2.2 and 3.2.3 for the definitions of all other selection variables used.

6.3.3. q^2 selection

In order to measure the branching fractions of $\Lambda_b^0 \to p\mu^-\overline{\nu}_\mu$ and $\Lambda_b^0 \to \Lambda_c^+\mu^-\overline{\nu}_\mu$ decays in the desired regions of $q^2 = m_{\mu\nu}^2$, a reconstruction of the neutrino 4-momentum is required.

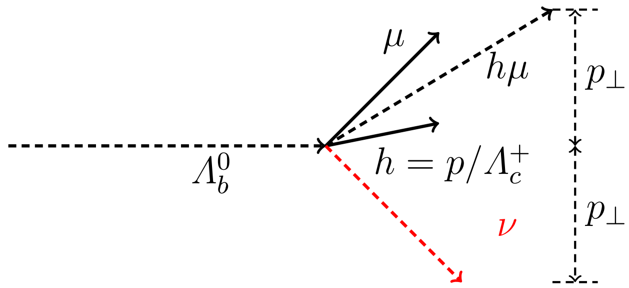

Figure 6.1: Illustration of momentum conservation with respect to the Λ_b^0 flight direction.

This is made possible through the constraints from the flight direction and the mass of the Λ_b^0 baryon. Momentum conservation with respect to the flight direction allows for the component of the neutrino momentum transverse to this direction to be determined, as illustrated in Fig. 6.1. The component of the neutrino momentum parallel to the flight direction, $p(\nu)_\parallel$, which is the only remaining unknown, can then be solved for by using the Λ_b^0 mass constraint,

$$(p_\nu + p_{h\mu})^2 = m_{\Lambda_b^0}^2 \ , \tag{6.1}$$

where

$$p_\nu = \left(\sqrt{p_\parallel^2(\nu) + p_\perp^2}, 0, -p_\perp, p_\parallel(\nu)\right) \tag{6.2}$$

$$p_{h\mu} = \left(\sqrt{p_\parallel^2(h\mu) + p_\perp^2 + m_{h\mu}^2}, 0, p_\perp, p_\parallel(h\mu)\right) \ . \tag{6.3}$$

Here, $m_{h\mu}$ and $p_\parallel(h\mu)$, are respectively the visible mass and the momentum component parallel to the Λ_b^0 flight direction for the $h\mu$ pair. Solving equation 6.1 leads to quadratic solutions for the $p(\nu)_\parallel$,

$$p(\nu)_\parallel = \frac{-b - \sqrt{b^2 - 4ac}}{2a} \ , \tag{6.4}$$

in which

$$
\begin{aligned}
a &= 4(p_\perp^2 + m_{p\mu}^2) && (6.5)\\
b &= 4p_{||}(h\mu)\left(2p_\perp^2 - m_{\text{miss}}^2\right) && (6.6)\\
c &= 4p_\perp^2\left(p_{||}^2(h\mu) + m_{\Lambda_b^0}^2\right) - |m_{\text{miss}}^2|^2 && (6.7)\\
m_{\text{miss}}^2 &= m_{\Lambda_b^0}^2 - m_{h\mu}^2\ . && (6.8)
\end{aligned}
$$

After preselection around 20% of $\Lambda_b^0 \to p\mu^-\overline{\nu}_\mu$ candidates in simulation are found to have unphysical solutions for $p_{||}(\nu)$ ($b^2 < 4ac$) due to detector resolution. Candidates with unphysical solutions are removed from the analysis. It is possible to show that the condition for unphysical solutions, $b^2 < 4ac$, is satisfied when

$$
16\left[p_{||}^2(h\mu) + 4(p_\perp^2 + m_{h\mu}^2)\right]\left[|m_{\text{miss}}^2|^2 - 4p_\perp^2 m_{\Lambda_b^0}^2\right] < 0\ , \tag{6.9}
$$

which implies that

$$
p_\perp > \frac{m_{\text{miss}}^2}{2m_{\Lambda_b^0}}\ . \tag{6.10}
$$

This is an important result as it corresponds to when the corrected mass is greater than the mass of the Λ_b^0 baryon:

$$
\sqrt{m_{h\mu}^2 + p_\perp^2} + p_\perp > m_{\Lambda_b^0}\ . \tag{6.11}
$$

Therefore removing unphysical solutions results in a truncation in corrected mass at $m_{\Lambda_b^0}$.

Having reconstructed the neutrino 4-momentum up to a 2-fold ambiguity, it is now possible to reconstruct q^2 ($m_{\mu\nu}$). Fig 6.2 shows the fractional resolution for the q^2 reconstruction for simulated $\Lambda_b^0 \to p\mu^-\overline{\nu}_\mu$ and $\Lambda_b^0 \to \Lambda_c^+\mu^-\overline{\nu}_\mu$ decays when selecting either the correct/false solution or a solution at random. While the distribution for the correct solution is Gaussian the distribution for false solution has much wider tails with the reconstructed value of q^2 often being much lower than the true value. Fig. 6.3 shows the Root Mean Square (RMS) for the $q^2_{\text{reco}} - q^2_{\text{true}}$ distribution as a function of q^2. The resolutions for the correct q^2 solutions are $\sim$1.0 GeV$^2/c^4$ and $\sim$0.6 GeV$^2/c^4$ for $\Lambda_b^0 \to p\mu^-\overline{\nu}_\mu$ and $\Lambda_b^0 \to \Lambda_c^+\mu^-\overline{\nu}_\mu$ decays, respectively. Meanwhile the resolution for the random solution rises with q^2 from around 2.2-4.1 GeV$^2/c^4$ and 1.4-2.6 GeV$^2/c^4$ for $\Lambda_b^0 \to p\mu^-\overline{\nu}_\mu$ and $\Lambda_b^0 \to \Lambda_c^+\mu^-\overline{\nu}_\mu$ decays, respectively.

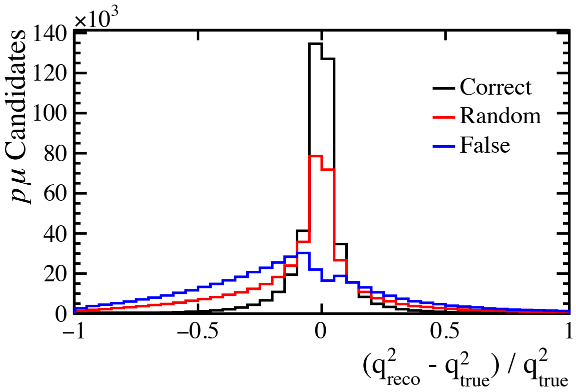

Figure 6.2: Fractional q^2 resolution, $(q^2_{\text{reco}} - q^2_{\text{true}})/q^2_{\text{true}}$, for simulated $\Lambda_b^0 \to p\mu^-\overline{\nu}_\mu$ decays (left) and $\Lambda_b^0 \to \Lambda_c^+\mu^-\overline{\nu}_\mu$ decays (right) when choosing the correct solution, the false solution or a reconstructed solution at random.

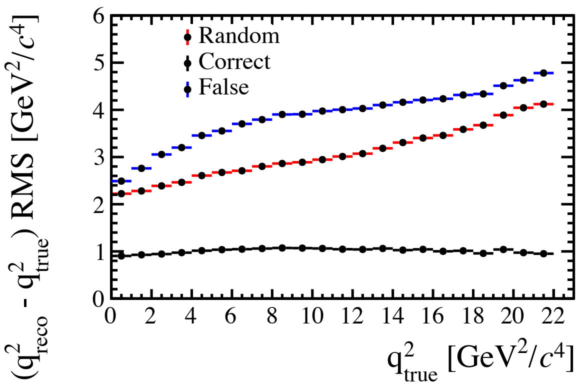

Figure 6.3: Root Mean Square (RMS) of the $q^2_{\text{reco}} - q^2_{\text{true}}$ value distributions as a function of q^2 for true simulated $\Lambda_b^0 \to p\mu^-\overline{\nu}_\mu$ decays (left) and $\Lambda_b^0 \to \Lambda_c^+\mu^-\overline{\nu}_\mu$ decays (right) when choosing the correct, false or a random reconstructed solution.

In order to select $\Lambda_b^0 \to p\mu^-\overline{\nu}_\mu$ and $\Lambda_b^0 \to \Lambda_c^+\mu^-\overline{\nu}_\mu$ decays with $q^2 > 15$ GeV$^2/c^4$ and $q^2 > 7$ GeV$^2/c^4$, respectively, it is required that both q^2 solutions satisfy these criteria. This is in order to minimise inwards migration, in which candidates with a true q^2 below the cut value are accepted. Conversely this choice of selection criteria will maximise outwards migration in which candidates with a true q^2 value within the required range are rejected. However, given that the theory uncertainty on the $\Lambda_b^0 \to p\mu^-\overline{\nu}_\mu$ and $\Lambda_b^0 \to \Lambda_c^+\mu^-\overline{\nu}_\mu$ form factors is largest towards low q^2 it is more important to minimise inwards migration. Table 6.4 and Table 6.5 show the migration in and out of the required regions in q^2 for $\Lambda_b^0 \to p\mu^-\overline{\nu}_\mu$ and $\Lambda_b^0 \to \Lambda_c^+\mu^-\overline{\nu}_\mu$ decays. These numbers are computed using simulation re-weighted to the form factor predictions in Reference [42]. Although requiring both solutions to be within these regions results in a loss of 58.5% (51.1%) of $\Lambda_b^0 \to p\mu^-\overline{\nu}_\mu$ ($\Lambda_b^0 \to \Lambda_c^+\mu^-\overline{\nu}_\mu$) candidates the migration in is only 1.9% (4.7%) which is much lower than when placing the requirement on one solution at random, 14.0% (17.5%). This is also illustrated in Fig 6.4 which shows the q^2 selection efficiency after all other selection criteria have been applied for both choices. The large loss of signal and normalisation candidates is acceptable given that the analysis is not statistically limited.

Table 6.4: Migration in and out of the high q^2 region due to detector resolution as determined with simulated $\Lambda_b^0 \to p\mu^-\overline{\nu}_\mu$ decays, which have been re-weighted to the relativistic LQCD predictions of [42]. The migration in is defined as the percentage of candidates selected which do not actually have a q^2 value above $15\,\mathrm{GeV}^2/c^4$. The migration out is the percentage of candidates which do have a q^2 value above $15\,\mathrm{GeV}^2/c^4$ but fail the selection criteria.

Selection	Migration in (%)	Migration out (%)
Correct solution $> 15\,\mathrm{GeV}^2/c^4$	3.9	5.2
Random solution $> 15\,\mathrm{GeV}^2/c^4$	14.0	31.3
Both solutions $> 15\,\mathrm{GeV}^2/c^4$	1.9	58.5

Table 6.5: Migration in and out of the high q^2 region due to detector resolution as determined with simulated $\Lambda_b^0 \to \Lambda_c^+\mu^-\overline{\nu}_\mu$ decays, which have been re-weighted to the relativistic LQCD predictions of [42]. The migration in is defined as the percentage of candidates selected which do not actually have a q^2 value above $7\,\mathrm{GeV}^2/c^4$. The migration out is the percentage of candidates which do have a q^2 value above $7\,\mathrm{GeV}^2/c^4$ but fail the selection criteria.

Selection	Migration in (%)	Migration out (%)
Correct solution $> 7\,\mathrm{GeV}^2/c^4$	6.2	7.0
Random solution $> 7\,\mathrm{GeV}^2/c^4$	17.5	28.3
Both solutions $> 7\,\mathrm{GeV}^2/c^4$	4.7%	51.8%

6.3.4. Isolation BDT

A large amount of background comes from B decays in which the proton and muon candidates are produced in conjunction with additional charged particles. By reconstructing and identifying the tracks associated with these charged particles it is possible to remove the majority of this

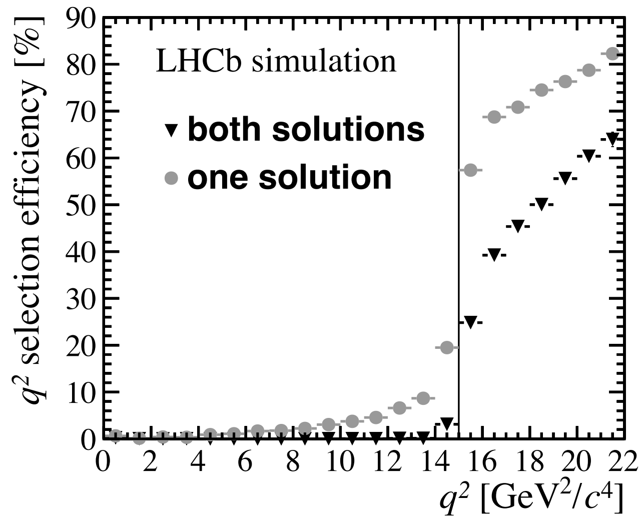

Figure 6.4: The q^2 selection efficiency as a function of q^2 for simulated $\Lambda_b^0 \to p\mu^-\overline{\nu}_\mu$ (left) and $\Lambda_b^0 \to \Lambda_c^+\mu^-\overline{\nu}_\mu$ (right) decays. For the case where a q^2 solution chosen at random is greater than 15 GeV^2/c^4 (left) or 7 GeV^2/c^4 (right) there is still a substantial efficiency that candidates with a true q^2 below 15 GeV^2/c^4 (left) or 7 GeV^2/c^4 (right) are selected. This is minimised by requiring that both solutions satisfy the q^2 selection criteria.

background ensuring that the proton and muon vertex is well isolated from any tracks in the event. A Boosted Decision Tree (BDT) is trained, using the TMVA package [80], to discriminate these tracks from other types of tracks in the event as illustrated in Fig 6.5. The BDT combines together the discriminating power of a number of variables associated with the tracks. The variables in order of discriminating power from most to least are the IP χ^2 with respect to the primary vertex, the IP χ^2 for the track with respect to the $p\mu$ vertex, the p_{T} of the track, the track χ^2, the track ghost probability and the cosine of the opening angle between the track momentum and the momentum of the combined $p\mu$ pair.

The BDT is trained using simulated tracks. A sample of 150,000 and 99,521 reconstructed tracks from simulated $\Lambda_b^0 \to (\Lambda_c^+ \to pX)\mu^-\overline{\nu}_\mu$ decays, excluding the tracks associated with the proton and muon, are used respectively as the background training and testing samples. Meanwhile, the signal training and testing samples consist respectively of 200,000 and 2,779,328 reconstructed tracks from a sample of B events in which all tracks in the event are selected apart from those from the simulated B decay. For both samples tracks are required to have an IP χ^2 with respect to the $p\mu$ vertex less than 50.

The BDT is formed by successively training 800 decision trees and combining their individual classification responses into one output. Each decision tree is trained by sequentially splitting the

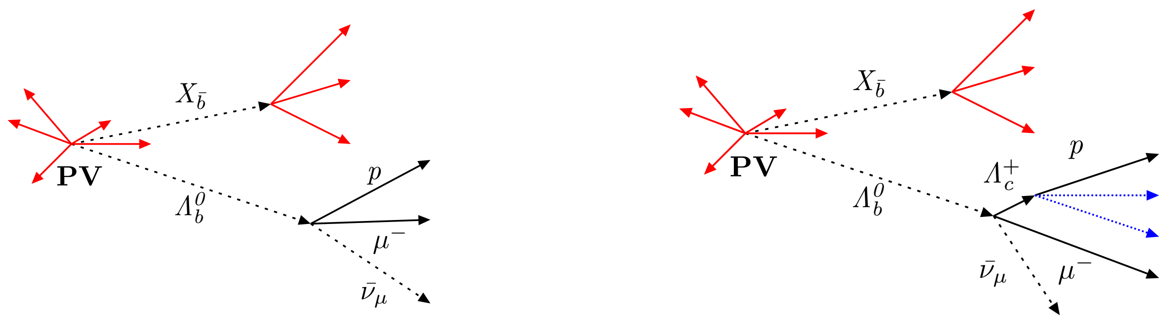

Figure 6.5: Decay topologies for signal $\Lambda_b^0 \to p\mu^-\overline{\nu}_\mu$ decays (left) and background $\Lambda_b^0 \to \Lambda_c^+\mu^-\overline{\nu}_\mu$ decays (right). In the case that background decays have additional charged tracks as shown in blue these backgrounds are removed by identifying these tracks as opposed to other tracks in the event shown in red, which originate from another b-hadron or the primary vertex.

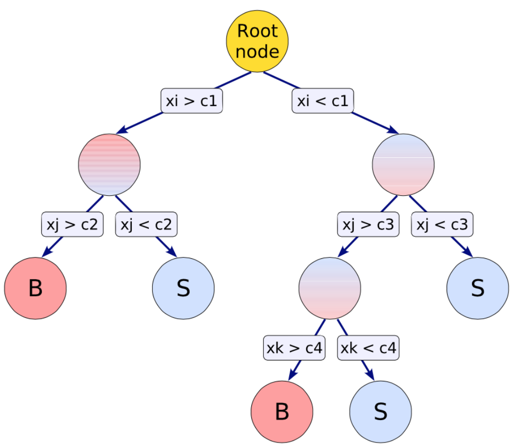

Figure 6.6: Schematic view of a decision tree taken from [80]. Starting from a root node a sequential set of cuts, which each maximise the separation between background and signal at a given node, are applied. The final subsets of the parameter space selected by these splits, known as the leaves of the tree, are labelled signal or background based on their dominate composition.

training sample into subsets using rectangular cuts on the N chosen variables, $\vec{x} = \{x_1, x_2, ..., x_N\}$, as shown in Fig 6.6. At each stage of splitting the variable and associated cut value which results in the greatest separation of signal and background is chosen. This is done by comparing the Gini index, $p(1-p)$, before and after a potential split where here p is the signal purity; this index falls off to zero for complete separation. A maximum depth of five splits was allowed and subsets of samples with less than 5% of the total training statistics were not split further. The final subsets, which are known as the leaves of the tree, are classified as signal, $h(\vec{x}) = 1$ or background $h(\vec{x}) = -1$, where here $h(\vec{x})$ is the classifier output for a single tree.

The boosting of the trees for the BDT employs the AdaBoost algorithm. After training the i^{th} tree a boost weight, α_i, is calculated using the fraction of events misclassified for that tree, ρ_i as

$$\alpha_i = \frac{1-\rho_i}{\rho_i} \ . \tag{6.12}$$

Events which were misclassified in the training sample are weighted according to the boost weight. Having re-weighted and subsequently renormalised the sample, the next decision tree is trained using the re-weighted sample. The final classification output for the BDT is given by

$$h_{\text{BDT}}(\vec{x}) = \frac{1}{N_{\text{trees}}} \sum_{i=1}^{N_{\text{trees}}} \ln(\alpha_i) h_i(\vec{x}) \ , \tag{6.13}$$

where N_{trees} is the number of decision trees that are trained. Fig 6.7 shows the BDT output for training and testing samples superimposed. Good agreement between the testing and training distributions shows that the BDT does not suffer from overtraining, which is when a multivariate classifier is sensitive to statistical fluctuations in the training samples.

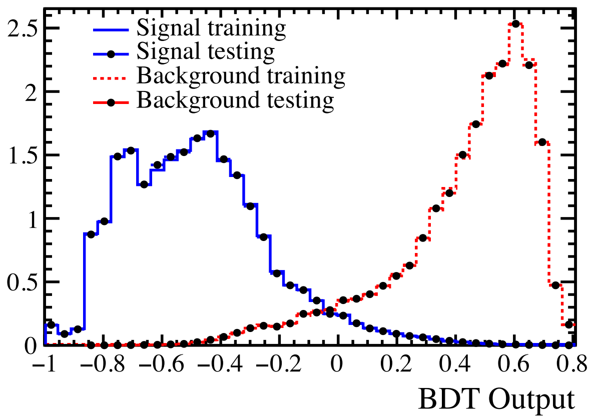

Figure 6.7: BDT output for testing and training samples. Here background consists of a sample of tracks from simulated $\Lambda_b^0 \to (\Lambda_c^+ \to pX)\mu^-\overline{\nu}_\mu$ decays while signal consists of all the tracks reconstructed in simulated $\Lambda_b^0 \to p\mu^-\overline{\nu}_\mu$ events; the tracks associated with the proton and muon are excluded in both cases.

In order to identify and reject the backgrounds where the proton and muon candidate come from a B decay in which one or more additional charged particles are produced, the BDT is run on every track in the event with an IP χ^2 with respect to $p\mu$ vertex below 50. Fig 6.8 compares the maximum BDT output per event in simulation for $\Lambda_b^0 \to p\mu^-\overline{\nu}_\mu$ decays with that for a number of background decays. Candidate events for which the maximum isolation BDT is greater than

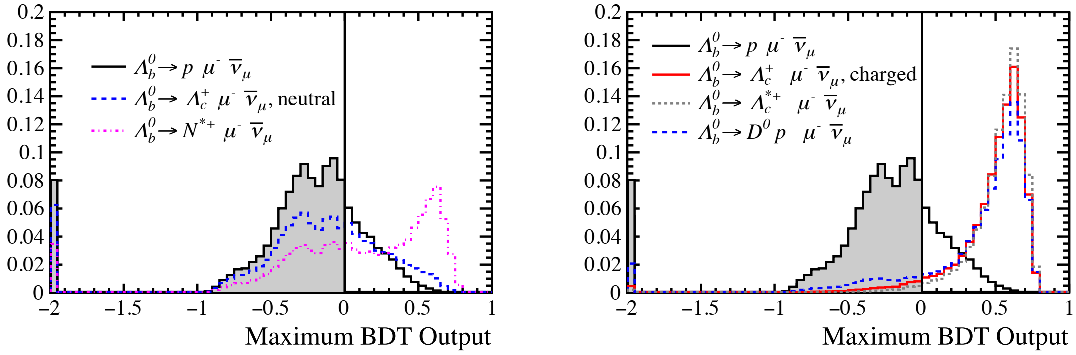

Figure 6.8: Maximum BDT output distributions obtained when running the isolation BDT over all tracks in an event for simulated signal $\Lambda_b^0 \to p\mu^-\overline{\nu}_\mu$ decays and a variety of simulated background decays. The output of -2 corresponds to the case when no tracks with and IP $\chi^2 < 50$ with respect to the $p\mu$ vertex are found. For the $|V_{ub}|$ analysis, candidate events with a maximum BDT output > 0 were rejected, thus removing the majority of background from $\Lambda_b^0 \to N^{*+}\mu^-\overline{\nu}_\mu$, $\Lambda_b^0 \to D^0 p\mu^-\overline{\nu}_\mu$, $\Lambda_b^0 \to \Lambda_c^{*+}\mu^-\overline{\nu}_\mu$ and $\Lambda_b^0 \to (\Lambda_c^+ \to pX)\mu^-\overline{\nu}_\mu$ decays.

0 are rejected; this criterion is equivalent to requiring that the $p\mu$ vertex is well isolated from any other tracks in the event. Although, after preselection, this selection criterion is only 68% efficient on simulated $\Lambda_b^0 \to p\mu^-\overline{\nu}_\mu$ decays, it rejects around 85% of $\Lambda_b^0 \to D^0 p\mu^-\overline{\nu}_\mu$ decays, 61% of $\Lambda_b^0 \to N^{*+}\mu^-\overline{\nu}_\mu$ decays, 97% of $\Lambda_b^0 \to \Lambda_c^{*+}\mu^-\overline{\nu}_\mu$ decays and 95% of $\Lambda_b^0 \to (\Lambda_c^+ \to pX)\mu^-\overline{\nu}_\mu$ decays where X includes at least one charged particle. This sacrifice in signal is justified by the large rejection of the $b \to c$ background which is $O(100)$ times larger than the signal. Given that the analysis was not statistically limited the selection was not optimised for maximal signal significance. While the isolation effectively removes many background types only 35% of $\Lambda_b^0 \to (\Lambda_c^+ \to pX)\mu^-\overline{\nu}_\mu$ decays where X represents solely neutral particles are rejected. This background category is the dominant background for the analysis after the final selection.

Fig 6.9 compares the performance of the BDT in discriminating on a track by track basis to the performance of the maximum BDT in discriminating between simulated $\Lambda_b^0 \to p\mu^-\overline{\nu}_\mu$ and $\Lambda_b^0 \to (\Lambda_c^+ \to pX)\mu^-\overline{\nu}_\mu$ decays (where X includes at least one charged particle) on a event by event basis. The performance is quantified as the rejection of background type tracks/events, $1 - \xi_{\text{background}}$, for a given signal efficiency, ξ_{signal}. For the chosen selection criterion the BDT has a signal efficiency of ∼95% and a background rejection of ∼93%. On the other hand, when making the same requirement on the maximum BDT output per event the signal efficiency is much lower at ∼68% while the background rejection is slightly higher at ∼95%. This is due to the fact that in a single signal-type event there are many signal-type tracks meanwhile for a background-type event there are only ever 1-3 tracks of the background type.

The distribution of the maximum BDT output in data is shown for opposite-sign and same-sign proton and muon combinations in Fig 6.10. A clear peaking structure is seen representing backgrounds involving additional charged tracks.

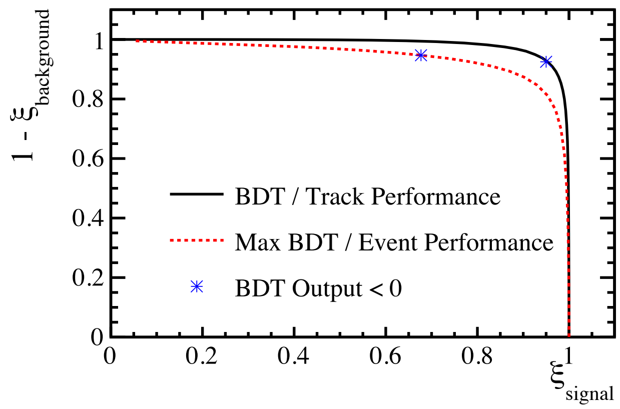

Figure 6.9: A comparison of the performance of the BDT on a track by track basis (solid line) with that of the maximum BDT output per event (dashed line). This performance is measured by the background rejection, $1 - \xi_{\text{background}}$ for a given signal efficiency, ξ_{signal}. The performance achieved by requiring tracks or events respectively to have a BDT output or maximum BDT output < 0 is marked on the curves.

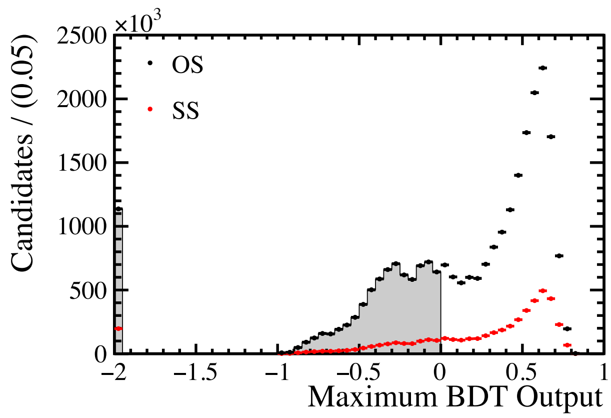

Figure 6.10: Maximum BDT Output distribution for proton and muon candidates of the same-sign (SS) and opposite-sign (OS) passing the preselection.

The same isolation criterion is applied when selecting candidates for the normalisation mode, $\Lambda_b^0 \to (\Lambda_c^+ \to pK^-\pi^+)\mu^-\overline{\nu}_\mu$, however in this case the kaon and pion tracks are ignored when finding the maximum BDT output for the event.

6.3.5. The corrected mass

In order to distinguish signal $\Lambda_b^0 \to p\mu^-\overline{\nu}_\mu$ decays and normalisation $\Lambda_b^0 \to (\Lambda_c^+ \to pK^-\pi^+)\mu^-\overline{\nu}_\mu$ decays from partially reconstructed B decays, which survive the isolation requirements, a fit is made to the corrected mass of the $h\mu$ combination ($h = p/\Lambda_c^+$). The corrected mass is defined as

$$m_{\text{corr}} = \sqrt{m_{h\mu}^2 + p_{\text{T}}^2} + p_{\text{T}} \ , \tag{6.14}$$

where p_{T} is the component of the neutrino's momentum transverse to the Λ_b^0 flight direction, which can be determined by applying momentum conservation as illustrated in Fig 6.1. Given a decay such as $B \to h\mu^-\overline{\nu}$ with one massless particle, the corrected $h\mu^-$ mass will peak at the B mass. On the other hand the corrected mass will peak lower for decays in which massive particles are missing. Fig 6.11 demonstrates this by comparing the proton and muon true and reconstructed corrected masses for simulated $\Lambda_b^0 \to p\mu^-\overline{\nu}_\mu$ decays to that of simulated $\Lambda_b^0 \to (\Lambda_c^+ \to pK^0)\mu^-\overline{\nu}_\mu$ and $\Lambda_b^0 \to (\Lambda_c^+ \to pK^0\pi^0)\mu^-\overline{\nu}_\mu$ decays. Although the corrected mass computed using truth information, as shown in Fig 6.11 is highly discriminating there is a substantial resolution associated with reconstructing the corrected mass, which is shown in Fig 6.12. This results in a less prominent peaking structure for the signal shape and a greater leakage of backgrounds into the signal region. There is more leakage of $\Lambda_b^0 \to (\Lambda_c^+ \to pK^0)\mu^-\overline{\nu}_\mu$ decays into the signal region than $\Lambda_b^0 \to (\Lambda_c^+ \to pK^0\pi^0)\mu^-\overline{\nu}_\mu$ decays given that only one particle in addition to the neutrino is missing as opposed to two. For this reason decays such as $\Lambda_b^0 \to (\Lambda_c^+ \to pK^0)\mu^-\overline{\nu}_\mu$, $\Lambda_b^0 \to (\Lambda_c^+ \to p\pi^0)\mu^-\overline{\nu}_\mu$ and $\Lambda_b^0 \to (N^{*+} \to p\pi^0)\mu^-\overline{\nu}_\mu$ are the most dangerous backgrounds.

The resolution associated with reconstructing the corrected mass is dominated by an imperfect knowledge of the Λ_b^0 flight direction which results in a large uncertainty on the transverse momentum component of the neutrino, $p_\perp$. This uncertainty is dominated by the uncertainty on the positions of the primary and secondary vertex positions which are defined as $\vec{x}_{\text{PV}} = (x', y', z')$ and $\vec{x}_{\text{SV}} = (x, y, z)$, respectively. The transverse component of the neutrino momentum can be defined in terms of

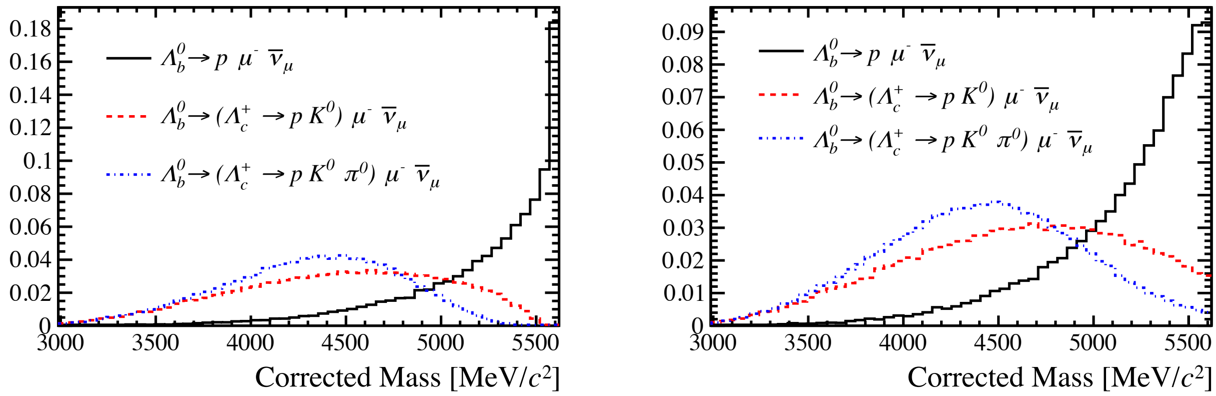

Figure 6.11: A comparison of the proton and muon corrected mass for simulated signal $\Lambda_b^0 \to p\mu^-\overline{\nu}_\mu$ decays to that for simulated background decays $\Lambda_b^0 \to (\Lambda_c^+ \to pK^0)\mu^-\overline{\nu}_\mu$ and $\Lambda_b^0 \to (\Lambda_c^+ \to pK^0\pi^0)\mu^-\overline{\nu}_\mu$. On the left the corrected mass is computed using Monte Carlo truth information meanwhile on the right the reconstructed quantity is shown.

these positions and the momentum of the $p\mu$ pair, $\vec{p} = (p_x, p_y, p_z)$, as

$$p_T^2 = \left| \vec{p} - (\vec{x}_{\mathrm{SV}} - \vec{x}_{\mathrm{PV}}) \frac{\vec{p} \cdot (\vec{x}_{\mathrm{SV}} - \vec{x}_{\mathrm{PV}})}{|\vec{x}_{\mathrm{SV}} - \vec{x}_{\mathrm{PV}}|^2} \right|^2 . \tag{6.15}$$

The 4-momentum of the combined $p\mu$ pair is defined as $p_{p\mu} = (E, p_x, p_y, p_z)$. The full uncertainty on the corrected mass, $m_{\mathrm{corr}}(x', y', z', x, y, z, E, p_x, p_y, p_z)$, associated with the vertex positions and the 4-momentum of the $p\mu$ pair is

$$\sigma'^2_{m_{\mathrm{corr}}} = \sum_{i=1}^{3} \sum_{j=1}^{3} \frac{\partial m_{\mathrm{corr}}}{\partial x^i_{\mathrm{PV}}} \frac{\partial m_{\mathrm{corr}}}{\partial x^j_{\mathrm{PV}}} M_{ij} + \sum_{n=1}^{7} \sum_{m=1}^{7} \frac{\partial m_{\mathrm{corr}}}{\partial k^m} \frac{\partial m_{\mathrm{corr}}}{\partial k^n} J_{mn} , \tag{6.16}$$

where here $\vec{k} = (x, y, z, E, p_x, p_y, p_z)$ and J is the associated covariance matrix. Meanwhile, the matrix, M, contains the covariance information corresponding to the primary vertex $\vec{x}_{\mathrm{PV}}$. Under the assumption that the uncertainty on the corrected mass is dominated by the uncertainty on the vertex positions this expression simplifies to

$$\sigma^2_{m_{\mathrm{corr}}} = \sum_{i=1}^{3} \sum_{j=1}^{3} \frac{\partial m_{\mathrm{corr}}}{\partial x^i_{\mathrm{PV}}} \frac{\partial m_{\mathrm{corr}}}{\partial x^j_{\mathrm{PV}}} M_{ij} + \sum_{n=1}^{3} \sum_{m=1}^{3} \frac{\partial m_{\mathrm{corr}}}{\partial k^m} \frac{\partial m_{\mathrm{corr}}}{\partial k^n} J_{mn} . \tag{6.17}$$

Fig 6.12 compares the corrected mass uncertainty computed using solely the covariance information for the primary and secondary vertex positions, $\sigma_{m_{\rm corr}}$, to that including the impact of the uncertainty on the $p\mu$ 4-momentum, $\sigma'_{m_{\rm corr}}$. Fig 6.12 also shows the improvement in the corrected mass resolution, $m_{\rm corr}^{\rm reco} - m_{\rm corr}^{\rm true}$, when requiring candidates either have $\sigma_{m_{\rm corr}} < 100$ MeV/c^2 or $\sigma'_{m_{\rm corr}} < 100$ MeV/c^2. While the selection criterion $\sigma'_{m_{\rm corr}} < 100$ MeV/c^2 results in a slightly narrower $m_{\rm corr}^{\rm reco} - m_{\rm corr}^{\rm true}$ distribution this condition results in a efficiency loss of 11% relative to the condition $\sigma_{m_{\rm corr}} < 100$. For this reason a selection was made using $\sigma_{m_{\rm corr}}$ as opposed to $\sigma'_{m_{\rm corr}}$.

The requirement to reject candidates with a corrected mass uncertainty above 100 MeV/c^2 reduces the RMS of the $m_{\rm corr}^{\rm reco} - m_{\rm corr}^{\rm true}$ distribution from 250 MeV/c^2 to 156 MeV/c^2. Although this tight selection criterion selects only around 23% of signal after preselection there is a significant improvement in the separation between signal and background corrected mass shapes as shown in Fig 6.13.

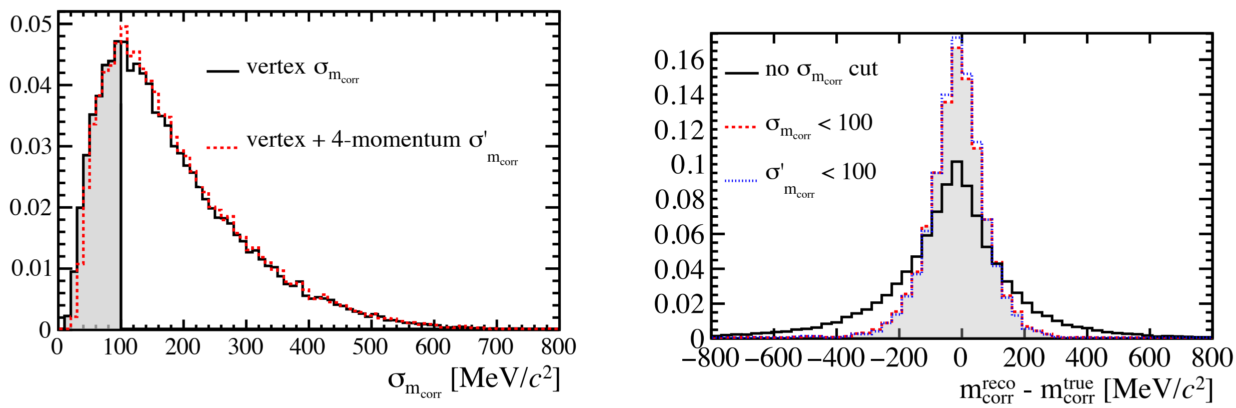

Figure 6.12: The corrected mass uncertainty, $\sigma_{m_{\rm corr}}$, distribution for simulated $\Lambda_b^0 \to p\mu^-\overline{\nu}_\mu$ decays. In the $|V_{ub}|$ analysis candidates with corrected mass uncertainty above 100 MeV/c^2 are rejected (left). The $m_{\rm corr}^{\rm reco} - m_{\rm corr}^{\rm true}$ distribution for simulated $\Lambda_b^0 \to p\mu^-\overline{\nu}_\mu$ decays is shown by the solid line meanwhile the dashed requirement shows candidates which meet the additional requirements of $\sigma_{m_{\rm corr}} < 100$ MeV/c^2 and $\sigma'_{m_{\rm corr}} < 100$ MeV/c^2 (right).

The choice of the selection criterion $\sigma_{m_{\rm corr}} < 100$ MeV/c^2 was made in order to limit systematic uncertainties as opposed to optimising on a statistical basis. The cut value of 100 MeV/c^2 corresponds to the peak of the corrected mass uncertainty distribution, this results in a smaller impact for any potential mismatch in corrected mass uncertainty distribution in simulation to that in data. This effect is quantified later in section 7.4.1 using a kaon and muon combination from $B^+ \to (J/\psi \to \mu^+\mu^-)K^+$ decays as a proxy for the signal proton and muon. Fig 6.14 shows the RMS of the $m_{\rm corr}^{\rm reco} - m_{\rm corr}^{\rm true}$ distribution as a function of $\sigma_{m_{\rm corr}}$ and $x_{\rm cut}$, where $\sigma_{m_{\rm corr}} < x_{\rm cut}$.Initially

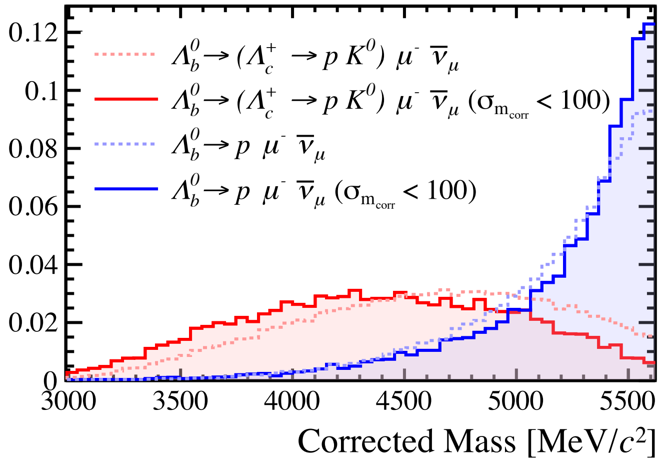

Figure 6.13: A comparison of the proton and muon corrected mass distributions between simulated signal $\Lambda_b^0 \to p\mu^-\overline{\nu}_\mu$ decays and background $\Lambda_b^0 \to (\Lambda_c^+ \to pK^0)\mu^-\overline{\nu}_\mu$ decays. The dashed lines correspond to when no selection is made using $\sigma_{m_{\mathrm{corr}}}$ meanwhile the solid lines correspond to when $\sigma_{m_{\mathrm{corr}}} < 100$ MeV/c^2 is required.

as a tighter selection on $\sigma_{m_{\mathrm{corr}}} < x_{\mathrm{cut}}$ is made the RMS falls at an increasing rate until there is almost a linear relationship. However for cut values below 150 MeV/c^2 the RMS begins to fall at a decreasing rate.

For the selection of the normalisation mode, $\Lambda_b^0 \to (\Lambda_c^+ \to pK^-\pi^+)\mu^-\overline{\nu}_\mu$, no cut on the $p\mu$ or $\Lambda_c^+\mu$ corrected mass uncertainty is made.

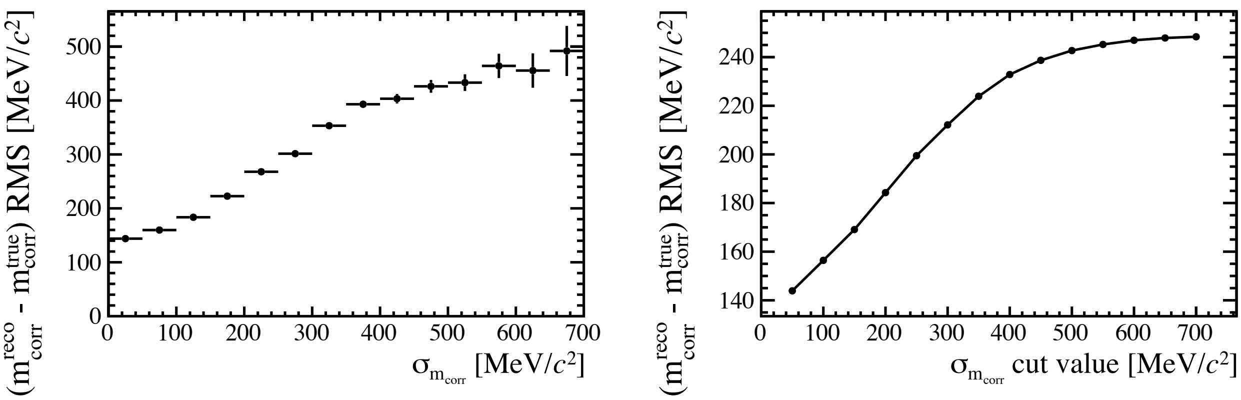

Figure 6.14: RMS of the $m_{\mathrm{corr}}^{\mathrm{reco}} - m_{\mathrm{corr}}^{\mathrm{true}}$ distribution in bins of corrected mass uncertainty, $\sigma_{m_{\mathrm{corr}}}$, for simulated $\Lambda_b^0 \to p\mu^-\overline{\nu}_\mu$ decays (left). RMS of the $m_{\mathrm{corr}}^{\mathrm{reco}} - m_{\mathrm{corr}}^{\mathrm{true}}$ distribution as a function of x where the requirement $\sigma_{m_{\mathrm{corr}}} < x_{\mathrm{cut}}$ is made (right).

6.3.6. Selection on data

Fig. 6.15 shows the corrected mass distribution for opposite-sign and same-sign proton and muon data candidates as successive selections are made on q^2, the isolation BDT and the corrected mass uncertainty. By selecting the best resolution candidates, which have a well isolated $p\mu$ vertex, it is possible to see a peaking structure at the Λ_b^0 mass. Fig 6.16 shows an event display for $\Lambda_b^0 \to p\mu^-\overline{\nu}_\mu$ candidate passing the final selection with a corrected mass above 5500 MeV/c^2.

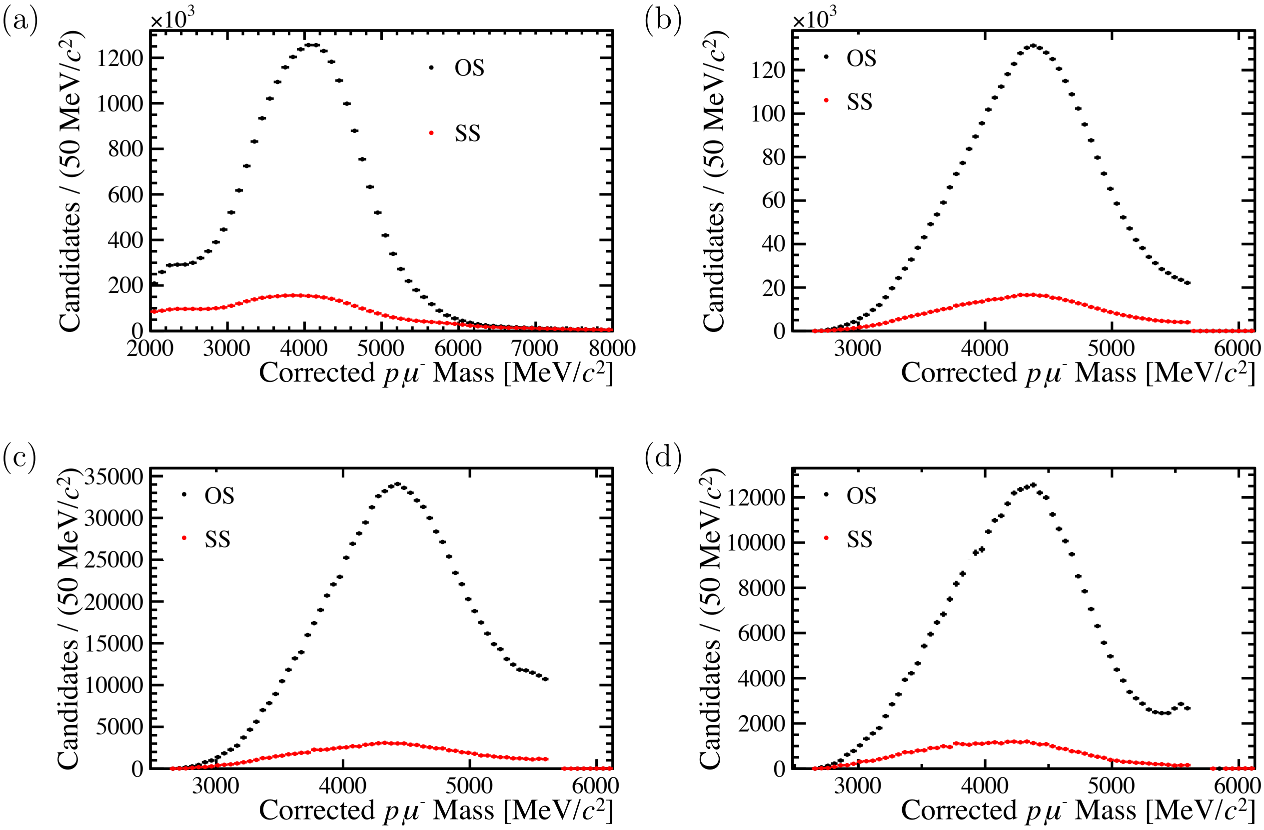

Figure 6.15: Corrected mass distributions for proton and muon candidates of the same sign (SS) and opposite sign (OS) which pass a sequence of successive selection criteria: (a) preselection, (b) $q^2_{1,2} > 15$ GeV$^2/c^4$, (c) Maximum BDT < 0 and (d) $\sigma_{m_{corr}} < 100$ MeV/c^2. After the full selection has been applied (in (d)) a peaking structure can be seen a the mass of the Λ_b^0 baryon ($m_{\Lambda_b^0} \sim 5620\,$MeV/$c^2$).

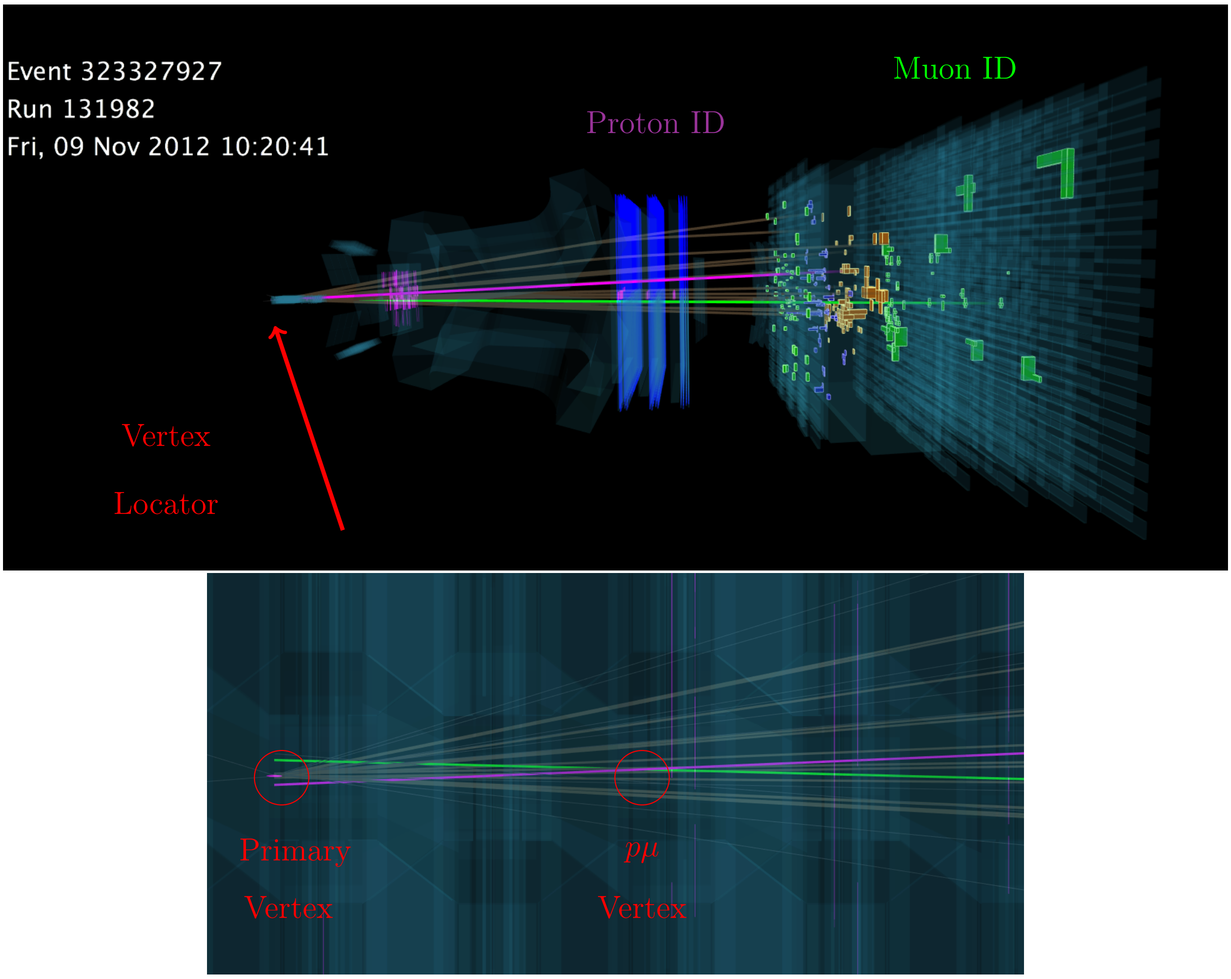

Figure 6.16: An event display for a $\Lambda_b^0 \to p\mu^- \overline{\nu}_\mu$ candidate with a corrected mass above 5500 MeV/c^2. The track of the muon is shown in green leaving hits in the muon chambers while the proton's track is shown in pink. A zoomed in view of the VELO shows the primary vertex and the displaced $p\mu$ vertex.

Chapter 7.

Determination of $|V_{ub}|/|V_{cb}|$, $|V_{ub}|$ and $\mathcal{B}_{\Lambda_b^0\to p\mu^-\overline{\nu}_\mu}$

This chapter presents the analysis performed in order to measure the ratio of branching of $\Lambda_b^0 \to p\mu^-\overline{\nu}_\mu$ and $\Lambda_b^0 \to \Lambda_c^+\mu^-\overline{\nu}_\mu$ decays. Fits to the corrected mass of $\Lambda_b^0 \to p\mu^-\overline{\nu}_\mu$ and $\Lambda_b^0 \to \Lambda_c^+\mu^-\overline{\nu}_\mu$ decays, which are used to determine the yields of the two decays, are described in sections 7.1 and 7.3. A variety of data-driven constraints used in the signal fit are outlined in section 7.2. Subsequently, the computation of the relative efficiency for selecting the two modes is discussed in section 7.4. Finally, the main results of the analysis are presented in section 7.5.

7.1. Normalisation fit

7.1.1. Fit procedure

For both the signal and normalisation fits a, χ^2, is constructed according to

$$\chi^2(\vec{k}) = \sum_{i=1}^{N_{\text{bins}}} \left(\frac{n^i_{\text{model}}(\vec{k}) - n^i_{\text{data}}}{\sqrt{(\sigma^i_{\text{data}})^2 + (\sigma^i_{\text{model}}(\vec{k}))^2}} \right)^2 + \sum_{i=1}^{N_{\text{cons}}} \left(\frac{\mu^i_{\text{constraint}} - k^i}{\sigma^i_{\text{constraint}}} \right)^2, \tag{7.1}$$

where n^i_{data} is the number of observed candidates in data in the i^{th} bin of corrected mass and $\sigma^i_{\text{data}} = \sqrt{n^i_{\text{data}}}$ is its associated error. The expected number of candidates, $n^i_{\text{model}}(\vec{k})$, and its associated uncertainty, $\sigma^i_{\text{model}}(\vec{k})$, are a function of the M fit parameters, $\vec{k} = (k^1, k^2, ..., k^M)$, as determined by the fit model. Gaussian constraints are placed on the first N_{cons} parameters in $\vec{k}$ according to constraint values, $\vec{\mu}_{\text{constraint}}$, and their associated uncertainties, $\vec{\sigma}_{\text{constraint}}$. The final values for the fit parameters are determined by minimising the χ^2 with respect to the parameters.

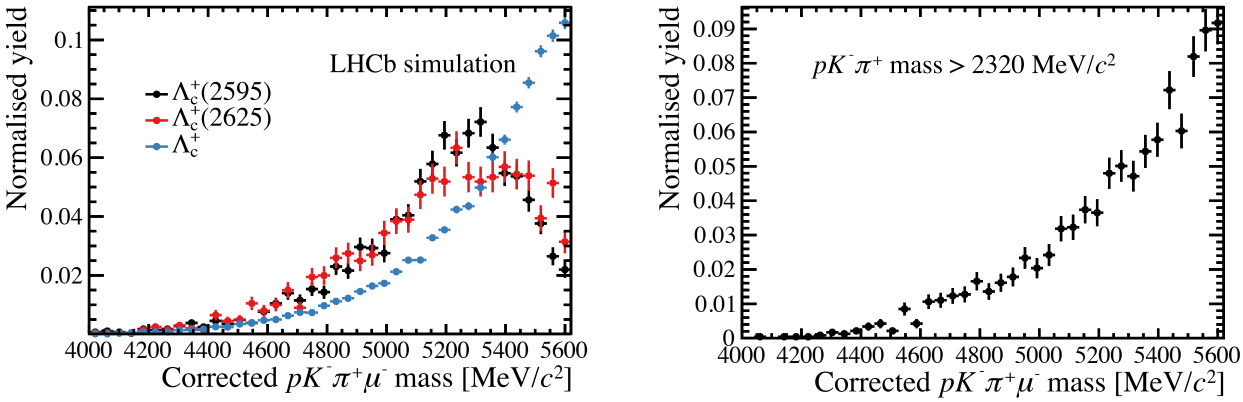

Figure 7.1: A comparison of the $pK^-\pi^+\mu^-$ corrected mass for simulated $\Lambda_b^0 \to \Lambda_c^+\mu^-\overline{\nu}_\mu$, $\Lambda_b^0 \to \Lambda_c^+(2625)\mu^-\overline{\nu}_\mu$ and $\Lambda_b^0 \to \Lambda_c^+(2595)\mu^-\overline{\nu}_\mu$ decays (left) reveals that there is a clear separation between corrected mass shape of the ground state mode from that of the excited modes. Corrected mass shape for $pK^-\pi^+\mu^-$ candidates in the upper sideband of the $pK^-\pi^+$ invariant mass (right). These histograms are used are used as PDFs in the normalisation fit.

7.1.2. Normalisation fit model

The normalisation fit model is described by

$$n^i_{\text{norm. model}}(\vec{k}) = \vec{k^i} \cdot \vec{p^i} \, , \tag{7.2}$$

where $\vec{p} = (p^i_{\text{comb.}}, p^i_{\Lambda_c^+}, p^i_{\Lambda_c^{*+}})$ are discrete PDFs describing the probability for a given combinatorial $pK^-\pi^+\mu^-$, $\Lambda_b^0 \to (\Lambda_c^+ \to pK^-\pi^+)\mu^-\overline{\nu}_\mu$ or $\Lambda_b^0 \to \Lambda_c^{*+}\mu^-\overline{\nu}_\mu$ process to have a corrected mass in the i^{th} corrected mass bin range. For the normalisation fit, the only free parameters, $\vec{k} = (N_{\text{comb.}}, N_{\Lambda_c^+}, N_{\Lambda_c^{*+}})$, are the yields for each of the fit components. The PDFs describing $\Lambda_b^0 \to (\Lambda_c^+ \to pK^-\pi^+)\mu^-\overline{\nu}_\mu$ and $\Lambda_b^0 \to \Lambda_c^{*+}\mu^-\overline{\nu}_\mu$ decays are normalised histograms taken from simulation as shown in Fig 7.1. Meanwhile, the PDF, describing the background from combinatorial $pK^-\pi^+\mu^-$ is taken from data in the upper $pK^-\pi^+$ mass sideband. It is assumed that there is no combinatorial $\Lambda_c^+\mu^-$ background given that no peak at the Λ_c^+ mass is seen in the $pK^-\pi^+$ invariant mass distribution for the same-sign $\Lambda_c^+\mu^+$ sample.

7.1.3. $pK^-\pi^+$ mass constraint

For the normalisation fit, a single constraint is made on the yield for the $pK^-\pi^+\mu^-$ combinatorial background component. The yield of the $pK^-\pi^+\mu^-$ combinatorial background is estimated to be $N_{\text{comb.}} = 1160 \pm 100$ in the region $2270\,\text{MeV}/c^2 < m_{pK^-\pi^+} < 2320\,\text{MeV}/c^2$ by performing an unbinned maximum-likelihood fit to the $pK^-\pi^+$ mass, which is shown in Fig 7.2. The signal mass PDF is described according to a sum of two Crystal-Ball functions with common tail parameters and different widths. A single Crystal-Ball function is defined as

$$f(m,\alpha,n,\mu,\sigma) = N \cdot \begin{cases} e^{\frac{-(x-\mu)^2}{2\sigma^2}}, & \text{if } \frac{x-\mu}{\sigma} > -\alpha \\ (\frac{n}{|\alpha|})^n \cdot e^{\frac{-|\alpha|^2}{2}} \cdot (\frac{n}{|\alpha|} - |\alpha| - \frac{(x-\mu)}{\sigma})^{-n}, & \text{if } \frac{x-\mu}{\sigma} \leq -\alpha \,, \end{cases} \tag{7.3}$$

where, N is the normalisation parameter, μ and σ are the mean and width under the Gaussian regime, meanwhile α sets the transition point from Gaussian behaviour to an exponential tail with exponent, n. Meanwhile, background from $pK^-\pi^+\mu^-$ combinatorial background is parametrised by an exponential function,

$$f(m,c) = N \cdot e^{-cm} \,, \tag{7.4}$$

with exponent $c > 0$.

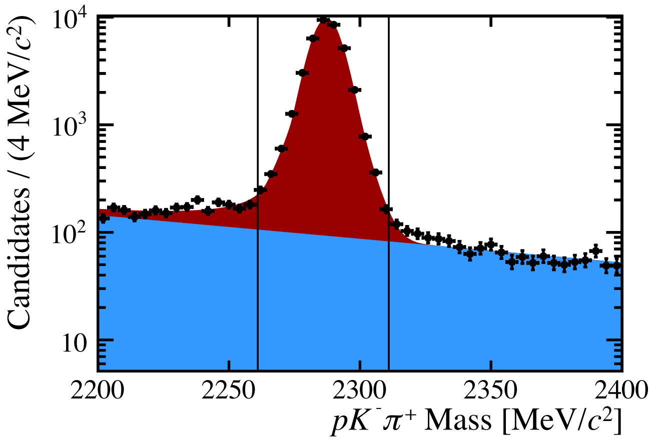

Figure 7.2: Fit to the $pK^-\pi^+$ invariant mass. While, with the logarithmic scale, it can be seen that the fit is not perfect on the high mass shoulder of the peak, this has no impact on the overall uncertainty of the normalisation fit.

7.1.4. Normalisation fit result

Fig 7.3 shows the fit to the corrected $pK^-\pi^+\mu^-$ mass for normalisation candidates within the required q^2 region ($> 7\,\mathrm{GeV}^2/c^4$) and $m_{pK^-\pi^+}$ mass window ($2270\,\mathrm{MeV}/c^2 < m_{pK^-\pi^+} < 2320\,\mathrm{MeV}/c^2$). The number of $\Lambda_b^0 \to \Lambda_c^+\mu^-\overline{\nu}_\mu$ candidates observed is 33570±560, which leads to a normalisation yield of $N_{\Lambda_b^0\to(\Lambda_c^+\to pK^-\pi^+)\mu^-\overline{\nu}_\mu} = 34255\pm571$ when accounting for the fraction of $\Lambda_b^0 \to (\Lambda_c^+ \to pK^-\pi^+)\mu^-\overline{\nu}_\mu$ decays (2%) which falls outside the selected window in $pK^-\pi^+$ invariant mass.

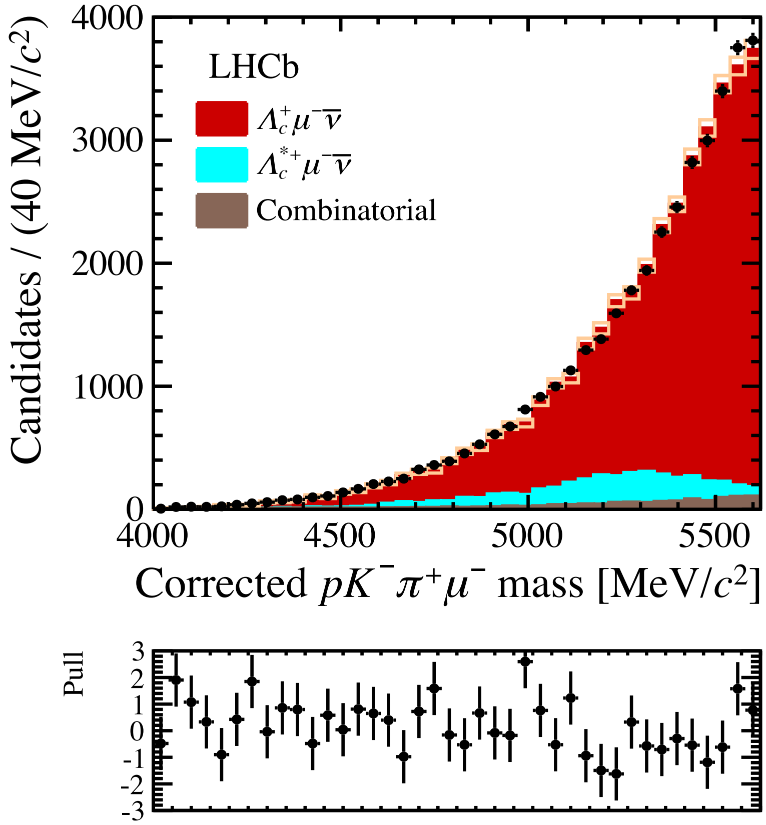

Figure 7.3: Fit to the $pK^-\pi^+\mu^-$ corrected mass of candidates surviving the normalisation selection. The yellow boxes display the uncertainty on the fit model's predicted number of events, n^i_{model}, which arises from the statistical uncertainty associated with finite simulation samples. The pull for each bin, $(n^i_{\mathrm{model}}(\vec{k}) - n^i_{\mathrm{data}})/\sqrt{(\sigma^i_{\mathrm{data}})^2 + (\sigma^i_{\mathrm{model}}(\vec{k}))^2}$, is shown below the fit.

7.2. Background estimation and constraints

While the normalisation fit has very little background, the signal fit faces a large amount of background from a wide range of decays. Furthermore, many of the decays which are backgrounds for the signal fit have very similar shapes in corrected mass to each other and poorly known branching fractions. For this reason, constraints on a number of parameters entering the fit are determined from data. This section outlines how various backgrounds entering the fit are constrained or estimated using data.

7.2.1. $\Lambda_b^0\to \Lambda_c^+\mu^-\overline{\nu}_\mu$ and $\Lambda_b^0\to \Lambda_c^{*+}\mu^-\overline{\nu}_\mu$ decays

Background from $\Lambda_b^0\to \Lambda_c^+\mu^-\overline{\nu}_\mu$ decays is separated into the neutral and charged categories defined earlier in section 6.1 . This is because the isolation BDT requirement will effect the two types of backgrounds differently.

The neutral category of $\Lambda_b^0\to \Lambda_c^+\mu^-\overline{\nu}_\mu$ decays is controlled by reconstructing $\Lambda_b^0\to(\Lambda_c^+\to pK_S^0)\mu^-\overline{\nu}_\mu$ decays in data. The yield of $\Lambda_b^0\to(\Lambda_c^+\to pK^0)\mu^-\overline{\nu}_\mu$ decays, $N_{\Lambda_b^0\to(\Lambda_c^+\to pK^0)\mu^-\overline{\nu}_\mu}$, is determined according to

$$N_{\Lambda_b^0\to(\Lambda_c^+\to pK^0)\mu^-\overline{\nu}_\mu} = \frac{N_{\Lambda_b^0\to(\Lambda_c^+\to pK_S^0)\mu^-} F_{\Lambda_c^+}}{\epsilon_{pK_S^0\mu|p\mu}\mathcal{B}_{K_S^0\to\pi^+\pi^-}} \ , \tag{7.5}$$

where here $N_{\Lambda_b^0\to(\Lambda_c^+\to pK_S^0)\mu^-}$ is the yield of reconstructed $\Lambda_b^0\to(\Lambda_c^+\to pK_S^0)\mu^-$ candidates, while, $\epsilon_{pK_S^0\mu|sel}$ is the efficiency, as determined from simulation, for selecting $\Lambda_b^0\to(\Lambda_c^+\to pK_S^0)\mu^-\overline{\nu}_\mu$ from $\Lambda_b^0\to(\Lambda_c^+\to pK^0)\mu^-\overline{\nu}_\mu$ decays given that the full $\Lambda_b^0\to p\mu^-\overline{\nu}_\mu$ selection has been applied. The efficiency, $\epsilon_{pK_S^0\mu|sel}$, takes into account the factor of K^0 mesons that will be observed as K_S^0 meson as opposed to K_L^0 mesons. The branching fraction of $K_S^0\to\pi^+\pi^-$ decays, $\mathcal{B}_{K_S^0\to\pi^+\pi^-} = (69.20\pm0.05)\%$, is taken from [11]. Finally, $F(\Lambda_c^+)$, is the expected fraction of $\Lambda_b^0\to(\Lambda_c^+\to pK_S^0)\mu^-$ candidates that are from $\Lambda_b^0\to \Lambda_c^+\mu^-\overline{\nu}_\mu$ decays as opposed to $\Lambda_b^0\to \Lambda_c^{*+}\mu^-\overline{\nu}_\mu$ decays.

The yield of $\Lambda_b^0\to(\Lambda_c^+\to pK_S^0)\mu^-$ candidates is obtained by fitting the pK_S^0 invariant mass. Given the poorly known reconstruction efficiency for downstream K_S^0 candidates, limited statistics and the prescale of events with corrected mass below 4000 MeV/c^2, three selection choices for $\Lambda_b^0\to(\Lambda_c^+\to pK_S^0)\mu^-$ candidates are considered. Results for these three scenarios are shown in Table 7.1, meanwhile, the corresponding fits are shown in Fig. 7.4.

Situation	$N_{\Lambda_b^0\to(\Lambda_c^+\to pK_S^0)\mu^-}$	$\epsilon_{pK_S^0\mu\|p\mu}$	$F_{\Lambda_c^+}$	$N_{\Lambda_b^0\to(\Lambda_c^+\to pK^0)\mu^-\overline{\nu}_\mu}$
$M_{\rm corr} > 4$ GeV	227 ± 17	0.0101 ± 0.0008	0.91 ± 0.02	29327 ± 3297
long K_S^0 & $M_{\rm corr} > 4$ GeV	118 ± 13	0.0054 ± 0.0006	0.91 ± 0.02	30042 ± 4614
whole $M_{\rm corr}$	155 ± 15	0.0136 ± 0.0010	0.897 ± 0.02	29519 ± 3591

Table 7.1: Summary of the measured efficiencies and yields, $N_{\Lambda_b^0\to(\Lambda_c^+\to pK_S^0)\mu^-}$, $\epsilon_{pK_S^0\mu|p\mu}$ and $N_{\Lambda_b^0\to(\Lambda_c^+\to pK^0)\mu^-\overline{\nu}_\mu}$, for three different selection scenarios. Here a $K_S^0 \to \pi^+\pi^-$ candidate is considered as long when both of the pion tracks are long tracks.

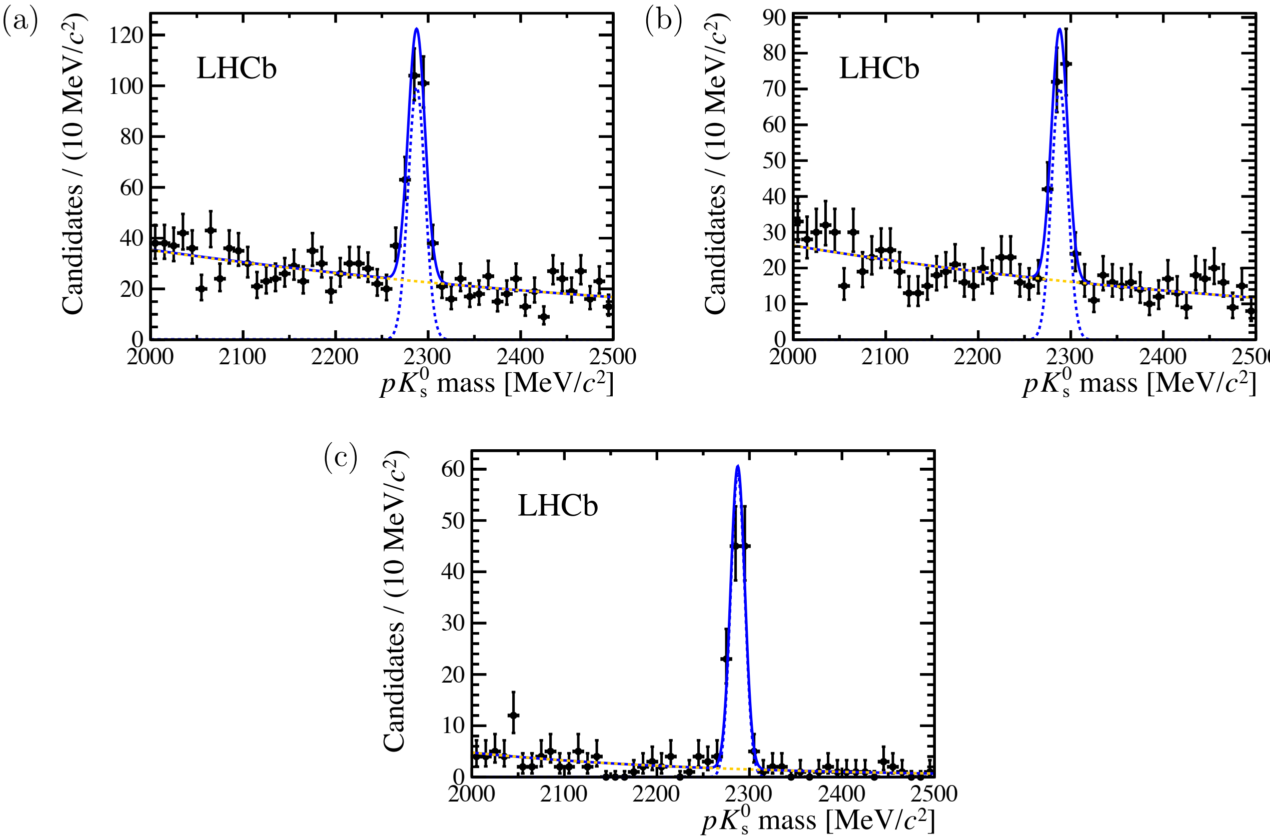

Figure 7.4: Mass fits to the pK_S^0 invariant mass distributions for the scenarios of (a) $m_{\rm corr} > 4$ GeV, (b) the full $m_{\rm corr}$ region is used and (c) only long K_S^0 are considered and $m_{\rm corr} > 4$ GeV.

The yield for a given neutral mode can be determined using the yield of $\Lambda_b^0 \to (\Lambda_c^+ \to pK^0)\mu^-\overline{\nu}_\mu$ decays using the expression

$$\begin{aligned} N_{\Lambda_b^0\to(\Lambda_c^+\to pX)\mu^-\overline{\nu}_\mu} &= N_{\Lambda_b^0\to(\Lambda_c^+\to pK^0)\mu^-\overline{\nu}_\mu} \cdot \frac{\epsilon_{\Lambda_c^+\to pX}}{\epsilon_{\Lambda_c^+\to pK^0}} \cdot \frac{\mathcal{B}_{\Lambda_c^+\to pX}}{\mathcal{B}_{\Lambda_c^+\to pK^0}} \\ &= N_{\Lambda_b^0\to(\Lambda_c^+\to pK^0)\mu^-\overline{\nu}_\mu} \cdot R_{\Lambda_c^+\to pX} \,, \end{aligned} \tag{7.6}$$

$\mathcal{B}_{\Lambda_c^+\to pX}/\mathcal{B}_{\Lambda_c^+\to pK^-\pi^+}$	PDG value
$\mathcal{B}_{\Lambda_c^+\to pK^0}/\mathcal{B}_{\Lambda_c^+\to pK^-\pi^+}$	0.47 ± 0.04
$\mathcal{B}_{\Lambda_c^+\to pK^0\pi^0}/\mathcal{B}_{\Lambda_c^+\to pK^-\pi^+}$	$0.66 \pm 0.05 \pm 0.07$
$\mathcal{B}_{\Lambda_c^+\to pK^0\eta}/\mathcal{B}_{\Lambda_c^+\to pK^-\pi^+}$	$0.25 \pm 0.04 \pm 0.04$
$\mathcal{B}_{\Lambda_c^+\to p\overline{K}^*(892)^0}/\mathcal{B}_{\Lambda_c^+\to pK^-\pi^+}$	0.31 ± 0.04
$\mathcal{B}_{\Lambda_c^+\to p\Delta(1232)^{++}K^-}/\mathcal{B}_{\Lambda_c^+\to pK^-\pi^+}$	0.17 ± 0.04
$\mathcal{B}_{\Lambda_c^+\to \Lambda(1520)\pi^+}/\mathcal{B}_{\Lambda_c^+\to pK^-\pi^+}$	0.35 ± 0.08
$\mathcal{B}_{\Lambda_c^+\to pK^-\pi^+\mathrm{nonresonant}}/\mathcal{B}_{\Lambda_c^+\to pK^-\pi^+}$	0.55 ± 0.06
$\mathcal{B}_{\Lambda_c^+\to p\overline{K^0}\pi^-\pi^+}/\mathcal{B}_{\Lambda_c^+\to pK^-\pi^+}$	0.51 ± 0.06
$\mathcal{B}_{\Lambda_c^+\to pK^-\pi^+\pi^0}/\mathcal{B}_{\Lambda_c^+\to pK^-\pi^+}$	$0.67 \pm 0.04 \pm 0.11$
$\mathcal{B}_{\Lambda_c^+\to pK^*(892)^-\pi^+}/\mathcal{B}_{\Lambda_c^+\to p\overline{K^0}\pi^-\pi^+}$	0.44 ± 0.14
$\mathcal{B}_{\Lambda_c^+\to p(K^-\pi^+_{\mathrm{nonresonant}}\pi^0}/\mathcal{B}_{\Lambda_c^+\to pK^-\pi^+}$	$0.73 \pm 0.12 \pm 0.05$
$\mathcal{B}_{\Lambda_c^+\to pK^-\pi^+\pi^+\pi^-}/\mathcal{B}_{\Lambda_c^+\to pK^-\pi^+}$	0.022 ± 0.015
$\mathcal{B}_{\Lambda_c^+\to pK^-\pi^+\pi^0\pi^0}/\mathcal{B}_{\Lambda_c^+\to pK^-\pi^+}$	$0.16 \pm 0.07 \pm 0.03$
$\mathcal{B}_{\Lambda_c^+\to pK^-\pi^+3\pi^0}/\mathcal{B}_{\Lambda_c^+\to pK^-\pi^+}$	$0.1 \pm 0.06 \pm 0.02$
$\mathcal{B}_{\Lambda_c^+\to p\pi^+\pi^-}/\mathcal{B}_{\Lambda_c^+\to pK^-\pi^+}$	0.069 ± 0.036
$\mathcal{B}_{\Lambda_c^+\to pf_0(980)}/\mathcal{B}_{\Lambda_c^+\to pK^-\pi^+}$	0.055 ± 0.036
$\mathcal{B}_{\Lambda_c^+\to p\pi^+\pi^+\pi^-\pi^-}/\mathcal{B}_{\Lambda_c^+\to pK^-\pi^+}$	0.036 ± 0.023
$\mathcal{B}_{\Lambda_c^+\to pK^+K^-}/\mathcal{B}_{\Lambda_c^+\to pK^-\pi^+}$	0.069 ± 0.036
$\mathcal{B}_{\Lambda_c^+\to p\phi}/\mathcal{B}_{\Lambda_c^+\to pK^-\pi^+}$	0.015 ± 0.0032

Table 7.2: Summary of the measurements for the branching fractions of $\Lambda_c^+ \to pX$ decay modes relative to the branching fraction of the decay mode $\Lambda_c^+ \to pK^-\pi^+$, which were available when the analysis work was carried out [11].

where the relative efficiency, $\epsilon_{\Lambda_c^+\to pX}/\epsilon_{\Lambda_c^+\to pK^0}$, of the $\Lambda_b^0 \to p\mu^-\overline{\nu}_\mu$ selection on the two modes is determined from simulation. The ratios of branching fractions, $\mathcal{B}_{\Lambda_c^+\to pX}/\mathcal{B}_{\Lambda_c^+\to pK^0}$, were computed using latest available measurements of $\mathcal{B}_{\Lambda_c^+\to pK^0}/\mathcal{B}_{\Lambda_c^+\to pK^-\pi^+}$ and $\mathcal{B}_{\Lambda_c^+\to pX}/\mathcal{B}_{\Lambda_c^+\to pK^-\pi^+}$ at the time of the analysis, which are shown in table 7.2. For a number of the $\Lambda_c^+ \to pX$ decay modes considered previous measurements of the branching fractions were not available. Predictions for the branching fractions of these modes are taken from default values used by the LHCb experiment for carrying out the simulation of inclusive samples of b-hadron decays.

The fraction, $F_{\Lambda_c^+}$, is determined from a fit to the corrected mass distribution of $pK^-\pi^+\mu^-$ candidates surviving the full $\Lambda_b^0 \to p\mu^-\overline{\nu}_\mu$ selection as shown in Fig.7.5. The yields of $\Lambda_b^0 \to \Lambda_c^{*+}\mu^-\overline{\nu}_\mu$

and $\Lambda_b^0 \to \Lambda_c^+\mu^-\overline{\nu}_\mu$ decays in the fit are found to be respectively, $N_{\Lambda_c^+} = 12864 \pm 270$ and $N_{\Lambda_c^{+*}} = 1473 \pm 253$. From this the fraction,

$$F_{\Lambda_c^+} = \frac{N_{\Lambda_c^+}}{N_{\Lambda_c^+} + N_{\Lambda_c^{+*}}} = 0.897 \pm 0.016 \, , \tag{7.7}$$

and the ratio,

$$R_{\Lambda_c^{*+}} = \frac{N_{\Lambda_c^{*+}}}{N_{\Lambda_c^+}} = 0.115 \pm 0.05 \, , \tag{7.8}$$

are computed. The ratio, $R(\Lambda_c^{*+})$, is used to constrain the background from $\Lambda_b^0 \to \Lambda_c^{*+}\mu^-\overline{\nu}_\mu$ decays to that from $\Lambda_b^0 \to \Lambda_c^+\mu^-\overline{\nu}_\mu$ decays in the final signal fit.

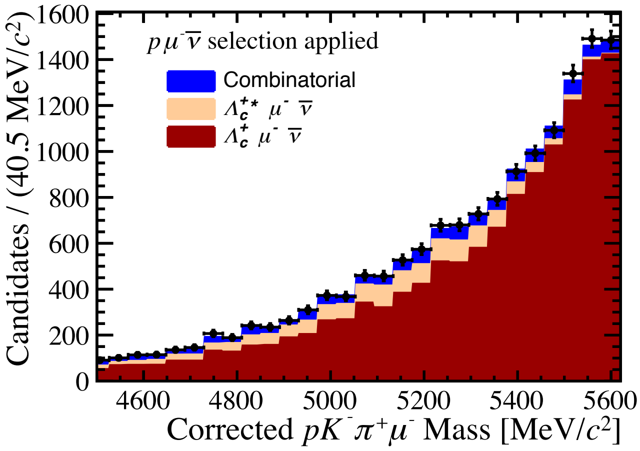

Figure 7.5: Fit to the corrected $pK^-\pi^+\mu^-$ mass distribution for $pK^-\pi^+\mu^-$ candidates surviving the $\Lambda_b^0 \to p\mu^-\overline{\nu}_\mu$ selection.

In a similar way the charged category of $\Lambda_b^0 \to \Lambda_c^+\mu^-\overline{\nu}_\mu$ background is controlled by determining the yield of $\Lambda_b^0 \to (\Lambda_c^+ \to pK^-\pi^+)\mu^-\overline{\nu}_\mu$ decays, expected after the final $\Lambda_b^0 \to p\mu^-\overline{\nu}_\mu$ selection has been applied,

$$N'_{\Lambda_b^0\to(\Lambda_c^+\to pK^-\pi^+)\mu^-\overline{\nu}_\mu} = \frac{N_{\Lambda_b^0\to(\Lambda_c^+\to pK^-\pi^+)\mu^-} F_{\Lambda_c^+}}{\epsilon_{pK^-\pi^+\mu^-|p\mu}} \, , \tag{7.9}$$

where $N_{\Lambda_b^0\to(\Lambda_c^+\to pK^-\pi^+)\mu^-} = 19553 \pm 142$ is the yield for $\Lambda_b^0 \to (\Lambda_c^+ \to pK^-\pi^+)\mu^-$ candidates observed in a fit to the $pK^-\pi^+$ invariant mass, as shown in Fig. 7.6, and $\epsilon_{pK^-\pi^+\mu^-|p\mu} = 4.2 \pm 0.15$ is the corresponding selection efficiency for the $pK^-\pi^+\mu^-$ candidates relative to the efficiency of the $\Lambda_b^0 \to p\mu^-\overline{\nu}_\mu$ selection on $\Lambda_b^0 \to (\Lambda_c^+ \to pK^-\pi^+)\mu^-\overline{\nu}_\mu$ decays. The relative efficiency, $\epsilon_{pK^-\pi^+\mu^-|p\mu}$, is greater than one because for the selected $\Lambda_b^0 \to (\Lambda_c^+ \to pK^-\pi^+)\mu^-$ candidates the maximum isolation BDT is computed ignoring the tracks of the kaon and pion candidates. The yield of a given charged mode, $\Lambda_b^0 \to (\Lambda_c^+ \to pY)\mu^-\overline{\nu}_\mu$, can now be determined as

$$\begin{aligned} N_{\Lambda_b^0\to(\Lambda_c^+\to pY)\mu^-\overline{\nu}_\mu} &= N'_{\Lambda_b^0\to(\Lambda_c^+\to pK^-\pi^+)\mu^-\overline{\nu}_\mu} \cdot \frac{\epsilon_{\Lambda_c^+\to pY}}{\epsilon_{\Lambda_c^+\to pK^-\pi^+}} \cdot \frac{\mathcal{B}_{\Lambda_c^+\to pY}}{\mathcal{B}_{\Lambda_c^+\to pK^-\pi^+}} \\ &= N'_{\Lambda_b^0\to(\Lambda_c^+\to pK^-\pi^+)\mu^-\overline{\nu}_\mu} \cdot R_{\Lambda_c^+\to pY}\ . \end{aligned} \tag{7.10}$$

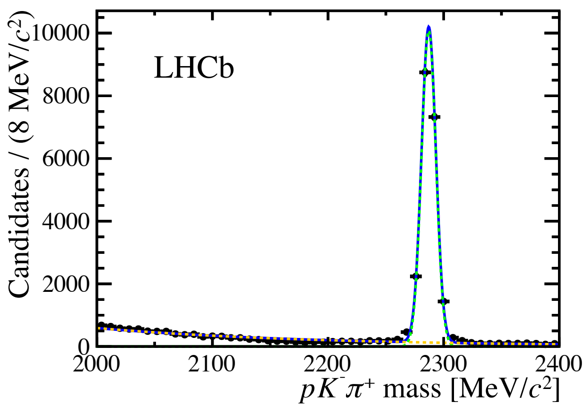

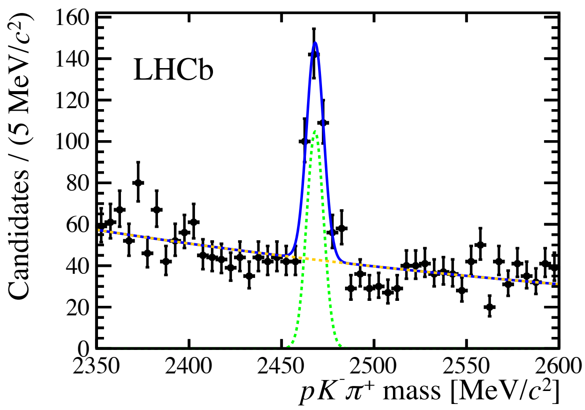

Figure 7.6: Fit to the $pK^-\pi^+$ invariant mass to determine the yield of $\Lambda_b^0 \to (\Lambda_c^+ \to pK^-\pi^+)\mu^-$ candidates (left). Observed $\Xi_c^+ \to pK^-\pi^+$ mass peak in the $pK^-\pi^+$ mass spectrum (right).

A mass peak corresponding to $\Xi_c^+ \to pK^-\pi^+$ decays is observed in the $pK^-\pi^+$ mass spectrum of selected $pK^-\pi^+\mu^-$ candidates as shown in Fig 7.6. This highlights a potential source of background from $\Xi_b \to \Xi_c\mu^-\overline{\nu}_\mu$ and $\Xi_b^- \to \Xi_c^0\mu^-\overline{\nu}_\mu$ decays. A fit to the $\Xi_c^+ \to pK^-\pi^+$ mass peak gives a yield of 244 ± 17, which is about a factor 70 smaller than the yield observed for $\Lambda_b^0 \to (\Lambda_c^+ \to pK^-\pi^+)\mu^-$ candidates, therefore, background from $\Xi_b \to \Xi_c\mu^-\overline{\nu}_\mu$ decays is ignored in the signal fit.

It it possible to use reconstructed $\Lambda_b^0 \to (\Lambda_c^+ \to pK_S^0)\mu^-\overline{\nu}_\mu$ and $\Lambda_b^0 \to (\Lambda_c^+ \to pK^-\pi^+)\mu^-\overline{\nu}_\mu$ decays to validate whether or not the simulation provides a reasonable description of the corrected mass shape of background from $\Lambda_b^0 \to \Lambda_c^+\mu^-\overline{\nu}_\mu$ decays. Fig. 7.7 shows the corrected $p\mu^-$ mass for $\Lambda_b^0 \to (\Lambda_c^+ \to pK_S^0)\mu^-$ candidates with the contribution from non-Λ_c^+ background removed using the *sPlot* technique [1] [81]. The corrected mass shape is compatible with the predicted shape of $\Lambda_b^0 \to (\Lambda_c^+ \to pK_S^0)\mu^-\overline{\nu}_\mu$ and $\Lambda_b^0 \to (\Lambda_c^{*+} \to (\Lambda_c^+ \to pK_S^0)\pi\pi)\mu^-\overline{\nu}_\mu$ decays from simulation.

[1] A statistical method for unfolding the signal distribution for a given variable based on a set of weights obtained from a Likelihood fit to an independent control variable, which is highly discriminating between signal and background.

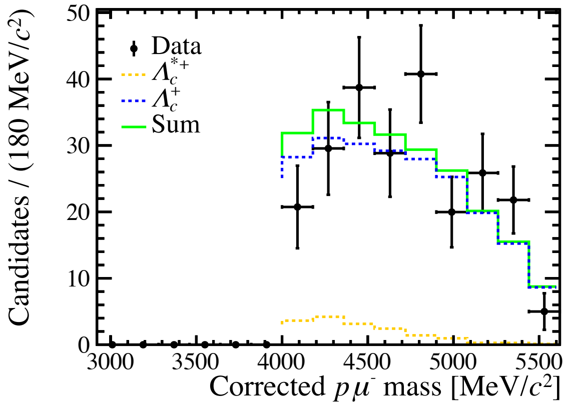

Figure 7.7: Fits to the corrected $p\mu$ mass distributions, left and right, which are obtained using the *sPlot* technique with weights determined from the mass fits in Fig. 7.4(a) and (b), respectively.

Fig 7.8 shows a comparison between the background-subtracted corrected $p\mu^-$ mass distribution of $\Lambda_b^0 \to (\Lambda_c^+ \to pK^-\pi^+)\mu^-\overline{\nu}_\mu$ candidates in data with that of simulated $\Lambda_b^0 \to (\Lambda_c^+ \to pK^-\pi^+)\mu^-\overline{\nu}_\mu$ decays. A poor agreement in the corrected mass shape is seen between data and simulation even after applying corrections for mismodeling of the Λ_b^0 production kinematics and proton PID in simulation. However, the discrepancy is resolved by accounting for the fact that the three-body decay $\Lambda_c^+ \to pK^-\pi^+$ is incorrectly modelled in the simulation. A re-weighting of the Dalitz distribution, $m^2_{pK^-}$-$m^2_{p\pi^+}$, for simulated $\Lambda_b^0 \to \Lambda_c^+\mu^-\overline{\nu}_\mu$ decays to that observed in data (see Fig 7.9) results in a much better agreement between the corrected mass distributions seen in data and simulation as shown in Fig 7.8.

Although it is possible to determine the Dalitz-distribution for $\Lambda_c^+ \to pK^-\pi^+$ decays by reconstructing $\Lambda_b^0 \to (\Lambda_c^+ \to pK^-\pi^+)\mu^-\overline{\nu}_\mu$ decays in data this is not possible for the dominant 3-body neutral modes, $\Lambda_c^+ \to pK^0\pi^0$ and $\Lambda_c^+ \to pK^0\eta$. To handle this, the PDF, $p(m_{\text{corr}})$, describing the corrected $p\mu^-$ mass shape for these backgrounds can be corrected by a second-order polynomial,

$$p'(m_{\text{corr}}) = p(m_{\text{corr}})(1 - s\frac{(m_{\text{corr}} - 4250)^2}{10^6})\ , \tag{7.11}$$

where the potential magnitude of shape variation through the parameter, s, is quantified by fitting the ratio of the corrected mass distribution seen in data to that seen in simulation for $\Lambda_b^0 \to (\Lambda_c^+ \to pK^-\pi^+)\mu^-\overline{\nu}_\mu$ decays as shown in Fig 7.10. For $\Lambda_b^0 \to (\Lambda_c^+ \to pK^-\pi^+)\mu^-\overline{\nu}_\mu$ decays the shape parameter is found to be $s = 0.37 \pm 0.04$.

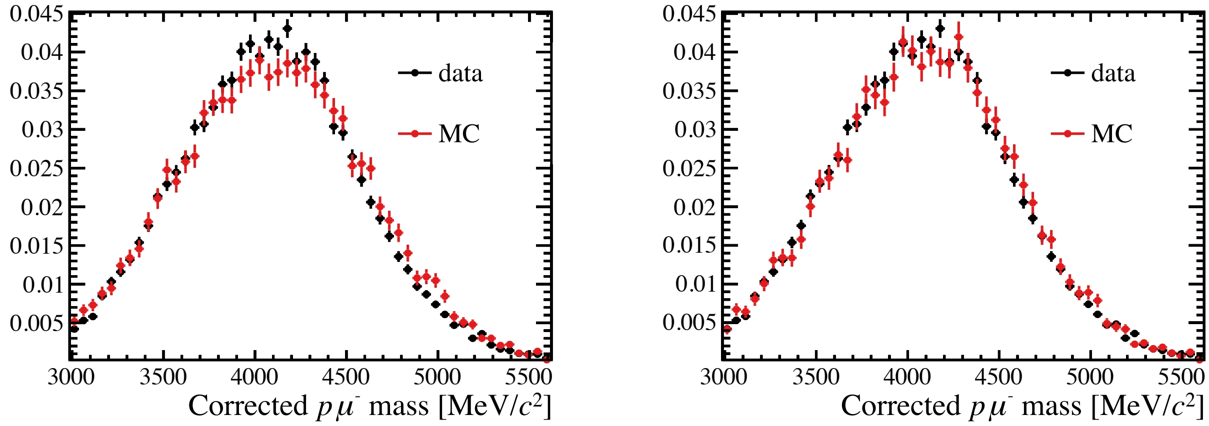

Figure 7.8: A comparison of the corrected $p\mu^-$ mass distributions in data and simulation which is re-weighted to correct for mismodeling of the proton PID and Λ_b^0 baryon kinematics (left). Agreement between data and simulation can be significantly improved by accounting for the mismodeling of the three body $\Lambda_c^+ \to pK^-\pi^+$ decay by re-weighting the Dalitz distribution ($m^2_{K^-\pi^+}$-$m^2_{p\pi^+}$) in simulation to that seen in data.

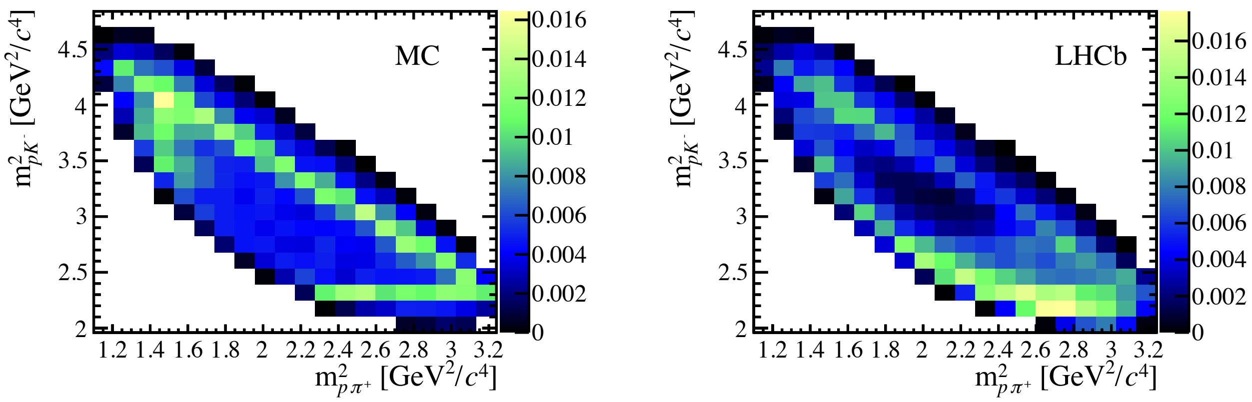

Figure 7.9: Dalitz distributions for $\Lambda_c^+ \to pK^-\pi^+$ normalisation candidates in simulation (left) and data (right).

7.2.2. $\Lambda_b^0 \to D^0 p\mu^-\overline{\nu}_\mu$

The selected $pK^-\pi^+\mu^-$ candidates can be used to constrain background from $\Lambda_b^0 \to D^0 p\mu^-\overline{\nu}_\mu$ decays by searching for the specific mode, $\Lambda_b^0 \to (D^0 \to K^-\pi^+)p\mu^-\overline{\nu}_\mu$. Fig 7.11 shows a fit to the observed $D^0 \to K^-\pi^+$ mass peak, which is used to determine the yield of $\Lambda_b^0 \to (D^0 \to K^-\pi^+)p\mu^-$ candidates, $N_{\Lambda_b^0\to(D^0\to K^-\pi^+)p\mu^-} = 580 \pm 45$. The yield of background from $\Lambda_b^0 \to D^0 p\mu^-\overline{\nu}_\mu$ decays is

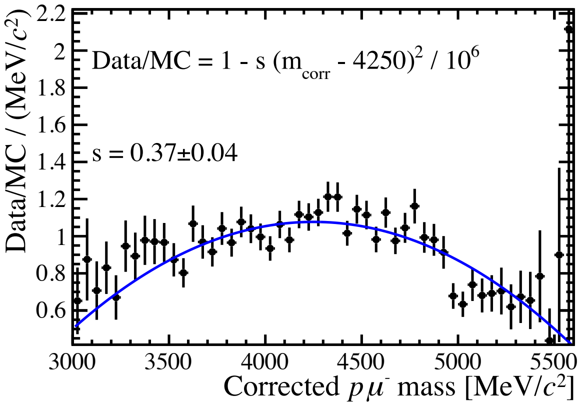

Figure 7.10: Ratio of the corrected $p\mu^-$ mass distribution of $\Lambda_b^0 \to (\Lambda_c^+ \to pK^-\pi^+)\mu^-\overline{\nu}_\mu$ candidates observed in data to that of simulated $\Lambda_b^0 \to \Lambda_c^+\mu^-\overline{\nu}_\mu$ decays.

computed using the expression

$$N_{\Lambda_b^0\to D^0 p\mu^-\overline{\nu}_\mu} = \frac{N_{\Lambda_b^0\to(D^0\to K^-\pi^+)p\mu^-}}{\epsilon_{\Lambda_b^0\to(D^0\to K^-\pi^+)p\mu^-|p\mu}} = 17294 \pm 2351\ , \tag{7.12}$$

where, $\epsilon_{\Lambda_b^0\to(D^0\to K^-\pi^+)p\mu^-|p\mu} = 0.034 \pm 0.008$, is the efficiency of selecting $\Lambda_b^0 \to (D^0 \to K^-\pi^+)p\mu^-$ candidates relative to the efficiency of the $\Lambda_b^0 \to p\mu^-\overline{\nu}_\mu$ selection on $\Lambda_b^0 \to D^0 p\mu^-\overline{\nu}_\mu$ decays as determined using simulation.

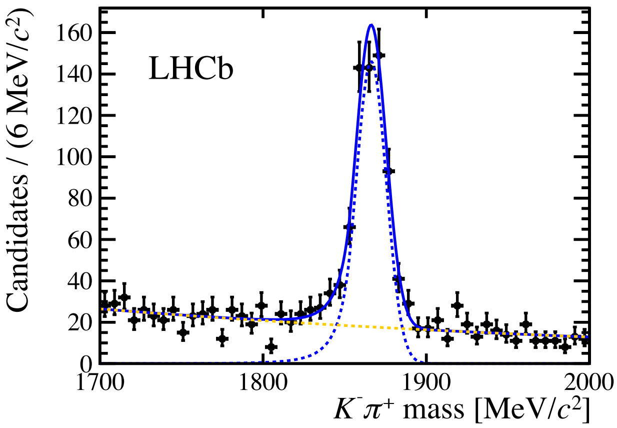

Figure 7.11: Fit to the $K^-\pi^+$ invariant mass to determine the yield of $\Lambda_b^0 \to D^0 p\mu^-\overline{\nu}_\mu$ decays.

7.2.3. Mis-ID

The normalisation and corrected mass shape of the background from kaons and pions which are misidentified as protons ($K/\pi \to p$ mis-ID) is obtained using a small sample of data ($\mathcal{L} \sim 6.7\,\mathrm{pb}^{-1}$) in which no proton identification selection is made.

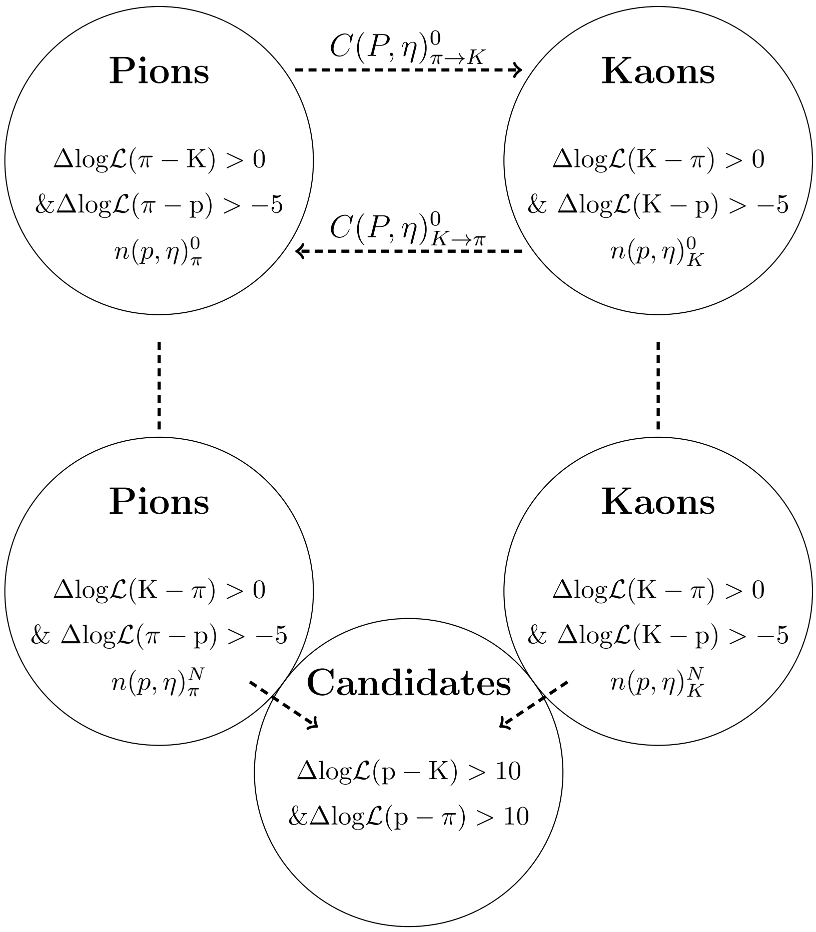

Figure 7.12: Diagram illustrating the iterative procedure used to derive the mis-ID from $K \to p$ and $\pi \to p$.

Subsets within the sample enriched in kaons (pions) are selected by requiring that the hadron candidate satisfies $\Delta\log\mathcal{L}(\mathrm{K}-\pi) > 0$ and $\Delta\log\mathcal{L}(\mathrm{K}-\mathrm{p}) > 0$ ($\Delta\log\mathcal{L}(\pi-\mathrm{K}) > 0$ and $\Delta\log\mathcal{L}(\mathrm{p}-\pi) > 0$). Under the first order assumption that the kaon (pion) subsample contains purely kaons (pions) the kinematic distribution, $n(P,\eta)^0_{K/\pi}$, of kaons (pions) in the full sample can be determined according to

$$n(P,\eta)^0_{\pi/K} = \frac{N(P,\eta)_{\pi/K}}{\epsilon(P,\eta)_{\pi/K}} \ , \tag{7.13}$$

where, $N(P,\eta)^0_{K/\pi}$, is the kinematic distribution of kaons/pions found within the kaon/pion subsamples and, $\epsilon(P,\eta)_{K/\pi}$, is the efficiency of the PID selection made for the kaons/pions as a function of the particle kinematics. The efficiency and mis-ID rates associated with PID selections also depend on the track multiplicity, T. This dependence is integrated out using the equation

$$\epsilon(P,\eta)_{\pi/K} = \int \epsilon(P,\eta,T)_{\pi/K}\hat{n}(T)^0_{\pi/K}dT \ , \tag{7.14}$$

where $\hat{n}(T)_{\pi/K}$ is the normalised track multiplicity distribution for events in the pion/kaon subsamples.

In reality the kaon and pion enriched samples will have some contamination from other hadron species. Given the small percentage ($\sim 3\%$) of $h\mu$ candidates, for which the hadron, h, will be a proton, contamination from protons is ignored. On the other hand, contamination from kaons and pions into the pion and kaon enriched regions, respectively, is likely to be significant. This is handled using an iterative procedure as illustrated in Fig 7.12. The kinematic distributions for kaons and pions are first determined from their respective enriched subsamples assuming no contamination as $n(P,\eta)^0_{K/\pi}$. Subsequently, the kinematic distributions are used to determine the expected contaminations, $C(P,\eta)^0_{K\to\pi} = M(P,\eta)_{K\to\pi}n(P,\eta)^0_K$ and $C(P,\eta)^0_{\pi\to K} = M(P,\eta)_{\pi\to K}n(P,\eta)^0_\pi$, of kaons and pions into the pion and kaon enriched subsamples, respectively. Here, $M(P,\eta)_{K\to\pi}$ and $M(P,\eta)_{\pi\to K}$ are the $K\to\pi$ and $\pi\to K$ mis-ID rates.

The next order kinematic distributions for kaons and pions, $n(P,\eta)^{i+1}_{K/\pi}$, are obtained by correcting the original $N(P,\eta)^i_{K/\pi}$ distributions for the estimated contamination from pions and kaons, respectively, and then dividing by the PID efficiencies, $\epsilon(P,\eta)_{K/\pi}$. This procedure can be summarised by the following update equations for $n(P,\eta)^{i+1}_{K/\pi}$:

$$n(P,\eta)^{i+1}_\pi = \frac{N(P,\eta)_\pi - M(P,\eta)_{K\to\pi}n(P,\eta)^i_K}{\epsilon(P,\eta)_\pi} \ , \tag{7.15}$$

and,

$$n(P,\eta)^{i+1}_K = \frac{N(P,\eta)_K - M(P,\eta)_{\pi\to K}n(P,\eta)^i_\pi}{\epsilon(P,\eta)_K} \ . \tag{7.16}$$

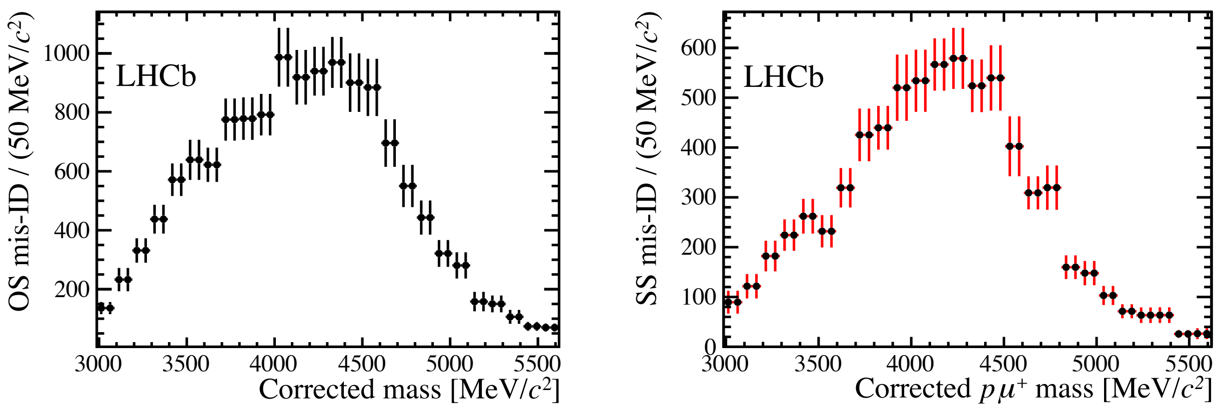

Figure 7.13: Estimated amount of opposite-sign (left) and same-sign (right) $K \to p$ and $\pi \to p$ mis-ID in bins of corrected mass. The mis-ID estimation is performed in 26 bins due to the limited statistics. Meanwhile, the final signal fit has 52 bins as used above.

At each iteration the mis-ID of $K \to p$ and $\pi \to p$ are given by

$$\int\int n(P,\eta)^i_{K/\pi} M(P,\eta)_{K/\pi\to p} dP d\eta \ , \tag{7.17}$$

where $M(P,\eta)_{K/\pi\to p}$ is the $K/\pi \to p$ mis-ID rate. The iterative procedure is carried out in bins of corrected $p\mu$ mass until convergence. This allows for the $K \to p$ and $\pi \to p$ mis-ID to be computed in each bin of corrected mass. The criteria for convergence is when there is no change greater than 0.1% in the total $K \to p$ and $\pi \to p$ mis-ID for any given bin between iterations.

In order to evaluate the errors on the total $K/\pi \to p$ mis-ID a Monte Carlo based approach is taken. Gaussian variations are made on the PID efficiencies and mis-ID rates, meanwhile, Poissonian variations are made on the starting kinematic distributions, $N(P,\eta)_{K/\pi}$. The uncertainty on the estimated $K \to p$ and $\pi \to p$ mis-ID in a given bin of corrected mass is calculated by computing the standard deviation on the $K \to p$ and $\pi \to p$ mis-ID estimated when using a number of the generated variations of the efficiencies, mis-ID rates and starting kinematic distributions.

Fig. 7.13 shows the corrected mass distributions for $K \to p$ and $\pi \to p$ opposite-sign and same-sign mis-ID, which are obtained using the iterative procedure outlined above. The integrals of these distributions give the total opposite-sign and same-sign mis-ID as, $N_{\text{mis-ID}} = 27533 \pm 3036$ and $N_{\text{SS mis-ID}} = 14503 \pm 1887$, respectively. The same-sign mis-ID background is used in the determination of the combinatorial background as described in the next section.

7.2.4. Combinatorial background

The combinatorial background shape is obtained by subtracting the estimated $K \to p$ and $\pi \to p$ same-sign mis-ID from the number of observed same-sign $p\mu$ candidates in bins of corrected mass. Fig. 7.14 shows the resulting combinatorial background shape. The combinatorial yield is taken as the integral of this distribution, $N_{\text{comb}} = 21833 \pm 2319$.

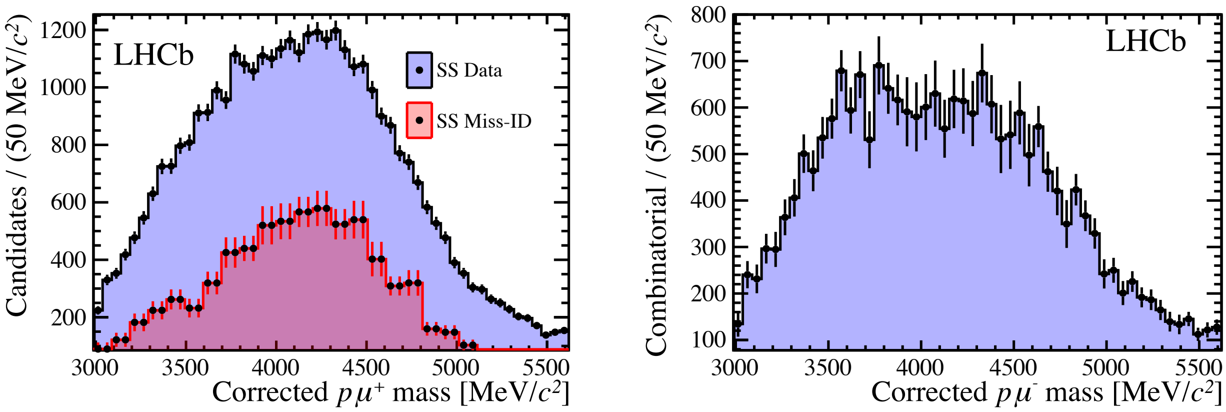

Figure 7.14: Corrected mass distribution for same-sign $p\mu^+$ candidates overlaid with the estimated same-sign mis-ID from $K \to p$ and $\pi \to p$ (left). Combinatorial background shape obtained from subtracting the estimated same-sign mis-ID from the number of same-sign $p\mu^+$ candidates in bins of corrected mass (right).

In order to validate the assumption that the opposite-sign and same-sign $p\mu$ combinatorial backgrounds have a similar corrected mass shape, opposite-sign and same-sign candidates above the Λ_b^0 mass in corrected mass are examined with no q^2 selection applied. Fig.7.15 shows the corrected mass of these candidates. The number of opposite-sign and same-sign candidates with a corrected mass above the Λ_b^0 mass are respectively 8577 and 8216. The ratio, $R_{\text{comb}} = N_{\text{OS}}/N_{\text{SS}} = 1.04 \pm 0.02$, is 4% different from unity; this difference can be accommodated by the uncertainty on the combinatorial background yield of $\sim$11%.

Throughout the discussion above, it is assumed that same-sign $p\mu$ combinations are dominated by combinatorial background. This is a good assumption as most non-combinatorial $p\mu^+$ background will primarily come from the decay of Λ_b^0 baryons which by charge conservation means there will be at least two additional charged tracks from the decay. These backgrounds are therefore significantly reduced by the isolation BDT selection criteria. In addition, one of the major sources of such same-sign $p\mu$ combinations is decays of the form $\Lambda_b^0 \to pJ/\psi X$ which will be selected equally

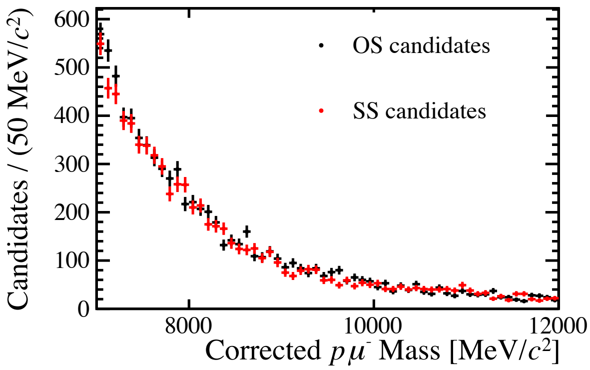

Figure 7.15: A comparison of the corrected mass above the Λ_b^0 mass in data for opposite-sign and same-sign $p\mu$ candidates (no q^2 selection is applied).

in both opposite-sign and same-sign $p\mu$ samples. The combinatorial background shape thereby naturally also accounts for any $\Lambda_b^0 \to pJ/\psi X$ decays surviving the isolation requirement.

7.3. Signal fit

7.3.1. Signal fit model

The signal fit is carried out using the same fit procedure as that for the normalisation fit, which is described in section 7.1.1. The expected number of events in the i^{th} bin of corrected mass is given by

$$\begin{aligned} n^i_{\text{sig. model}}(\vec{k}) =& n^i_{\Lambda_c^+\ \text{neutral}}(\vec{k}_{\Lambda_c^+\ \text{neutral}}) + n^i_{\Lambda_c^+\ \text{charged}}(\vec{k}_{\Lambda_c^+\ \text{charged}}) + n^i_{N^{*+}}(\vec{k}_{N^{*+}}) + n^i_{\Lambda_c^{*+}}(R_{\Lambda_c^{*+}}, \vec{k}_{\Lambda_c^+}) \\ &+ N_{\text{comb}} \cdot p^i_{\text{comb}} + N_{\text{mis-ID}} \cdot p^i_{\text{mis-ID.}} + N_{D^0} \cdot p^i_{D^0} + N_{\Lambda_b^0\to p\mu^-\overline{\nu}_\mu} \cdot p^i_{\Lambda_b^0\to p\mu^-\overline{\nu}_\mu}\ , \end{aligned} \tag{7.18}$$

where p^i_X and N_X are the PDF and yield associated with background X. The vectors $\vec{k}_{\Lambda_c^+\ \text{neutral}}$, $\vec{k}_{\Lambda_c^+\text{charged}}$ and $\vec{k}_{\Lambda_c^+} = (\vec{k}_{\Lambda_c^+\ \text{neutral}}, \vec{k}_{\Lambda_c^+\text{charged}})$ are subsets of the vector $\vec{k}$, which contain the free parameters relating to the neutral and charged categories of background from $\Lambda_b^0 \to \Lambda_c^+\mu^-\overline{\nu}_\mu$ decays. The number of expected candidates from the neutral and charged categories of $\Lambda_b^0 \to \Lambda_c^+\mu^-\overline{\nu}_\mu$

background decays are respectively given by

$$\begin{aligned} n^i_{\Lambda_c^+\ \mathrm{neutral}}(\vec{k}_{\Lambda_c^+\ \mathrm{neutral}}) =& N_{\Lambda_b^0\to(\Lambda_c^+\to pK^0)\mu^-\overline{\nu}_\mu}\times \\ & \left[p^i_{\Lambda_c^+\to pK^0} + \sum_X R_{\Lambda_c^+\to pX}\cdot p_{\Lambda_c^+\to pX}\right] , \end{aligned} \tag{7.19}$$

and

$$\begin{aligned} n^i_{\Lambda_c^+\mathrm{charged}}(\vec{k}_{\Lambda_c^+\mathrm{charged}}) =& N'_{\Lambda_b^0\to(\Lambda_c^+\to pK^-\pi^+)\mu^-\overline{\nu}_\mu}\times \\ & \left[p^i_{\Lambda_c^+\to pK^-\pi^+} + \sum_Y R_{\Lambda_c^+\to pY}\cdot p_{\Lambda_c^+\to pY}\right] , \end{aligned} \tag{7.20}$$

where X and Y respectively denote neutral and charged modes and $R_{\Lambda_c^+\to pX}$ and $R_{\Lambda_c^+\to pX}$ are defined in equation 7.6 and 7.10 of section 7.2.1. Meanwhile, $N_{\Lambda_b^0\to(\Lambda_c^+\to pK^0)\mu^-\overline{\nu}_\mu}$ and $N'_{\Lambda_b^0\to(\Lambda_c^+\to pK^-\pi^+)\mu^-\overline{\nu}_\mu}$ are the expected yields of $\Lambda_b^0\to(\Lambda_c^+\to pK^0)\mu^-\overline{\nu}_\mu$ and $\Lambda_b^0\to(\Lambda_c^+\to pK^-\pi^+)\mu^-\overline{\nu}_\mu$ decays which were measured in section 7.2.1.

The number of expected candidates from $\Lambda_b^0\to(\Lambda_c^{*+}\to(\Lambda_c^+\to pX)\pi\pi)\mu^-\overline{\nu}_\mu$ decays is constrained to the background from $\Lambda_b^0\to\Lambda_c^+\mu^-\overline{\nu}_\mu$ decays using the parameter $R_{\Lambda_c^{*+}}$ as

$$\begin{aligned} n^i_{\Lambda_c^{*+}}(R_{\Lambda_c^{*+}},\vec{k}_{\Lambda_c^+}) =& R_{\Lambda_c^{*+}}\times \\ & \Bigg[N_{\Lambda_b^0\to(\Lambda_c^+\to pK^0)\mu^-\overline{\nu}_\mu}\times\left[p^i_{\Lambda_c^{*+}\to(\Lambda_c^+\to pK^0)\pi\pi} + \sum_X R_{\Lambda_c^+\to pX}\cdot p_{\Lambda_c^{*+}\to(\Lambda_c^+\to pX)\pi\pi}\right] \\ & + N'_{\Lambda_b^0\to(\Lambda_c^+\to pK^-\pi^+)\mu^-\overline{\nu}_\mu}\times\left[p^i_{\Lambda_c^{*+}\to(\Lambda_c^+\to pK^-\pi^+)\pi\pi} + \sum_Y R_{\Lambda_c^+\to pY}\cdot p_{\Lambda_c^{*+}\to(\Lambda_c^+\to pY)\pi\pi}\right]\Bigg] . \end{aligned} \tag{7.21}$$

The final fit component is the background expected from $\Lambda_b^0\to N^{*+}\mu^-\overline{\nu}_\mu$ decays which is given by

$$n^i_{N^{*+}}(\vec{k}_{N^{*+}}) = N_{\Lambda_b^0\to p\mu^-\overline{\nu}_\mu}\times\sum_Z R_{\Lambda_b^0\to N^+(Z)\mu^-\overline{\nu}_\mu}\cdot p^i_{\Lambda_b^0\to N^+(Z)\mu^-\overline{\nu}_\mu} , \tag{7.22}$$

where here $Z=\{1440,1520,1535,1720\}$ and $R_{\Lambda_b^0\to N^+(Z)\mu^-\overline{\nu}_\mu}$ is the ratio of the branching fractions $\mathcal{B}_{\Lambda_b^0\to N^+(Z)\mu^-\overline{\nu}_\mu}/\mathcal{B}_{\Lambda_b^0\to p\mu^-\overline{\nu}_\mu}$ as predicted by the quark model of Pervin et al. [73]. The ratios $R_{\Lambda_b^0\to N^+(Z)\mu^-\overline{\nu}_\mu}$ are given a large freedom in the fit.

In total, the fit model depends on twenty-seven fit parameters,

$$\vec{k} = \left\{ \vec{k}_{\Lambda_c^+\ \mathrm{neutral}}, \vec{k}_{\Lambda_c^+\ \mathrm{charged}}, \vec{k}_{N^{*+}}, R_{\Lambda_c^{*+}}, N_{\mathrm{comb}}, N_{\text{mis-ID}}, N_{D^0}, s_{\Lambda_c^+\to pK^0\pi^0}, s_{\Lambda_c^+\to pK^0 eta}, N_{\Lambda_b^0\to p\mu^-\overline{\nu}_\mu} \right\} , \tag{7.23}$$

all of which are constrained apart from the signal yield, $N_{\Lambda_b^0\to p\mu^-\overline{\nu}_\mu}$. Table 7.3 shows all constrained fit parameters entering the fit together with the mean and standard deviation of the associated Gaussian constraints.

Parameter	Constraint ($\mu \pm \sigma$)	Reference	Fit value	Pull
$N_{\Lambda_b^0\to(\Lambda_c^+\to pK_0)\mu^-\overline{\nu}_\mu}$	30042 ± 4614	Tab. 7.1	33704 ± 2532	
$R_{\Lambda_c^+\to pK^0\eta}$	0.97 ± 0.18	Eq. 7.6	1.14 ± 0.18	
$R_{\Lambda_c^+\to pK^0\pi^0}$	2.68 ± 0.39	Eq. 7.6	3.07 ± 0.34	
$R_{\Lambda_c^+\to p\pi^0}$	0.069 ± 0.069	Eq. 7.6	0.038 ± 0.074	
$R_{\Lambda_c^+\to p\eta}$	0.030 ± 0.030	Eq. 7.6	0.012 ± 0.030	
$R_{\Lambda_c^+\to p\eta'}$	0.015 ± 0.015	Eq. 7.6	0.013 ± 0.015	
$R_{\Lambda_c^+\to\Delta^+\pi^0}$	0.042 ± 0.042	Eq. 7.6	0.040 ± 0.043	
$N'_{\Lambda_b^0\to(\Lambda_c^+\to pK^-\pi^+)\mu^-\overline{\nu}_\mu}$	4182 ± 175	Eq. 7.9	4197 ± 175	
$N_{\Lambda_b^0\to D^0 p\mu^-\overline{\nu}_\mu}$	17294 ± 2351	Eq. 7.12	17192 ± 2354	
N_{comb}	21833 ± 2319	Sec. 7.2.4	23176 ± 2333	
$N_{\text{mis-ID}}$	27533 ± 2036	Sec. 7.2.3	30955 ± 3071	
$R_{N(1440)^+}$	0.64 ± 0.64	Eq. 7.22	1.23 ± 0.40	
$R_{N(1520)^+}$	0.34 ± 0.34	Eq. 7.22	-0.25 ± 0.29	
$R_{N(1535)^+}$	0.31 ± 0.31	Eq. 7.22	0.028 ± 0.25	
$R_{N(1720)^+}$	0.23 ± 0.23	Eq. 7.22	0.39 ± 0.22	
$R_{\Lambda_c^+\to pK^0\pi^+\pi^-}$	0.70 ± 0.08	Eq. 7.10	0.70 ± 0.08	
$R_{\Lambda_c^+\to pK^-\pi^+\pi^0}$	0.59 ± 0.1	Eq. 7.10	0.60 ± 0.10	
$R_{\Lambda_c^+\to pK^{*-}\pi^+}$	0.24 ± 0.16	Eq. 7.10	0.28 ± 0.16	
$R_{\Lambda_c^+\to p\pi^+\pi^-}$	0.15 ± 0.08	Eq. 7.10	0.17 ± 0.08	
$R_{\Lambda_c^+\to pK^-\pi^+\pi^0\pi^0}$	0.61 ± 0.1	Eq. 7.10	0.59 ± 0.10	
$R_{\Lambda_c^+\to\text{other}}$	1.07 ± 1.07	Eq. 7.10	1.52 ± 1.06	
$R_{\Lambda_c^{+*}}$	0.115 ± 0.02	Eq. 7.8	0.119 ± 0.020	
$R_{\Lambda_c^+\to\Delta^+\eta}$	0.036 ± 0.036	Eq. 7.6	0.043 ± 0.032	
$R_{\Lambda_c^+\to\Delta^+\eta'}$	0.013 ± 0.013	Eq. 7.6	0.017 ± 0.013	
$s_{\Lambda_c^+\to pK^0\pi^0}$	0.4 ± 0.4	Eq. 7.11	0.37 ± 0.13	
$s_{\Lambda_c^+\to pK^0\eta}$	0.4 ± 0.4	Eq. 7.11	0.13 ± 0.34	

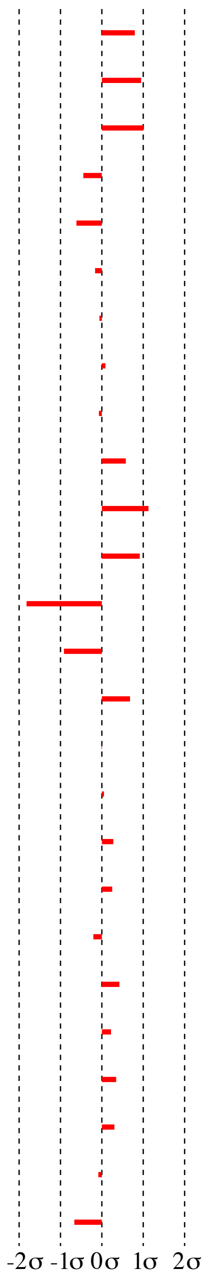

Table 7.3: A summary of the constraints, fit values and associated pulls for parameters entering the fit.

A Monte Carlo approach is used to confirm that the fit's signal yield, $N_{\Lambda_b^0\to p\mu^-\overline{\nu}_\mu}$, and the associated uncertainty on this are unbiased estimators. Pseudo-datasets are generated by assuming a fixed signal yield, $N^{\text{true}}_{\Lambda_b^0\to p\mu^-\overline{\nu}_\mu} = 17,500$, and generating all other fit parameters with Gaussian

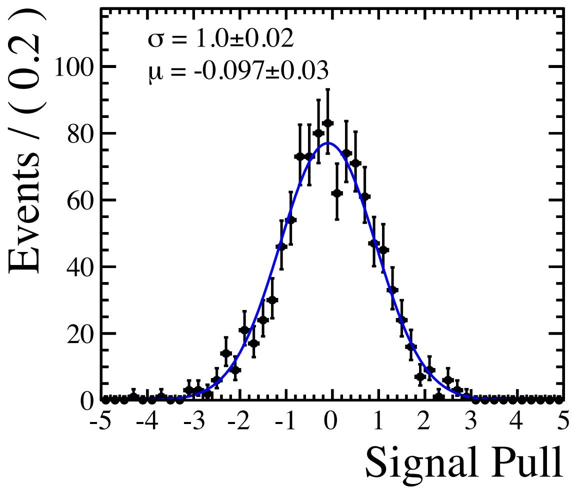

Figure 7.16: Pull distribution for the signal yield resulting from fits to a thousand pseudo-datasets.

variations according to their associated constraints. Fig. 7.16 shows the corresponding pull distribution for the signal yield when carrying out the signal fit on a thousand of these generated pseudo-datasets. The pull distribution exhibits Gaussian behaviour with a mean, $\mu = -0.097 \pm 0.03$, and $\sigma = 1.0 \pm 0.02$.

7.3.2. Signal fit shapes

The discrete PDFs, p_X^i, which describe the shape in corrected mass of various signal and background processes are taken as normalised histograms as determined from simulation or estimated in data for the case of the combinatorial and mis-ID backgrounds (see Fig. 7.13 and Fig. 7.14). Fig. 7.17 demonstrates the separation between the signal corrected mass shape and that of a number of backgrounds considered in the fit. All of the corrected mass shapes used in the fit are fixed in shape apart from those describing the two most dominant background decays, $\Lambda_b^0 \to (\Lambda_c^+ \to pK^0\pi^0)\mu^-\overline{\nu}_\mu$ and $\Lambda_b^0 \to (\Lambda_c^+ \to pK^0\eta)\mu^-\overline{\nu}_\mu$. The shape of these backgrounds are allowed polynomial variations parametrised by shape parameters, $s_{\Lambda_c^+\to pK^0\pi^0}$ and $s_{\Lambda_c^+\to pK^0 eta}$, as defined in equation 7.11 and illustrated in Fig 7.18.

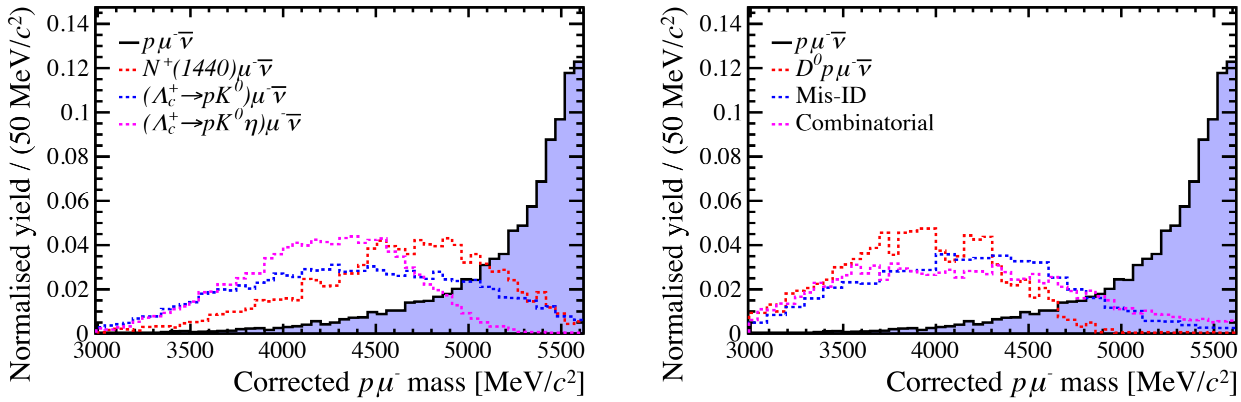

Figure 7.17: A comparison of the corrected mass shape for $\Lambda_b^0 \to p\mu^-\overline{\nu}_\mu$ decays to that of a number of backgrounds.

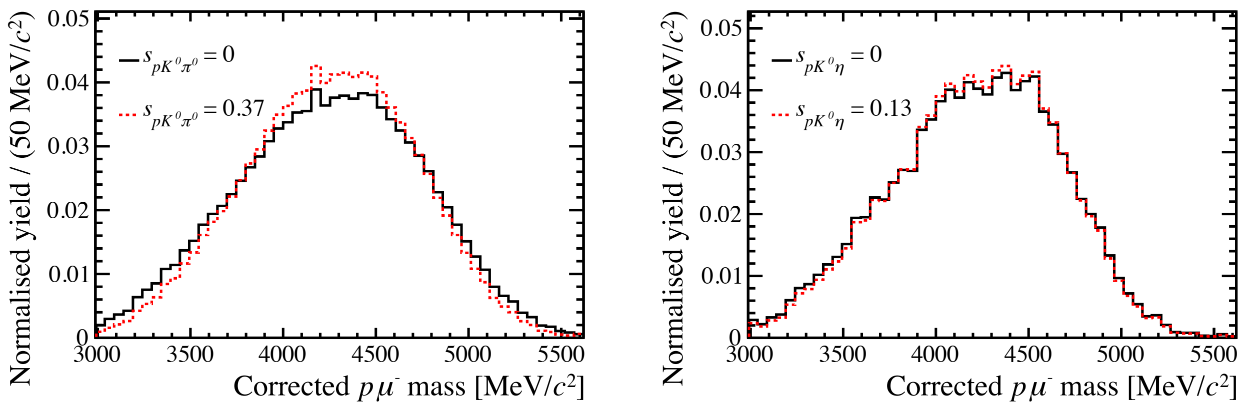

Figure 7.18: Corrected mass shape for $\Lambda_b^0 \to (\Lambda_c^+ \to pK^0\pi^0)\mu^-\overline{\nu}_\mu$ (left) and $\Lambda_b^0 \to (\Lambda_c^+ \to pK^0\eta)\mu^-\overline{\nu}_\mu$ (right) decays before and after the fit. This reflects the allowed freedom in the shapes through the polynomial shape parameters, $s_{\Lambda_c^+\to pK^0\pi^0}$ and $s_{\Lambda_c^+\to pK^0\eta}$.

7.3.3. Signal fit result

The final fit to the corrected $p\mu^-$mass is shown in Fig. 7.19. The observed number of $\Lambda_b^0 \to p\mu^-\overline{\nu}_\mu$ candidates is $N_{\Lambda_b^0\to p\mu^-\overline{\nu}_\mu} = 17,687 \pm 733$. The final values of all other fit parameters and the pulls of these from the mean values of their associated Gaussian constraints are shown in Table 7.3. The minimised χ^2 for the fit is 94.3, while the number of degrees of freedom is 78 which gives, $\chi^2/n_{\rm d.o.f} = 1.22$; the associated p-value for obtaining this result is 0.1.

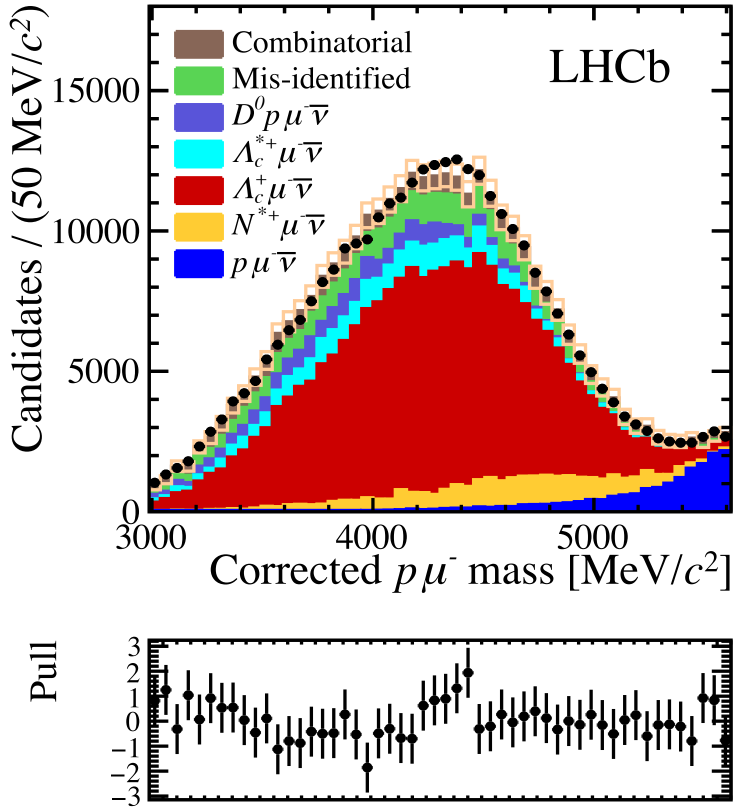

Figure 7.19: Fit to the $p\mu^-$ corrected mass of candidates surviving the signal selection. The yellow boxes display the uncertainty on the fit model's predicted number of events, $n^i_{\text{sig. model}}$, which arises from the statistical uncertainty associated with finite simulation samples.

The only shape in corrected mass that rises towards the endpoint of the Λ_b^0 mass is the shape of $\Lambda_b^0 \to p\mu^-\overline{\nu}_\mu$ decays. This fit shape is clearly necessary to describe the rising structure seen in data in the high corrected mass region. This is the discovery of $\Lambda_b^0 \to p\mu^-\overline{\nu}_\mu$ decays and first observation of a semileptonic $b \to u$ transition at a hadron collider.

7.3.4. Signal fit systematics

The uncertainty on the signal fit yield incorporates a number of systematic effects relating to the modelling of background decays through the freedom for background yields and the two neutral Λ_c^+ shape parameters to vary. However, the signal fit does not account for any possible variations in the corrected mass shapes associated with varying the form factors of the background and signal decays. Fig. 7.20 shows the impact on the corrected mas shape of varying the form factors of

$\Lambda_b^0 \to \Lambda_c^+\mu^-\overline{\nu}_\mu$ and $\Lambda_b^0 \to p\mu^-\overline{\nu}_\mu$ decays within their associated LQCD uncertainties. The variation in the shape is small and, therefore, its impact on the signal yield is neglected. On the other hand, for $\Lambda_b^0 \to N^{*+}\mu^-\overline{\nu}_\mu$ decays the uncertainty on the form factors is taken to be much larger; this results in significant variations in the corrected $p\mu^-$mass shape as shown in Fig. 7.20(c).

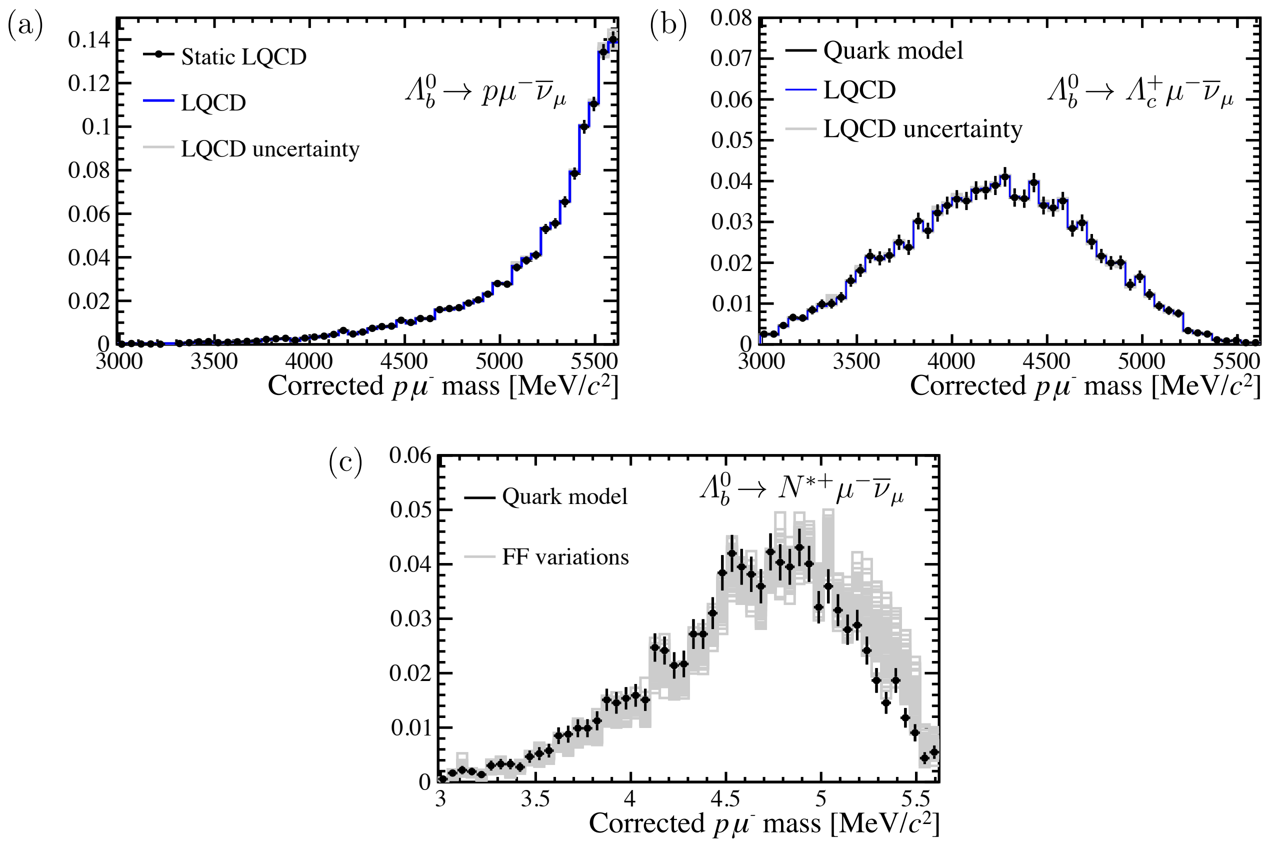

Figure 7.20: Corrected $p\mu^-$ mass distribution of simulated $\Lambda_b^0 \to p\mu^-\overline{\nu}_\mu$ (a) and $\Lambda_b^0 \to \Lambda_c^+\mu^-\overline{\nu}_\mu$ (b) decays before and after re-weighting to the relativistic LQCD predictions. Meanwhile, (c) shows the corrected $p\mu^-$ mass distribution for simulated $\Lambda_b^0 \to N^{*+}\mu^-\overline{\nu}_\mu$ decays before and after re-weighting according to large Gaussian variations on the form factor parameters.

The impact of possible variations in the form factors of $\Lambda_b^0 \to N^{*+}\mu^-\overline{\nu}_\mu$ decays on the signal yield is taken as a systematic. This systematic is computed by carrying out fits with the nominal fit model to pseudo-datasets, where each separate dataset is generated using independent variations of the form factors of the considered $\Lambda_b^0 \to N^{*+}\mu^-\overline{\nu}_\mu$ decays. Fig. 7.21 compares the distribution of signal yields resulting from fits to pseudo-datasets generated with and without the $\Lambda_b^0 \to N^{*+}\mu^-\overline{\nu}_\mu$ form factor variations. The systematic is taken as the difference in quadrature of the standard deviations of the distributions divided by the true signal yield; this results in a systematic of 2.2% on the signal yield.

The final systematic effect considered is the poor knowledge of the widths of the N^{*+} states. This is quantified by obtaining the corrected mass shape of $\Lambda_b^0 \to N^{*+}\mu^-\overline{\nu}_\mu$ decays when re-weighting the N^{*+} mass shape to a number of Breit-wigner mass shapes of varying widths. The widths are drawn from a Gaussian with a mean taken as the PDG quoted width and a standard deviation of 50 MeV. The impact of the shape variation on the signal yield is again determined using fits to pseudo-datasets, which leads to a systematic of 0.7% on the signal yield.

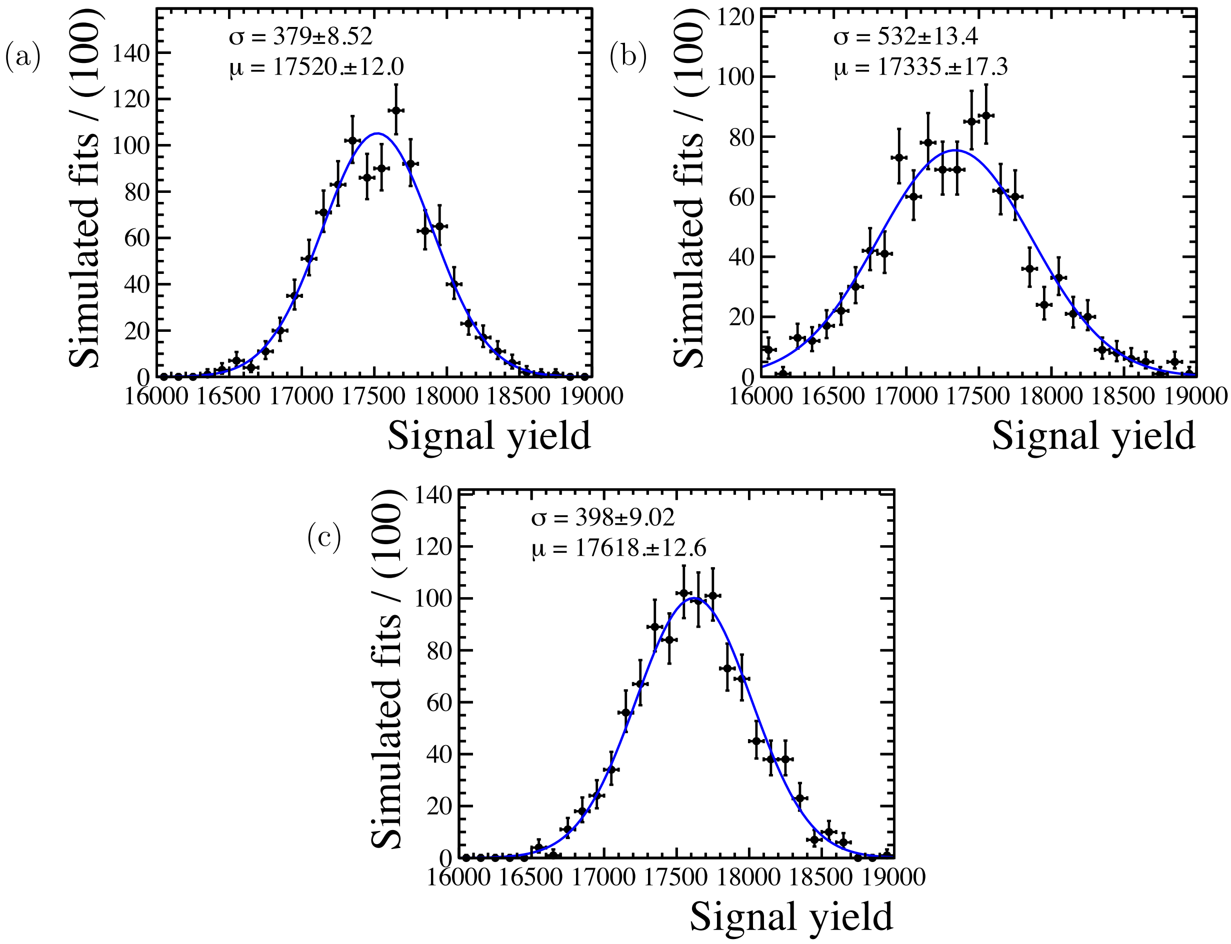

Figure 7.21: (a) Distribution of the signal yield from fits to a thousand pseudo-datasets generated with the nominal fit model. Meanwhile, (b) and (c) show the distribution in the signal yields when fitting pseudo-datasets generated with variations in the $\Lambda_b^0 \to N^{*+}\mu^-\overline{\nu}_\mu$ form factors and widths, respectively.

7.4. Relative Efficiency

7.4.1. Relative efficiency calculation

In order to convert the ratio of $\Lambda_b^0 \to p\mu^-\overline{\nu}_\mu$ and $\Lambda_b^0 \to \Lambda_c^+\mu^-\overline{\nu}_\mu$ yields into a branching fraction measurement, the relative efficiency for selecting these decays in the relevant q^2 regions ($q^2 > 15\,\mathrm{GeV}^2/c^4$ and $q^2 > 7\,\mathrm{GeV}^2/c^4$) is required.

The relative efficiency is determined from simulation after having applied the required q^2 selections using the following expression,

$$\begin{aligned}\epsilon_{rel} =& 2 \cdot \frac{\epsilon_{\mathrm{gen}|\Lambda_b^0\to p\mu^-\overline{\nu}_\mu}}{\epsilon_{\mathrm{gen}|\Lambda_b^0\to\Lambda_c^+\mu^-\overline{\nu}_\mu}} \cdot \frac{\epsilon_{\mathrm{presel|gen\&}\Lambda_b^0\to p\mu^-\overline{\nu}_\mu}}{\epsilon_{\mathrm{presel|gen\&}\Lambda_b^0\to\Lambda_c^+\mu^-\overline{\nu}_\mu}} \cdot \epsilon_{m_{\mathrm{corr}}\mathrm{error|presel}} \cdot \frac{\epsilon_{\mathrm{iso|presel\&m_{corr}error\&}\Lambda_b^0\to p\mu^-\overline{\nu}_\mu}}{\epsilon_{\mathrm{iso|presel\&}\Lambda_b^0\to\Lambda_c^+\mu^-\overline{\nu}_\mu}} \\ &\cdot \frac{1}{\epsilon_{\mathrm{truth|sel\&}\Lambda_b^0\to\Lambda_c^+\mu^-\overline{\nu}_\mu}} \cdot \frac{\epsilon_{\mathrm{PID|sel\&}\Lambda_b^0\to p\mu^-\overline{\nu}_\mu}}{\epsilon_{\mathrm{PID|sel\&}\Lambda_b^0\to\Lambda_c^+\mu^-\overline{\nu}_\mu}}\ ,\end{aligned} \tag{7.24}$$

where the relative efficiency factorises into the relative efficiencies for generator level selections applied to the simulation samples, the preselection, the corrected mass error selection, the isolation selection, truth-matching and the PID selection. Each of these relative efficiencies are discussed in more detail below. The factor of two arises due to the fact that only $1\mathrm{fb}^{-1}$ is used for the normalisation fit.

The relative efficiency of any selection requirements made in the generation of the simulation samples is given by

$$\frac{\epsilon_{\mathrm{gen}|\Lambda_b^0\to p\mu^-\overline{\nu}_\mu}}{\epsilon_{\mathrm{gen}|\Lambda_b^0\to\Lambda_c^+\mu^-\overline{\nu}_\mu}} = 0.645\ . \tag{7.25}$$

This efficiency is less than one because for the simulated $\Lambda_b^0 \to p\mu^-\overline{\nu}_\mu$ decays both the proton and muon are required to have a polar angle in the interval $10-400$ mrad, meanwhile, for the simulated $\Lambda_b^0 \to \Lambda_c^+\mu^-\overline{\nu}_\mu$ decays only the Λ_b^0 baryon is required to meet this angular acceptance criteria.

The relative efficiency of the preselection of signal and normalisation modes is

$$\frac{\epsilon_{\mathrm{presel|gen\&}\Lambda_b^0\to p\mu^-\overline{\nu}_\mu}}{\epsilon_{\mathrm{presel|gen\&}\Lambda_b^0\to\Lambda_c^+\mu^-\overline{\nu}_\mu}} = 8.71\ , \tag{7.26}$$

where this includes the efficiency of reconstruction and the chosen trigger requirements. The large value of this relative efficiency is due to the need to reconstruct two additional tracks and the looser generator level cuts employed for the normalisation mode.

The efficiency of the corrected mass error selection, which is applied to only the signal candidates, is given by

$$\epsilon_{m_{\rm corr}\ {\rm error|gen}} = 0.228\ . \tag{7.27}$$

Although this efficiency is calculated using simulated $\Lambda_b^0\to p\mu^-\overline{\nu}_\mu$ decays a correction is applied by studying $B^+\to (J/\psi\to\mu^+\mu^-)K^+$ decays in data. A clean sample of $B^+\to (J/\psi\to\mu^+\mu^-)K^+$ decays can be obtained in data by fully reconstructing the decay and selecting a window around the B^+ mass of $\pm 40\,\mathrm{MeV}/c^2$. The opposite-sign kaon and muon combination can now be used as a proxy for the signal proton and muon combination. Fig. 7.22 demonstrates the similarity between the corrected mass error distribution for $K^+\mu^-$ and $p\mu^-$ combinations from simulated $B^+\to (J/\psi\to\mu^+\mu^-)K^+$ and $\Lambda_b^0\to p\mu^-\overline{\nu}_\mu$ decays. Meanwhile, it also shows a comparison of the corrected mass error distribution for $B^+\to J/\psi K^+$ decays in simulation and data, where the fraction below $100\,\mathrm{MeV}/c^2$ is $32.5\pm 0.1\%$ for simulation and $33.4\pm 0.3\%$ for data. The ratio of these fractions in taken as a relative 3% correction to the efficiency.

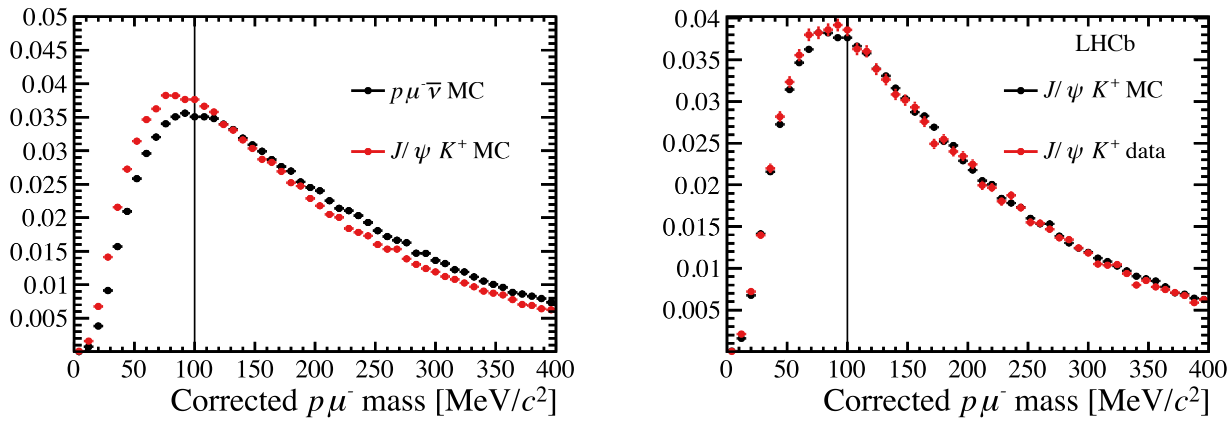

Figure 7.22: Corrected mass error distributions for simulated $B^+\to J/\psi K^+$ and $\Lambda_b^0\to p\mu^-\overline{\nu}_\mu$ decays (left). A correction to the efficiency of the corrected mass error selection is made by comparing the corrected mass error distribution in simulation to that in data for $B^+\to J/\psi K^+$ decays as shown on the right.

The relative efficiency of the isolation selection is given by

$$\frac{\epsilon_{\text{iso}|\text{presel}\&m_{\text{corr}}\text{ error}\&\Lambda_b^0\to p\mu^-\overline{\nu}_\mu}}{\epsilon_{\text{iso}|\text{presel}\&\Lambda_b^0\to\Lambda_c^+\mu^-\overline{\nu}_\mu}} = 1.049 \pm 0.014\ . \tag{7.28}$$

This efficiency is close to one given the good agreement between the isolation BDT output distributions between simulated $\Lambda_b^0 \to \Lambda_c^+\mu^-\overline{\nu}_\mu$ and $\Lambda_b^0 \to p\mu^-\overline{\nu}_\mu$ decays as shown in Fig. 7.23. In order to validate whether or not the isolation BDT output is well simulated a comparison is made between the isolation BDT output for $\Lambda_b^0 \to \Lambda_c^+\mu^-\overline{\nu}_\mu$ decays in data and simulation (see Fig. 7.23). Re-weighting the isolation BDT output in simulation to that seen in data reduces the relative isolation efficiency by 1.4% to 1.035; this is taken as a systematic uncertainty.

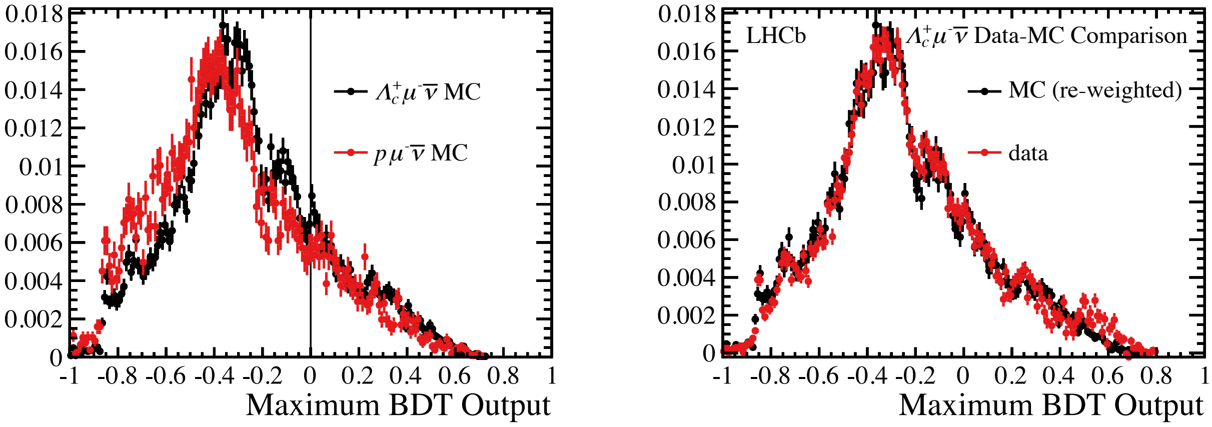

Figure 7.23: A comparison of the isolation BDT output distributions for simulated $\Lambda_b^0 \to p\mu^-\overline{\nu}_\mu$ and $\Lambda_b^0 \to \Lambda_c^+\mu^-\overline{\nu}_\mu$ decays (left). The simulation of the isolation BDT output is validated by comparing the background subtracted distribution for $\Lambda_b^0 \to \Lambda_c^+\mu^-\overline{\nu}_\mu$ candidates in data to the simulated distribution.

There is an efficiency for requiring that proton, kaon, pion and muon candidate particles in simulation correspond to the particles generated in $\Lambda_b^0 \to p\mu^-\overline{\nu}_\mu$ and $\Lambda_b^0 \to \Lambda_c^+\mu^-\overline{\nu}_\mu$ decays. While this truth-matching efficiency will cancel between signal and normalisation for candidate protons and muons, it must be taken into account for the additional pion and kaon candidates in the case of the normalisation mode. This efficiency is determined from the ratio of yields of fits to the $\Lambda_c^+ \to pK^-\pi^+$ mass peak for simulated $\Lambda_b^0 \to (\Lambda_c^+ \to pK^-\pi^+)\mu^-\overline{\nu}_\mu$ decays selected with and without truth-matching requirements applied to the kaon and pion candidates. The truth-matching efficiency for the kaons and pions is found to be

$$\epsilon_{\text{truth}|\text{sel}\&\Lambda_b^0\to\Lambda_c^+\mu^-\overline{\nu}_\mu} = 0.96 \pm 0.001\ . \tag{7.29}$$

The final efficiency required is the relative efficiency of the PID selection, which is given by

$$\frac{\epsilon_{PID|\text{sel}\&\Lambda_b^0 \to p\mu^-\overline{\nu}_\mu}}{\epsilon_{PID|\text{sel}\&\Lambda_b^0 \to \Lambda_c^+\mu^-\overline{\nu}_\mu}} = 1.173 \pm 0.002 \, . \tag{7.30}$$

The main difference in the PID selection efficiencies for $\Lambda_b^0 \to p\mu^-\overline{\nu}_\mu$ and $\Lambda_b^0 \to \Lambda_c^+\mu^-\overline{\nu}_\mu$ decays is due to the PID selection applied to the kaon and pion candidates for $\Lambda_b^0 \to \Lambda_c^+\mu^-\overline{\nu}_\mu$ decays. In addition, there will also be a slight difference in the kinematics of the proton coming from each decay. The kaon, pion and proton PID efficiencies, $\epsilon_{K/\pi/p}(P, \eta, T)$, are applied as weights to the simulated $\Lambda_b^0 \to p\mu^-\overline{\nu}_\mu$ and $\Lambda_b^0 \to (\Lambda_c^+ \to pK^-\pi^+)\mu^-\overline{\nu}_\mu$ candidates in order to determine the PID selection efficiencies for these decays. Before these weights are applied the track multiplicity distributions in simulation are re-weighted to agree with that observed in data as shown in Fig. 7.24. The uncertainties on the efficiences provided from the PID callibration samples are propagated to the overall relative PID efficiency using a Monte Carlo based approach as was described in section 7.2.3. Fig. 7.24 shows the distribution of relative PID selection efficiencies arising from this approach; the RMS of which is 0.002.

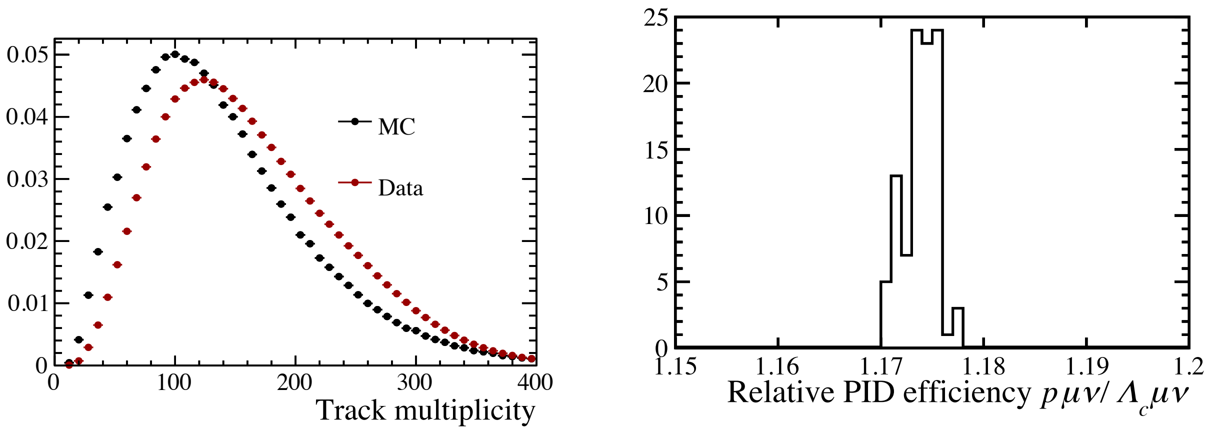

Figure 7.24: A comparison of the track multiplicity distributions in data and simulation (left). Relative PID efficiency between $\Lambda_b^0 \to p\mu^-\overline{\nu}_\mu$ and $\Lambda_b^0 \to \Lambda_c^+\mu^-\overline{\nu}_\mu$ decays (right).

7.4.2. Efficiency corrections and systematics

A number of corrections must be applied to the relative efficiency to account for differences between simulation and data, q^2 migration and, finally, the difference between the simulated form factors from those predicted by relativistic LQCD.

The correction to the relative efficiency due to migration in and out of the selected q^2 region, M_{in} and M_{out}, as defined in section 6.3.3, is given by

$$\frac{(1 - M_{\text{out}|\Lambda_b^0\to p\mu^-\overline{\nu}_\mu})}{(1 - M_{\text{in}|\Lambda_b^0\to p\mu^-\overline{\nu}_\mu})} \frac{(1 - M_{\text{in}|\Lambda_b^0\to\Lambda_c^+\mu^-\overline{\nu}_\mu})}{(1 - M_{\text{out}|\Lambda_b^0\to\Lambda_c^+\mu^-\overline{\nu}_\mu})} = 0.95 \pm 0.004 \ , \tag{7.31}$$

The form factor correction is assessed by re-weighting simulation according to the relativistic LQCD predictions using the prescription described in equation 5.18. Fig. 7.25 shows the correction to the relative efficiency obtained when re-weighting simulation according to a hundred variations of $\Lambda_b^0 \to p\mu^-\overline{\nu}_\mu$ and $\Lambda_b^0 \to \Lambda_c^+\mu^-\overline{\nu}_\mu$ relativistic LQCD form factors. The relative efficiency correction is found to be

$$C_{\text{FF}} = 0.985 \pm 0.010 \ . \tag{7.32}$$

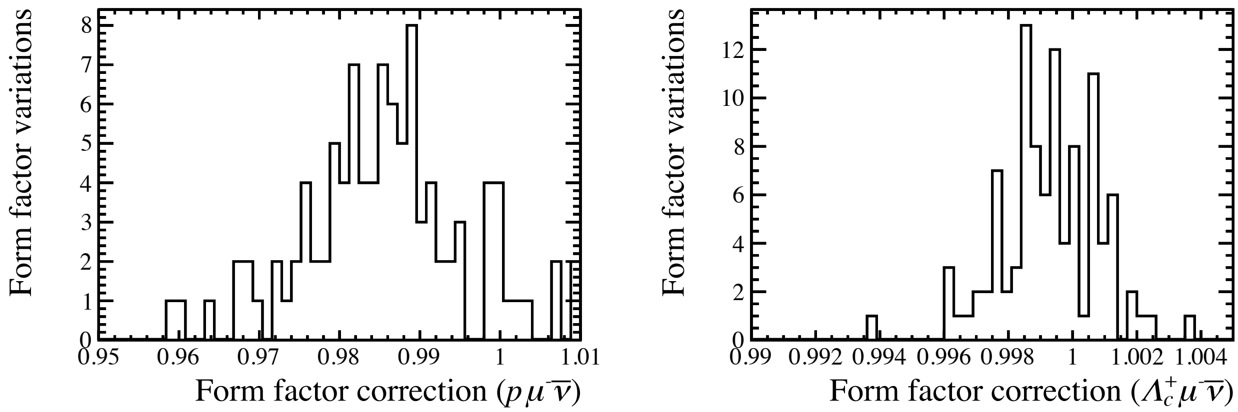

Figure 7.25: Distribution of the form factor correction to the relative efficiency ratio under variations in the form factors.

Simulation fails to perfectly emulate the tracking and trigger performance, the kinematics of Λ_b^0 baryons produced within LHCb and the Dalitz structure of the decay $\Lambda_c^+ \to pK^-\pi^+$. In order to assess the potential impact of these factors on the relative selection efficiency, a number of data-driven corrections are made to simulated events. These corrections are discussed in more detail below.

The track reconstruction efficiency for the LHCb detector has been well measured using $J/\psi \to \mu^+\mu^-$ decays [59]. The difference between data and simulation, which is shown in Fig. 7.26, is applied to selected signal and normalisation proton, muon, kaon and pion tracks in simulation having first re-weighted the track-multiplicity distribution to match that in data. The net effect is a minimal correction to the relative selection efficiency of

$$C_{\text{tracking}} = 0.995 \pm 0.03 , \tag{7.33}$$

where here, although the statistical error is negligible (0.2%), a systematic uncertainty of 1.5% is assigned for each track to account for possible material interactions. This systematic effect will cancel in the efficiency ratio for the proton and muon, and therefore, is only considered for the kaon and pion.

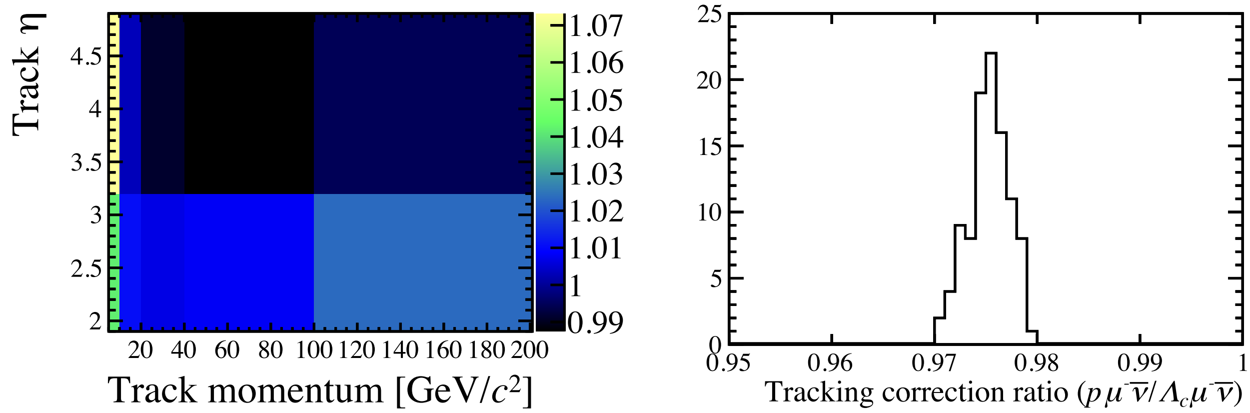

Figure 7.26: Tracking efficiency ratio between data and simulation for long tracks (left), which is made using the results from Reference [59]. Correction to the relative selection efficiency when applying the tracking efficiency corrections to all signal and normalisation candidate tracks (right).

In order to quantify how well the simulation reproduces the trigger, the TISTOS efficiency, ϵ_{TISTOS}, which is defined in section 3.2.4, is compared in simulation and data. Given that a TOS requirement was made in the preselection of $\Lambda_b^0 \to p\mu^-\overline{\nu}_\mu$ candidates, the comparison is made using $B^+ \to (J/\psi \to \mu^+\mu^-)K^+$ decays using the kinematic variables, $(\Sigma_{p,\mu}p_T)$ and the corrected mass of the $K\mu$ pair, as shown in Fig. 7.27. The correction to the relative selection efficiency (see Fig. 7.28) is obtained by re-weighting simulated $\Lambda_b^0 \to p\mu^-\overline{\nu}_\mu$ and $\Lambda_b^0 \to \Lambda_c^+\mu^-\overline{\nu}_\mu$ decays by the observed differences; this gives the correction

$$C_{\text{trigger}} = 1.032 \pm 0.032 . \tag{7.34}$$

The uncertainty shown here, arises from the statistical uncertainty associated with the re-weighting procedure. This is driven by the statistics available in the data sample of $B^+ \to (J/\psi \to \mu^+\mu^-)K^+$ decays.

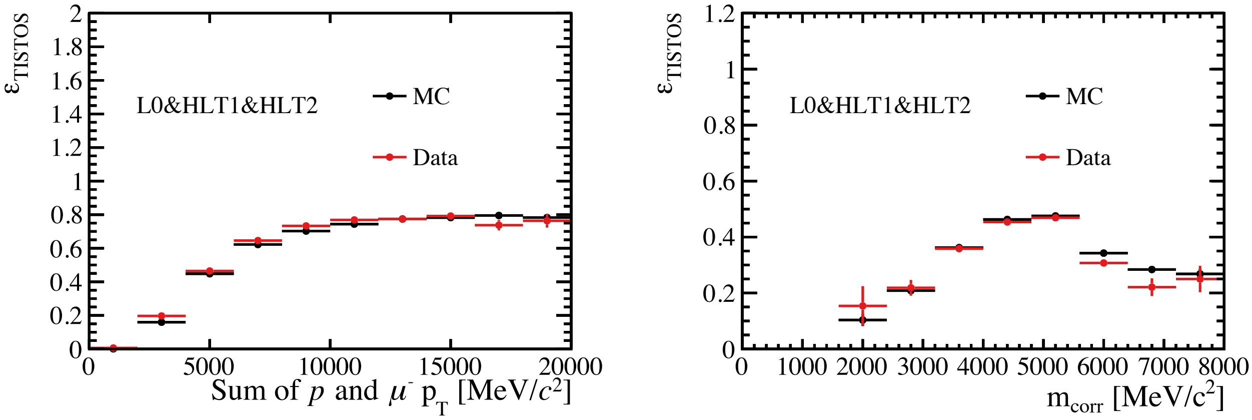

Figure 7.27: A comparison of the TISTOS efficiency for $B^+ \to J/\psi K^+$ decays in data and simulation as a function of $\Sigma_{p,\mu}p_T$ amd m_{corr}.

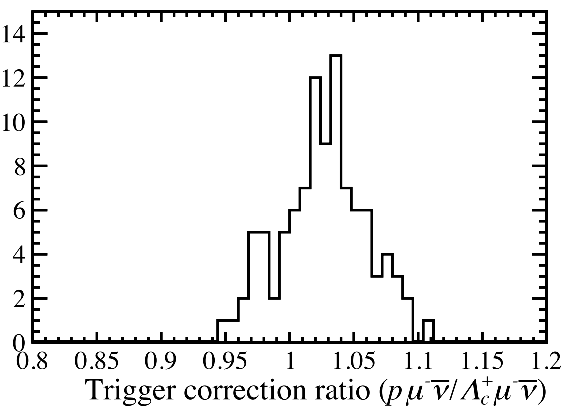

Figure 7.28: Distribution of the trigger correction given statistical variations in the re-weighting of $\Sigma_{p,\mu}p_T$ amd m_{corr}.

The kinematics of Λ_b^0 baryons produced from $pp \to b\bar{b}X$ interactions will influence the relative efficiency for selecting $\Lambda_b^0 \to p\mu^-\overline{\nu}_\mu$ and $\Lambda_b^0 \to \Lambda_c^+\mu^-\overline{\nu}_\mu$ decays. In order to validate whether or not simulation properly describes the kinematics of Λ_b^0 baryons produced within LHCb a study of $\Lambda_b^0 \to pK^+J/\psi$ decays is made. A clean selection sample of $\Lambda_b^0 \to pK^+J/\psi$ decays in data is selected by vetoing any mass reflections from decays of B^0, B^+ and B_s^0 mesons. Fig 7.29 shows a fit to the invariant mass of selected pK^-J/ψ candidates. Data in the mass window,

$5586 < m_{pK^-J/\psi} < 5666\,\mathrm{MeV}/c^2$, is subtracted of combinatorial background, which is modelled using data in the upper mass sideband ($m_{pK^-J/\psi} > 5750\,\mathrm{MeV}/c^2$). Fig 7.30 shows that there is a clear discrepancy between the background subtracted momentum and transverse momentum distributions of $\Lambda_b^0 \to pK^+J/\psi$ candidates in data to the corresponding distributions in simulation. The correction to the relative selection efficiency is determined by correcting the Λ_b^0 kinematics for simulated $\Lambda_b^0 \to p\mu^-\overline{\nu}_\mu$ and $\Lambda_b^0 \to \Lambda_c^+\mu^-\overline{\nu}_\mu$ decays; this results in a correction of

$$C_{\Lambda_b^0\mathrm{prod}} = 1.073 \pm 0.005. \tag{7.35}$$

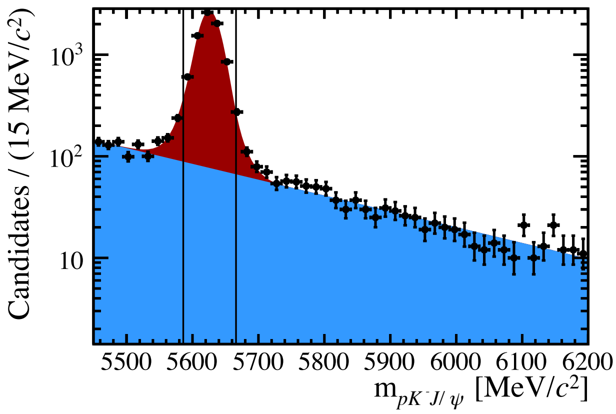

Figure 7.29: Fit to the invariant mass of pK^-J/ψ candidates

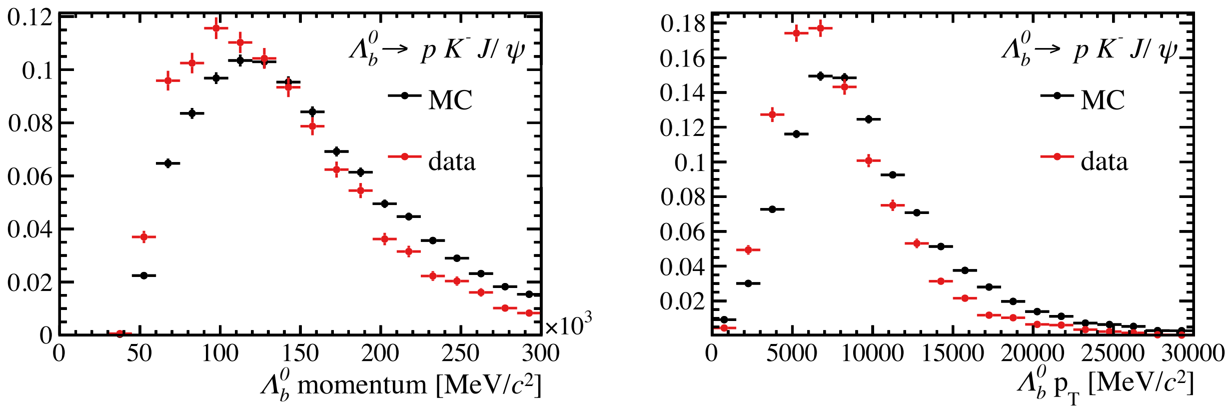

Figure 7.30: Comparison of the momentum and transverse momentum, p_T, distributions for pK^-J/ψ candidates in data and simulation.

As described in section 7.2.1, for $\Lambda_b^0 \to \Lambda_c^+\mu^-\overline{\nu}_\mu$ decays there is a discrepancy between the $m^2_{pK^-}$ and $m^2_{p\pi^+}$ Dalitz distribution seen in simulation and data (see Fig. 7.9). A correction to the relative selection efficiency of

$$C_{\Lambda_c^+ decay} = 0.998 \pm 0.03 \; , \tag{7.36}$$

is determined by re-weighting the $\Lambda_c^+ \to pK^-\pi^+$ Dalitz distribution in simulation to that observed in data. If the Dalitz-structure is instead parametrised by m_{pK^-} and the helicity angle of the pK^- system (the "square-Dalitz" parametrisation), a comparison of data and simulation yields a relative efficiency correction of 1.03. The difference between the two corrections is taken as a 3% systematic.

The final correction to the relative selection efficiency accounts for updated measurements of the lifetimes of Λ_b^0 and Λ_c^+ baryons, $\tau_{\Lambda_b^0} = 1.48 \pm 0.02$ ps and $\tau_{\Lambda_c^+} = 0.2$ ps, which can be compared to values used in simulation, $\tau_{\Lambda_b^0} = 1.426$ ps and $\tau_{\Lambda_c^+} = 0.19$ ps. This correction is quantified by re-weighting the lifetime distribution of Λ_b^0 and Λ_c^+ baryons in simulation to the latest measured values. This gives a correction of

$$C_{\Lambda_c^+ \& \Lambda_b^0 \mathrm{lifetimes}} = 1.042 \pm 0.015 \; , \tag{7.37}$$

where the uncertainty is dominated by the uncertainty on the Λ_b^0 lifetime.

7.4.3. Final corrected relative efficiency

The relative efficiency after having applied all corrections is found to be

$$\epsilon_{\mathrm{rel}} = 3.52 \pm 0.20 \; . \tag{7.38}$$

Table 7.4 summarises the factors and corrections which enter into the calculation of this final value.

Given the speculation that a right-handed current contributing to $b \to u$ transitions could resolve the $|V_{ub}|$ puzzle, the impact of a non-zero right-handed current with, $V_{ub}^R = V_{ub}^L \cdot \epsilon_u^R$, on the relative efficiency is considered. In order to quantify this impact, the q^2 distribution of simulated $\Lambda_b^0 \to p\mu^-\overline{\nu}_\mu$ decays is re-weighted according to the possible variations in the differential rate for non-zero values of ϵ_u^R as shown in Fig 2.8 in section 2.3. Fig 7.31 shows the correction to the relative efficiency as a function of the parameter, ϵ_u^R.

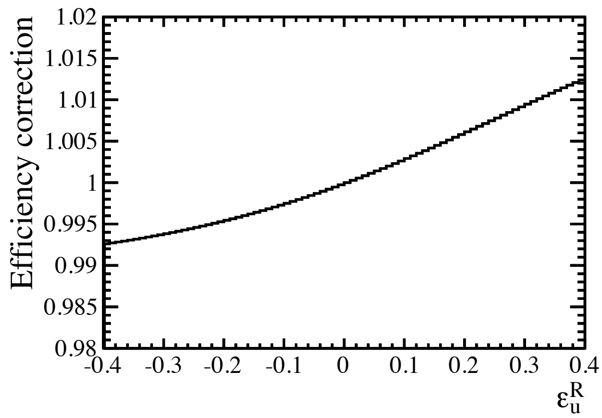

Figure 7.31: Correction to the relative efficiency given a right-handed current parametrised by, $V_{ub}^R = V_{ub}^L \cdot \epsilon_u^R$.

Source	Relative efficiency
Prescale	2
Generator selection	0.645
Truth matching	1.04 ± 0.001
Stripping & trigger	8.71
m_{corr} error	0.228
Isolation	1.049 ± 0.014
PID	1.173 ± 0.002
Source	Correction
Form factors	0.985 ± 0.01
q^2 migration	0.95 ± 0.004
Tracking	0.995 ± 0.03
Trigger	1.032 ± 0.032
Λ_b^0 production	1.073 ± 0.005
Λ_c^+ decay model	0.998 ± 0.03
Λ_b^0 and Λ_c^+ lifetimes	1.042 ± 0.015
Total	3.52 ± 0.20

Table 7.4: Summary of the efficiencies and corrections entering the calculation of the relative selection efficiency between the signal and normalisation channels.

Source	Relative uncertainty (%)
$\mathcal{B}(\Lambda_c^+ \to pK\pi)$	$^{+4.7}_{-5.3}\%$
Trigger	$\pm3.2\%$
Tracking	$\pm3.0\%$
Λ_c^+ decay model	3.0%
N^{*+} form factors	2.2%
Λ_c^+ & Λ_b^0 lifetimes	1.5%
Isolation	1.4%
Form factor	1.0%
N^{*+} widths	0.7%
Λ_b^0 production	0.5%
q^2 migration	0.4%
PID	0.2%
Truth matching	0.1%
m_{corr} error	Negligible
Total	$^{+7.8}_{-8.2}\%$

Table 7.5: Summary of systematic uncertainties. The systematic uncertainties that are included in the fit as Gaussian constraints are not included here.

7.5. Results

7.5.1. Measurement of the ratio of branching fractions

The ratio of branching fractions for $\Lambda_b^0 \to p\mu^-\overline{\nu}_\mu$ and $\Lambda_b^0 \to \Lambda_c^+\mu^-\overline{\nu}_\mu$ decays, in the required regions of $q^2 > 15\,\mathrm{GeV}^2/c^4$ and $q^2 > 7\,\mathrm{GeV}^2/c^4$, is measured as

$$\begin{aligned}\frac{\mathcal{B}_{\Lambda_b^0\to p\mu^-\overline{\nu}_\mu|q^2>15\,\mathrm{GeV}^2/c^4}}{\mathcal{B}_{\Lambda_b^0\to\Lambda_c^+\mu^-\overline{\nu}_\mu|q^2>7\,\mathrm{GeV}^2/c^4}} &= \frac{N_{\Lambda_b^0\to p\mu^-\overline{\nu}_\mu|q^2>7\,\mathrm{GeV}^2/c^4}}{N_{\Lambda_b^0\to(\Lambda_c^+\to pK^-\pi^+)\mu^-\overline{\nu}_\mu|q^2>15\,\mathrm{GeV}^2/c^4}} \cdot \frac{\mathcal{B}_{\Lambda_c^+\to pK^-\pi^+}}{\epsilon_{\mathrm{rel}}} \\ &= (1.00 \pm 0.04 \pm 0.08) \times 10^{-2}\ ,\end{aligned} \tag{7.39}$$

where the first uncertainty is statistical and the second uncertainty is systematic. The yields, relative efficiency and $\mathcal{B}_{\Lambda_c^+\to pK\pi}$ are summarised in Table 7.6. Meanwhile, the various systematic uncertainties entering into this ratio are given in Table 7.5. The largest systematic uncertainty is on the Belle measurement of the branching fraction, $\mathcal{B}_{\Lambda_c^+\to pK\pi}$. The next largest sources of experimental uncertainty are the systematic uncertainties associated with the trigger, tracking and Λ_c^+ decay model which are ∼3%. Given that the trigger systematic is dominated by the statistical uncertainty on the $B^+\to J/\psi K^+$ control mode this will reduce with more data. A more realistic simulation of the Λ_c^+ decay model, Λ_c^+/Λ_b^0 lifetimes, isolation BDT response and Λ_b^0 production kinematics could help reduce the corresponding systematic uncertainties. On the other hand, the tracking systematic is irreducible as it is a result of the potential material interactions of the two additional tracks of the normalisation decay. Finally, precise predictions for the $\Lambda_b^0\to N^{*+}\mu^-\overline{\nu}_\mu$ form factors from LQCD or LCSR could help to reduce the N^* form factor systematic.

Result	Value	Reference
$N_{\Lambda_b^0\to p\mu^-\overline{\nu}_\mu}$	17687 ± 733	7.3.3
$N_{\Lambda_b^0\to(\Lambda_c^+\to pK^-\pi^+)\mu^-\overline{\nu}_\mu}$	34255 ± 571	7.1.4
$\epsilon_{\rm rel}$	3.52 ± 0.20	7.4.3
$\mathcal{B}_{\Lambda_c^+\to pK\pi}$	$0.0684^{+0.0047}_{-0.0053}$	[70]

Table 7.6: Experimental results entering the calculation of the ratio of branching fractions.

Fig. 7.32 shows a correction to the measured ratio of branching fractions given the presence of a right-handed coupling. A third-order polynomial fit is made in order to parametrise the correction as a function of ϵ_R.

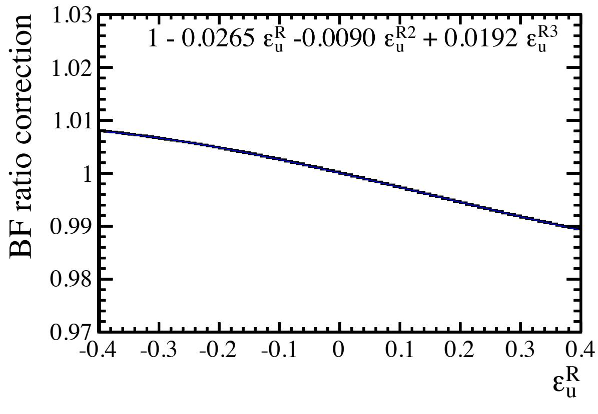

Figure 7.32: Correction to the measured ratio of branching fractions of $\Lambda_b^0\to p\mu^-\overline{\nu}_\mu$ and $\Lambda_b^0\to\Lambda_c^+\mu^-\overline{\nu}_\mu$ decays given the presence of a right-handed coupling with strength, $V_{ub}^R = V_{ub}^L\cdot\epsilon_u^R$. A third-order polynomial fit to the correction is shown by the solid blue curve.

7.5.2. Determination of $|V_{ub}|/|V_{cb}|$, $|V_{ub}|$ and $\mathcal{B}_{\Lambda_b^0\to p\mu^-\overline{\nu}_\mu}$

The ratio of CKM elements, $|V_{ub}|/|V_{cb}|$, is now determined using equation 4.1 from section 4 as

$$\begin{aligned}\frac{|V_{ub}|}{|V_{cb}|} &= \left(\frac{\mathcal{B}_{\Lambda_b^0\to p\mu^-\overline{\nu}_\mu|q^2>15\,\mathrm{GeV}^2/c^4}}{\mathcal{B}_{\Lambda_b^0\to \Lambda_c^+\mu^-\overline{\nu}_\mu|q^2>7\,\mathrm{GeV}^2/c^4}} R_{FF}\right)^{\frac{1}{2}} \\ &= 0.083 \pm 0.004 \pm 0.004\ ,\end{aligned} \tag{7.40}$$

where the first uncertainty is experimental and the second uncertainty is theoretical. Finally, combining this expression with the world average for $|V_{cb}|$ from exclusive decays, $|V_{cb}| = (39.5 \pm 0.8) \times 10^{-3}$, results in the first determination of $|V_{ub}|$ from a hadron collider,

$$|V_{ub}| = (3.27 \pm 0.15 \pm 0.16 \pm 0.06) \times 10^{-3}\ , \tag{7.41}$$

where here the first uncertainty is due to the experimental measurement, the second uncertainty arises from the LQCD predictions and the final uncertainty comes from $|V_{cb}|$. Table 7.7 shows the values of $|V_{ub}|/|V_{cb}|$ and $|V_{ub}|$ obtained if instead the BESIII or HFAG averaged value of $\mathcal{B}(\Lambda_c^+ \to pK^-\pi^+)$ is used. A comparison of these measurements of $|V_{ub}|$ from $\Lambda_b^0 \to p\mu^-\overline{\nu}_\mu$ decays with the world averages of measurements of $|V_{ub}|$ made using $\overline{B}^0 \to \pi^+ l^- \bar{\nu}_l$ decays and inclusive $B \to X_u l^- \bar{\nu}_l$ decays is shown in Fig 7.33. This comparison includes recent determinations of $|V_{ub}|$ from $\overline{B}^0 \to \pi^+ l^- \bar{\nu}_l$ decays using the more recent LQCD calculations [36, 37] for the $\overline{B}^0 \to \pi^+ l^- \bar{\nu}_l$ form factors.

The branching fraction of $\Lambda_b^0 \to p\mu^-\overline{\nu}_\mu$ decays is determined from the measured ratio of branching fractions using equation 4.4 as

$$\mathcal{B}_{\Lambda_b^0\to p\mu^-\overline{\nu}_\mu} = (4.1 \pm 1.0) \times 10^{-4}\ . \tag{7.42}$$

$\mathcal{B}_{\Lambda_c^+\to pK^-\pi^+}$	$\lvert V_{ub}\rvert/\lvert V_{cb}\rvert$	$\lvert V_{ub}\rvert$
Belle	$0.082 \pm 0.004 \pm 0.004$	$(3.27 \pm 0.15 \pm 0.16 \pm 0.06) \times 10^{-3}$
BESIII	$0.076 \pm 0.004 \pm 0.004$	$(3.02 \pm 0.15 \pm 0.15 \pm 0.05) \times 10^{-3}$
HFAG	$0.080 \pm 0.003 \pm 0.004$	$(3.17 \pm 0.14 \pm 0.16 \pm 0.05) \times 10^{-3}$

Table 7.7: values of $|V_{ub}|/|V_{cb}|$ and $|V_{ub}|$ computed using different values of the branching fractions of $\Lambda_c^+ \to pK^-\pi^+$.

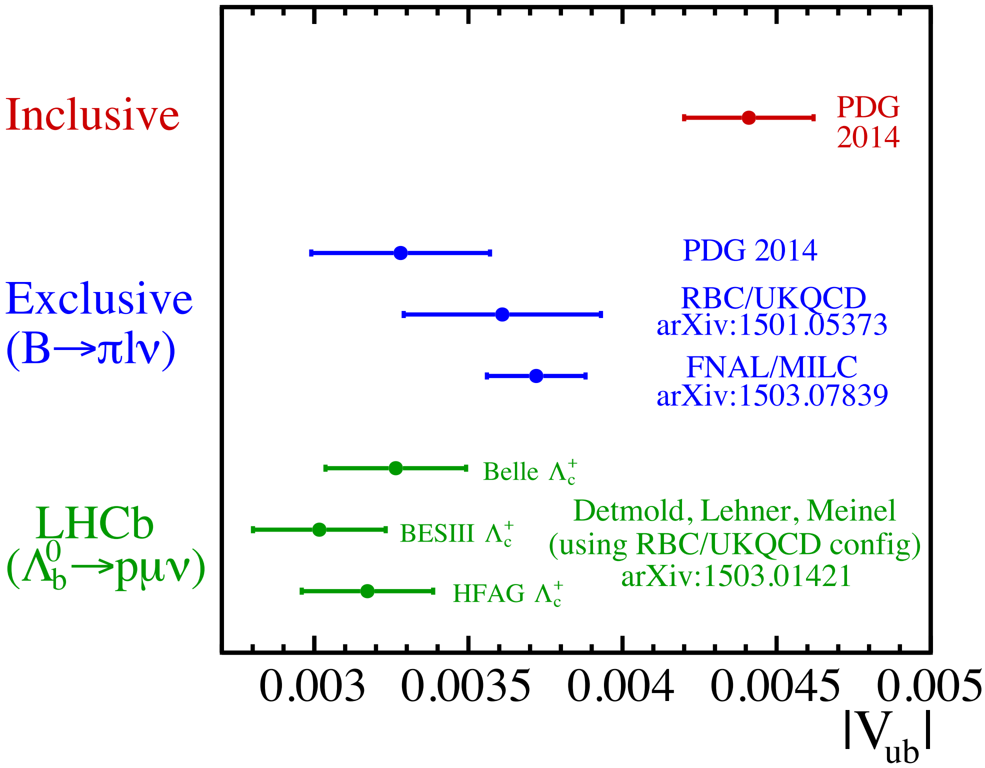

Figure 7.33: A comparison of previous measurements of $|V_{ub}|$ from $\overline{B}^0 \to \pi^+ l^- \bar{\nu}_l$ and inclusive $B \to X_u l^- \bar{\nu}_l$ decays with the measurement from $\Lambda_b^0 \to p\mu^-\overline{\nu}_\mu$ decays. In addition to the 2014 PDG average of $|V_{ub}|$ from $\overline{B}^0 \to \pi^+ l^- \bar{\nu}_l$ decays two updated determinations of $|V_{ub}|$ from these decays are shown, which use new LQCD predictions for the $\overline{B}^0 \to \pi^+ l^- \bar{\nu}_l$ form factors. The three determinations of $|V_{ub}|$ from $\Lambda_b^0 \to p\mu^-\overline{\nu}_\mu$ decays reflect the choice of the value of $\mathcal{B}_{\Lambda_c^+\to pK^-\pi^+}$ from the Belle, BESIII or HFAG values.

Chapter 8.

Implications

8.1. Inclusive and exclusive determinations of $|V_{ub}|$ and $|V_{cb}|$

The measurement of $|V_{ub}|$ using $\Lambda_b^0 \to p\mu^-\overline{\nu}_\mu$ decays is 3.5σ below the average of $|V_{ub}|$ measurements [11] from inclusive, $B \to X_u l\nu$, decays. This increases the tension between exclusive and inclusive measurements of $|V_{ub}|$.

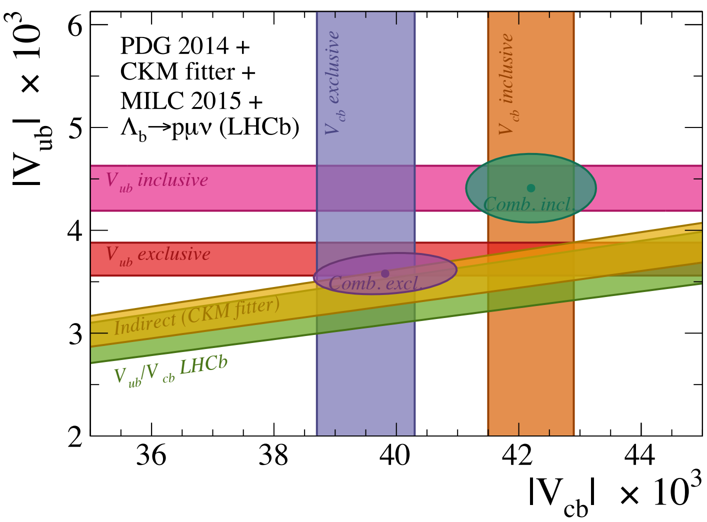

Figure 8.1: Comparison of global fits for $|V_{ub}|$ and $|V_{cb}|$ using constraints from solely exclusive or inclusive measurements of $|V_{ub}|$, $|V_{cb}|$ and $|V_{ub}|/|V_{cb}|$. The indirect constraint on $|V_{ub}/V_{cb}|$ from the global fits of the CKMfitter is also plotted. Figure taken from [82].

Given that the fundamental measurement made is a measurement of the ratio of CKM elements $|V_{ub}|$ and $|V_{cb}|$, there is less ambiguity when comparing the constraint of this measurement in the $|V_{ub}|$-$|V_{cb}|$ plane to the constraints from other exclusive and inclusive measurements of these CKM elements as shown in Fig 8.1. The constraint on the ratio, $|V_{ub}|/|V_{cb}|$, is consistent with the constraints from exclusive measurements of $|V_{ub}|$ and $|V_{cb}|$. In addition, there is good agreement between between the constraint on $|V_{ub}|/|V_{cb}|$ from $\Lambda_b^0 \to p\mu^-\overline{\nu}_\mu$ decays and the indirect constraint from the global CKM fits of the CKMfitter group [29]. Fig 8.1 also shows the best fit values for $|V_{ub}|$ and $|V_{cb}|$ based on global fits to solely exclusive or inclusive measurements. There is a clear discrepancy between the exclusive and inclusive fit values for $|V_{ub}|$ and $|V_{cb}|$. While the values for $|V_{ub}|$ and $|V_{cb}|$ from the exclusive measurements are consistent with the indirect constraint from CKMfitter, there is clearly tension between the inclusive fitted values and the indirect constraint.

8.2. The unitarity triangle

The measurement of $|V_{ub}|/|V_{cb}|$ provides a new constraint on the length of the side of the unitarity triangle, R_u, which is opposite the angle β. Fig 8.2 shows a comparison of the constraints on the unitary triangle's length, R_u, from exclusive and inclusive determinations of $|V_{ub}|/|V_{cb}|$. In addition, constraints on the apex from the world averages of γ measurements (CKMfitter [29]), sin2β from $B^0 \to J/\psi K_s^0$ decays (HFAG [83]) and $\Delta m_d/\Delta m_s$ measurements (HFAG [83]) are shown. The constraint on R_t from the HFAG average of $\Delta m_d/\Delta m_s$ measurements is 0.893 ± 0.013 as derived in Reference [84] using the latest lattice inputs for $B^0_{d/s}$-$\bar{B}^0_{d/s}$ mixing.

The CKM observables R_t and β alone tightly constrain the apex of the unitarity triangle given their low uncertainties. A simple likelihood fit (see equation 2.43) for the apex just using R_t and β as constraints gives $R_u = 0.374$. The constraint on R_u from $\Lambda_b^0 \to p\mu^-\overline{\nu}_\mu$, $\overline{B}^0 \to \pi^+ l^- \bar{\nu}_l$ and inclusive $B \to Xl\nu$ decays differ from $R_u = 0.374$ by 0.5σ, 1.4σ and 2.9σ, respectively.

8.3. Implications for a right-handed $b \to u$ coupling

Fig 8.3 shows the global fit for a right-handed coupling of strength, $V_{ub}^R = \epsilon_u^R V_{ub}^L$, based on $B^- \to \tau^-\bar{\nu}_\tau$, $\overline{B}^0 \to \pi^+ l^- \bar{\nu}_l$ and inclusive $B \to X_u l\nu$ decays. The $\chi^2/n_{\mathrm{d.o.f}}$ for this fit is $\sim$1.4/1 ($p-$value $= 0.2$) and it led to speculation that a right-handed current, in addition to the SM left-handed current could explain the apparent inconsistency in the different $|V_{ub}|$ measurements [38–40]. The inclusion of the constraint from $|V_{ub}|$ from $\Lambda_b^0 \to p\mu^-\overline{\nu}_\mu$ decays (see Fig 8.3) no longer makes it possible to get a consistent fit with the $\chi^2/n_{\mathrm{d.o.f}}$ increasing to $\sim$12.5/2 ($p-$value $= 1.93 \times 10^{-3}$).

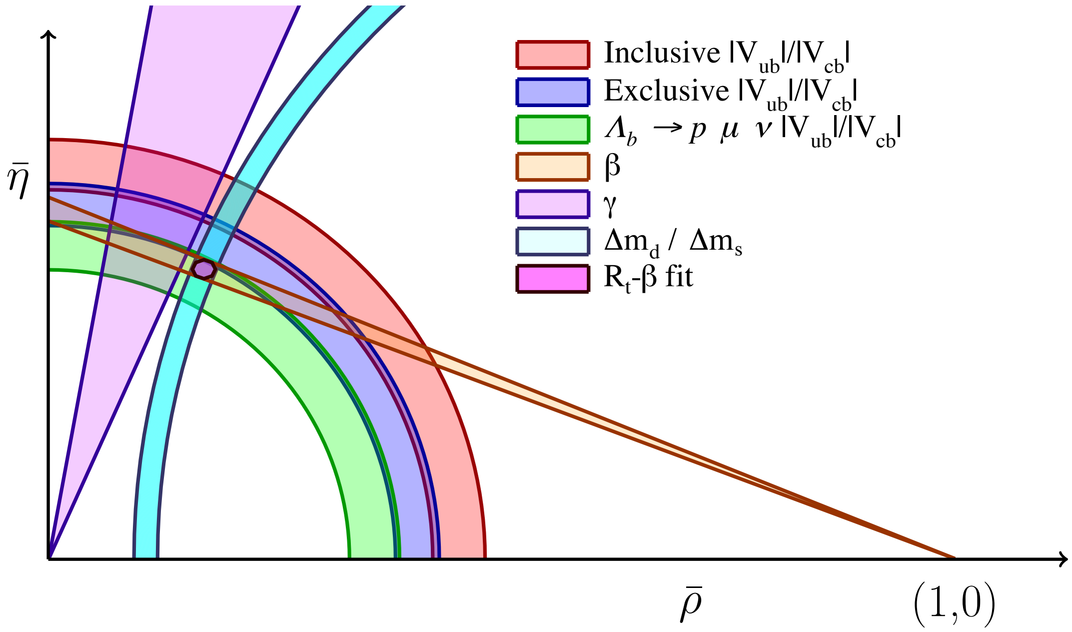

Figure 8.2: Comparison of constraints on the unitarity triangle from exclusive and inclusive measurements of $|V_{ub}|/|V_{cb}|$. A fit for the apex of the unitarity triangle using solely the contraints from β and $\Delta m_d/\Delta m_s$ is shown. The results for coordinate values of the apex from this fit are $\bar{\rho} = 0.165 \pm 0.012$ and $\bar{\eta} = 0.333 \pm 0.010$.

In addition, the constraints from measurements of $|V_{ub}|$ from $\overline{B}^0 \to \pi^+ l^- \overline{\nu}_l$ and $\Lambda_b^0 \to p\mu^-\overline{\nu}_\mu$ decays are consistent with the standard model, $\epsilon_u^R = 0$.

8.4. Outlook for $|V_{ub}|$ from $\Lambda_b^0 \to p\mu^-\overline{\nu}_\mu$ decays and the LHCb

On the theoretical side, the uncertainty on $|V_{ub}|$ is dominated by the finite volume and chiral extrapolation systematic uncertainties associated with the Lattice calculation. Future improvements in lattice techniques and computing power should enable lattice calculations with larger finite volumes and up and down quark masses closer to their physical values.

Experimentally, the uncertainty on $|V_{ub}|$ is dominated by the uncertainty on $\mathcal{B}_{\Lambda_c^+ \to pK^-\pi^+}$ (see Table 7.5). Although not considered here, the recent tension between the Belle [70] and BESIII measurements [71] of $\mathcal{B}_{\Lambda_c^+ \to pK^-\pi^+}$ produces an ambiguity in the measurement of $|V_{ub}|/|V_{cb}|$ and $|V_{ub}|$ from $\Lambda_b^0 \to p\mu^-\overline{\nu}_\mu$ decays. It is clear that additional measurements are required to reduce the

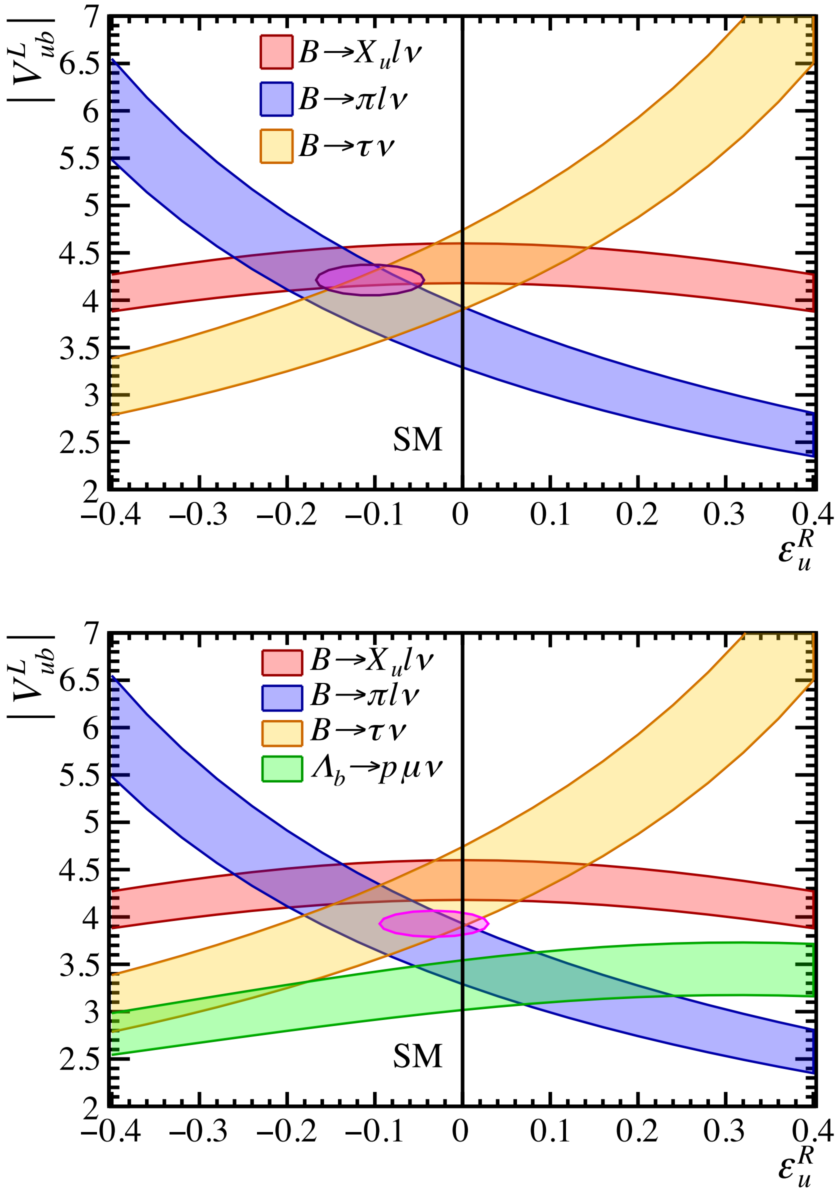

Figure 8.3: Fits for ϵ_u^R and $|V_{ub}^L|$ without and with the inclusion of the constraint of the measurement of $|V_{ub}|$ from $\Lambda_b^0 \to p\mu^-\overline{\nu}_\mu$ decays. Here, V_{ub}^L is the coupling strength for a left-handed $b \to u$ current, meanwhile, the parameter ϵ_u^R parametrises the coupling strength of a right-handed $b \to u$ current, $V_{ub}^R = V_{ub}^L \cdot \epsilon_u^R$.

uncertainty on $\mathcal{B}_{\Lambda_c^+ \to pK^-\pi^+}$ and resolve the discrepancy between the Belle and BESIII measurements of this branching fraction. As discussed in section 7.5.2, a number of the systematic uncertainties on the ratio of branching fractions of $\Lambda_b^0 \to p\mu^-\overline{\nu}_\mu$ and $\Lambda_b^0 \to \Lambda_c^+\mu^-\overline{\nu}_\mu$ decays may be reduced by having higher statistics in calibration samples, a more realistic simulation and a better modelling of background decays.

One could also consider a measurement of the branching fraction of $\Lambda_b^0 \to p\mu^-\overline{\nu}_\mu$ decays in bins of q^2 across the full q^2 region. This could allow for the q^2 dependence of the form factors to be constrained or potentially measured in data. In addition, the measurement would give sensitivity to ϵ_u^R. However, the limited resolution for the reconstruction of q^2, which was discussed in section 6.3.3, would make this a difficult measurement requiring a complicated unfolding.

Chapter 9.

Conclusions

The CKM matrix element $|V_{ub}|$ is an important parameter in constraining global fits to the unitarity of the CKM matrix. The discrepancy between exclusive and inclusive measurements of $|V_{ub}|$ has been a long-standing puzzle in flavour physics. Whether this is a systematic issue with the lattice QCD predictions used in the determination of exclusive measurements, an issue with the theoretical extrapolations employed by inclusive measurements, an effect of physics beyond the SM or a problem with the experimental measurements is unknown. The puzzle has resulted in a number of proposals which attempt to explain the discrepancy with an addition of a right-handed coupling to the Standard Model.

The first determination of $|V_{ub}|$ at a hadron collider and in a baryon decay has been performed using $\Lambda_b^0 \to p\mu^-\overline{\nu}_\mu$ decays, which are observed for the first time. The measurement was made using pp collision events produced by the LHC at $\sqrt{s} = 8\,\text{TeV}$ and collected by the LHCb experiment in 2012. The total integrated luminosity for the dataset was around $2\,\text{fb}^{-1}$. Using this dataset, the ratio of branching fractions of $\Lambda_b^0 \to p\mu^-\overline{\nu}_\mu$ and $\Lambda_b^0 \to \Lambda_c^+\mu^-\overline{\nu}_\mu$ decays is measured allowing for a determination of the ratio of CKM elements $|V_{ub}|/|V_{cb}|$. This provides an unforeseen avenue for constraining the CKM sector of the SM at the LHC. The measurement, $|V_{ub}| = (3.27 \pm 0.23) \times 10^{-3}$, is in agreement with the existing exclusive measurements made using $\overline{B}^0 \to \pi^+ l^- \bar{\nu}_l$ decays thereby increasing the tension between inclusive and exclusive measurements while at the same time disfavouring a right-handed coupling as an explanation for the discrepancy. The constraint on the unitarity triangle from the determination of $|V_{ub}|/|V_{cb}| = 0.083 \pm 0.06$ is consistent with current constraints on the unitarity triangle from sin2β, γ, Δm_d and Δm_s measurements.

The measurement of $|V_{ub}|$ presented in this thesis has demonstrated the feasibility of performing exclusive $|V_{ub}|$ measurements with the LHCb detector. As a result of this, a number of new exclusive $b \to u$ semileptonic and leptonic decays are now being searched for at the LHC including

$\overline{B}{}^0_s \to K^+\mu^-\overline{\nu}_\mu$, $B^- \to p\bar{p}\mu^-\overline{\nu}_\mu$ and $B^+ \to \mu^-\mu^+\mu^-\overline{\nu}_\mu$. These searches are employing similar strategies to the those developed to search for $\Lambda^0_b \to p\mu^-\overline{\nu}_\mu$ decays. A measurement of $|V_{ub}|$ from $\overline{B}{}^0_s \to K^+\mu^-\overline{\nu}_\mu$ decays could provide the most precise determination of $|V_{ub}|$ given the low uncertainty on the form factors [36] and the ability to normalise to branching fractions with a smaller relative uncertainty than that of $\Lambda^+_c \to pK^-\pi^+$. While at the LHC there are predicted to be far less $\overline{B}{}^0_s \to K^+\mu^-\overline{\nu}_\mu$ decays than $\Lambda^0_b \to p\mu^-\overline{\nu}_\mu$ decays a measurement using $\overline{B}{}^0_s \to K^+\mu^-\overline{\nu}_\mu$ decays could potentially have smaller systematic uncertainties.

Bibliography

[1] LHCb, R. Aaij *et al.*, *Determination of the quark coupling strength $|V_{ub}|$ using baryonic decays*, Nature Phys. **11** (2015) 743, `arXiv:1504.0156`.

[2] N. Cabibbo, *Unitary symmetry and leptonic decays*, Phys. Rev. Lett. **10** (1963) 531.

[3] M. Kobayashi and T. Maskawa, *CP violation in the renormalizable theory of weak interaction*, Prog. Theor. Phys. **49** (1973) 652.

[4] A. D. Sakharov, *Violation of CP in variance, C asymmetry, and baryon asymmetry of the universe*, Sov. Phys. Usp. **34** (1991) 392.

[5] BaBar collaboration, P. del Amo Sanchez *et al.*, *Study of $B \to \pi\ell\nu$ and $B \to \rho\ell\nu$ decays and determination of $|V_{ub}|$*, Phys. Rev. **D83** (2011) 032007, `arXiv:1005.3288`.

[6] BaBar collaboration, J. Lees *et al.*, *Branching fraction and form-factor shape measurements of exclusive charmless semileptonic B decays, and determination of $|V_{ub}|$*, Phys. Rev. **D86** (2012) 092004, `arXiv:1208.1253`.

[7] BaBar, J. P. Lees *et al.*, *Study of $\bar{B} \to X_u\ell\bar{\nu}$ decays in $B\bar{B}$ events tagged by a fully reconstructed B-meson decay and determination of $|V_{ub}|$*, Phys. Rev. **D86** (2012) 032004, `arXiv:1112.0702`.

[8] Belle collaboration, H. Ha *et al.*, *Measurement of the decay $B^0 \to \pi^-\ell^+\nu$ and determination of $|V_{ub}|$*, Phys. Rev. **D83** (2011) 071101, `arXiv:1012.0090`.

[9] Belle collaboration, A. Sibidanov *et al.*, *Study of exclusive $B \to X_u\ell\nu$ decays and extraction of $|V_{ub}|$ using full reconstruction tagging at the Belle experiment*, Phys. Rev. **D88** (2013) 032005, `arXiv:1306.2781`.

[10] Belle Collaboration, P. Urquijo *et al.*, *Measurement of $|V_{ub}|$ from inclusive charmless semileptonic B decays*, Phys. Rev. Lett. **104** (2010) 021801.

[11] Particle Data Group, K. A. Olive *et al.*, *Review of particle physics*, Chin. Phys. **C38** (2014) 090001.

[12] H. J. Rothe, *Lattice Gauge Theories: An Introduction; 4th ed.*, World Scientific Lecture Notes in Physics, World Scientific, Singapore, 2012.

[13] C. Dominguez, *Introduction to QCD sum rules*, Mod. Phys. Lett. **A28** (2013) 1360002, `arXiv:1305.7047`.

[14] S. L. Glashow, *Partial symmetries of weak interactions*, Nucl. Phys. **22** (1961) 579.

[15] S. Weinberg, *A model of leptons*, Phys. Rev. Lett. **19** (1967) 1264.

[16] A. Salam, *Weak and electromagnetic interactions*, in *Eelementary Particle Theory, Proceedings Of The Nobel Symposium Held 1968 At Lurem, Sweden, Stockholm*, pp. 367–377, 1968.

[17] P. W. Higgs, *Broken symmetries, massless particles and gauge fields*, Phys. Lett. **12** (1964) 132.

[18] P. W. Higgs, *Spontaneous symmetry breakdown without massless bosons*, Phys. Rev. **145** (1966) 1156.

[19] C. R. H. G. S. Guranlnik and T. W. B. Kibble, *Global conservation laws and massless particles*, Phys. Rev. Lett. **13** (1964) 585.

[20] T. W. B. Kibble, *Symmetry breaking in non-abelian gauge theories*, Phys. Rev. **155** (1967) 1554.

[21] L.-L. Chau and W.-Y. Keung, *Comments on the Parametrization of the Kobayashi-Maskawa matrix*, Phys. Rev. Lett. **53** (1984) 1802.

[22] L. Wolfenstein, *Parametrization of the Kobayashi-Maskawa matrix*, Phys. Rev. Lett. **51** (1983) 1945.

[23] C. Jarlskog, *Commutator of the quark mass matrices in the standard electroweak model and a measure of maximal* CP *nonconservation*, Phys. Rev. Lett. **55** (1985) 1039.

[24] BaBar, B. Aubert *et al.*, *Measurement of the time-dependent CP asymmetry in* $B^0 \to D^{(*)}$ *(CP) h0 decays*, Phys. Rev. Lett. **99** (2007) 081801, `arXiv:hep-ex/0703019`.

[25] BaBar, B. Aubert *et al.*, *Measurement of Time-Dependent CP Asymmetry in B0 —> c anti-c K(*)0 Decays*, Phys. Rev. **D79** (2009) 072009, `arXiv:0902.1708`.

[26] LHCb, R. Aaij *et al.*, *Measurement of the time-dependent* CP *asymmetry in* $B^0 \to J/\psi K^0_{\rm S}$ *decays*, Phys. Lett. **B721** (2013) 24, `arXiv:1211.6093`.

[27] BaBar, B. Aubert *et al.*, *Evidence for CP violation in* $B^0 \to J/\psi\pi^0$ *decays*, Phys. Rev. Lett. **101** (2008) 021801, `arXiv:0804.0896`.

[28] LHCb, R. Aaij *et al.*, *Measurement of the CKM angle* γ *from a combination of* $B^\pm \to Dh^\pm$ *analyses*, Phys. Lett. **B726** (2013) 151, `arXiv:1305.2050`.

[29] J. Charles *et al.*, *Current status of the Standard Model CKM fit and constraints on* $\Delta F = 2$ *New Physics*, Phys. Rev. **D91** (2015) 073007, `arXiv:1501.0501`.

[30] UTfit group, A. Bevan *et al.*, *UTfit homepage*, `http://www.utfit.org/UTfit/WebHome`. Accessed: 2016-05-07.

[31] CKMfitter group, J. Charles *et al.*, *CKMfitter homepage*, `http://ckmfitter.in2p3.fr`.

Accessed: 2016-04-01.

[32] K. G. Wilson, *Non-lagrangian models of current algebra*, Phys. Rev. **179** (1969) 1499.

[33] Y. Grossman, Y. Nir, and M. P. Worah, *A Model independent construction of the unitarity triangle*, Phys. Lett. **B407** (1997) 307, `arXiv:hep-ph/9704287`.

[34] A. Lenz *et al.*, *Anatomy of New Physics in $B-\bar{B}$ mixing*, Phys. Rev. **D83** (2011) 036004, `arXiv:1008.1593`.

[35] T. Aushev *et al.*, *Physics at Super B Factory*, `arXiv:1002.5012`.

[36] J. M. Flynn *et al.*, *$B \to \pi\ell\nu$ and $B_s \to K\ell\nu$ form factors and $|V_{ub}|$ from 2+1-flavor lattice QCD with domain-wall light quarks and relativistic heavy quarks*, Phys. Rev. **D91** (2015) 074510, `arXiv:1501.0537`.

[37] Fermilab Lattice, MILC, J. A. Bailey *et al.*, *$|V_{ub}|$ from $B \to \pi\ell\nu$ decays and (2+1)-flavor lattice QCD*, Phys. Rev. **D92** (2015) 014024, `arXiv:1503.0783`.

[38] A. Crivellin, *Effects of right-handed charged currents on the determinations of $|V_{ub}|$ and $|V_{cb}$*, Phys. Rev. **D81** (2010) 031301, `arXiv:0907.2461`.

[39] C.-H. Chen and S.-h. Nam, *Left-right mixing on leptonic and semileptonic $b \to u$ decays*, Phys. Lett. **B666** (2008) 462, `arXiv:0807.0896`.

[40] F. U. Bernlochner, Z. Ligeti, and S. Turczyk, *New ways to search for right-handed current in $B \to \rho l\bar{\nu}$ decay*, Phys. Rev. **D90** (2014) 094003, `arXiv:1408.2516`.

[41] A. Crivellin and S. Pokorski, *Can the differences in the determinations of V_{ub} and V_{cb} be explained by New Physics?*, Phys. Rev. Lett. **114** (2015) 011802, `arXiv:1407.1320`.

[42] W. Detmold, C. Lehner, and S. Meinel, *$\Lambda_b \to p\ell^-\bar{\nu}_\ell$ and $\Lambda_b \to \Lambda_c\ell^-\bar{\nu}_\ell$ form factors from lattice QCD with relativistic heavy quarks*, Phys. Rev. **D92** (2015) 034503, `arXiv:1503.0142`.

[43] K. G. Wilson, *Confinement of Quarks*, Phys. Rev. **D10** (1974) 2445, [,45(1974)].

[44] S. D. et al., *Hybrid Monte Carlo*, Phys. Lett. **B195** (1987) 216.

[45] B. Sheikholeslami and R. Wohlert, *Improved Continuum Limit Lattice Action for QCD with Wilson Fermions*, Nucl. Phys. **B259** (1985) 572.

[46] E. Eichten and B. R. Hill, *An effective field theory for the calculation of matrix elements involving heavy quarks*, Phys. Lett. **B234** (1990) 511.

[47] RBC, UKQCD, Y. Aoki *et al.*, *Continuum Limit Physics from 2+1 Flavor Domain Wall QCD*, Phys. Rev. **D83** (2011) 074508, `arXiv:1011.0892`.

[48] Y. Iwasaki and T. Yoshie, *Renormalization group improved action for SU(3) lattice gauge theory and the string tension*, Phys. Lett. **B142** (1984) 449, `arXiv:1011.0892`.

[49] LHCb collaboration, R. Aaij *et al.*, *Measurement of* $\sigma(pp \to b\bar{b}X)$ *at* $\sqrt{s} = 7$ *TeV in the forward region*, Phys. Lett. **B694** (2010) 209, `arXiv:1009.2731`.

[50] BaBar Collaboration, B. Aubert *et al.*, *The BaBar detector*, Nucl. Instrum. Meth. **A479** (2002) 1, `arXiv:hep-ex/0105044`.

[51] Belle Collaboration, A. Abashian *et al.*, *The Belle Detector*, Nucl. Instrum. Meth. **A479** (2002) 117.

[52] LHCb collaboration, *Detector Geometry webpage*, `http://lhcb-geom.web.cern.ch/lhcb-geom/`. Accessed: 2014-09-23.

[53] LHCb collaboration, A. A. Alves Jr. *et al.*, *The LHCb detector at the LHC*, JINST **3** (2008) S08005.

[54] LHCb Collaboration, A.-N. et al, *LHCb reoptimized detector design and performance: Technical Design Report*, Technical Design Report LHCb, CERN, Geneva, 2003.

[55] M. Kucharczyk, P. Morawski, and M. Witek, *Primary Vertex Reconstruction at LHCb*, Tech. Rep. LHCb-PUB-2014-044. CERN-LHCb-PUB-2014-044, CERN, Geneva, Sep, 2014.

[56] LHCb collaboration, R. Aaij *et al.*, *LHCb Detector Performance*, Int. J. Mod. Phys. **A30** (2015) 1530022, `arXiv:1412.6352`.

[57] LHCb collaboration, M. Adinolfi *et al.*, *Performance of the LHCb RICH detector at the LHC*, Eur. Phys. J. **C73** (2013) 2431, `arXiv:1211.6759`.

[58] LHCb collaboration, F. Archilli *et al.*, *Performance of the Muon Identification at LHCb*, JINST **8** (2013) P10020, `arXiv:1306.0249`.

[59] LHCb collaboration, R. Aaij *et al.*, *Measurement of the track reconstruction efficiency at LHCb*, JINST **10** (2015) P02007, `arXiv:1408.1251`.

[60] LHCb collaboration, J. Albrecht, V. V. Gligorov, G. Raven, and S. Tolk, *Performance of the LHCb High Level Trigger in 2012*, J. Phys. Conf. Ser. **513** (2014) 012001, `arXiv:1310.8544`.

[61] M. Williams *et al.*, *The HLT2 Topological Lines*, LHCb-PUB-2011-002.

[62] S. Tolk, J. Albrecht, F. Dettori, and A. Pellegrino, *Data driven trigger efficiency determination at LHCb*, LHCb-PUB-2014-039.

[63] T. Sjöstrand, S. Mrenna, and P. Skands, *PYTHIA 6.4 physics and manual*, JHEP **05** (2006) 026, `arXiv:hep-ph/0603175`.

[64] T. Sjöstrand, S. Mrenna, and P. Skands, *A brief introduction to PYTHIA 8.1*, Comput. Phys. Commun. **178** (2008) 852, `arXiv:0710.3820`.

[65] D. J. Lange, *The EvtGen particle decay simulation package*, Nucl. Instrum. Meth. **A462** (2001) 152.

[66] P. Golonka and Z. Was, *PHOTOS Monte Carlo: A precision tool for QED corrections in Z and W decays*, Eur. Phys. J. **C45** (2006) 97, `arXiv:hep-ph/0506026`.

[67] Geant4 collaboration, J. Allison *et al.*, *Geant4 developments and applications*, IEEE Trans. Nucl. Sci. **53** (2006) 270; Geant4 collaboration, S. Agostinelli *et al.*, *Geant4: A simulation toolkit*, Nucl. Instrum. Meth. **A506** (2003) 250.

[68] LHCb collaboration, R. Aaij *et al.*, *Study of the kinematic dependences of* Λ_b^0 *production in* pp *collisions and a measurement of the* $\Lambda_b^0 \to \Lambda_c^+\pi^-$ *branching fraction*, JHEP **08** (2014) 143, `arXiv:1405.6842`.

[69] LHCb collaboration, R. Aaij *et al.*, *Measurement of* b *hadron production fractions in 7 TeV* pp *collisions*, Phys. Rev. **D85** (2012) 032008, `arXiv:1111.2357`.

[70] Belle collaboration, A. Zupanc *et al.*, *Measurement of the branching fraction* $\mathcal{B}(\Lambda_c^+ \to pK^-\pi^+)$, Phys. Rev. Lett. **113** (2014) 042002, `arXiv:1312.7826`.

[71] BESIII, M. Ablikim *et al.*, *Measurements of absolute hadronic branching fractions of* Λ_c^+ *baryon*, Phys. Rev. Lett. **116** (2016) 052001, `arXiv:1511.0838`.

[72] W. Detmold *et al.*, $\Lambda_b \to pl^-\overline{\nu_l}$ *form factors from LQCD with static b quarks*, Phys. Rev. **D88** (2013) 014512.

[73] M. Pervin, W. Roberts, and S. Capstick, *Semileptonic decays of heavy* Λ *baryons in a quark model*, Phys. Rev. **C72** (2005) 035201, `arXiv:nucl-th/0503030`.

[74] N. Isgur and G. Karl, *Hyperfine Interactions in Negative Parity Baryons*, Phys. Lett. **B72** (1977) 109.

[75] N. Isgur and G. Karl, *P Wave Baryons in the Quark Model*, Phys. Rev. **D18** (1978) 4187.

[76] N. Isgur, D. Scora, B. Grinstein, and M. B. Wise, *Semileptonic B and D Decays in the Quark Model*, Phys. Rev. **D39** (1989) 799.

[77] B. D. Keister and W. N. Polyzou, *Useful bases for problems in nuclear and particle physics*, J. Comput. Phys. **134** (1997) 231, `arXiv:nucl-th/9611049`.

[78] C. Bourrely, I. Caprini, and L. Lellouch, *Model-independent description of* $B \to \pi l\nu$ *decays and a determination of* $|V_{ub}|$, Phys. Rev. **D79** (2009) 013008, `arXiv:0807.2722`, [Erratum: Phys. Rev.D82,099902(2010)].

[79] A. Khodjamirian, C. Klein, T. Mannel, and Y. M. Wang, *Form Factors and Strong Couplings of Heavy Baryons from QCD Light-Cone Sum Rules*, JHEP **09** (2011) 106, `arXiv:1108.2971`.

[80] A. Hocker *et al.*, *TMVA - Toolkit for Multivariate Data Analysis*, PoS **ACAT** (2007) 040, `arXiv:physics/0703039`.

[81] M. Pivk and F. R. Le Diberder, *sPlot: A statistical tool to unfold data distributions*, Nucl. Instrum. Meth. **A555** (2005) 356, `arXiv:physics/0402083`.

[82] M. Kenzie. personal communication.

[83] Heavy Flavor Averaging Group (HFAG), Y. Amhis *et al.*, *Averages of b-hadron, c-hadron, and τ-lepton properties as of summer 2014*, `arXiv:1412.7515`.

[84] M. Blanke and A. J. Buras, *Universal Unitarity Triangle 2016 and the tension between $\Delta M_{s,d}$ and ε_K in CMFV models*, Eur. Phys. J. **C76** (2016) 197, `arXiv:1602.0402`.

Appendix A.

Form factor conversions

A.1. Static LQCD form factors

This appendix provides conversions between the EvtGen convention for the $\Lambda_b^0 \to p\mu^-\overline{\nu}_\mu$ form factors (see equation 5.4 in section 5.1.2) and the HQET convention used in Reference [72] (see equation 5.6 in section 5.2.1).

$$\begin{aligned}
F_1 &= c_\gamma(F_1^{\mathrm{HQET}} - F_2^{\mathrm{HQET}}) \\
F_2 &= c_p F_1^{\mathrm{HQET}} + (2c_\gamma + c_p)F_2^{\mathrm{HQET}} \\
F_3 &= 0 \\
G_1 &= c_\gamma(F_1^{\mathrm{HQET}} + F_2^{\mathrm{HQET}}) \\
G_2 &= -c_p F_1^{\mathrm{HQET}} + (2c_\gamma + c_p)F_2^{\mathrm{HQET}} \\
G_3 &= 0 \ ,
\end{aligned} \tag{A.1}$$

where,

$$c_p = \frac{2\alpha_s}{3\pi} \ , \tag{A.2}$$

and,

$$c_{gamma} = 1 - \frac{4\alpha_s}{3\pi} \ . \tag{A.3}$$

A.2. Helicity form factors

This appendix provides conversions between the EvtGen convention for the $\Lambda_b^0 \to p\mu^-\overline{\nu}_\mu$ and $\Lambda_b^0 \to \Lambda_c^+\mu^-\overline{\nu}_\mu$ form factors (see equation 5.4 in section 5.1.2) and the helicity convention of the form factors (see equation 2.53 in section 2.3).

$$
\begin{aligned}
F_1 &= f_\perp \\
F_2 &= (f_0 - f_\perp)\frac{m_{\Lambda_b}(m_{\Lambda_b} - m_X)}{q^2} + \frac{(f_+ - f_\perp)(m_{\Lambda_b} + m_X)\, m_{\Lambda_b}}{q^2 - (m_{\Lambda_b} + m_X)^2}\left(\frac{(m_{\Lambda_b}^2 - m_X^2)}{q^2} - 1\right) \\
F_3 &= (f_\perp - f_0)\frac{m_X(m_{\Lambda_b} - m_X)}{q^2} + \frac{(f_+ - f_\perp)(m_{\Lambda_b} + m_X)\, m_{\Lambda_b}}{q^2 - (m_{\Lambda_b} + m_X)^2}\left(\frac{(m_{\Lambda_b}^2 - m_X^2)}{q^2} + 1\right) \\
G_1 &= g_\perp \\
G_2 &= (g_\perp - g_0)\frac{m_{\Lambda_b}(m_{\Lambda_b} + m_X)}{q^2} + \frac{(g_+ - g_\perp)(m_{\Lambda_b} - m_X)\, m_{\Lambda_b}}{(m_{\Lambda_b} - m_X)^2 - q^2}\left(\frac{(m_{\Lambda_b}^2 - m_X^2)}{q^2} - 1\right) \\
G_3 &= (g_0 - g_\perp)\frac{m_X(m_{\Lambda_b} + m_X)}{q^2} + \frac{(g_+ - g_\perp)(m_{\Lambda_b} - m_X)\, m_{\Lambda_b}}{(m_{\Lambda_b} - m_X)^2 - q^2}\left(\frac{(m_{\Lambda_b}^2 - m_X^2)}{q^2} + 1\right)
\end{aligned}
\tag{A.4}
$$

A.3. LCSR form factors

This appendix provides conversions between the EvtGen convention for the $\Lambda_b^0 \to p\mu^-\overline{\nu}_\mu$ form factors (see equation 5.4 in section 5.1.2) and the convention of the form factors used in Reference [79] (see equation 5.16 in section 5.2.4).

$$
\begin{aligned}
F_1 &= f_1 - \frac{(m_{\Lambda_b} + m_X)}{m_{\Lambda_b}} f_2 \\
F_2 &= f_2 + f_3 \\
F_3 &= \frac{m_X}{m_{\Lambda_b}}(f_2 + f_3) \\
G_1 &= g_1 - \frac{(m_{\Lambda_b} - m_X)}{m_{\Lambda_b}} g_2 \\
G_2 &= g_3 - g_2 \\
G_3 &= -\frac{m_X}{m_{\Lambda_b}}(g_2 + g_3)\ ,
\end{aligned}
\tag{A.5}
$$

Appendix B.

Isospin calculations for $N^{*+} \rightarrow (\Delta \rightarrow p\pi)\pi$ and $N^{*+} \rightarrow p\pi$ decays

This appendix describes how the branching fractions of $N^{*+} \rightarrow (\Delta \rightarrow p\pi)\pi$ and $N^{*+} \rightarrow p\pi$ decays are estimated from the PDG quoted branching fractions of $N^{*+} \rightarrow (\Delta \rightarrow N\pi)\pi$ and $N^{*+} \rightarrow N\pi$ using isospin arguments.

The N^{*+} baryon has isospin quantum numbers, $I = 1/2$, and $M = 1/2$. The isospin state of the N^{*+} baryon, $|I, M\rangle = |1/2, 1/2\rangle$, can be decomposed into isopin state $|i_1, m_1\rangle$ and $|i_2, m_2\rangle$ using the appropiate Clebsch-Gordan coefficients. In particular the decompositon describing $N^{*+} \rightarrow N\pi$ is given by

$$
\begin{aligned}
|1/2, 1/2\rangle &= \frac{2}{3}|1, 1\rangle|1/2, -1/2\rangle - \frac{1}{3}|1, 0\rangle|1/2, 1/2\rangle \\
|N^{*+}\rangle &\rightarrow \frac{2}{3}|\pi^+\rangle|n\rangle - \frac{1}{3}|\pi^0\rangle|p\rangle \ .
\end{aligned}
\tag{B.1}
$$

The PDG quoted branching fraction for $N^+(1440) \rightarrow N\pi$ is $\approx 65\%$. This together with isospin decomposition of the $|N^{*+}\rangle$ state given in equation B.1 implies that the branching fraction of $N^+(1440) \rightarrow p\pi^0$ is $\approx 22\%$.

In a similar manner the rates for $N^{*+} \to \Delta\pi$ transitions are determined using the following isospin decomposition of the $|N^{*+}\rangle$ state into $|\Delta\rangle$ and $|\pi\rangle$:

$$\begin{aligned} |1/2, 1/2\rangle &= \frac{1}{2}|3/2, 3/2\rangle|1, -1\rangle - \frac{1}{3}|3/2, 1/2\rangle|1, 0\rangle + \frac{1}{6}|3/2, -3/2\rangle|1, 1\rangle \\ |N^{*+}\rangle &\to \frac{1}{2}|\Delta^{++}\rangle|\pi^-\rangle - \frac{1}{3}|\Delta^+\rangle|\pi^0\rangle + \frac{1}{6}|\Delta^0\rangle|\pi^+\rangle \ . \end{aligned} \tag{B.2}$$

To estimate the rates of $N^{*+} \to (\Delta \to N\pi)\pi$ transitions the following isospin decompositions of the $|\Delta^{++}\rangle$, $|\Delta^+\rangle$ and $|\Delta^0\rangle$ are also requred:

$$\begin{aligned} |3/2, 3/2\rangle &= |1, 1\rangle|1/2, 1/2\rangle \\ |\Delta^{++}\rangle &\to |\pi^+\rangle|p\rangle \ , \end{aligned} \tag{B.3}$$

$$\begin{aligned} |3/2, 1/2\rangle &= \frac{1}{3}|1, 1\rangle|1/2, -1/2\rangle + \frac{1}{3}|1, 0\rangle|1/2, 1/2\rangle \\ |\Delta^+\rangle &\to \frac{1}{3}|\pi^+\rangle|n\rangle + \frac{2}{3}|\pi^0\rangle|p\rangle \ , \end{aligned} \tag{B.4}$$

and

$$\begin{aligned} |3/2, -1/2\rangle &= \frac{2}{3}|1, 0\rangle|1/2, -1/2\rangle + \frac{1}{3}|1, -1\rangle|1/2, 1/2\rangle \\ |\Delta^0\rangle &\to \frac{2}{3}|\pi^0\rangle|n\rangle + \frac{1}{3}|\pi^-\rangle|p\rangle \ . \end{aligned} \tag{B.5}$$

Table B.1 summarises the branching fractions of $N^+(1440) \to N\pi$ and $N^+(1440) \to (\Delta \to N\pi)\pi$ estimated using the isospin decompositions above.

$\mathcal{B}_{N^+(1440)\rightarrow X}$	PDG
$\mathcal{B}_{N^+(1440)\rightarrow N\pi}$	65%
$\mathcal{B}_{N^+(1440)\rightarrow \Delta\pi}$	25%
$\mathcal{B}_{N^+(1440)\rightarrow X}$	PDG + isospin
$\mathcal{B}_{N^+(1440)\rightarrow p\pi^0}$	22%
$\mathcal{B}_{N^+(1440)\rightarrow (\Delta^{++}\rightarrow p\pi^+)\pi^-}$	13%
$\mathcal{B}_{N^+(1440)\rightarrow (\Delta^{+}\rightarrow p\pi^0)\pi^0}$	1%
$\mathcal{B}_{N^+(1440)\rightarrow (\Delta^{0}\rightarrow p\pi^-)\pi^+}$	6%

Table B.1: Estimates for the branching fractions of a number of $N^{*+} \rightarrow N\pi$ and $N^{*+} \rightarrow \Delta\pi$ decays. The estimates are made using the PDG quoted values for $\mathcal{B}_{N^{*+}\rightarrow N\pi}$ and $\mathcal{B}_{N^{*+}\rightarrow \Delta\pi}$ together with isospin arguments.

Appendix C.

Licenses

AMERICAN PHYSICAL SOCIETY LICENSE
TERMS AND CONDITIONS

May 12, 2016

This Agreement between William Sutcliffe ("You") and American Physical Society ("American Physical Society") consists of your license details and the terms and conditions provided by American Physical Society and Copyright Clearance Center.

License Number	3866490429592
License date	May 12, 2016
Licensed Content Publisher	American Physical Society
Licensed Content Publication	Physical Review D
Licensed Content Title	Current status of the standard model CKM fit and constraints on $\mathrm{\ensuremath{\Delta}}F=2$ new physics
Licensed Content Author	J. Charles et al. ((CKMfitter Group))
Licensed Content Date	Apr 9, 2015
Licensed Content Volume Number	91
Type of Use	Thesis/Dissertation
Requestor type	Student
Format	Electronic
Portion	chart/graph/table/figure
Number of charts/graphs /tables/figures	1
Portion description	Figure 10
Rights for	Main product
Duration of use	Life of Current Edition
Creation of copies for the disabled	no
With minor editing privileges	no
For distribution to	Worldwide
In the following language(s)	Original language of publication
With incidental promotional use	no
The lifetime unit quantity of new product	0 to 499
The requesting person/organization is:	William Sutcliffe
Order reference number	None
Title of your thesis / dissertation	Determination of the quark coupling strength, Vub, with baryonic decays
Expected completion date	May 2016

Figure C.1: License to re-use Fig. 2.5 in chapter 2.

AMERICAN PHYSICAL SOCIETY LICENSE
TERMS AND CONDITIONS

May 09, 2016

This Agreement between William Sutcliffe ("You") and American Physical Society ("American Physical Society") consists of your license details and the terms and conditions provided by American Physical Society and Copyright Clearance Center.

License Number	3864811463661
License date	May 09, 2016
Licensed Content Publisher	American Physical Society
Licensed Content Publication	Physical Review D
Licensed Content Title	${\mathrm{\ensuremath{\Lambda}}}_{b}\ensuremath{\rightarrow}p{\ensuremath{\ell}}^{\ensuremath{-}}{\overline{\ensuremath{\nu}}}_{\ensuremath{\ell}}$
Licensed Content Author	William Detmold, Christoph Lehner, and Stefan Meinel
Licensed Content Date	Aug 4, 2015
Licensed Content Volume Number	92
Type of Use	Thesis/Dissertation
Requestor type	Student
Format	Electronic
Portion	chart/graph/table/figure
Number of charts/graphs/tables/figures	2
Portion description	figure 14, figure 15
Rights for	Main product
Duration of use	Life of Current Edition
Creation of copies for the disabled	no
With minor editing privileges	no
For distribution to	Worldwide
In the following language(s)	Original language of publication
With incidental promotional use	no
The lifetime unit quantity of new product	0 to 499
The requesting person/organization is:	William Sutcliffe
Order reference number	None
Title of your thesis / dissertation	Determination of the quark coupling strength, Vub, with baryonic decays
Expected completion date	May 2016
Expected size (number of pages)	150
Requestor Location	William Sutcliffe 170 Blythe Road London, United Kingdom W140HD Attn: William Sutcliffe
Billing Type	Invoice
Billing Address	William Sutcliffe 170 Blythe Road

Figure C.2: License to re-use the bottom two plots in Fig. 5.4 in chapter 5.

List of figures

List of tables